Politecnico di Torino

ScuDo
Scuola di Dottorato ~ Doctoral School
WHAT YOU ARE, TAKES YOU FAR

Doctoral Dissertation
Doctoral Program in Mechanical Engineering (33^{rd}cycle)

Effect of wear on the dynamics of structures with friction contacts

By

Lakshminarayana Reddy Tamatam

******

Supervisor(s):
Prof. Stefano Zucca
Prof. Daniele Botto

Doctoral Examination Committee:
Prof. Matthew R.W. Brake, Referee, Rice University, USA
Prof. Chao Xu, Referee, Northwestern Polytechnical University, China

Politecnico di Torino
2021

Declaration

I hereby declare that, the contents and organization of this dissertation constitute my own original work and does not compromise in any way the rights of third parties, including those relating to the security of personal data.

Lakshminarayana Reddy Tamatam
2021

* This dissertation is presented in partial fulfillment of the requirements for **Ph.D. degree** in the Graduate School of Politecnico di Torino (ScuDo).

I would like to dedicate this thesis to my parents and my sister, who have motivated me and stood by my side thick and thin.

Acknowledgements

First and foremost, I would like to express my sincere gratitude to my supervisors Prof. Stefano Zucca and Prof. Daniele Botto, for their invaluable support, timely advice and positive attitude throughout the journey. It has been a great pleasure to work under their supervision and for sharing their knowledge.

I also thank European Commission (EACEA) for providing this wonderful opportunity through Marie-Skłodowska Curie Action - Horizon 2020 ITN - Project EXPERTISE (models, EXperiments and high PERformance computing for Turbine mechanical Integrity and Structural dynamics in Europe).

I thank Mr. Federico Funghi from Baker Hughes (Nuovo Pignone s.r.l), Florence, Italy, for the support and discussion regarding the Industrial test case - Gas turbine combustor leaf seal. I also thank Dr. José Gracia and Mr. Christoph Niethammer for hosting me at High Performance Computing Center (HLRS), Stuttgart, Germany and helping me with the basics of HPC and optimizing my software.

I thank my fellow Expertise researchers and AERMEC researchers for all the discussions and fun times in and outside of the university.

Lastly, I would like to thank all my teachers, professors, family and friends who accompanied and motivated me in my whole life.

This project has received funding from the European Union's Horizon 2020 research and innovation programme under the Marie Skłodowska-Curie grant agreement No 721865.

Abstract

A typical aeroengine is made of many assemblies such as multiple stages of turbine and compressor blades, combustor section, fan section to name a few. These assemblies have many components connected by mechanical joints. These joints create interfaces which are subjected to various static and dynamic loads causing vibration during operation. In the turbomachinery field, the components are designed pushing structural envelopes for performance and efficiency. Hence, during the design phase, accurate prediction of operational vibration levels is critical. The cyclic and rotational nature of the components lead to high modal density and avoiding the resonances in the operating frequency range is next to impossible. Hence, the ideal option is to control the peak vibration levels. The crucial contacts such as bladed disk shroud contacts, blade-root joints and under-platform dampers are designed carefully to provide friction damping by allowing micro-sliding at these contacts. However, the contact interfaces introduce nonlinearity due to friction and inturn affect the dynamic response. The current linear solvers are not sufficient any more, as the results lead to great simplification and do not reflect realistic scenarios. Hence, robust nonlinear solvers considering friction contacts are necessary.

The micro-sliding at the contacts naturally leads to fretting wear. Fretting wear over a large number of cycles leads to high cycle fatigue (HCF), which is a dominant failure mode of turbomachinery components during operation. In addition, the partial or full sliding at the contacts leads to energy dissipation. This energy dissipation accumulated over a number of cycles leads to loss of material and alters the contact conditions. These new contact conditions affect the contact preload and alter the dynamic response, sometimes crossing over vibration amplitude limits. Especially, the blade tip shroud contacts are designed to provide structural rigidity, sealing and low vibration amplitudes and are assembled with a certain prestress. The fretting wear and reducing preload conditions can change the dynamic behaviour of the blade. In extremities, the blade can act as a free standing cantilever beam leading to

unfavourable conditions. Therefore, the robust routines studying nonlinear dynamic behaviour including the effect of fretting wear and the evolution of the contact interface with changing preload are today more relevant than ever.

The objective of this dissertation is two parts - numerical and experimental. The numerical part is to develop a prediction tool to simulate the nonlinear behaviour arising due to friction contact and study the impact of fretting wear and changing preload. This is achieved by developing a coupled static/dynamic harmonic balance method (HBM) with a 2D Jenkins element contact model with variable normal load and adding a wear model using wear energy approach and an adaptive wear logic to accelerate wear. The prediction tool is studied on various numerical test cases, including a realistic turbine bladed disk with shroud contacts. Furthermore, as an industrial test case, the tool is applied on a gas turbine combustor leaf seal to predict the complex nonlinear dynamic behaviour arising due to soft contacts. The software is developed in `MATLAB` and is optimized to run on a super-computer.

For the experimental part, a novel forced response test rig is designed to simulate a friction contact with varying preload arising due to fretting wear. The test rig design, system identification and a set of long-term results until full loss of contact are presented. Next, the effect of fretting wear on the friction contact evolution, hysteresis loops, contact preload and the impact on the evolution of system dynamics are discussed. The experimental results are then validated with the numerical prediction from the reformulated HBM tool.

Contents

List of Figures xvii

List of Tables xxv

Abbreviations xxvii

1 Introduction 1

1.1 Motivation. 1

1.1.1 Sources of vibrations. 2

1.1.2 Fretting wear. 4

1.1.3 Effect of fretting wear on the nonlinear dynamics. 6

1.2 Research objectives. 7

1.3 Thesis overview. 8

1.4 Overview of Project EXPERTISE. 10

2 Literature review 13

2.1 Introduction. 13

2.2 Dynamic analysis. 13

2.3 Contact models. 16

2.4 Contact stiffness. 18

2.4.1 Analytical formulation. 18

2.4.2 Numerical formulation. 19
2.5 Wear models. 20
2.6 Wear analysis. 21
2.7 Effect of wear on the nonlinear dynamic analysis. 22
2.8 Summary. 24

3 Numerical methodology **25**
3.1 Introduction. 25
3.2 Harmonic Balance Method. 25
3.2.1 Governing equations of a generic system. 26
3.2.2 Governing equations of a bladed disk with shroud contacts. . 28
3.2.3 Implementation of cyclic symmetry constraints. 31
3.3 Contact model. 34
3.4 Modelling of Wear. 38
3.5 Summary. 41

4 Numerical test cases **43**
4.1 Introduction. 43
4.2 Cantilever beam test case. 44
4.2.1 Beam description. 44
4.2.2 Results. 47
4.3 Realistic shrouded bladed disk test case. 53
4.3.1 Bladed disk description. 53
4.3.2 Results. 56
4.4 Summary. 62

5 Novel forced response test rig **63**
5.1 Introduction. 63

5.2 Novel test rig. . . . 64
5.2.1 Description of the test rig. . . . 64
5.2.2 Contact loading mechanism. . . . 68
5.2.3 Instrumentation and data acquisition system. . . . 71
5.2.4 Test plan. . . . 72
5.3 Experimental results and discussion. . . . 73
5.3.1 System identification. . . . 73
5.3.2 Effect of excitation amplitude. . . . 78
5.3.3 Determination of excitation frequency and excitation force. . 79
5.3.4 Full-range test results. . . . 82
5.3.4.1 Contact area evolution. . . . 82
5.3.4.2 Evolution of hysteresis loops and contact preload. 87
5.3.4.3 Wear volume versus dissipated energy. . . . 90
5.3.4.4 Impact of wear on the FRFs. . . . 91
5.4 Numerical prediction using nonlinear solver. . . . 94
5.4.1 Reformulation of HBM. . . . 94
5.4.2 Real surface input. . . . 98
5.5 HBM simulation and comparison with experimental results. . . . 100
5.5.1 Contact area evolution. . . . 101
5.5.2 Evolution of hysteresis loops and contact preload. . . . 104
5.5.3 Impact of wear on the FRFs. . . . 108
5.6 Summary. . . . 110

6 Industrial test case: Gas turbine combustor leaf seal 113

6.1 Introduction. . . . 113
6.2 Leaf seal description. . . . 114
6.3 Kinematic and operating envelope. . . . 116

6.4 Interpretation of the scheme of results presented using sample plots. 118
6.5 Modal analysis and forced excitation results. 120
6.5.1 Forced response results. 122
6.5.2 Contact status insights corresponding to forced response plots. 124
6.6 Discussion. 127
6.7 Summary. 131

7 High performance computing **133**
7.1 Introduction. 133
7.2 Necessity of HPC. 134
7.3 Challenges of using HPC. 135
7.4 Tips for better programming. 137
7.5 Code parallelization - identification. 137
7.6 HPC test case: Profiling. 138
7.7 External packages. 145
7.7.1 `PETSc`. 145
7.7.2 `Trilinos`. 146
7.7.3 `Python`. 147
7.8 Comments on programming languages. 149
7.9 Summary. 150
7.10 Further reading resources. 151

8 Conclusions **153**
8.1 Brief overview of the current work. 153
8.2 Key takeaways. 155
8.3 Recommendations and future works. 156
8.4 Dissemination work. 158

References 159

Appendix A Craig-Bampton Component Mode Synthesis 177

Appendix B Novel forced response test rig drawings 181

Appendix C User manual for the novel forced response test rig 201

C.1 Test rig components. 201

C.2 Instrumentation and connections. 203

C.3 Specimen preparation. 206

C.4 Setting up Testlab software for conducting experiments. 206

C.5 Additional notes. 207

Appendix D How to run a MATLAB program in a HPC 209

List of Figures

1.1 General Electric GE9X engine [1]. 1

1.2 A schematic showing multiphysical nature of tribological interactions when two bodies come into contact under various loading conditions [13]. 4

1.3 The effect of wear on the turbine blades and the change in contact interface [22, 23]. 5

1.4 An example showing very different dynamic behaviour of the same system at two different contact preloads [23]. 6

1.5 Graphical representation of expected outcome. 8

1.6 Distribution of ESRs into various work packages. 10

1.7 Timeline of the PhD journey. 11

3.1 (a) Full bladed disk with shroud contacts (b) A fundamental blade-disk sector (c) Cyclic symmetry notation. 28

3.2 A schematic view of the isolated bladed disk segment. 29

3.3 (a) Jenkin's element contact model with variable normal load, (b) A typical hysteresis loop. 34

3.4 Alternating Frequency Time (AFT) method. 36

3.5 Schematic showing the interference between the two bodies. 40

3.6 Solution flowchart showing an overview of various steps to obtain the full results with nonlinear dynamic response and fretting wear. . 42

4.1 (a) 3D Model of a cantilever beam, (b) a close-up view of the contact patch, (c) FE mesh of the beam and (d) contact elements connection. 45

4.2 Contact patch with 169 elements and the centre response node (red dot). 46

4.3 Excitation mode (first bending mode at 406 Hz) (top) and highlighting static deflection state with and without body 2 (bottom). 46

4.4 Cumulative wear depth plots at the contact patch for complete loss of contact for different ratios of $v_{w,max}/\delta_{max}$. [Numerical] 48

4.5 Response plot showing the backbone of the nonlinear response obtained with progressing wear around the first bending mode, along with reference free and stick states for $v_{w,max} = 5\%$ of δ_{max}. [Numerical] 49

4.6 A result matrix showing - starting, intermediate and ending wear iteration just before the full loss of contact for the given test case highlighting the beam physical state, cumulative wear depth until that particular wear iteration and the contact status at that wear iteration. [Numerical] 50

4.7 Wear iteration versus the number of vibration cycles plot showing the trend as the wear progresses from the start state to the complete loss of contact for $v_{w,max} = 5\%$ of δ_{max} [Note: the number of cycles is adaptive at each wear iteration]. [Numerical] 51

4.8 Maximum response at each wear iteration vs the cumulative number of cycles for different values of $v_{w,max}$. [Numerical] 52

4.9 FE model of the blade sector, boundary and loading conditions. . . . 54

4.10 (a) Highlight of the right shroud contact showing 20 contact nodes (b) Pictorial representation of the applied node-to-node contact model. 55

4.11 Nodal diameter diagram shrouded blade with stuck contact. [Numerical] 56

4.12 Response to various EO excitations with reference linear free and stick state peaks. [Numerical] 56

4.13 FRF for various excitation loads with a fixed static load $(EO = 1)$. [Numerical] 57

4.14 Tabular representation of the cumulative wear plot and contact status plot of the right shroud contact at different wear iterations until the loss of contact for given loading conditions. [Numerical] 58

4.15 Response graph showing the backbone of the nonlinear response ($EO = 1$) obtained as wear progresses around first bending mode with free and stick states for reference for $v_{w,max}$ = 5% of δ_{max}. [Numerical] 59

4.16 Impact of wear on the number of vibration cycles at each wear iteration until full loss of contact for $v_{w,max}$ = 5% of δ_{max}. [Note: the number of cycles is adaptive at each wear iteration]. [Numerical] . . 60

4.17 Maximum response at each wear iteration vs the cumulative number of cycles for different values of $v_{w,max}$. [Numerical] 60

5.1 Rendered image of the test rig along with the named reference axes. 65

5.2 Actual images of the test rig, shaker, L-separator assembly, top and bottom specimens. 66

5.3 Contact pair, mid-wear and fully worn specimens. 66

5.4 Close-up view and cross-section at the contact (a) rendered image (b) real image. 67

5.5 Exploded view of the contact loading system. 69

5.6 Cross-section of the screw-lift based contact loading mechanism. . . 70

5.7 Instrumentation of the test rig. 71

5.8 Test plan embedding surface scans, frequency sweeps and wear cycles at a fixed frequency. 72

5.9 Roving hammer impact locations to characterize the test rig and visualize the experimental mode shapes. 74

5.10 Sample mode shape visualization at two different modes for open configuration. 74

5.11 Sample mode shape visualization at two different modes for stuck configuration. 75

5.12 Frequency response function of the test rig with shaker excitation for open and closed contacts. (Tangential, Normal and Axial directions are with respect to the contact). [Experimental] 77

5.13 FRF of the test rig for various excitation at a fixed preload as recorded by the accelerometer in tangential direction (top). Corresponding receptance as recorded by the relative displacement laser (bottom). [Experimental] 78

5.14 Steady-state hysteresis loops for various excitation at 290Hz frequency. (Each curve plots 100 cycles at each excitation.) [Experimental] 80

5.15 Normal and tangential contact force at one cycle. [Experimental] . . 81

5.16 Worn surface images of upper and lower specimens at various wear intervals. [Experimental] 84

5.17 Optical images of the evolution of surface areas of upper and lower specimens. [Experimental] 85

5.18 Worn area with respect to the cumulative energy dissipated. [Experimental] 86

5.19 Evolution of hysteresis loops with wear for 16 million cycles. [Experimental] 87

5.20 Evolution of contact preload with wear until full loss of contact versus (a) energy dissipated (b) number of cycles. [Experimental] . 88

5.21 Evolution of average dissipated energy in one cycles versus number of cycles. [Experimental] 89

5.22 Total wear volume vs. cumulative energy dissipated. [Experimental] 91

5.23 Effect of wear on the FRFs subject to different excitation amplitudes for 16 million wear cycles. [Experimental] 92

5.24 Loading mechanism highlighting the linear DOFs at the moving platform and nonlinear DOFs at the contact patch. (The rest of the test rig which is not shown remains unchanged). 95

5.25 Real surface waviness after discarding roughness and the down-sampled version to match the contact area discretization of upper and lower specimens. [Experimental] 99

5.26 Evolution of contact area on upper specimen with respect to cumulative number of cycles. [Experimental (left), Numerical (right)] . . . 102

5.27 3D profile of total wear obtained through numerical simulation until full of contact. [Numerical] 103

5.28 Evolution of worn contact area - comparison of numerical simulations with experimental results. 104

5.28 Evolution of hysteresis loops with wear until full loss of contact (a) Experimental (top) (b) Numerical simulation (Simulation 1) (bottom). 105

5.29 Evolution of contact preload with wear versus (a) cumulative energy dissipated (b) cumulative number of cycles. – experimental and numerical simulation comparison. 106

5.30 Evolution of average dissipated energy in one cycle versus cumulative number of cycles - experimental and numerical simulation comparison. 107

5.31 Effect of wear on the forced response dynamics until full of contact (a) Experimental (b) Numerical simulation. 109

6.1 Gas turbine combustor leaf seal. 114

6.2 Schematic of the Leaf Seal and the boundary conditions – side view (left), Simplified schematic used for the dynamic analysis (right). . . 115

6.3 3D FE Mesh of the Leaf Seal with highlighted upper and lower contact patches (in green). 116

6.4 Kinematic envelope showing the inward and outward leaf seal inclination driven by the liner displacement. [Note the partial contact area (edges or centre) when the leaf seal is not in vertical position due to the nature of curved contact]. 117

6.5 Sample response curve showing “linear free” and “linear stick” cases corresponding to an arbitrary node DOF in order to compare the nonlinear response. [Numerical] 119

6.6 Sample response curves pattern showing the corresponding nodes of the leaf seal to follow the pattern in the results section. 119

6.7 Sample contact pressure plots and contact status plots corresponding to the upper and lower contact patches to follow the pattern in the results section. 120

6.8 (a) Leaf Seal (free condition), (b) Leaf Seal with springs (free condition), (c) Leaf Seal with springs and grounded contacts (stick condition). 120

6.9 Nonlinear response for the vertical leaf seal with static liner configuration. Top (0th harmonic); Bottom (1st harmonic) (blue – linear free state, green – linear stick state, red – nonlinear response). [Numerical] 123

6.10 Contact pressure distribution and contact status of the upper and lower contact patch corresponding to the highlighted point 1. [Numerical] 125

6.11 Contact pressure distribution and contact status of the upper and lower contact patch corresponding to the highlighted point 2. [Numerical] 125

6.12 Contact pressure distribution and contact status of the upper and lower contact patch corresponding to the highlighted point 3. [Numerical] 126

6.13 Contact pressure distribution and contact status of the upper and lower contact patch corresponding to the highlighted point 4. [Numerical] 126

6.14 Contact pressure distribution and contact status of the upper and lower contact patch corresponding to the highlighted point 5. [Numerical] 127

6.15 Typical hysteresis loop (a) and nonlinear contact force with friction limit envelope (b) in the nonlinear frequency range. [Numerical] . . 129

7.1 Overview of MPI vs OpenMP [174]. 135

7.2 Amdahl's law and parallel portion identification [177, 174]. 138

7.3 Pseudo code-flow to interpret profiler results. 140

7.4 Effect of number of Harmonics on computational speed. 144

7.5 Effect of number of harmonics on FRF. [Numerical] 144

7.6 Bird's eye view of various external packages available for parallelization. 148

C.1 Core components of the test rig. 202

C.2 Associated electrical and electronic instruments of the test rig. . . . 203

C.3 Close-up images of various connections for clarity. 205

C.4 Final view of the test rig. 205

List of Tables

4.1 Parameters for the cantilever beam test case. 44

4.2 Comparison of the impact of wear analysis with nonlinear dynamic response solver for different values of $v_{w,max}$. 52

4.3 Parameters for the shrouded bladed disk and the contact patch. . . . 53

4.4 Comparison of the impact of wear analysis with nonlinear dynamic response solver for different values of $v_{w,max}$. 61

5.1 Adopted criteria for the design of the test rig. 64

5.2 Experimental modal analysis results obtained using roving hammer test for open and stuck contact. 76

5.3 Energy dissipated per cycle for various excitation (Normal preload of 31N). 81

6.1 Tabular representation of various normalized liner displacement conditions. 118

6.2 Linear modal analysis of the flat leaf seal with free and fully stuck contact configurations. 121

7.1 Profiler results: 0+1 harmonics run on 1 HPC node. 142

7.2 Profiler results: 0+3 harmonics run on 1 HPC node. 142

7.3 Effect of number of Harmonics with 16 cores on 1 node. 143

Abbreviations

AFT	Alternating Frequency-Time
BEM	Boundary Element Method
CB-CMS	Craig-Bampton Component Mode Synthesis
DLFT	Dynamic Lagrangian Frequency-Time
DOF	Degree of Freedom
DTI	Direct Time Integration
EO	Engine Order
FEM	Finite Element Method
FRF	Frequency Response Function
GTE	Gas Turbine Engine
HBM	Harmonic Balance Method
HPC	High Performance Computing
IBPA	Inter-Blade Phase Angle
ND	Nodal Diameter
nH	Number of Harmonics
ROM	Reduced Order Model
SAM	Semi Analytical Method

Chapter 1

Introduction

1.1 Motivation.

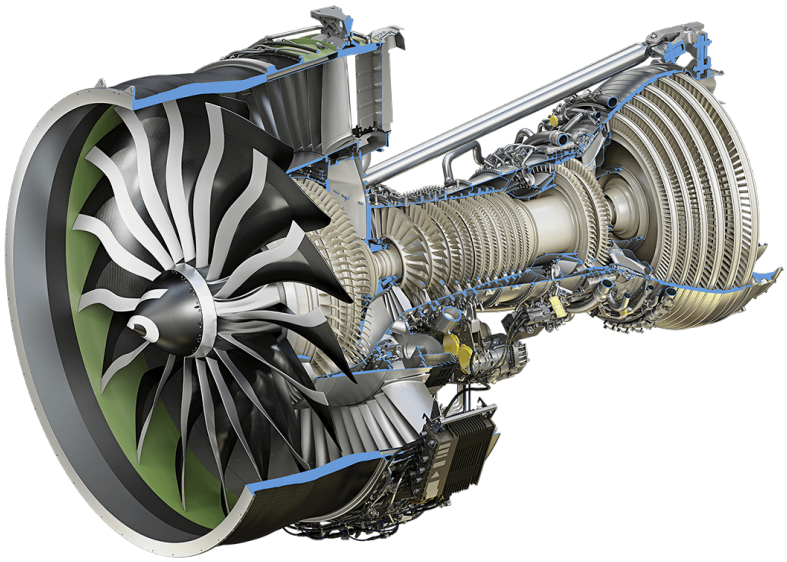

Fig. 1.1 General Electric GE9X engine [1].

A typical gas turbine aero-engine such as General Electric GE9X engine, as shown in Figure 1.1 is one of the most critical components of an aeroplane. Gas turbine engines are extensively used to power aircraft, oil and gas exploration, pumping natural gas through pipelines, power generation plants, marine propulsion, and some surface vehicles such as concept racing cars, motorcycles and locomotives. Gas

turbine and steam turbine engines are primarily used due to their very high power-to-weight ratio and small sizes for the same power rating. They have smooth rotation and balanced due to their rotating nature and can run at very high speeds on a wide variety of fuels [2–4]. However, they are more complex to design and manufacture with high engine costs due to the use of special materials. Over the decades, the design of the engines has vastly improved due to better manufacturing processes and the development of special materials leading to higher operating temperatures with improved efficiency due to cleaner combustion and lower emissions. The materials with superior high-temperature capability by the invention of single-crystal superalloys and thermal barrier coatings allow the engine to run at even higher temperatures extracting more power out of the engine.

A gas turbine typically has four main sections - compressor section with multiple stages of compressor blades, combustor section with continuous combustion chambers, turbine section with multiple stages of turbine blades and a nozzle to direct the exiting hot gases. The compressor and turbine section primarily consists of low and high-pressure sections to achieve required pressure ratios. Optionally there could be a fan section in front of the compressor section with a bypass for additional thrust generation.

The resulting engine design is a culmination of various choices made to optimize performance, efficiency, safety, environmental impact, cost of manufacture and running costs. The critical components of the engine such as bladed disks are subjected to perform at its structural, mechanical limits under various mechanical and thermal loads, which leads to high stresses in these components during operation.

1.1.1 Sources of vibrations.

There are many sources of vibrations in an engine during operation, which can be classified under structural and aeroelastic by nature [5, 6]. The components undergo high mechanical stresses during operation. The static stresses are generated due to thermal loads, static fluid pressures and rotation induced centrifugal loads. Additional dynamic loads from different sources create dynamic stresses.

Mechanical effects such as rubbing between blades and casing, torsional and lateral dynamics from the rotor shaft also create uncertainty in vibration prediction. One-off extreme events such as ingestion of foreign objects (birds or ice) and

domestic objects due to failure of individual blades can lead to major safety hazard [7]. The rotating nature of bladed disks and the acting pressure fields takes the form of a travelling wave, resulting in dynamic loading with frequencies as integer-multiples of rotational frequency. When the excitation frequency coincides with one of the natural frequency of the engine, the forced response amplitudes can reach very high levels. These resonance zones are commonly identified using Campbell diagram [8]. Campbell diagram can be analytically computed by plotting eigenfrequencies as a function of rotation speed or experimentally through waterfall plot by measuring vibration response spectrum as a function of rotation speed.

Flutter arises due to unstable aeroelastic interaction caused by the fluid-vibrating structure and cascade effect. This results in unsteady pressure distribution on the blade. Depending on the conditions, it could be self-excited and self-sustained and either reduce or increase the vibration amplitudes. Designers consciously try to avoid the flutter phenomenon from occurring and resulting in instabilities. However, unlike synchronous excitation, the resulting frequency is generally not an integer-multiple of rotational speed [5]. Other aeroelastic nature of vibrations such as vortex shedding and partial loading driven rotating instabilities must also be studied. In the end, the structural mechanical integrity is of priority, and the vibration levels are the central concern in gas turbine engine design.

To reduce the vibrations, different strategies are looked out to mitigate bladed disk vibrations. To avoid the excitation of resonant frequencies and instabilities, mechanical configuration such as blade count and dynamic characteristics such as natural frequencies are modified. Even after this, if the resonances are not entirely avoided, one can look to exploit the damping of the system. The major damping of the system is comprised of aerodynamic damping and mechanical damping, including material and mechanical joints. Generally, the material damping is relatively small, and the damping from the joints contributes the most. Hence, joint damping by friction is the most studied and implemented by allowing dry friction sliding in mechanical joints [9]. The interfaces such as blade-root joints, tip shroud contacts, midspan dampers and under-platform dampers are common ones to control the vibrations by allowing relative slip [7, 10–12]. Though proven to reduce the maximum vibration levels significantly in the operating range, it comes at the cost of wear. The energy dissipation leads to fretting wear and loss of material. Hence, knowing the long-term effects of wear and its evolution and the impact on the dynamic response is crucial.

1.1.2 Fretting wear.

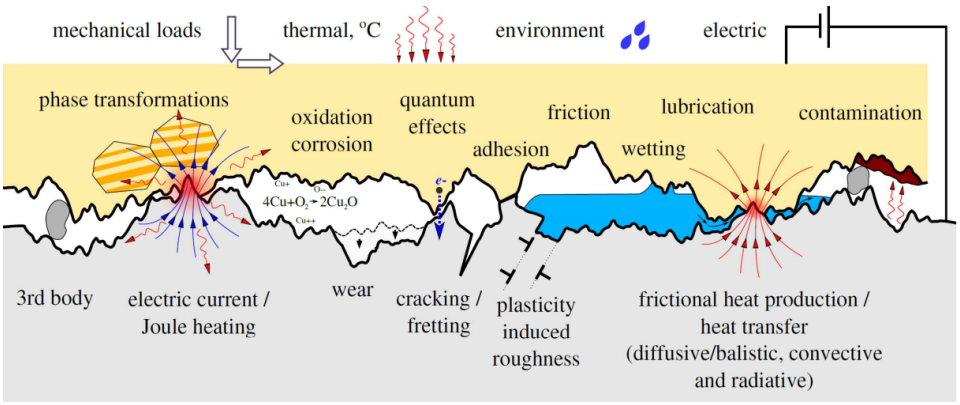

Fig. 1.2 A schematic showing multiphysical nature of tribological interactions when two bodies come into contact under various loading conditions [13].

Figure 1.2 from [13] beautifully represents the multiphysical nature of tribological interactions between two solid bodies when they come in contact under various loading conditions, including mechanical, thermal, etc. Though specifically for turbomachinery components, only a few of the indicated effects might be in play, yet this introduces great difficulty in modelling the effect on the dynamic response of the engine. So far, largely, the effect of tribology and wear was ignored while performing dynamic analysis. Out of necessity to design for better efficiency and accurate life span evaluation of the components, considering the wear effects are mandatory for high fidelity predictions. The difficulty arises due to the multi-scale interactions happening at the contact ranging from the atomic scale to the macro scale. However, the dynamic analysis largely focuses on macro-scale analysis. Considering multi-scale analysis poses unique numerical challenges and lacking fundamental knowledge given the complexity, and needs rethinking and innovative ways to perform practically feasible and computationally efficient numerical modelling. Of all the different types of wear the contacts experiences, fretting wear is the dominant one as observed experimentally. Fretting wear is defined as the damage caused to the contact interfaces due to oscillatory displacement at low amplitudes. There is no rigid definition of low amplitudes owing to the complex nature of interaction. Largely, fretting damage is classified under three categories - stick regime (low damage fretting), stick-slip regime (fretting fatigue) and gross slip regime (fretting wear) [14, 15]. The limiting condition for gross slip regime can be up to 150-300

microns of tangential relative displacement. Over the limit, it can be considered as reciprocating sliding regime with wear mechanisms identical to unidirectional sliding must be considered [14]. Hence, reciprocating sliding should not be confused with gross slip regime. The cyclic loadings induce fretting activating fretting fatigue of the material and fretting wear of the contacting surfaces. Fretting fatigue causes crack nucleation and propagation and cause high cycle fatigue (HCF). The fretting wear leads to loss of material at the contact. Due to high working temperatures and the presence of oxygen, the loss of material leads to oxide debris and corrosion. The debris can either be trapped, creating a third body layer or ejected out of the contact [16, 17]. These effects can lead to a chain of events such as delamination, damage of thermal coatings, surface fatigue, adhesive and abrasive wear [13, 18–21]. These are not yet fully understood today.

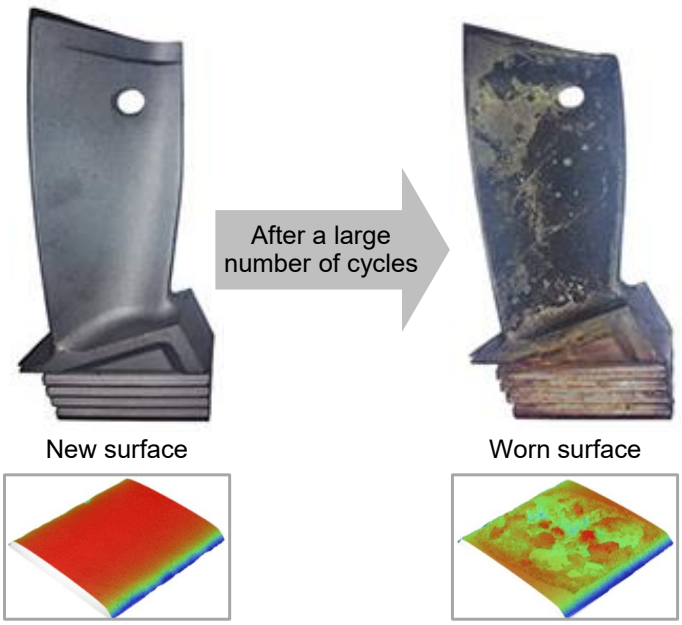

Fig. 1.3 The effect of wear on the turbine blades and the change in contact interface [22, 23].

When an engine is subjected to the operation, over an accumulated number of cycles, the contact interfaces at the mechanical joints undergo surface modifications. This is due to the contacts undergo relative sliding either by design to provide structural damping or unintended joint flexibility introduced in reality. The mechanical joints are never perfect and the definition of perfect is dependent on the subjected loads. Either they could be fully stuck under small loads or undergo relative mo-

tion under higher loads. This introduces nonlinearity into the dynamics modelling approach. For instance, Figure 1.3 shows an extreme example where the turbine blade contact conditions are drastically worsened due to various factors. Also, in a different setting, a sample scan of the contact interface studied by the author before and after wear shows a major change in the contact interface. Anticipating and incorporating these types of contact condition changes due to wear in the dynamics prediction tools are necessary. Experimental evidence such as these motivate the researchers to understand the underlying phenomenon and the best way to predict them with better confidence.

1.1.3 Effect of fretting wear on the nonlinear dynamics.

Fretting wear affects the contacting surfaces by modifying the stiffness of the contact and effective engaged area and inturn energy dissipation. These microscopic changes affect the global dynamics of the engine. Hence, studying the evolution of the joints through hysteresis loops, energy dissipation, and static preload conditions are necessary to accurately predict the changes in the nonlinear dynamic response of the structure. Due to its outlined complexity, there is very little research done so far combining the effect of fretting wear and the nonlinear dynamics. However, it is increasingly necessary to start at some point and make progress in both numerical prediction and experimental observation combining the wear and dynamics. Figure 1.4 shows an example from a friction test rig studying the effect of different contact preloads on the dynamic behaviour of the test rig [23]. All else being the same, only change in preload can greatly affect the vibration levels and shift in resonance frequencies. Hence, it is crucial to consider wear in dynamic prediction tools.

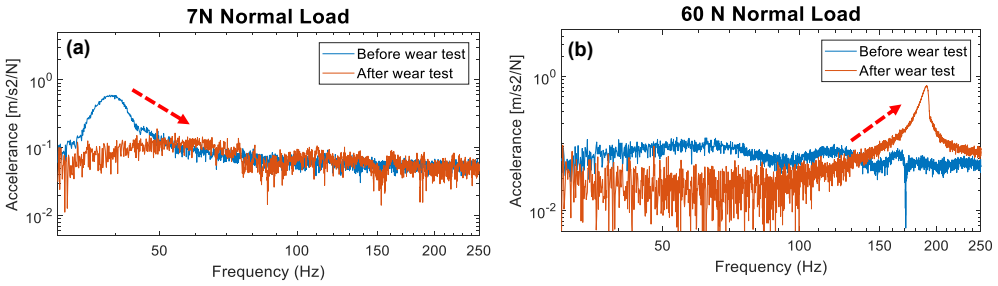

Fig. 1.4 An example showing very different dynamic behaviour of the same system at two different contact preloads [23].

1.2 Research objectives.

The main goal of this doctoral research is to understand the effect of fretting wear on the dynamics of structures with dry friction contacts. This is achieved by undertaking both numerical and experimental approach. The expected outcome is shown pictorially in Figure 1.5. To achieve the goal, the following objectives are defined:

1. Develop an efficient prediction tool to simulate the nonlinear dynamic behaviour arising due to friction contact and study the effect of fretting wear.
2. Implement a coupled static/dynamic HBM with a 2D Jenkins element contact model with varying normal load for the dynamic analysis. Add a wear model using the wear energy approach and define an accelerated wear logic. Perform various numerical test cases, including a realistic bladed disk with shroud contacts with changing preload.
3. Design and develop a novel forced response test rig to simulate a friction contact with varying preload arising due to fretting wear. Perform full-range large number of fretting cycles tests until full loss of contact by capturing intermediate contact surface scans and evolution of system dynamics.
4. Validate the experimental results of dynamics with wear with equivalent HBM numerical simulation.

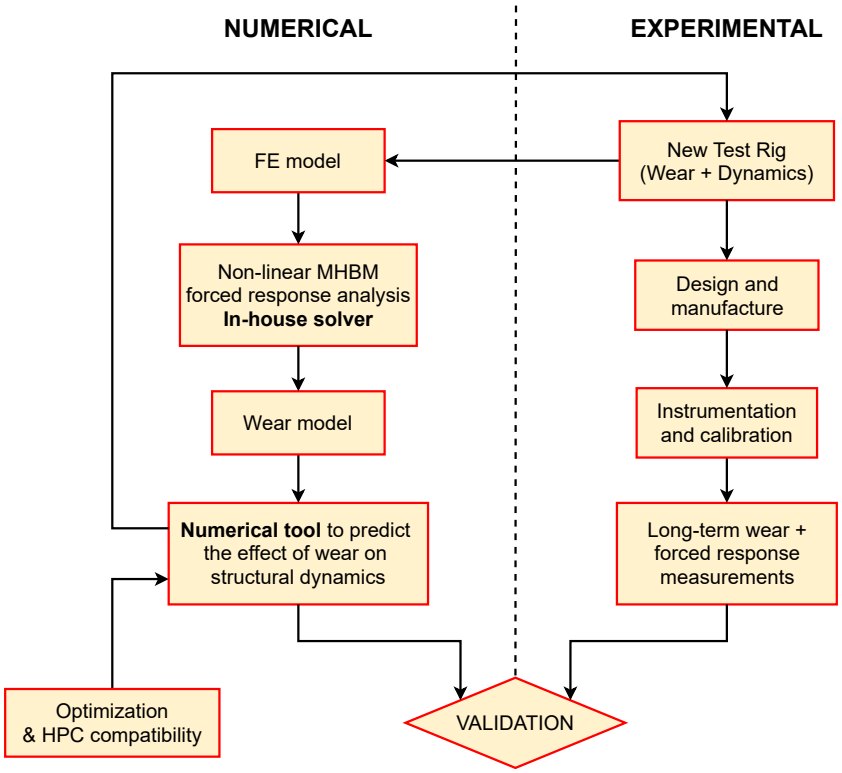

Fig. 1.5 Graphical representation of expected outcome.

1.3 Thesis overview.

The thesis is divided into eight chapters, the first one being the introduction and motivation outlined here.

CHAPTER 2 provides a brief literature review on advances in dynamic analysis considering nonlinearity arising due to friction contact. The chapter also presents various contact models, analytical and numerical methods to compute contact stiffness, wear models and fretting wear modelling approaches and the combination of fretting wear on nonlinear dynamic analysis.

CHAPTER 3 provides a numerical methodology to study the nonlinear dynamic response of a generic system with friction contact. This chapter then extends the procedure to model a turbine bladed disk with cyclic symmetry boundary conditions. The chosen contact model is then embedded in the dynamic solver. A wear energy approach based wear model is discussed, and accelerated wear using adaptive wear

logic is used to couple wear to the nonlinear solver. A comprehensive solution flow chart to perform complete analysis with wear is presented.

CHAPTER 4 presents two numerical test cases by applying the methodology developed in this research. Firstly, a simple cantilever beam with a known friction contact is used as a test case to prove the methodology. Then, the method is extended to a realistic bladed disk with shroud contact with cyclic symmetry boundary condition. Various aspects of the results such as contact interface evolution, the effect of wear on the dynamic response, the effect of accelerated wear parameter and its effect on computational time needed are discussed.

CHAPTER 5 details a novel experimental test rig designed in the context of current research. The test rig is designed to experimentally study the effect of fretting wear over millions of cycles on the long-term forced response dynamics. A contact loading mechanism with changing preload capability due to wear is used to mimic a shroud contact in a bladed disk. The experimental results presented include the test rig dynamic characterization, contact specimen surface scans and various forced response curves during different wear intervals. For the first time, long-term forced response due to fretting wear with changing preload until full loss of contact is studied. The second part of the chapter provides numerical simulation results of the experimental setup using a reformulated version of the HBM. The results are validated and compared on various aspects with respect to the evolution of contact interface, worn contact area, static preload, hysteresis loops and the forced response dynamics.

CHAPTER 6 presents an industrial test case. A gas turbine combustor leaf seal is used as a numerical industrial test case to study the complex nonlinear dynamics of the leaf seal subjected to various kinematic and operating envelope and curved nature of contacts experiencing intermittent contact. The developed HBM tool is used to model the leaf seal system and apply the contact model to study the complex dynamics exhibiting softening behaviour.

CHAPTER 7 presents a brief overview of High Performance Computing (HPC) in the context of an in-house developed HBM tool. The experience and learning from a secondment at HLRS Supercomputing Center in Stuttgart, Germany, is presented. The main objective was to improve the computational efficiency and identify bottlenecks in the HBM code relating to the dynamic analysis. A detailed performance study with one numerical test case is presented, along with the comments from a

novice user perspective. Also, a feasibility check with available third party libraries is surveyed, and its relative merits are presented.

The conclusions are presented in CHAPTER 8 by outlining the novel contributions and essential findings with a perspective on how the current work fits in the big picture of virtual analysis of the steady-state nonlinear dynamic analysis with friction contacts, including the effect of fretting wear.

1.4 Overview of Project EXPERTISE.

The current research is carried out under the framework of Horizon 2020 European Training Network (ETN), funded by the European Commission under Marie Skłodowska-Curie Actions. Project EXPERTISE is comprised of 15 early-stage researchers (ESR) divided into four work packages working on contact modelling, joint identification, structural dynamics and high-performance computing. The ESRs are spread around in various universities, research institutes and industries spanning across Europe depending on their research topic. The ultimate aim of the project is to develop advanced tools for the dynamic analysis of large-scale models of turbomachinery components to pave the way towards the virtual simulation of the whole engine. Figure 1.6 shows the distribution of ESRs into different work packages.

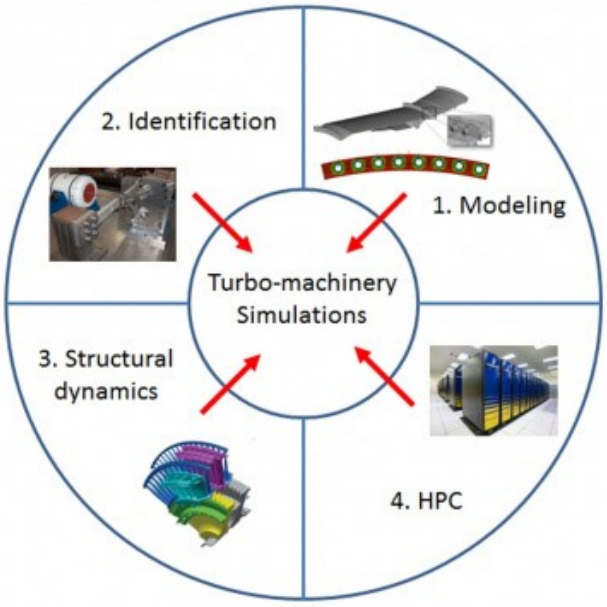

Fig. 1.6 Distribution of ESRs into various work packages.

The present research falls under Work Package 1, focussing on the advanced modelling of friction contacts as ESR3. More specifically, studying the effect of wear on the dynamics of structures with friction contacts. Figure 1.7 shows the overview of the PhD journey over a period of 3 years by connecting various aspects of research with brief pointers and external research institutes and industrial collaborations.

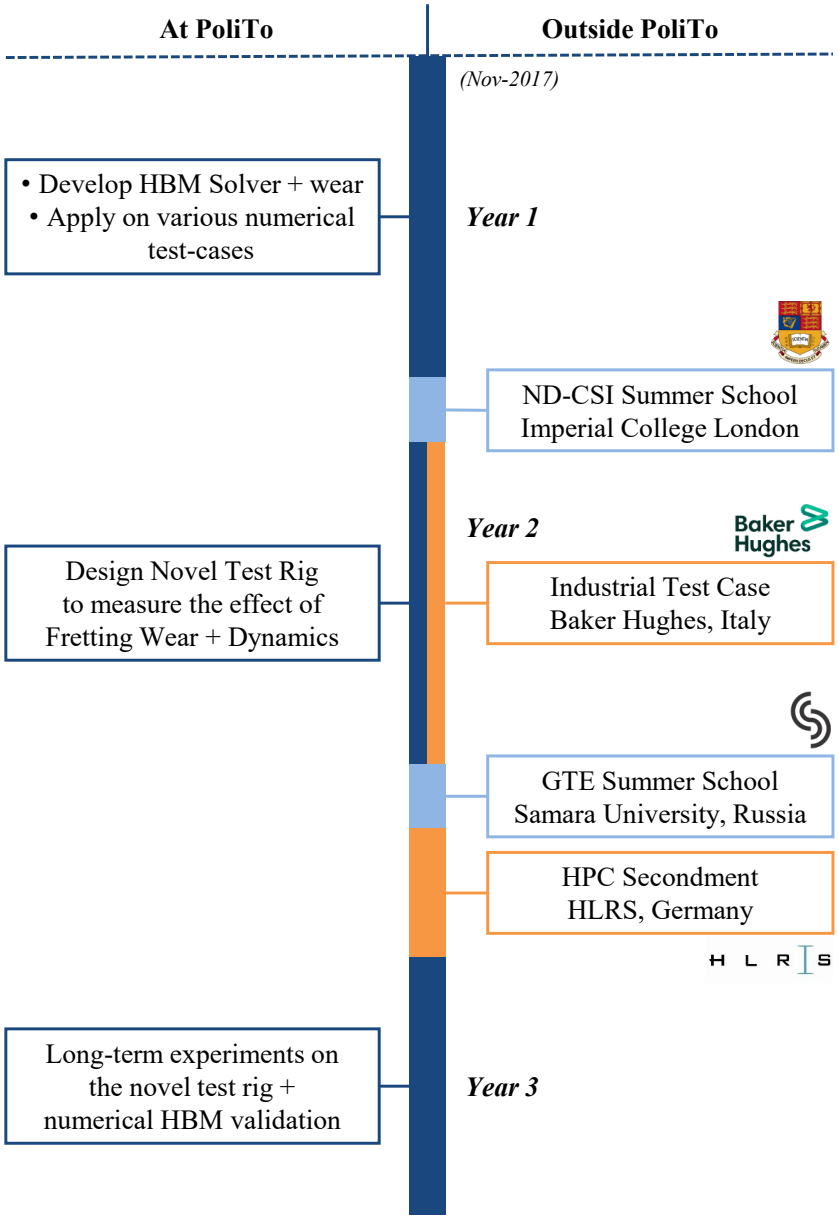

Fig. 1.7 Timeline of the PhD journey.

Chapter 2

Literature review

2.1 Introduction.

This chapter presents the overview of existing numerical and experimental works available in the literature that are relevant to the main topic of this research. The focus will be on the numerical methods to obtain the nonlinear dynamic forced response of a system by considering friction contact nonlinearity with various contact models and the techniques available for wear modelling, especially fretting wear, which is occurred during the steady-state operation. Also, the ways to incorporate the wear model into the dynamic analysis solver. Finally, the state-of-the-art methods available today to predict the nonlinear dynamics of turbomachinery structures with fretting wear will be described.

2.2 Dynamic analysis.

Knowing the accurate dynamic response of the system under excitation is vital to design reliable and efficient structures. An assembled structure such as bladed disks has many interfaces between the components. The nonlinearities could be introduced by means of geometric, material or friction contacts. The friction contact at the interfaces introduces strong nonlinearity to the system by undergoing different contact states in each vibration cycle, thereby shifting resonance frequencies and modifying damping at different modes.

Commercial codes can predict linear responses accurately, and the research codes with some calibration can predict quasi-linear or weakly nonlinear systems to a reasonable extent. However, strong nonlinearity such as introduced by friction contacts, still needs accurate prediction of realistic problems. Linearity is defined as the response of the structure being proportional to the excitation amplitude. Weak nonlinearity does not couple multiple modes and exciting only one natural frequency result in a response at that natural frequency. Anything deviating from it and resulting in multi-harmonic responses can be considered strongly nonlinear.

In the current context, the interest is to obtain the steady-state response of a system under steady-state harmonic excitation undergoing fretting wear. There exist other transient and steady-state responses for various excitations such as random excitation, impacts, sudden state changes, etc. which is out of the scope of current work.

To perform dynamic analysis considering friction contacts, one needs robust iterative solvers and accurate contact models to solve the nonlinear ordinary differential equations of motion. Various contact models are discussed in the next section.

There are primarily two ways to compute the dynamics of the system, namely, time-domain and frequency-domain based techniques. In a time-domain method ([24, 25]) such as Direct Time Integration (DTI), the solution includes first transient response and then achieve a steady-state response. But it is computationally demanding with scalability issues and is not a feasible solution for practical scenarios and large scale systems with many degrees of freedom (DOF). However, time-domain methods are useful to study responses under non-harmonic excitation as the transient results in such cases are essential.

Since the interest is to obtain steady-state response directly, a frequency-domain based Harmonic Balance Method (HBM) is more suitable. Since HBM is not commercially available, ad-hoc research codes are to be developed. HBM assumes a periodic response for a periodic excitation. The nonlinear forces and displacements are expressed as truncated Fourier series, thereby introducing approximation based on the number of retained harmonics chosen. For the verification process, DTI can be used to compare the approximate solution obtained using HBM with the exact solution. The book by Krack and Gross [26] provides a detailed description of HBM and examples of nonlinear vibration problems. HBM offers speedy solution times and is much less computationally demanding relative to the time domain methods.

Many examples of successful HBM application on various mechanical structures, including turbine bladed disks with different friction contacts can be found in the literature [10, 12, 24, 27–37]. There exists other commonly used alternatives such as Extended Periodic Motion Concept (EPMC) and quasi-static nonlinear analysis to compute the nonlinear modes and nonlinear FRFs of non-conservative systems by introducing artificial damping to make the motions periodic and to circumvent high computational costs. These methods are beyond the scope of the current work, hence, an interested reader can refer to [38–42] for detailed information. The review article by Krack et al. [7] holistically sums up the vibration prediction of bladed disks coupled by friction joints. The experimental works of [43–48] studying the dynamic response of systems with friction contact could help validate the HBM predictions.

A proven coupled static/dynamic HBM is chosen for the forced dynamic response prediction part in this current PhD work. This coupled approach allows the automatic update of the static preload distribution over the contact area during the nonlinear dynamic analysis, without any need for a separate static analysis as shown in [49, 50]. The coupled approach is more relevant in blade tip shroud analysis, where the static preload is strongly affected by the wear at tips, affecting the vibration amplitudes. The shrouds are usually assembled with an initial preload to provide certain designed structural stiffness and sealing. However, over its operational lifetime, wear could result from micro-slip at the contact interfaces and cause loss of preload and lead to fretting wear and high vibrational amplitudes. If over a certain limit, the resulting large amplitudes could be detrimental to the engine and lead to degraded functioning. In the worst case, when the preload goes to zero, the blade becomes a free-standing cantilever beam and cause excessive vibrations leading to unwanted stresses. However, the coupled approach poses a unique problem compared to separate static and dynamic routine in terms of convergence issues due to the non-uniqueness of solution due to friction in the stuck state. Ferhatoglu and Zucca [51, 52] investigated closely by studying the coupled HBM on realistic bladed disk contacts.

The detailed methodology of the HBM is presented in the next chapter.

2.3 Contact models.

The nonlinear dynamic response prediction is directly dependent on the type and parameters of the contact model being used. There has been a number of modelling approaches for structures with mechanical joints such as bladed disks. Some examples include detailed finite element (FE) models of joint components such as global bolted joint model for FE analysis [46, 53–56], continuum element approaches using zero thickness elements [57], lumped models [58, 59, 47], whole-joint modelling using hysteresis elements [60–63] and node-to-node coupling with friction contact elements [64, 50]. A very inclusive and thorough up-to-date literature review is found in the review papers of Rizvi et al. [65], Krack et al. [7] and the recent book by Brake on advances in joint modelling [9].

There are primarily two classes of friction elements, namely, node-to-node and patch-to-patch coupling friction elements. They both have their own merits and downsides. Many friction elements describe a point-to-point contact based on Coulomb friction law. These contact models are relatively easy to model and implement. The basic of them all is a 1D Jenkins element [66]. The Jenkins elements can be extended into 2D and 3D elements with coupled tangential directions and with a variable normal load. These friction elements can be one-dimensional [67], two-dimensional [59, 68, 69] or three-dimensional [70–74] where the relative motion is in one, two or three dimensions, respectively.

One limitation to the node-to-node contact elements is that they cannot capture micro-slip effects with just one element. A single element can have only three possible states in one vibration cycle, namely, stick, slip and separation. To overcome this limitation, one has to use many such friction elements in combination by discretization of the contact area to capture the micro-slip behaviour. These additional elements add complexity to the dynamic system and increase the size of the nonlinear system to be solved. To overcome this, one can use patch-to-patch models. Commonly found hysteretic models include Iwan [60, 61, 75], Bouc-Wen [76, 77, 63], Valanis [78], LuGre [79] and Dahl [80] among many others. However, these models can implicitly include micro-slip behaviour, but these models are more complex to implement compared to node-to-node elements and also require inputs to the one or more state variables they carry. These node-to-node and patch-to-patch contact models have been improvised over-time and made computationally efficient by deriving partial derivatives analytically and applied to various realistic systems with friction

interfaces such as bladed disks, under-platform dampers, blade tip shroud coupling, etc. [10, 11, 29–31, 34, 46, 47, 55, 56, 64, 81–87].

Bolted joints are an intrinsic part of almost all types of mechanical structures. Any reasonably complex structure uses these types of mechanical joints to connect different components and provide desired functionality. However, these joints can pose as highly nonlinear and complex to accurately model due to various parameters such as contact area, number of bolts, contacting interface surface properties, excitation load, preload, bolt, tension, distance between the bolts, etc. There has been intense research going on to understand the mechanics and dynamics of bolted joints experimentally and to model them numerically using accurate contact models and computationally efficient techniques. Accurate modelling of bolted joints allow high fidelity prediction of the global dynamics of the structure and also help in determining the remaining life of the structure. Catalfamo et al. [88] studied the effects of experimental methods on the measurements of dynamics of a bolted joint structure. Dossogne et al. [89] studied the influence of interface geometry on the structural dynamic response experimentally. Brake et al. [90] provided detailed observations of variability and repeatability in jointed structures using Brake-Reuß beam. Mathis et al. [91] provided a detailed review of damping models on bolted joints. Multiple studies have studied the effect of contact pressure on the jointed interfaces during dynamic excitation [92, 87]. Brøns et al. [93] performed an interesting study using a high-speed camera to look closely at the bolted joints and the behaviour during dynamic excitation for different bolt tightening settings. Porter et al. [94] assessed the uncertainties in friction models of bolted structures. Balaji et al. [95–97] have studied the accurate and efficient way of joint modelling using surrogate system hypothesis, whole joint modelling and selective remeshing of interfaces and applying hyper-reduction techniques for small displacements at the contacts. Li et al. [20] have studied the fretting wear at bolted joint interfaces. The research is still ongoing to accurately model the joint connections, and adding the time effects of fretting wear only complicates the accurate numerical modelling. Linearising the joints is acceptable for small excitations; however, it is a severe limitation for efficient designs and high-performance components such as turbomachinery and aerospace applications.

The commercial FE solvers available today do not include these advanced contact models yet. Hence, the interested researchers have to code themselves and embed them in their own nonlinear solvers.

In this current research, 2D Jenkins element with a variable normal load is implemented, and the detailed working is presented in the next chapter.

2.4 Contact stiffness.

The 2D Jenkins contact model with variable normal load discussed above has three key input parameters, namely, friction coefficient (μ), normal contact stiffness (k_n) and tangential contact stiffness (k_t). The friction coefficient is obtained experimentally and dependent on the material of the contact pair. For the steady-state excitation of mechanical structures, it is seen that the friction coefficient establishes rather quickly and assumes a constant value within the first few cycles and stays constant throughout the test for dry contacts [23, 98]. However, obtaining normal and tangential contact stiffness is not that straightforward. The tangential contact stiffness can be obtained through experiments by calculating the slope of the stick curve of the hysteresis loops. For a generic contact geometry and different conditions, one has to resort to analytical and numerical formulations.

2.4.1 Analytical formulation.

The surface tractions of the elastic bodies under normal and shear loading conditions are necessary to compute the normal and tangential contact stiffness. The book on contact mechanics by KL Johnson [99] discussed in detail the elastic half-space theory, its assumptions, point loading, line loading, normal contact and tangential loading of elastic and inelastic bodies and also the Hertzian and Non-Hertzian contact of elastic bodies. This was a seminal work that led to many improved and more realistic formulations. Jaeger [100] proposed a new principle in contact mechanics by assuming a flat punch with a sharp edge on one end and a rounded edge on the other end. Later, Ciavarella et al. [101] proposed an analytical formulation for a more realistic flat punch with rounded edges as compared to the classic rigid-flat punch idealization. This study compared the differences between the old and new formulation and the effect of roundedness. This work was widely used in subsequent researches.

Albeit, the works so far was in the 2D formulation. Allara [102, 103] in his research work extended the previous 2D formulation to a 3D flat punch with rounded

edges. He successfully applied the new formulation to analyze the blade-root joint contacts in bladed disks with analytical results and experimental validation with a test rig.

Andresen et al. [104] proposed closed-form solutions for general asymmetrical half-plane contact problems with a tilted punch and rounded edges by considering normal and shear loads along with moments. In the subsequent study [105], they also studied half-plane contact problems considering friction subjected to alternating normal and shear loads in the steady-state. Alternating loads is more relatable to the turbomachinery contacts undergoing fretting wear with relative sliding at steady-state conditions. As a next step, they also studied [106] the steady-state cyclic behaviour of a half-plane contact under partial slip subject to the combination of normal and shear load, moment and differential bulk tension.

Recent advances in improved formulations include the works of Chauda and Segalman [107, 108] studying two-dimensional contact analysis using trigonometric polynomials and a first violation contact algorithm that correctly captures history dependence will aid to understand better and extract the contact information more accurately.

In the current research, the 3D analytical formulation by Allara [102] based on the 2D analytical contact formulation of Ciavarella et al. [101] is used to compute the normal and tangential contact stiffness of the contacting bodies. The computed contact stiffness for the whole joint interface is then distributed over the contact area using nodal distribution.

2.4.2 Numerical formulation.

Analytical formulations provide a theoretical foundation; however, they are limited to simple contact geometries. In reality, the contacting bodies have interfaces with complex profiles and a generic formulation to compute the contact stiffness is necessary. To this end, Botto and Lavella [109] proposed a computationally efficient lossless static reduction technique to characterize the contact and obtain normal and tangential contact stiffness. Ciuffreda [110] in his thesis extended Botto's formulation to study the effect of fretting wear on the evolution of tangential contact stiffness.

Armand et al. [111] proposed a Boundary Element Method (BEM) based Semi-Analytical Method (SAM) solver to compute contact stiffness for a generic contact under various types of loads for complex contact conditions. The study first compared the results with analytical formulation with standard spherical contact and found the results to be of excellent correlation. Also, the study proved to be computationally very efficient and low memory usage compared to refined FE models due to the usage of BEM based methodology.

2.5 Wear models.

To predict the effect of fretting wear on the forced response of a system, wear has to be first evaluated. Meng and Ludema [112] have provided an exhaustive summary of many wear models existing in the literature. These models can be used to directly compute the wear volume, which is the volume of material removed during the fretting wear. This can be used to update the new contact conditions after every few cycles and study the change in nonlinear dynamic analysis.

The most famous model for wear modelling is the one proposed by Archard for adhesive wear known as Archard's law [18]. It is known for its simplicity, and well correlation to the experimental evidence with a wide variety of materials under dry conditions [113]. Rabinowicz [114] extended the law to abrasive wear. These models assume that the wear is caused by adhesion between asperities and leads to fracture.

Thermodynamic wear models: Friction and wear caused due to its inherent irreversible processes cause disorder to a system by generating irreversible entropy to comply with the second law of thermodynamics. Klamecki [115] showed that friction is a dissipative process and presented a thermodynamic model by idealizing as a single body to which work and heat are applied and mass transfer occurs. Doelling et al. [116] and Ling et al. [117] studied the relation between the normalized wear and normalized entropy flow and reported a linear relationship between them. Zmitrowicz [118] built a thermodynamic model including an interfacial layer considering the third body. It is more complex as it considers a set of dependent variables to describe material properties, and the contact is derived from this model. Using entropy as a fundamental measure of degradation, Bryant et al. [119] proposed a thermodynamic characterization of degradation dynamics. They showed the material degradation

could be related to the production of entropy by the irreversible dissipative processes that are the signature of degradation. There are more models considering interfacial fluid [120], which is beyond the scope of the current work as the interest is in dry contacts.

In recent years, the wear energy approach [121] has got good traction and many researchers have implemented the wear model successfully. Because fretting is an event that involves atleast three different wear mechanisms simultaneously, it is well suited to the types of models that are formulated around thermodynamic or energetic concerns. Fouvry et al. [122] investigated the connection between the wear volume and the cumulative energy dissipation of a tribological system. They experimentally showed a linear relationship between the worn volume and the dissipated energy. The wear energy approach is easy to implement because the energy dissipated can be directly computed by taking the area under the hysteresis loops. Multiple studies have shown the wear energy approach in good agreement with the experimental results [123, 124].

For the current research, the wear energy approach will be considered given the simplicity to embed to the nonlinear solver with no additional computation cost and also for the reputation of accuracy and good correlation with experiments. The two key inputs - (a) energy dissipation, which can be obtained by taking the area under the hysteresis loops, both numerically and experimentally, and directly compared with each other, and (b) wear energy coefficient (α) can be easily obtained experimentally by taking the slope of the total worn area against the cumulative energy dissipation. The working principle of the wear energy approach and embedding to the nonlinear solver is discussed in the next chapter.

2.6 Wear analysis.

After choosing a wear model, a means to implement the wear analysis is needed. Finite Element Method (FEM) is the most commonly used tool to discretize the system and perform analysis with wear, which is modular and provide good accuracy and stability.

Boundary Element Method (BEM) is an alternative to FEM, which models by considering only boundary interactions. Sfantos et al. ([125, 126]) have proposed the

BEM techniques for wear simulation and optimization methods using incremental sliding BEM. Several other notable studies have provided methods to characterize and predict fretting wear using various numerical approaches and based on experimental evidences such as [13, 20, 122–124, 127–131, 16].

There exist many other interesting methods such as Finite Discrete Element Model (FDEM) in which multiple finite element bodies interact as distinct bodies to study fretting wear [132], Semi-Analytical Methods (SAM) [133, 134], eXtended Finite Element Method (X-FEM), which uses a mesh-less method to deal with discontinuities such as cracks and voids [135], Smoothed Particle Hydrodynamics (SPH) which is a mesh-less method used to study the solid and fluid dynamics problems such as wear study of a machining tool [136–138], Movable Cellular Automata (MCA) using the advantages of both discrete element method and cellular automaton with tribological applications such as wear in engines and rail-wheel contacts [139, 140] and Molecular Dynamics to simulate micro-scale wear mechanisms going up to atomic scale [141]. The interested reader can refer to the references as the detailed description is beyond the scope of the current work. In the current work, a Finite Element Method will be used to discretize the mechanical system at hand using commercial software and the wear energy approach for fretting wear will be used.

2.7 Effect of wear on the nonlinear dynamic analysis.

Knudsen [142, 143] was among the first ones to study the effect of fretting wear on vibro-impact dynamics of nonlinear impact oscillators. The considered cantilever beams were modelled as Bernoulli beams. Newmark's time integration technique was used for dynamic analysis, and the work-rate concept was used to quantify wear. The analysis was carried out for both harmonic and random excitation. Global and local stability and bifurcation analysis were done to characterize the vibro-impacts. However, the methodology is limited to small systems with fewer DOFs, as for the large systems, the methodology would be computationally very demanding and might take a long time to reach a steady-state using time integration techniques.

Jareland et al. [83] studied the effects of wear and mistuning on bladed disks. They used a simplified bar model presented by themselves for the friction elements to represent under-platform dampers. They used HBM and wear energy approach

for wear computation. For a tuned system, they showed that wear led to a decrease in vibration amplitude when micro-slip is dominating and wear led to an increase in vibration amplitude when macro-slip is dominating. For the mistuned case, they experimentally observed that the vibration amplitude increased slightly with the wear in dampers.

Petrov [144] simulated the effect of progressive loss of friction dampers based on dissipated energy at the contact in a tuned and mistuned bladed disk system. He showed that for a tuned case, the resonance amplitudes of the blade with lost damper and adjacent blades increased significantly, and the far away blades were barely affected. For a mistuned case, only blades with lost dampers saw changes in vibration amplitudes.

Salles et al. [145–148] are one of the first studies to use numerical analysis coupling dynamics and wear. They used frequency-domain based Dynamic Lagrangian Frequency Time (DLFT) and HBM techniques and a multi-scale approach to analyze the effect of fretting wear at the under-platform dampers and at the blade root joints. They used slow scale for fretting wear phenomena and fast scale for dynamics evolution. The variables are decomposed into Fourier series assuming a steady-state, and an Alternating Frequency Time (AFT) technique is used to compute the nonlinear contact forces. In this regard, Armand et al. [149, 134] implemented a multi-scale approach by using the combination of semi-analytical method solver using BEM for fretting wear predictions and HBM technique to predict the effect of wear numerically on the dynamic response. Later they also extended the work [150] by incorporating the roughness into the contact area and predicted the effect of fretting wear on the dynamic response of the system. The present authors themselves studied the effect of fretting wear on the dynamics using a coupled HBM and wear energy approach on various numerical test cases [151, 152].

Other notable researchers evaluated fretting wear as a result of vibrations of the systems rather than the effects of wear on the dynamics of the systems [153–155].

Albeit, the studies addressing coupled wear and dynamics are so far only numerical predictions. Today's need is to experimentally assess the effect of fretting wear on the dynamics of structures and validate the proposed numerical models.

To the author's knowledge, Fantetti et al. [23] is the only research that experimentally studied the effect of wear on the evolution of system dynamics with a friction contact. They then validated using a constitutive numerical model - modified

Bouc-Wen model [76, 77]. They presented the evolution of fretting wear during the running-in phase leading up to steady-state and its corresponding impact on the dynamics by means of intermediate hammer tests. The study was done from a very short number of cycles up to a few millions cycles. The study visually depicted the fretting wear generated at the contact has on the resonant frequencies and damping of the test rig.

Other than that, there are a few fretting test rigs specifically designed to study the fretting wear and its effects on bladed disk contacts. The two versions of fretting rigs ([130, 156]) at Politecnico di Torino AERMEC were designed to study the effect of a large number of wear cycles also at high temperatures on the contact parameters, namely friction coefficient, contact stiffness and energy dissipation. Studying the effect of wear on the dynamics of these rigs is not so straightforward as they were not designed with that intention. The fretting test rig at Imperial College London [157] was built to study the effect of fretting wear and the evolution of contact stiffness over a small to a large number of wear cycles. It is good to note that these test rigs perform under constant normal load throughout the tests and to the author's knowledge there is no possibility to study the effect of changing normal load conditions within the test. In [23] the effect of wear on the dynamics of the friction rig was investigated together with the steady-state evolution of contact parameters.

Throughout the current work, a combination of coupled static/dynamic HBM with a wear energy approach to predict fretting wear is used.

2.8 Summary.

This chapter presented a brief literature review concerning the dynamic analysis of a generic structure with friction contact nonlinearity. Also, various available contact models, comments on the analytical and numerical formulation for contact stiffness, various wear models and fretting wear analysis, and finally coupling the effect of wear on the nonlinear dynamic analysis was discussed.

Chapter 3

Numerical methodology

3.1 Introduction.

The purpose of this chapter is to describe the coupled static/dynamic Harmonic Balance Method (HBM) methodology in detail in relation to the dynamics of a structure with a 2D Jenkins element with a variable normal load contact model. Then a wear formulation - wear energy approach is coupled to the solver, and an acceleration wear technique using an adaptive wear logic is presented. Finally, bringing all the individual pieces together, a flowchart is presented to obtain a full solution.

3.2 Harmonic Balance Method.

HBM is a frequency-domain based technique to solve a set of time-domain nonlinear ordinary differential equations by converting them into frequency-domain nonlinear algebraic expressions by expressing the displacements and forces as truncated Fourier series. When only a fundamental harmonic is considered, it is called classical HBM. But more harmonics are needed to be considered in the presence of strong nonlinearities such as friction contact. The HBM formulation with multiple harmonics is called multi-HBM. The following sections provide the methodology for a generic system and extend it bladed disks to include a cyclic symmetry boundary condition by taking only the blade-disk fundamental sector.

3.2.1 Governing equations of a generic system.

The governing equation of motion of a generic system with friction contact interfaces is written as:

$$\mathbf{M}\ddot{\mathbf{Q}}(t)+\mathbf{C}\dot{\mathbf{Q}}(t)+\mathbf{K}\mathbf{Q}(t)=\mathbf{F}(t)+\mathbf{F}_c\left(\mathbf{Q},\dot{\mathbf{Q}},t\right) \tag{3.1}$$

where $\mathbf{M}$ is the mass matrix; $\mathbf{C}$ is the viscous damping matrix and $\mathbf{K}$ is the stiffness matrix, where $\mathbf{M},\mathbf{C},\mathbf{K}\in\mathbb{R}^{\mathrm{N}\times\mathrm{N}}$. $\mathbf{Q}(t)\in\mathbb{R}^{\mathrm{N}\times 1}$ is a nodal displacement vector; $\dot{\mathbf{Q}}$ is the time derivative of $\mathbf{Q}$; $\mathbf{F}(t)\in\mathbb{R}^{\mathrm{N}\times 1}$ is the excitation force vector and $\mathbf{F}_c\left(\mathbf{Q},\dot{\mathbf{Q}},t\right)\in\mathbb{R}^{\mathrm{N}\times 1}$ is the nonlinear contact force interaction vector. The components of the displacement vector $\mathbf{Q}$ is given by:

$$\mathbf{Q}=\left[\mathbf{q}_c{}^T\ \mathbf{q}_a{}^T\ \mathbf{q}_o{}^T\right]^T \tag{3.2}$$

where $\mathbf{q}_c$, $\mathbf{q}_a$ and $\mathbf{q}_o$ are the displacements of contact interface node DOFs, accessory node DOFs, and other node DOFs of the system respectively. $\mathbf{q}_a$ node DOFs include input and output node DOFs.

Since the contact DOF $\mathbf{q}_c$ and the accessory DOF $\mathbf{q}_a$ are usually much smaller in comparison to the other DOF $\mathbf{q}_o$, a reduction of the size of the nonlinear model is typically performed before computing the nonlinear solution. Usually FE models are very finely discretized to obtain the stress states. However, one can still use the same fine FE models and apply reduced order modelling to dynamically reduce the size of the system. There are different Component Mode Synthesis (CMS) available such as Craig Bampton method (CB) [158] and MacNeal and Rubin method (MR) [159, 160]. In this work, the classical CB-CMS reduction method is applied, retaining the contact interface DOFs $\mathbf{q}_c$ and $\mathbf{q}_a$ accessory DOFs as physical coordinates – cumulatively called as master nodes, and adding a certain number of fixed-interface modes η. The detailed procedure of CB-CMS is provided in the Appendix A.

$$\mathbf{q}=\left[\mathbf{q}_c{}^T\ \mathbf{q}_a{}^T\ \eta^T\right]^T \tag{3.3}$$

where $\mathbf{q}\in\mathbb{R}^{\mathrm{n}\times 1}$ and $\mathrm{n}\ll\mathrm{N}$. The equation 3.1 can be rewritten as:

$$\mathbf{m}\ddot{\mathbf{q}}(t)+\mathbf{c}\dot{\mathbf{q}}(t)+\mathbf{k}\mathbf{q}(t)=\mathbf{f}(t)+\mathbf{f}_c(\mathbf{q},\dot{\mathbf{q}},t) \tag{3.4}$$

where $\mathbf{m}$ is the mass matrix; $\mathbf{c}$ is the viscous damping matrix; $\mathbf{k}$ is the stiffness matrix, where $\mathbf{m},\mathbf{c},\mathbf{k}\in\mathbb{R}^{n\times n}$. $\mathbf{q}(t)\in\mathbb{R}^{n\times 1}$ is a nodal displacement vector; $\mathbf{f}(t)\in\mathbb{R}^{n\times 1}$ is the excitation force vector and $\mathbf{f}_c(\mathbf{q},\dot{\mathbf{q}},t)\in\mathbb{R}^{n\times 1}$ is the nonlinear contact force interaction vector obtained after performing the Craig-Bampton reduction method.

To solve the equation 3.4 for periodic excitation using HBM ([26]), the periodic quantities (i.e. displacements and forces) with an angular frequency of ω are expressed as truncated series of harmonic terms:

$$\begin{aligned}\mathbf{q}(t) &= \Re\left(\sum_{h=0}^{H}\hat{\mathbf{q}}^{(h)}e^{ih\omega t}\right);\quad \mathbf{f}(t) = \Re\left(\sum_{h=0}^{H}\hat{\mathbf{f}}^{(h)}e^{ih\omega t}\right);\\ \mathbf{f}_c(\mathbf{q},\dot{\mathbf{q}},t) &= \Re\left(\sum_{h=0}^{H}\hat{\mathbf{f}}_c^{(h)}(\hat{\mathbf{q}})\,e^{ih\omega t}\right)\end{aligned} \tag{3.5}$$

where $\Re(\cdot)$ represents the real part of the quantity.

By applying Galerkin's procedure with the multi-harmonic approximation, the time domain nonlinear differential equation 3.4 is transformed into a nonlinear algebraic equation with Fourier coefficients as defined in equation 3.5, and the balance equation is written as:

$$\mathbf{d}^{(h)}\hat{\mathbf{q}}^{(h)} = \hat{\mathbf{f}}^{(h)}+\hat{\mathbf{f}}_c^{(h)}\ with\ h=0..H \tag{3.6}$$

where $\mathbf{d}^{(h)} = \left(-(h\omega)^2\mathbf{m}+ih\omega\mathbf{c}+\mathbf{k}\right)$ is the h^{th} dynamic stiffness matrix of the system. The equation 3.6 consists the static $(h=0)$ and dynamic $(h=1..H)$ equations of the system coupled to each other by Fourier coefficients of the nonlinear contact force $\hat{\mathbf{f}}_c$ depending on the Fourier coefficients of the displacement $\hat{\mathbf{q}}$. The number of harmonics H is chosen in a way to approximate the dynamics of the structure with sufficient accuracy. The residual equation is formulated by rewriting equation 3.6 as:

$$\mathbf{RES}^{(h)} = \mathbf{d}^{(h)}\hat{\mathbf{q}}^{(h)} - \hat{\mathbf{f}}^{(h)} - \hat{\mathbf{f}}_c^{(h)} \; with \; h = 0..H \tag{3.7}$$

3.2.2 Governing equations of a bladed disk with shroud contacts.

One can expand the previous methodology to a bladed disk with a shroud contact interface. Figure 3.1 shows a full bladed disk with identical sectors, a fundamental blade-disk sector and a schematic view of cyclic symmetry notation. The bladed disk is a tuned system made of identical fundamental sectors arranged in a cyclical manner. Since the bladed disks are cyclic in nature, one can exploit the analysis by reducing the full bladed disk model to a single fundamental sector by applying proper boundary conditions at the sector interfaces in the nonlinear dynamic analysis [161, 10].

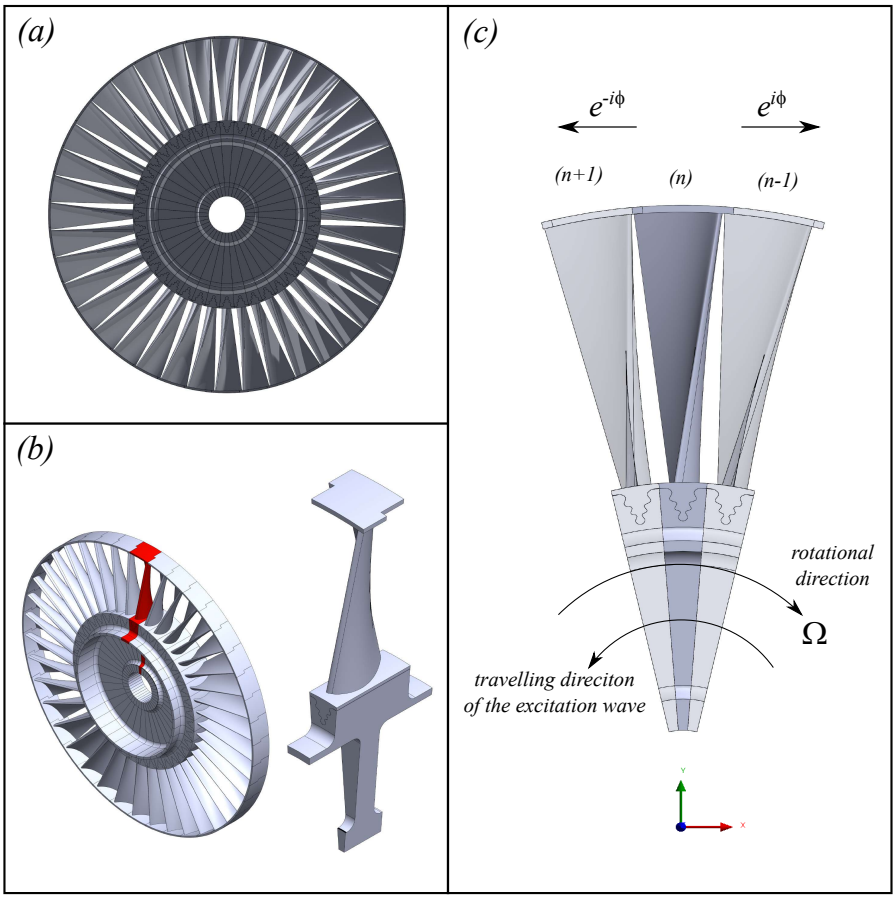

Fig. 3.1 (a) Full bladed disk with shroud contacts (b) A fundamental blade-disk sector (c) Cyclic symmetry notation.

The equation of motion for a tuned bladed disk with contact interfaces with N_s sectors can be obtained by modifying equation 3.1 as:

$$\begin{gathered}\mathbf{M}^{(n)}\ddot{\mathbf{Q}}(t)+\mathbf{C}^{(n)}\dot{\mathbf{Q}}(t)+\mathbf{K}^{(n)}\mathbf{Q}(t)= \\ {}^{(n)}\mathbf{F}(t)+{}^{(n)}\mathbf{F}_{c,l}\left(\Delta\mathbf{q}_{c,l},\Delta\dot{\mathbf{q}}_{c,l},t\right)+{}^{(n)}\mathbf{F}_{c,r}\left(\Delta\mathbf{q}_{c,r},\Delta\dot{\mathbf{q}}_{c,r},t\right)\end{gathered} \tag{3.8}$$

where $n = 1..N_s$ is a sector number; $\mathbf{M},\mathbf{C},\mathbf{K} \in \mathbb{R}^{\mathrm{N}\times\mathrm{N}}$ denote the mass matrix, viscous damping matrix and the stiffness matrix respectively of n^{th} isolated bladed disk segment without cyclic boundary conditions; ${}^{(n)}\mathbf{Q}(t) \in \mathbb{R}^{\mathrm{N}\times 1}$ is a nodal displacement vector; ${}^{(n)}\mathbf{F}(t) \in \mathbb{R}^{\mathrm{N}\times 1}$ is the excitation force vector acting on n^{th} blade, and ${}^{(n)}\mathbf{F}_{c,l}$, ${}^{(n)}\mathbf{F}_{c,r} \in \mathbb{R}^{\mathrm{N}\times 1}$ are nonlinear contact force interaction vectors at the shrouds of the left and the right adjacent sectors respectively depending on the relative displacements and velocities. These contact forces depend on the relative displacements in a nonlinear fashion at the shroud contact.

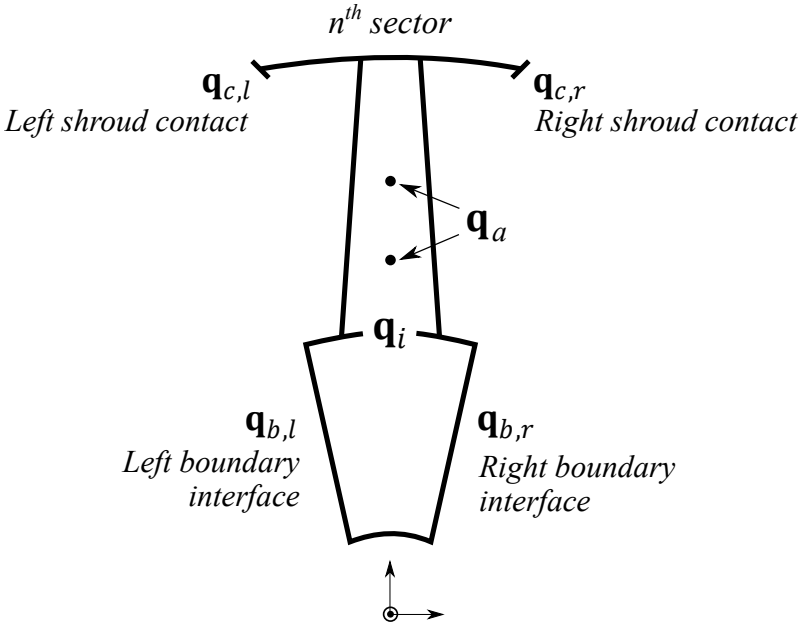

Fig. 3.2 A schematic view of the isolated bladed disk segment.

The displacement vector at n^{th} isolated bladed disk segment is written as:

$${}^{(n)}\mathbf{Q} = \left[{}^{(n)}\mathbf{q}_{b,l}{}^{T}\ {}^{(n)}\mathbf{q}_{b,r}{}^{T}\ {}^{(n)}\mathbf{q}_{a}{}^{T}\ {}^{(n)}\mathbf{q}_{c,l}{}^{T}\ {}^{(n)}\mathbf{q}_{c,r}{}^{T}\ {}^{(n)}\mathbf{q}_{i}{}^{T}\right]^{T} \tag{3.9}$$

where ${}^{(n)}\mathbf{q}_{b,l}$ and ${}^{(n)}\mathbf{q}_{b,r}$ are the nodal displacements of the left boundary segment interface and right boundary segment interface, respectively, as shown in Figure 3.2. ${}^{(n)}\mathbf{q}_{c,l}$ and ${}^{(n)}\mathbf{q}_{c,r}$ are the displacements of left and right shroud contact nodes, respectively. ${}^{(n)}\mathbf{q}_{a}$ are the accessory nodes which contains the displacements of loading and response nodes, and ${}^{(n)}\mathbf{q}_{i}$ contains the displacements of other interior nodes of the system of the n^{th} segment.

Similar to the generic system, to solve the equation 3.8 for periodic excitation using HBM ([26]), the periodic quantities (i.e. displacements and forces) with an angular frequency of ω are expressed as truncated series of harmonic terms:

$$
\begin{aligned}
{}^{(n)}\mathbf{Q}(t) = \Re\left(\sum_{h=0}^{H} {}^{(n)}\hat{\mathbf{Q}}^{(h)} e^{ih\omega t}\right);\ {}^{(n)}\mathbf{F}(t) = \Re\left(\sum_{h=0}^{H} {}^{(n)}\hat{\mathbf{F}}^{(h)} e^{ih\omega t}\right);\\
{}^{(n)}\mathbf{F}_{c,l}\left(\Delta\mathbf{q}_{c,l}, \Delta\dot{\mathbf{q}}_{c,l}, t\right) = \Re\left(\sum_{h=0}^{H} {}^{(n)}\hat{\mathbf{F}}_{c,l}^{(h)} e^{ih\omega t}\right);\\
{}^{(n)}\mathbf{F}_{c,r}\left(\Delta\mathbf{q}_{c,r}, \Delta\dot{\mathbf{q}}_{c,r}, t\right) = \Re\left(\sum_{h=0}^{H} {}^{(n)}\hat{\mathbf{F}}_{c,r}^{(h)} e^{ih\omega t}\right)
\end{aligned}
\tag{3.10}
$$

By applying Galerkin's procedure with the multi-harmonic approximation, the time domain nonlinear differential equation 3.8 is transformed into a nonlinear algebraic equation with Fourier coefficients as defined in equation 3.10, and the balance equation is written as:

$$
\mathbf{D}^{(h)}{}^{(n)}\hat{\mathbf{Q}}^{(h)} = {}^{(n)}\hat{\mathbf{F}}^{(h)} + {}^{(n)}\hat{\mathbf{F}}_{c,l}^{(h)} + {}^{(n)}\hat{\mathbf{F}}_{c,r}^{(h)} \; with\; h = 0..H \tag{3.11}
$$

where $\mathbf{D}^{(h)} = \left(-(h\omega)^2\mathbf{M} + ih\omega\mathbf{C} + \mathbf{K}\right)$ is the h^{th} dynamic stiffness matrix of the system. The equation 3.11 consists of the static $(h = 0)$ and dynamic $(h = 1..H)$ equations of the system coupled to each other by Fourier coefficients of the nonlinear contact force ${}^{(n)}\hat{\mathbf{F}}_{c,l}^{(h)}$ and ${}^{(n)}\hat{\mathbf{F}}_{c,r}^{(h)}$ depending on the Fourier coefficients of the relative displacements and velocities. The number of harmonics H is chosen in a way to approximate the steady state dynamics of the structure with sufficient accuracy. The equation 3.11 has to be solved iteratively for the unknown displacement vector of n^{th} segment because of the nonlinear contact forces. Note the size of the dynamic stiffness matrix $\mathbf{D} \in \mathbb{C}^{(N(H+1)\times N(H+1))}$ and the force vectors ${}^{(n)}\hat{\mathbf{F}}$, ${}^{(n)}\hat{\mathbf{F}}_{c,l}$, ${}^{(n)}\hat{\mathbf{F}}_{c,r} \in$

$\mathbb{C}^{(N(H+1)\times 1)}$. The system of equations still refer to the single fundamental bladed disk sector. The cyclic symmetry boundary conditions will be implemented in the next steps. However, note that in case one is interested in the analysis of mistuned bladed disk, the cyclic symmetry constraints breakdown and the next section stand void.

3.2.3 Implementation of cyclic symmetry constraints.

The turbine bladed disk is assumed to be excited by a travelling wave type excitation, [see. 10, 161] for a detailed explanation. The IBPA is given as: $\phi = \frac{2\pi}{N}.EO$, where N is the number of blades, and EO is the engine order that, in the Campbell diagram, crosses the resonance under investigation. Reducing the number of DOFs required for the nonlinear forced response analysis is done in two steps. First, the disk interface segment boundary DOFs are reduced using cyclic symmetry constraints and then similar constraints are applied to the shroud contact node DOFs.

Reducing the disk segment boundary DOFs using cyclic symmetry constraints:

Since the bladed disk experiences a travelling wave type excitation, the steady-state vibration response is assumed to also represents a travelling wave. This results in a relationship between the right segment interface nodal DOF, and the left segment interface nodal DOF. Owing to the cyclic symmetry conditions based on the assumption that the turbine bladed disk is made of the similar bladed-disk fundamental sector, one can write the following coupling relationship for the displacements at the segment boundary DOFs:

$$ {}^{(n)}\hat{\mathbf{q}}_{b,l}^{(h)} = {}^{(n)}\hat{\mathbf{q}}_{b,r}^{(h)} e^{-ih\phi} \tag{3.12} $$

Redefining the reduced displacement vector of unknowns by considering the right-side boundary segment for h^{th} harmonic component and n^{th} sector as:

$$ {}^{(n)}\hat{\mathbf{Q}}^{(h)} = \hat{\mathbf{T}}_{CS\,red}^{(h)(n)} \hat{\mathbf{Q}}^{(h)} \tag{3.13} $$

Thereby making the new reduced displacement vector of unknowns as:

$$ {}^{(n)}_{red}\hat{\mathbf{Q}}^{(h)} = \left[{}^{(n)}\hat{\mathbf{q}}_{b,r}{}^{(h)^T} \; {}^{(n)}\hat{\mathbf{q}}_{a}{}^{(h)^T} \; {}^{(n)}\hat{\mathbf{q}}_{c,l}{}^{(h)^T} \; {}^{(n)}\hat{\mathbf{q}}_{c,r}{}^{(h)^T} \; {}^{(n)}\hat{\mathbf{q}}_{i}{}^{(h)^T} \right]^T \tag{3.14} $$

$$ \hat{\mathbf{T}}^{(h)}_{CS} = \begin{bmatrix} \mathbf{I}(e^{-ih\phi}) & 0 & 0 & 0 & 0 \\ \mathbf{I} & 0 & 0 & 0 & 0 \\ 0 & \mathbf{I} & 0 & 0 & 0 \\ 0 & 0 & \mathbf{I} & 0 & 0 \\ 0 & 0 & 0 & \mathbf{I} & 0 \\ 0 & 0 & 0 & 0 & \mathbf{I} \end{bmatrix} \tag{3.15} $$

where $\hat{\mathbf{T}}^{(h)}_{CS}$ is the cyclic symmetry constraint matrix for h^{th} harmonic component; $\mathbf{I}$ is the identity matrix of an appropriate size corresponding to the size of DOFs. Substituting the vector ${}^{(n)}\hat{\mathbf{Q}}^{(h)}$ in equation 3.11 by the cyclic constraint relation as given in equation 3.13 for $h = 0..H$ and left-multiplying by the corresponding complex conjugate transpose of $\hat{\mathbf{T}}^{(h)}_{CS}$ results in:

$$ {}_{red}\hat{\mathbf{D}}^{(h)} {}^{(n)}_{red}\hat{\mathbf{Q}}^{(h)} = {}^{(n)}_{red}\hat{\mathbf{F}}^{(h)} + {}^{(n)}_{red}\hat{\mathbf{F}}^{(h)}_{c,l} + {}^{(n)}_{red}\hat{\mathbf{F}}^{(h)}_{c,r} \; with \; h = 0..H \tag{3.16} $$

where ${}_{red}\hat{\mathbf{D}}^{(h)} = \left(-(h\omega)^2\hat{\mathbf{M}}^{(h)} + ih\omega\hat{\mathbf{C}}^{(h)} + \hat{\mathbf{K}}^{(h)}\right)$ is the h^{th} dynamic stiffness matrix of the system. Note that the $\hat{\mathbf{M}}$, $\hat{\mathbf{C}}$, $\hat{\mathbf{K}} \in \mathbb{C}^{(j(H+1)\times j(H+1))}$ complex mass matrix, viscous damping matrix, and the stiffness matrix respectively, are Hermitian because of the application of the cyclic symmetry constraints and ${}^{(n)}_{red}\hat{\mathbf{F}}$, ${}^{(n)}_{red}\hat{\mathbf{F}}_{c,l}$, ${}^{(n)}_{red}\hat{\mathbf{F}}_{c,r} \in \mathbb{C}^{(j(H+1)\times 1)}$ where $j < N$ because of the successful elimination of the left boundary segment interface DOFs.

Reducing the shroud contact DOFs using cyclic symmetry constraints:

The displacement vector of unknowns can further be reduced by applying cyclic symmetry constraints at the shroud contact DOFs and writing in relative displacement terms. Writing in relative displacements terms reduces the number of shroud contact DOFs by half as one can consider only the number of shroud contact DOFs of one side and reduce the size of the system required for nonlinear analysis. The relative displacement at the right-side shroud contact and the nonlinear contact force can be written as:

$$
\begin{aligned}
{}^{(n)}\Delta\hat{\mathbf{q}}_{c,r}^{(h)} &= {}^{(n)}\hat{\mathbf{q}}_{c,r}^{(h)} - {}^{(n-1)}\hat{\mathbf{q}}_{c,l}^{(h)} \\
{}^{(n)}\Delta\hat{\mathbf{q}}_{c,r}^{(h)} &= {}^{(n)}\hat{\mathbf{q}}_{c,r}^{(h)} - {}^{(n)}\hat{\mathbf{q}}_{c,l}^{(h)} e^{ih\phi} \\
{}^{(n)}\hat{\mathbf{f}}_{c,r}^{(h)} &= -{}^{(n)}\hat{\mathbf{f}}_{c,l}^{(h)} e^{ih\phi}
\end{aligned}
\tag{3.17}
$$

The new displacement vector of unknowns in terms of relative displacements at the shroud contact becomes:

$$
{}^{(n)}_{rel}\hat{\mathbf{Q}}^{(h)} = \left[{}^{(n)}\hat{\mathbf{q}}_{b,r}{}^{(h)^T} \; {}^{(n)}\hat{\mathbf{q}}_{a}{}^{(h)^T} \; {}^{(n)}\Delta\hat{\mathbf{q}}_{c,r}{}^{(h)^T} \; {}^{(n)}\hat{\mathbf{q}}_{i}{}^{(h)^T} \right]^T \tag{3.18}
$$

This leads to cutting down the shroud contact unknown DOFs by half by considering either right or left contact, hence reducing the size of the nonlinear computation. Similarly, a relative displacement cyclic symmetry transformation matrix [162] can be defined, and the balance equation 3.16 can be rewritten as:

$$
{}_{rel}\hat{\mathbf{D}}^{(h)}\,{}^{(n)}_{rel}\hat{\mathbf{Q}}^{(h)} = {}^{(n)}_{rel}\hat{\mathbf{F}}^{(h)} + {}^{(n)}_{rel}\hat{\mathbf{F}}^{(h)}_{c,r} \; with \; h = 0..H \tag{3.19}
$$

where ${}_{rel}\hat{\mathbf{D}} \in \mathbb{C}^{(k(H+1)\times k(H+1))}$ and ${}^{(n)}_{rel}\hat{\mathbf{F}}$, ${}^{(n)}_{rel}\hat{\mathbf{F}}_{c,r} \in \mathbb{C}^{(k(H+1)\times 1)}$ where $k < j$.

Since the number of shroud contact nodes, boundary nodes and accessory nodes DOFs is much smaller than the number of internal DOFs, as described for the generic system, the classical Craig-Bampton reduction method [158] is applied, retaining as physical coordinates the right segment interface nodes, right shroud contact nodes, accessory nodes DOFs – collectively called as master nodes, and adding a certain number of fixed-interface modes η.

$$
{}^{(n)}\hat{\mathbf{q}}^{(h)} = \left[{}^{(n)}\hat{\mathbf{q}}_{b,r}{}^{(h)^T} \; {}^{(n)}\hat{\mathbf{q}}_{a}{}^{(h)^T} \; {}^{(n)}\Delta\hat{\mathbf{q}}_{c,r}{}^{(h)^T} \; {}^{(n)}\eta^T \right]^T \tag{3.20}
$$

where ${}^{(n)}\hat{\mathbf{q}} \in \mathbb{C}^{m(H+1)\times 1}$ and $m \ll k$. Finally, the equation 3.19 can be reformulated using equation 3.20 as:

$$
\hat{\mathbf{d}}^{(h)}\,{}^{(n)}\hat{\mathbf{q}}^{(h)} = {}^{(n)}\hat{\mathbf{f}}^{(h)} + {}^{(n)}\hat{\mathbf{f}}^{(h)}_{c,r} \; with \; h = 0..H \tag{3.21}
$$

By rearranging equation 3.21, the residual equation is written as:

$$
\mathbf{RES}^{(h)} = \hat{\mathbf{d}}^{(h)}\,{}^{(n)}\hat{\mathbf{q}}^{(h)} - {}^{(n)}\hat{\mathbf{f}}^{(h)} - {}^{(n)}\hat{\mathbf{f}}^{(h)}_{c,r} \; with \; h = 0..H \tag{3.22}
$$

The built-in nonlinear solution algorithm such as `fsolve` in MATLAB takes only the equations in real form. Hence, the complex form residual equation 3.7 and equation 3.22 is split into its real and imaginary components to real form. The residual is minimized by defining appropriate tolerance limits to find the solution to the vector of unknown displacements as:

$$\mathbf{RES} = \left[\mathbf{RES}^{(0)}, \Re\left(\mathbf{RES}^{(1)}\right), \Im\left(\mathbf{RES}^{(1)}\right) \ldots \Re\left(\mathbf{RES}^{(H)}\right), \Im\left(\mathbf{RES}^{(H)}\right)\right]^{\mathrm{T}} \tag{3.23}$$

3.3 Contact model.

As mentioned in the section 2.3, a node-to-node 2D Jenkins element with a variable normal load to compute the contact forces is chosen, as shown in Figure 3.3(a). A typical hysteresis loop for a contact undergoing stick and full sliding is shown in Figure 3.3(b). The balance equations to be solved requires nonlinear contact forces from the contact interface as an input. The contact element is characterized by two linear springs in the tangential and normal direction with tangential (k_t) and normal (k_n) contact stiffness at each node pair. The contact interface is discretized into multiple nodes to capture micro-slip behaviour. Each node pair is able to characterize and simulate three possible contact states – stick, slip and separation during one vibration cycle.

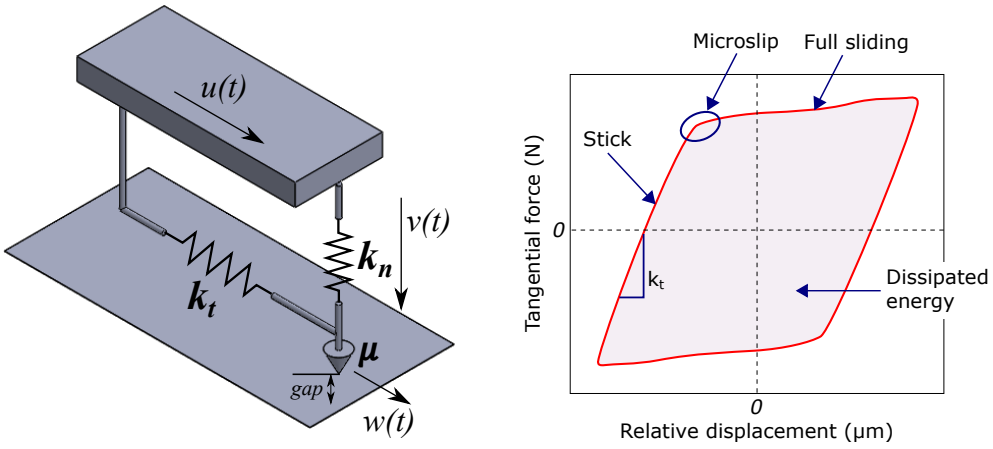

Fig. 3.3 (a) Jenkin's element contact model with variable normal load, (b) A typical hysteresis loop.

At each element, the contact forces – tangential force $T(t)$ and the normal force $N(t)$ depend on the relative tangential and normal displacements of the corresponding node pair, namely $u(t)$ and $v(t)$, respectively [31]. The Coulomb law defines the friction limit as $\mu N(t)$, where μ is the coefficient of friction. A slider-type representation is used to connect the two bodies to consider the friction phenomena occurring at the interface in the tangential direction. When the tangential force exceeds the friction limit, the slider starts moving, and the amount of slip between the nodes is recorded as $w(t)$.

Since the contact is a unilateral constraint, the normal contact force $N(t)$ is defined at each time t as:

$$N(t) = \max(k_n v(t), 0) \tag{3.24}$$

When $v(t)$ is negative, no normal contact force is allowed, and separation occurs, hence referred to as separation state.

For the tangential direction, the tangential contact force $T(t)$ is dependent on the contact state as defined by:

$$T(t) = \begin{cases} k_t \{u(t) - w(t)\} & stick\ state \\ \mu N(t)\, sign(\dot{w}) & slip\ state \\ 0 & separation \end{cases} \tag{3.25}$$

The contact forces are computed using predictor-corrector logic [10]. At each time t a predictor step is performed assuming the stick contact conditions:

$$[T^p(t) = k_t [u(t) - w(t)] = k_t [u(t) - w(t - \Delta t)] \tag{3.26}$$

Where Δt is the time step, then a corrector step is performed to compute the actual value of $T(t)$ given by:

$$T(t) = \begin{cases} T^p(t) & stick\ state \\ \mu N(t)\, sign(T^p(t)) & slip\ state \\ 0 & separation \end{cases} \tag{3.27}$$

The slider displacement $w(t)$ is computed as:

$$w(t) = \begin{cases} w(t-\Delta t) & stick\ state \\ u(t) - \mu N(t)\, sign\left(T(t)\right)/k_t & slip\ state \\ u(t) & separation \end{cases} \tag{3.28}$$

The approximation introduced due to the predictor-corrector method is minimized by choosing a finer time step Δt (for instance, 2e8 time steps).

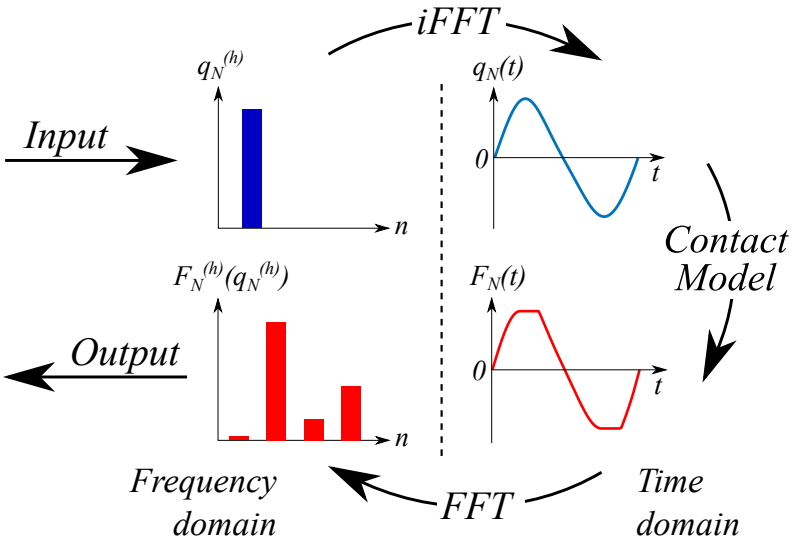

Fig. 3.4 Alternating Frequency Time (AFT) method.

Computing nonlinear forces in the frequency domain is quite challenging. The literature shows that the nonlinear forces are more accurately computed in the time domain, but the vibration problem is solved efficiently in the frequency domain. Hence, based on Cameron and Griffin [163–165], an Alternate Frequency/Time (AFT) method is employed. The relative displacements are converted from the frequency domain to the time domain by applying Inverse Fast Fourier Transform and then run through the contact model. The nonlinear contact forces are obtained in the time domain. Then by applying Fast Fourier Transform to convert back to the Fourier coefficients in the frequency domain with truncation of the number of harmonics chosen, as shown in Figure 3.4.

Newton-Raphson logic is implemented for the iterative procedure to find the solution to the vector of unknown displacements. The tangential stiffness matrix

(Jacobian) needed to compute the residual for the Newton-Raphson method is computationally intensive if to use a `MATLAB` built-in finite difference method (FDM) for large systems. Hence an analytical Jacobian is implemented based on the works of [10, 166] by computing piece-wise partial derivatives of the contact forces. The computed partial derivatives are then assembled in the global tangent stiffness matrix. This dramatically increases the speed of the solution by many folds, especially predominant for larger systems.

The computed nonlinear contact forces and in turn the accuracy of the dynamic response prediction are primarily based on the accurate input of the normal and tangential contact stiffness. As mentioned in the section 2.4, the tangential (k_t) and normal (k_n) contact stiffness for the whole joint interface are computed based on the closed-form solutions of 3D formulation by Allara [102], which is based on 2D formulation of Ciavarella and Hills [101]. Then the computed contact stiffness are distributed over the discretized contact interface according to the node-to-node formulation based on individual elemental area contribution of each node in the interface.

Continuation techniques:
With the information equipped from the above sections, for a structure with known parameters, boundary and loading conditions, one can compute the response of a system at a particular frequency. To construct a FRF for a given frequency range, a suitable continuation technique is chosen and a set of points are computed.

In the current scope of work, the simplest of all, the natural continuation with a fixed frequency step is used. One can run a forward or a backward frequency sweep and the frequency step can be decided depending on the resolution needed. Firstly, the frequency range is defined and the starting frequency point is usually outside the resonance region. The converged solution is highly dependent on the initial guess. If the guess is too far from the solution, sometimes the solver might not converge. For an initial guess to the iterative solver, the linear solution corresponding to the start of the frequency is given as input. This is by assuming the real solution of the nonlinear system is close to that of the linear solution at that frequency outside of the resonance zone. The drawback of this continuation technique is if the system possesses multiple solutions at one frequency due to nonlinearities, it cannot find the solution, and the turning points cannot be captured.

To overcome the above problem, an arc-length continuation based on [167] is implemented as an option in the current solver. The systems with partial separation could exhibit softening or hardening behaviour leading to jump phenomena and multiple solutions at one particular frequency in the nonlinear frequency range. The arc-length continuation is based on the predictor-corrector strategy, where the first calculation is performed with the classical Newton-Raphson method. The following steps are based on defining a unit vector tangent to the solution and controlling the step length of the predictor step. A corrector step is obtained by searching for the solution in a direction orthogonal to the predictor step. Then, the system of equations is augmented to include the excitation frequency as unknown. In this way, nonlinear systems with turning points are captured and the resolution of the solved points are taken care based on the defined step length [31].

3.4 Modelling of Wear.

As mention in the literature review section 2.5, the wear energy approach is implemented in the present nonlinear solver. During the first pass, where no wear has taken place, the nonlinear dynamic forced response is computed with pristine contact surfaces without any wear. The nodal wear depth v_w is defined and computed as:

$$v_w = Z_W \frac{\alpha E}{A} \tag{3.29}$$

where A is the area associated with the node pair, α is the wear coefficient for a particular contact pair, and E is the energy dissipated over one cycle. It is worth mentioning that A depends on the finite element mesh discretization over the contact surface, while α is an experimentally obtained parameter for a specific material couple ([98, 129, 168]) and E is obtained by evaluating the area under the hysteresis loop. The control parameter of equation 3.29 is Z_W – number of cycles. During the wear analysis, both the contacting interfaces will lose normal height. The nodal wear depth v_w is the total loss of normal height including both the contacting interfaces and is divided equally between the interfaces assuming identical wear profiles on both surfaces. However, in the dynamic analysis only the relative difference in height of the contacting interface is used. Also, this type of wear modelling does not allow for the growth of oxide layers and assume that the wear will result in the coarsening of the interface.

The process of updating the contact surface due to wear after one cycle is called a wear iteration. With materials typical of turbine blades, the wear depth obtained at each vibration cycle is so small that no significant effect on the forced response of the system is observed if a wear iteration is performed at each vibration cycle. Hence, a wear acceleration technique is used, where the wear depth v_w associated at each node pair is considered for Z_W number of cycles.

In this work, an adaptive strategy is used, and the value of Z_W at each wear iteration is computed as:

$$Z_W = floor\left(\frac{v_{w,max}}{max\left(\Delta h_{ij}\right)}\right) \tag{3.30}$$

where, $v_{w,max}$ is a user-defined parameter for the maximum step size for each wear increment and Δh_{ij} is the nodal wear depth at the contact patch for one vibration cycle. Choosing $v_{w,max}$ is empirical at this stage, as there are no guidelines from the experiments on what value is most suitable in terms of the accuracy of results. However, a few thumb rules presented below, which one can use to define the parameter $v_{w,max}$:

- the maximum wear depth allowed for each wear iteration, directly selected by the user
  For example, consider an assembly with a contact interface that is functional up to a contact wear depth of 100 µm. In this case, the user can arbitrarily discretize this maximum allowable wear depth into 100 parts and define $v_{w,max}$ as 1 µm. By doing this, the user can visualize the contact evolution and the effect on the nonlinear response plots at 100 intervals by limiting the maximum wear depth of 1 µm between the intervals before the functional failure of the assembly.
- the percentage of the maximum static deflection (δ_{max}) for the given contact preload in the open contact condition
  This method is more quantitative than the previous arbitrary method. $v_{w,max}$ is defined as a parameter of the static loading condition when the contact is open. Irrespective of the geometry, size and loading scenario of the system, $v_{w,max}$ can be defined as a percentage of the maximum static deflection at the contact in the absence of the second body. $v_{w,max}$ can be chosen as a percentage of the maximum static deflection (δ_{max}). δ_{max} can be visualized

as shown in Figure 3.5. For example, in a shrouded turbine blade, δ_{max} at the shroud contact is the maximum static deflection for given static loads acting on the blade in the absence of the shroud coupling. This provides a ballpark estimate of how much the blade deflects in a free condition. This static deflection can then be used to discretize the wear iteration steps by defining them as a percentage. The ratio $v_{w,max}/\delta_{max}$ parametrizes the wear iteration and eliminates the dependency on static load. This method allows one to visualize the intermediate stages of the effect of fretting wear on contact evolution and subsequent dynamic response.

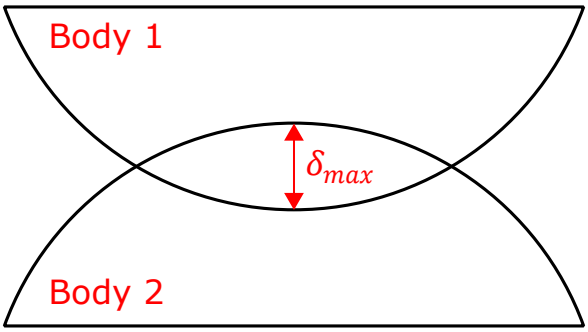

Fig. 3.5 Schematic showing the interference between the two bodies.

- the maximum tolerable error in wear depth
  This is more of a special case. Suppose one can consider that the user needs a very high accuracy of wear depth evolution in each wear iteration. Then $v_{w,max}$ can be defined directly as the value of this wear depth tolerance. For example, defining very small jumps from one wear iteration to the next leads to the high accuracy of wear evolution profile and capturing small changes. By this, the user can visualize a very smooth evolution, but of course, burdened with the additional computational cost.

The parameter $v_{w,max}$ controls Z_W. It turns out that Z_W leads to a trade-off between the accuracy of the results and the computation time needed. A low value of Z_W will allow for a more accurate but more time-consuming analysis. The opposite will happen if a high value of Z_W is selected.

Once the term v_w is computed using equation 3.29, the wear iteration is performed by updating the 0^{th} order Fourier coefficient of the normal relative displacement at the contact in the following way:

$$v(t) = \sum_{h=0}^{H} \hat{\mathbf{v}}^{(h)} e^{ih\omega t} - v_w \tag{3.31}$$

After the wear iteration, the forced response of the updated system is computed by solving the updated balance equations, taking into account the effect of the wear depth on the static preload and the nonlinear dynamics of the system simultaneously.

It is here worth mentioning that equation 3.31 allows for a direct update of the governing equations of the system since the static term $(h = 0)$ is included in the set of nonlinear equations to solve using coupled approach. Thus, this method allows computing the effect of wear on the forced response with 'changing preload' without the need for a separate nonlinear static analysis routine to compute the contact preload distribution.

Figure 3.6 gives an overview of various steps with pre-processing and solution phase to perform the full analysis of the effect of wear on the nonlinear dynamic response. The pre-processing can be done using any standard commercial software such as `ANSYS, ABAQUS`. In this work, `ANSYS V19.0` is solely used to generate the FE model, perform CB-CMS and extract the reduced mass and stiffness matrices. For the solution phase, `MATLAB R2018` is used.

3.5 Summary.

This chapter presented the numerical methodology to perform a nonlinear dynamic analysis of a generic system having friction contacts. The methodology was then extended to a structure with cyclic symmetry boundary conditions. A detailed description of frequency-domain based coupled static/dynamic HBM was described. An alternating frequency time (AFT) routine was presented to compute the nonlinear contact forces accurately. A 2D Jenkins element with a variable normal load contact model was used at node pairs of the discretized contact. Using the wear energy approach method, wear modelling was described and a way to incorporate nodal wear to the contact for dynamic analysis of the system. An accelerated wear strategy using adaptive wear logic was also described. Combining all of the above, a schematic step-by-step solution flowchart was presented to perform a full nonlinear dynamic response with fretting wear.

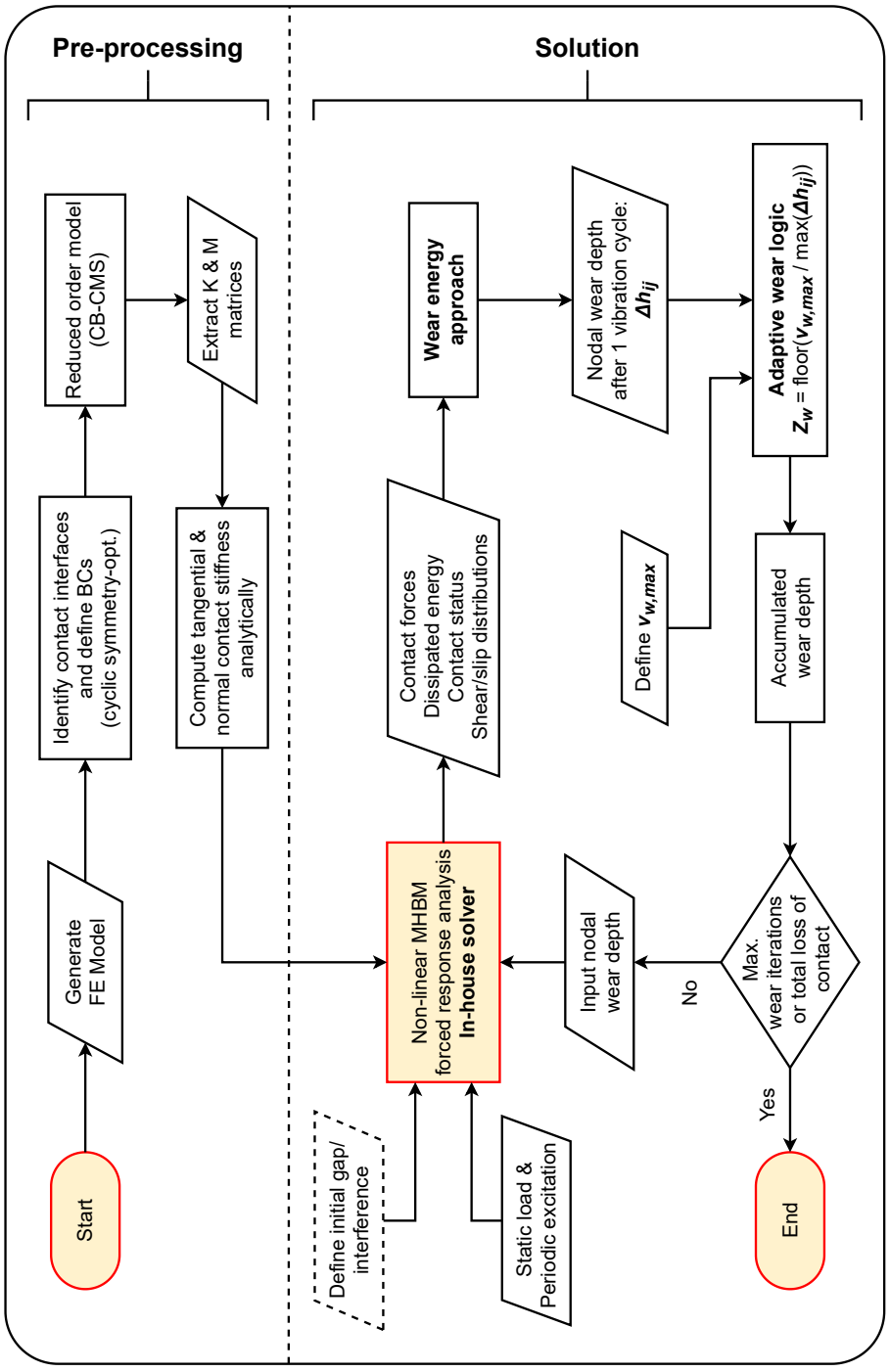

Fig. 3.6 Solution flowchart showing an overview of various steps to obtain the full results with nonlinear dynamic response and fretting wear.

Chapter 4

Numerical test cases

4.1 Introduction.

In this chapter, two numerical test cases are chosen, and the results are presented using the methodology developed in the previous chapter. As the focus of the research is the turbomachinery applications, naturally the main test case here is a realistic bladed disk with shroud contacts with cyclic symmetry boundary conditions. However, before jumping on to the test case, the proposed nonlinear solver is first evaluated on a simple cantilever beam with a known friction contact patch on the free end. The two test cases demonstrate the proposed methodology of incorporating a wear model and studying the effect of wear on the nonlinear dynamic response with changing contact preload as the wear progresses and the resulting contact interface evolution. The goal of the test cases is to choose the combination of static load and excitation in a way that there is accelerated wear and amplified energy dissipation at each cycle resulting in total loss of contact. This will help numerically understand the number of necessary wear iterations, wear profile evolution and subsequent evolution of forced response of the systems. Furthermore, these test cases will help in visualizing the effect of user-defined parameter $v_{w,max}$ for adaptive wear, on the accuracy of the results and computational cost. In this chapter, $v_{w,max}$ is chosen as a percentage of maximum static deflection under the application of static load. Hence, a preliminary static analysis is performed to compute the ballpark estimate of the maximum static deflection in the absence of the mating body.

4.2 Cantilever beam test case.

A cantilever beam with a friction contact at the free end is chosen as the first numerical test case. The static load and dynamic excitation are applied on the two orthogonal faces at the mid-section of the beam.

4.2.1 Beam description.

The contact patch location and the loading conditions are as shown in Figure 4.1(a) and (b). Table 4.1 shows the material properties and contact properties such as contact dimension, normal and tangential contact stiffness, number of contact elements, etc. The FE mesh is shown in Figure 4.1(c). The contact elements at the contact patch are connected as node-to-node pair to the ground with the 2D Jenkins element contact model with variable normal load, as shown in Figure 4.1(d). The beam is loaded at the mid-section so that as the wear progresses and the material is lost, the contact preload reduces, and the contact zone evolves.

Parameter	**Value**
Material	Steel
Young's modulus (E)	210 GPa
Density (ρ)	7860 kg/m^3
Beam dimension	200mm L x 20mm H x 20mm D
Contact patch dimension	20mm x 20mm
No. of contact elements	169
Tangential contact stiffness (k_t)	470 $N/\mu m$
Normal contact stiffness (k_n)	583 $N/\mu m$
Friction coefficient (μ)	0.5
Wear energy coefficient (α)	2e3 $\mu m^3/J$
Static load (F_{static})	20 kN
Static load/Excitation ratio (F_{static}/F_{ex})	2
Choice of $v_{w,max}$	$\{0.5\%, 1\%, 2\%, 5\%, 10\%\}$ of δ_{max}

Table 4.1 Parameters for the cantilever beam test case.

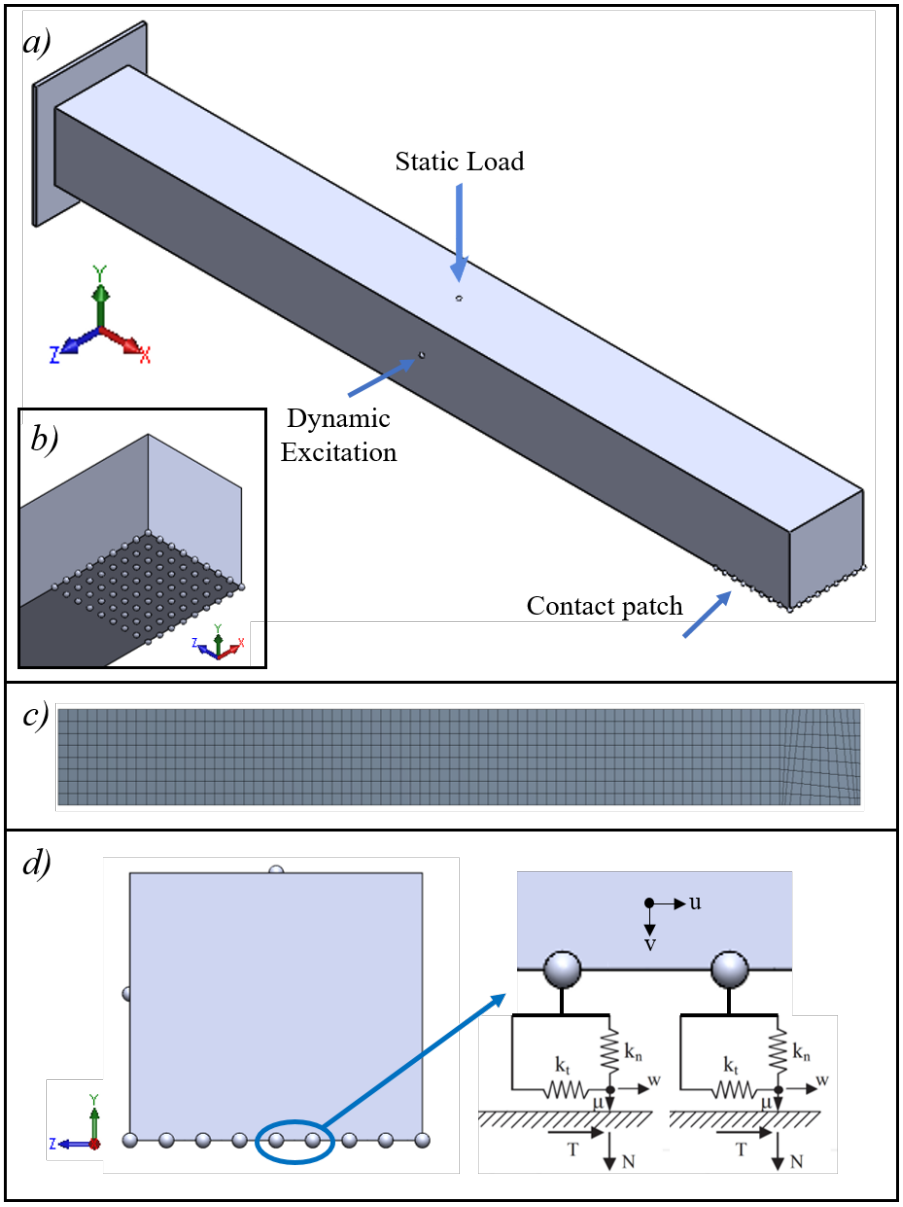

Fig. 4.1 (a) 3D Model of a cantilever beam, (b) a close-up view of the contact patch, (c) FE mesh of the beam and (d) contact elements connection.

The contact patch is made up of 169 node pairs, and the grid distribution is as shown in Figure 4.2 with a response node as the centre node of the contact patch. The grid is finer towards the boundary to better capture the effect of friction and evolution. Maximum static deflection (δ_{max}) in this case is considered as the maximum deflection at the contact patch for the applied static load for a free-standing beam, as shown in Table 4.1.

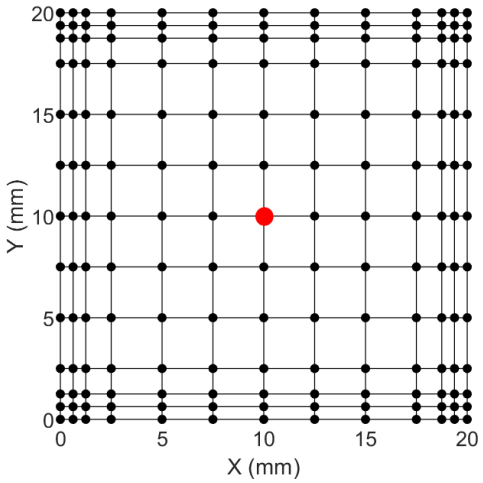

Fig. 4.2 Contact patch with 169 elements and the centre response node (red dot).

The beam is excited by a harmonic transverse force around the first bending mode, as shown in Figure 4.3, while a vertical static load provides the contact preload. Figure 4.3 also shows the static deflection and the shape at the initial contact condition with the second body (in this case, ground) and at the free condition when the second body is absent.

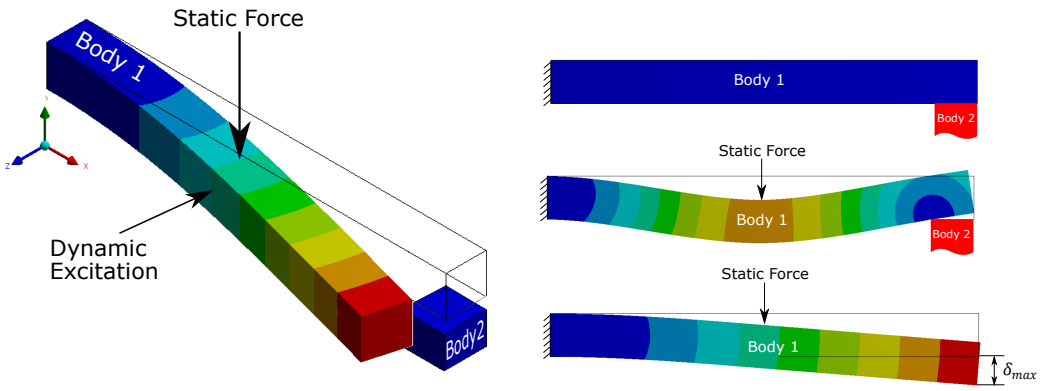

Fig. 4.3 Excitation mode (first bending mode at 406 Hz) (top) and highlighting static deflection state with and without body 2 (bottom).

The FE model is generated using ANSYS, and the contact interface and boundary conditions are identified and defined in ANSYS. A Craig-Bampton [158] reduced order modelling is performed by defining nodes at the friction contact and loading nodes as master nodes and retaining the first 15 fixed interface modes to reduce the size of the system needed for the nonlinear dynamic analysis. Otherwise, the dynamic

analysis with all the DOFs from the FE model would be large and prohibitively time-consuming. Reduced mass and stiffness matrices are extracted after the reduction process. The reduced system has 534 DOFs. The solution algorithm is followed, as shown in Figure 3.6. 0^{th} and 1^{st} order harmonics are retained to solve the static and dynamic balance equations in the frequency-domain using HBM. Analytically computed tangential and normal contact stiffness is computed, taking into account the dimensions of the contact patch. These stiffness are distributed over the contact patch according to the elemental area contribution. The stiffness values remain unchanged throughout the wear simulation as observed from an experimental evidence [23] that the stiffness reaches a constant value in the first few minutes of the test from running-in to steady-state phase.

4.2.2 Results.

A preliminary linear analysis is performed to obtain free and stick states of the contact, and the responses at these states are assumed as a reference for comparison. The computed nonlinear response can then be compared with these two reference states. An initial gap/interference, if any, can also be defined using the current algorithm by offsetting in the direction normal to the contact. In the present case, the gap is set to 0 as the beam is resting on top of body 2 (ground) before the static forces are applied to the system. Then both static and periodic forces are applied at the indicated excitation nodes. The contact forces, dissipated energy, contact status of each node and the shear/slip distributions are computed by solving equation 3.6. The wear energy approach, described in Section 3.4, is implemented to calculate the nodal wear depth at the contact patch for one vibration cycle. As the nodal wear depth is so minuscule at each vibration cycle, the dynamics is hardly affected. An adaptive wear acceleration logic as described in the previous section is implemented. The parameter $v_{w,max}$ reduces the number of wear iterations, thus reducing the computation time, compared to running dynamic analysis for each vibration cycle. $v_{w,max}$ is a user-defined value, the effect of the choice of $v_{w,max}$ is also quantified. The iterative loop is performed until the complete loss of contact. Figure 4.4 shows the fineness of end result of cumulative wear depth plots at the contact patch for different ratios of $v_{w,max}/\delta_{max}$. It can be seen for larger values, the cumulative wear depth plot is very coarse but provides quick results, whereas for small ratios of $v_{w,max}/\delta_{max}$, the plot is very smooth, but at a high computational cost.

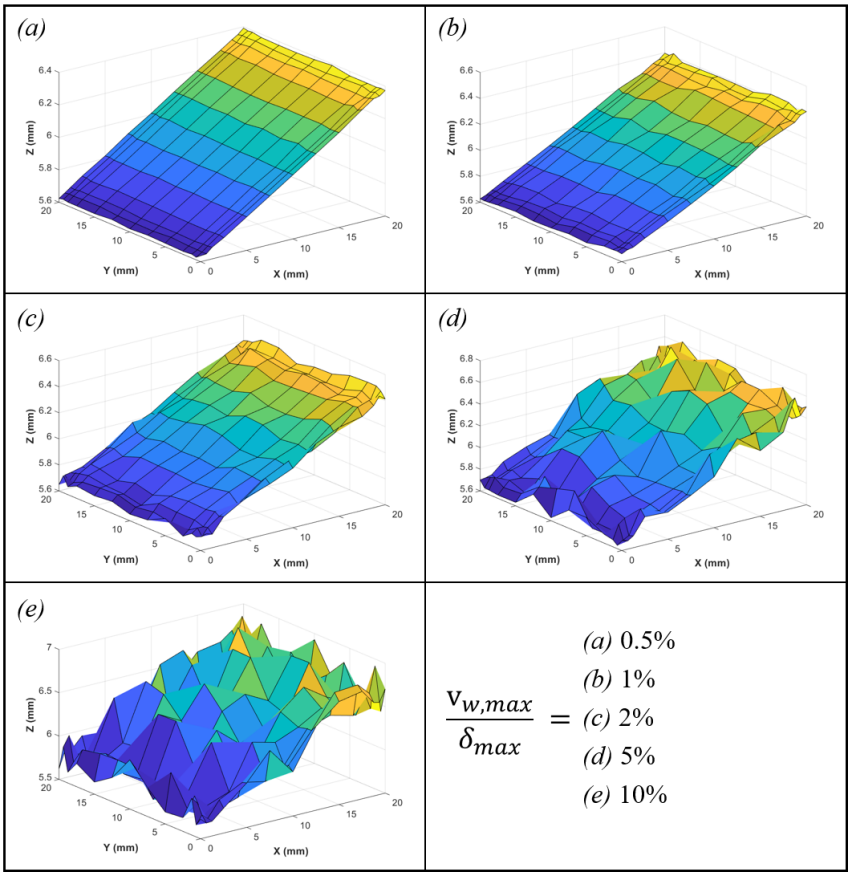

Fig. 4.4 Cumulative wear depth plots at the contact patch for complete loss of contact for different ratios of $v_{w,max}/\delta_{max}$. [Numerical]

Figure 4.5 shows the response curves of reference free and stick state along with the backbone curve of the maximum amplitude of response at each wear iteration for $v_{w,max} = 5\%$ of δ_{max}. It is evident and logical that, as the wear progresses, the contact preload reduces at the interface, and the contact tends towards the free state. The current formulation automatically takes into consideration the changing preload and is reflected in the response plots. With the pristine contact, the dynamic response of the system starts at the 'low-end' of the displacements. As the wear progresses, the peak response amplitude increases and the frequency shifts until it coincides with the free state when there is there no contact anymore. Figure 4.6 provides an insight into the physical state of the system, cumulative wear depth and the contact status at different wear iterations. The wear iterations are chosen at the beginning, intermediate and at the end of the wear just before the complete loss of contact.

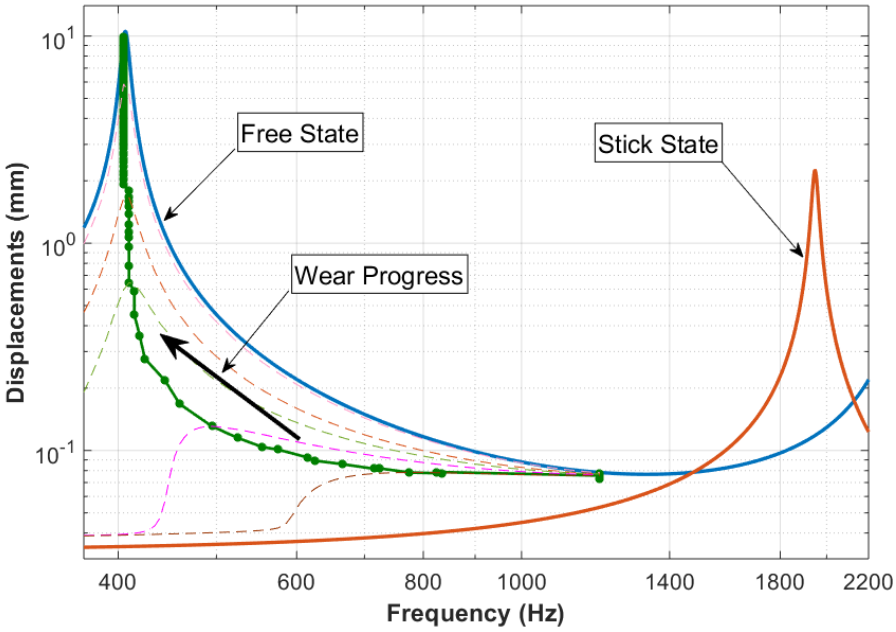

Fig. 4.5 Response plot showing the backbone of the nonlinear response obtained with progressing wear around the first bending mode, along with reference free and stick states for $v_{w,max} = 5\%$ of δ_{max}. [Numerical]

Figure 4.7 shows the plot of the number of vibration cycles at each wear iteration versus the number of wear iterations. For the shown plot, it took 183 wear iterations with the choice of $v_{w,max} = 5\%$ of δ_{max}. Here, each wear iteration can have a different number of vibration cycles as an adaptive logic is implemented. In other words, with the allowed wear depth of 5% of maximum static deflection at each wear iteration, it took 183 wear iterations to completely lose contact with the second body. Depending on the loading configuration, the shape of this graph can be different. In this example, as shown in Figure 4.6 of wear iteration 1, the contact started with a line contact at the inner edge of the contact between the body 1 and ground, and proceeded to establish an area contact with an increase in wear iterations. The close-up of the contact state at the beginning and at the end, is also shown in Figure 4.7. The criteria to complete one wear iteration is the amount of wear depth achieved, which is predetermined by the user input. At the start of the wear and towards the end, a relatively high number of cycles are needed to achieve this limit of wear depth to satisfy the wear iteration because of partial contact. However, when the contact is fully engaged, a lower number of cycles can satisfy the same wear depth criteria because of large contact, hence more energy dissipation.

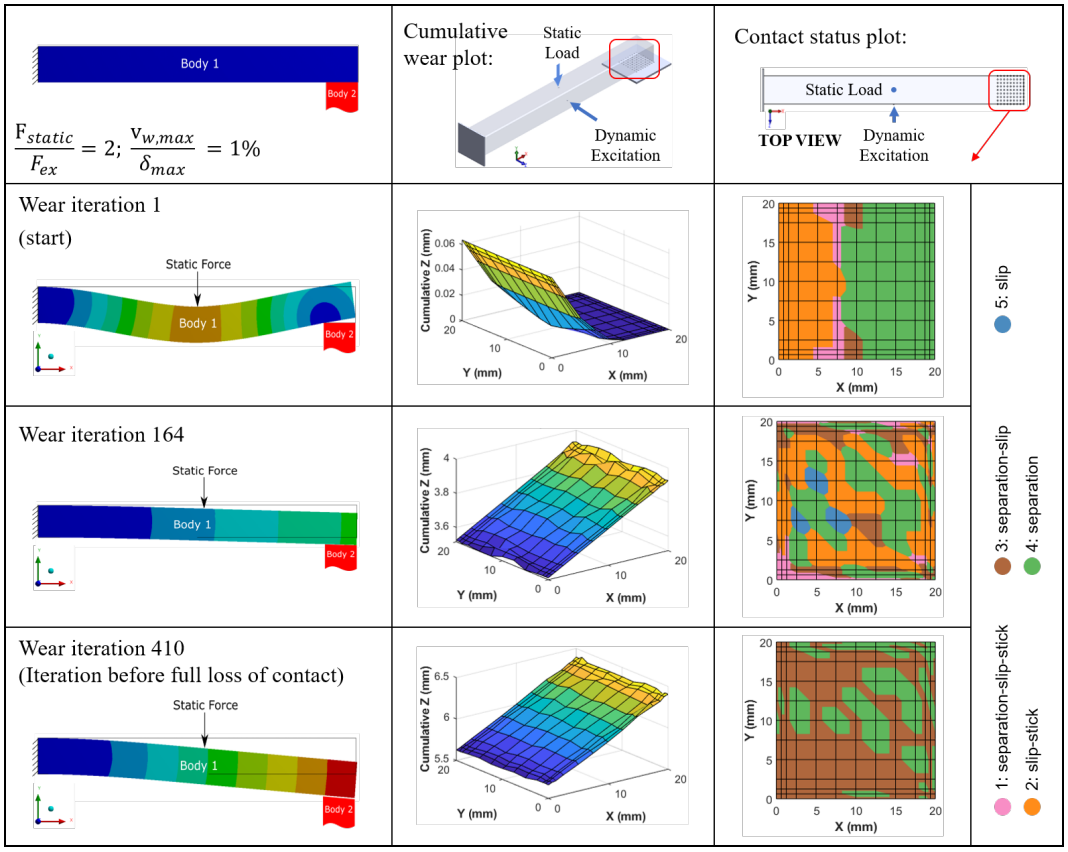

Fig. 4.6 A result matrix showing - starting, intermediate and ending wear iteration just before the full loss of contact for the given test case highlighting the beam physical state, cumulative wear depth until that particular wear iteration and the contact status at that wear iteration. [Numerical]

Figure 4.8 tracks only that particular maximum value of response amplitude corresponding to a particular wear iteration versus the cumulative number of cycles. It is evident the effect of $v_{w,max}$ on the number of cycles at which the maximum response starts increasing. The accuracy of the proposed method for different values of $v_{w,max}$ is investigated here, by using as a reference the analysis performed with $v_{w,max}/\delta_{max} = 0.5\%$, since no significant effects was observed by further reducing the ratio $v_{w,max}/\delta_{max}$. Ideally, the best benchmark would be the response computed with $Z_W = 1$ (one wear iteration per vibration cycle), but it is prohibitively time-consuming and unnecessary. It is clear that the choice of $v_{w,max}$ is the trade-off between the computational cost and the accuracy of results; the lower the value of $v_{w,max}$, the smoother the wear evolution and the contact patch wear profile is, due to the higher number of wear iterations. It is equivalent to slicing a pizza by either 4 parts or 16

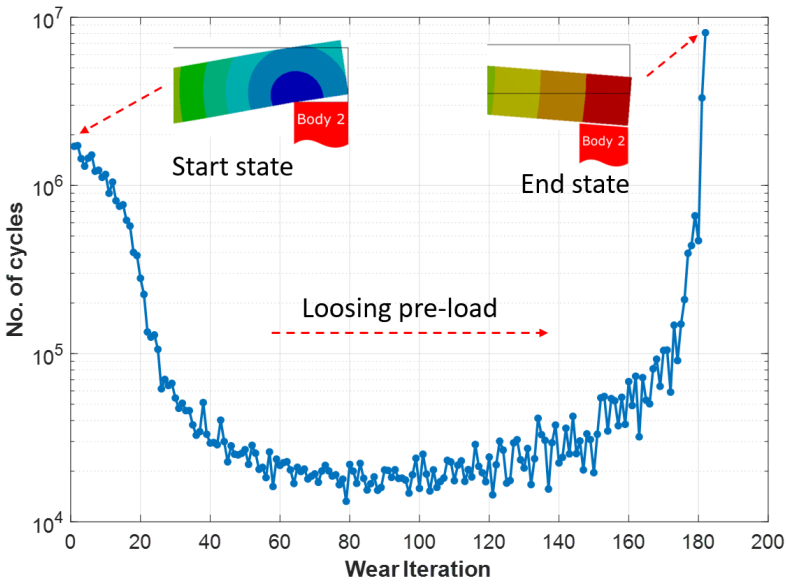

Fig. 4.7 Wear iteration versus the number of vibration cycles plot showing the trend as the wear progresses from the start state to the complete loss of contact for $v_{w,max} = 5\%$ of δ_{max} [Note: the number of cycles is adaptive at each wear iteration]. [Numerical]

parts. The whole remains the same, but the number of pieces increases. In the same way, a beam undergoing wear will still take the same number of cycles in reality. For numerical purposes, one can either have a fast simulation with coarse results or a slow simulation with fine results with good intermediate snapshots. In general, a reasonable strategy should be based on a convergence analysis of the response as the value of Z_W is progressively reduced. In this particular case, for relatively high values of $v_{w,max}$ (from 2% to 10% of δ_{max}) the analysis predicts the rapid increase in maximum response to occur earlier than the benchmark. Interestingly, when $v_{w,max}/\delta_{max} = 1\%$, opposite results are obtained, showing that a non-monotonic trend of the response during a convergence analysis can be observed.

Table 4.2 summarizes the comparison of the effect of the choice of $v_{w,max}$ on the computational time, the number of wear iterations necessary for the complete loss of contact, maximum wear depth and the error in the maximum wear depth taking $v_{w,max}/\delta_{max} = 0.5\%$ as the reference. The trade-off effect of $v_{w,max}$ is evident by comparing computational time vs error in wear depth. For more complex systems with more DOFs, the choice of choosing accuracy versus the speed of results in the early design phase will be clearly evident.

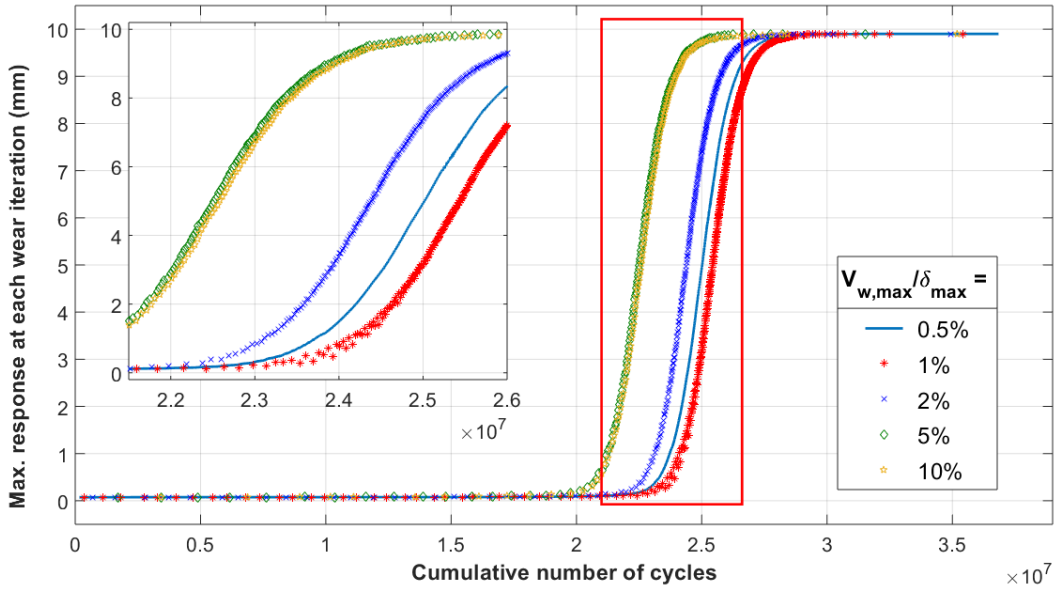

Fig. 4.8 Maximum response at each wear iteration vs the cumulative number of cycles for different values of $v_{w,max}$. [Numerical]

$\frac{v_{w,max}}{\delta_{max}}$	**Computational time**	**Total no. of wear iterations**	**Max. total wear depth (mm)**	**Relative error in wear depth (%)**
0.5 %	19 hr 32 min	577	6.3919	-
1 %	16 hr 10 min	411	6.4230	0.49
2 %	10 hr 17 min	291	6.4849	1.45
5 %	6 hr 0 min	183	6.6260	3.66
10 %	3 hr 57 min	130	6.9668	8.99

Table 4.2 Comparison of the impact of wear analysis with nonlinear dynamic response solver for different values of $v_{w,max}$.

4.3 Realistic shrouded bladed disk test case.

4.3.1 Bladed disk description.

A tuned shrouded bladed disk consisting of 40 identical blades is considered as a realistic numerical test case. The fundamental blade sector is as shown in Figure 4.9. The test case parameters are described in Table 4.3. This bladed disk is used as a test case to demonstrate the impact of fretting wear on the nonlinear dynamics with cyclic symmetry constraints. Exploiting the identical nature of cyclic structures, a fundamental sector consisting of only one blade is assumed with cyclic symmetry boundary conditions to reduce the size of the problem for nonlinear analysis. The disk is assumed to be infinitely rigid, and so fixed boundary conditions are applied at the blade root. In this way, the cyclic symmetry only operates through the blade-to-blade coupling at the tip shrouds. Maximum static deflection (δ_{max}) in this case is computed as the maximum deflection at the shroud contact patch in the absence of contact for the applied static load in such a way to produce a twisting effect of the blade.

Parameter	**Value**
Material	Steel
Young's modulus (E)	210 GPa
Density (ρ)	7860 kg/m^3
Beam dimension	As shown in 4.9
Contact patch dimension	20mm x 30mm
No. of contact elements	20 each on left and right shroud
Tangential contact stiffness (k_t)	93 $N/\mu m$
Normal contact stiffness (k_n)	113 $N/\mu m$
Friction coefficient (μ)	0.5
Wear energy coefficient (α)	2e3 $\mu m^3/J$
Static load (F_{static})	60 kN
Static load/Excitation ratio (F_{static}/F_{ex})	12
Choice of $v_{w,max}$	$\{0.5\%, 1\%, 2\%, 5\%, 10\%\}$ of δ_{max}

Table 4.3 Parameters for the shrouded bladed disk and the contact patch.

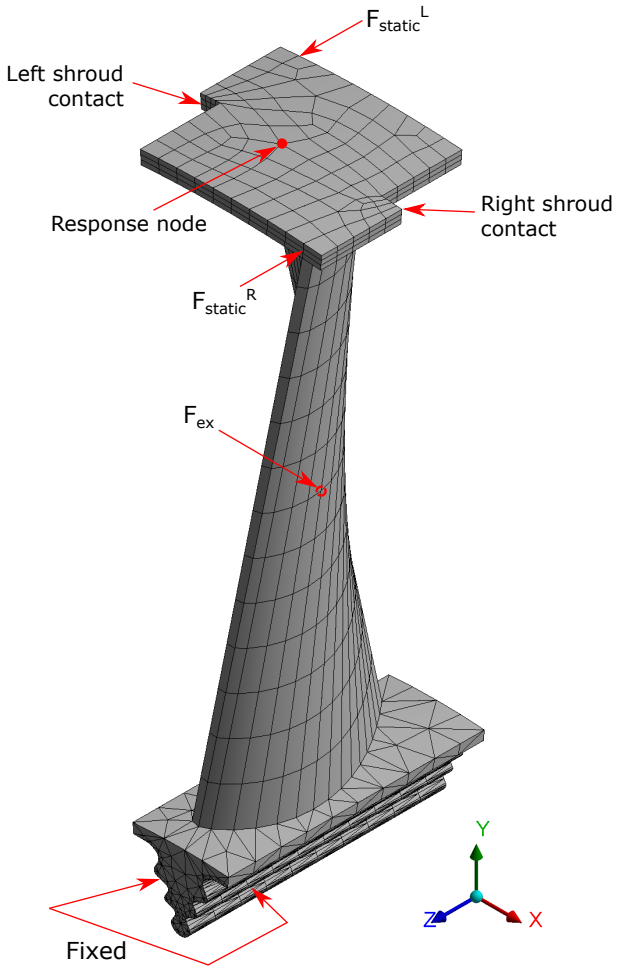

Fig. 4.9 FE model of the blade sector, boundary and loading conditions.

Static torque is applied to the blade by two static forces F_{static} to simulate the twisting effect, actually due to the centrifugal force in rotating blades, which produces the static preload at the shrouds. A concentrated periodic excitation F_{ex} is also applied at a mid-span node of the airfoil. Figure 4.10(a) highlights the shroud contact patch consisting of 20 contact elements each side with a 5x4 grid. Figure 4.10(b) shows the typical 2D Jenkins contact elements distribution between right contact patch with an adjacent blade left contact patch. The friction coefficient, contact stiffness and wear energy coefficient is defined as mentioned in Table 4.3. The number of contact elements might seem low for a study accounting wear, given wear is a complex phenomena. However, this is intended as a proof-of-concept and an in-depth analysis for design including more elements might be necessary. The nonlinear coupled HBM dynamic analysis is performed by retaining only the 0^{th} and the 1^{st} harmonics in the

balance equation. First bending mode with first Engine Order $(EO = 1)$ as shown in Figure 4.11 is chosen as the frequency of interest to analyse the effect of wear on the dynamics of the bladed disk.

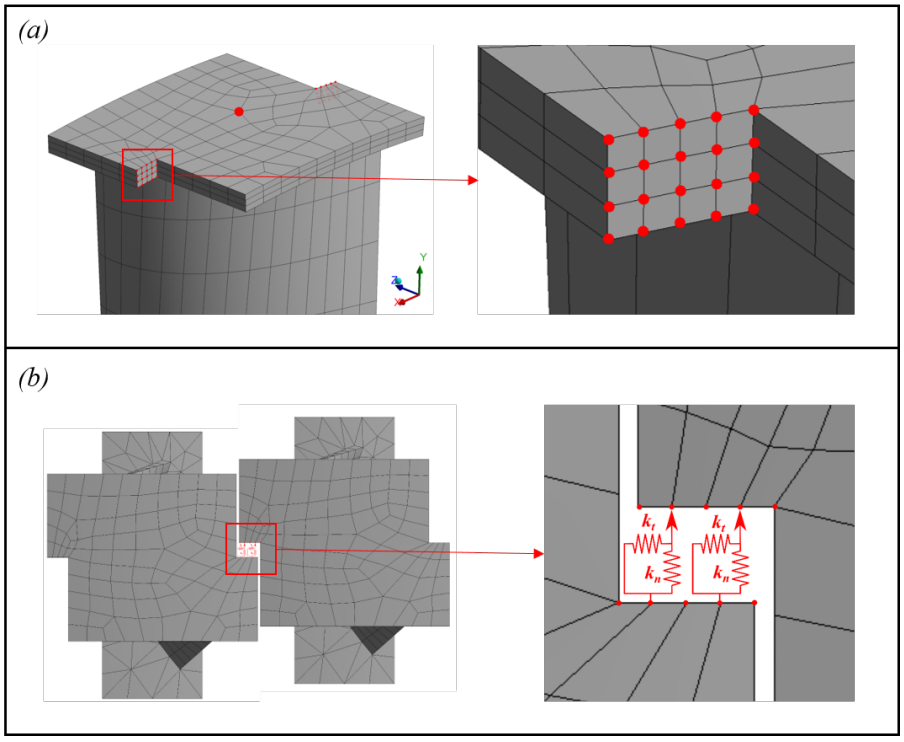

Fig. 4.10 (a) Highlight of the right shroud contact showing 20 contact nodes (b) Pictorial representation of the applied node-to-node contact model.

To define the adaptive wear parameter $v_{w,max}$, the following logic is applied. The static deflection of the blade is computed under the action of the static forces assuming no shroud contact. Then the average normal displacement of each contact surface is obtained. This value has been set as the maximum possible wear on each surface $v_{w,max}$, when such a depth is worn out, the blades would vibrate freely without any contact with the adjacent blades. Finally, the ratio $v_{w,max}/\delta_{max}$ is varied from 0.5% to 10% in steps as indicated in Table 4.3 to investigate its effect on the accuracy of the model in predicting the evolution of the system dynamics and the necessary computational effort.

4.3.2 Results.

Figure 4.11 shows the nodal diameter versus frequency relationship up to 15 ND for the stuck case. Figure 4.12 shows the nonlinear response for various engine order excitations along with the linear free state and stick state curves for the indicated loads.

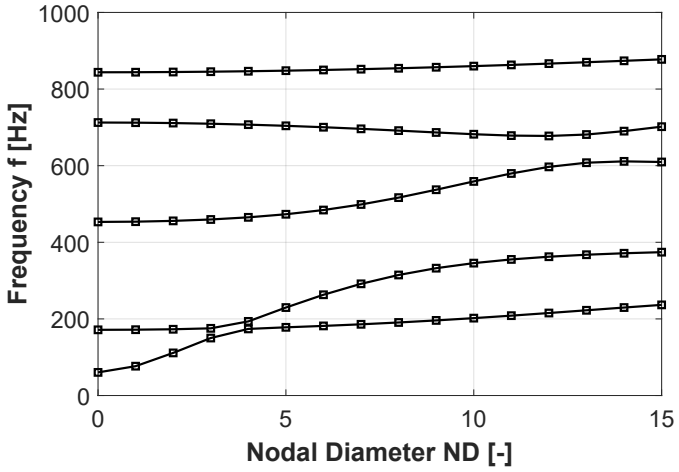

Fig. 4.11 Nodal diameter diagram shrouded blade with stuck contact. [Numerical]

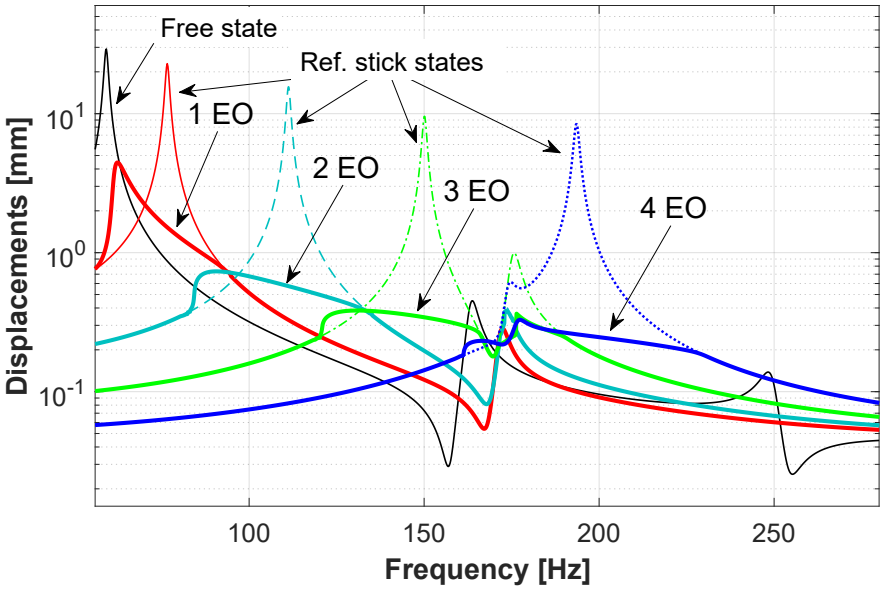

Fig. 4.12 Response to various EO excitations with reference linear free and stick state peaks. [Numerical]

Figure 4.13 shows the nonlinear FRF with fixed static load and varying excitation loads. The figure also includes a reference linear free state and stick state for comparison. With the increasing excitation force, the resonance frequency shifts towards the free state as the contact nodes experience a larger slip. For very large excitation forces, the bladed disk behaves closer to the free state condition.

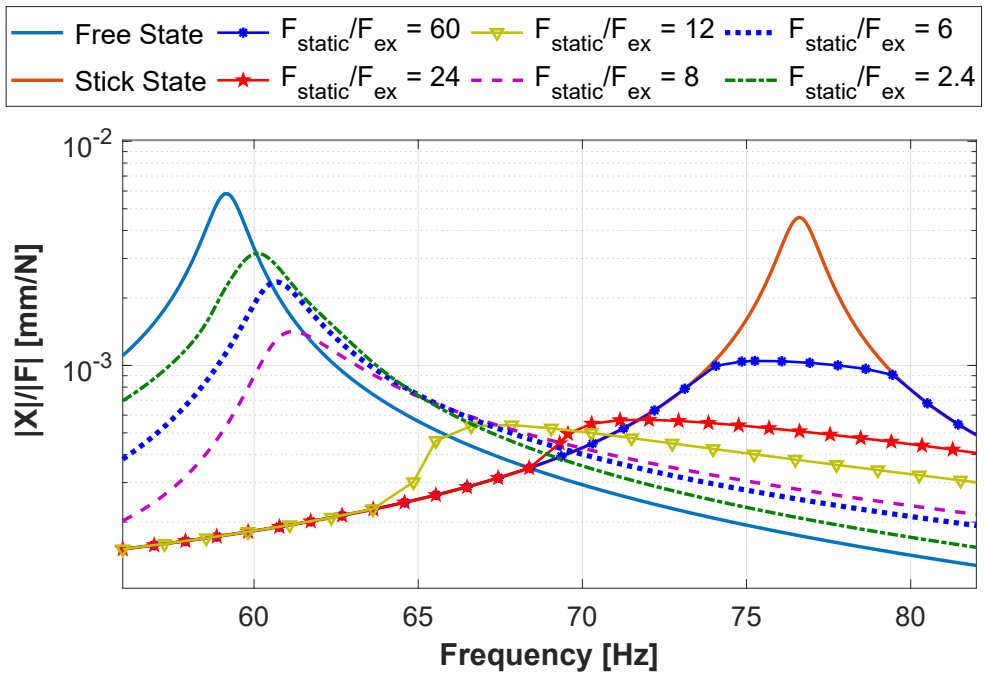

Fig. 4.13 FRF for various excitation loads with a fixed static load $(EO = 1)$. [Numerical]

Figure 4.14 shows the cumulative wear plot and the contact status plot at various wear iteration intervals. For the given loading conditions, the cumulative wear at the right shroud contact interface, the spatial wear distribution and the contact status at each node can be visualized. At the beginning of the wear, the contact is in the slip-stick state with uniform pressure distribution. As wear progresses, some of the contact nodes are in separation-slip-stick and eventually leading to separation-slip before the complete loss of contact. For simplicity, only one loading condition is shown. The same procedure can be used to visualize various loading conditions and the effect of the adaptive logic parameter ratio $v_{w,max}/\delta_{max}$ with an accurate insight at the contact interface behaviour.

$\frac{F_{static}}{F_{ex}} = 12$ $\frac{v_{w,max}}{\delta_{max}} = 5\%$	Cumulative wear plot: 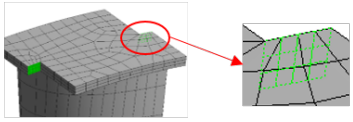	Contact status plot: 1: slip-stick 2: separation-slip-stick 3: separation-slip
Wear iteration 1 (start)	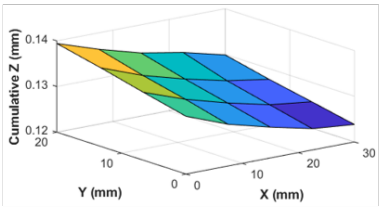	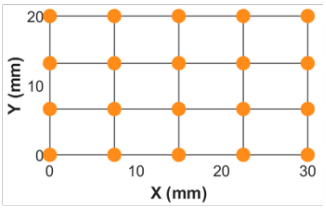
Wear iteration 12	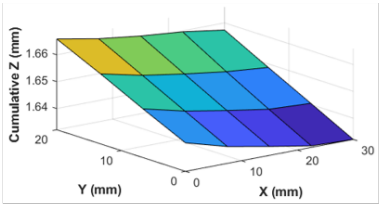	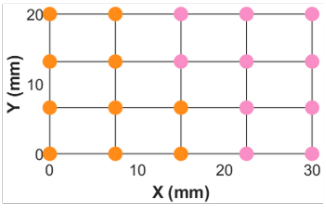
Wear iteration 27	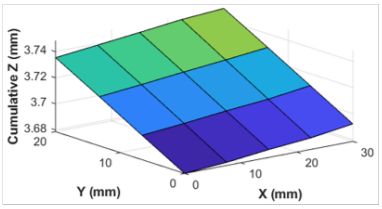	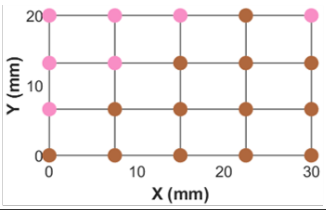
Wear iteration 62 (Iteration before full loss of contact)	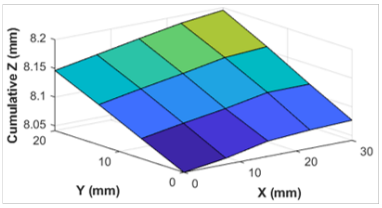	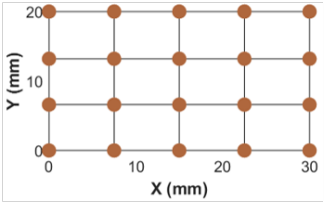

Fig. 4.14 Tabular representation of the cumulative wear plot and contact status plot of the right shroud contact at different wear iterations until the loss of contact for given loading conditions. [Numerical]

Figure 4.15 shows the response with the impact of wear and the backbone of the response curves with the progress of wear. The contact preload is continuously changing as the contact loosens due to wear. This loss of contact impacts the dynamic behaviour of the bladed disk. The coupled formulation used in this method is able to effectively update contact preload distribution in the nonlinear analysis, including the static component.

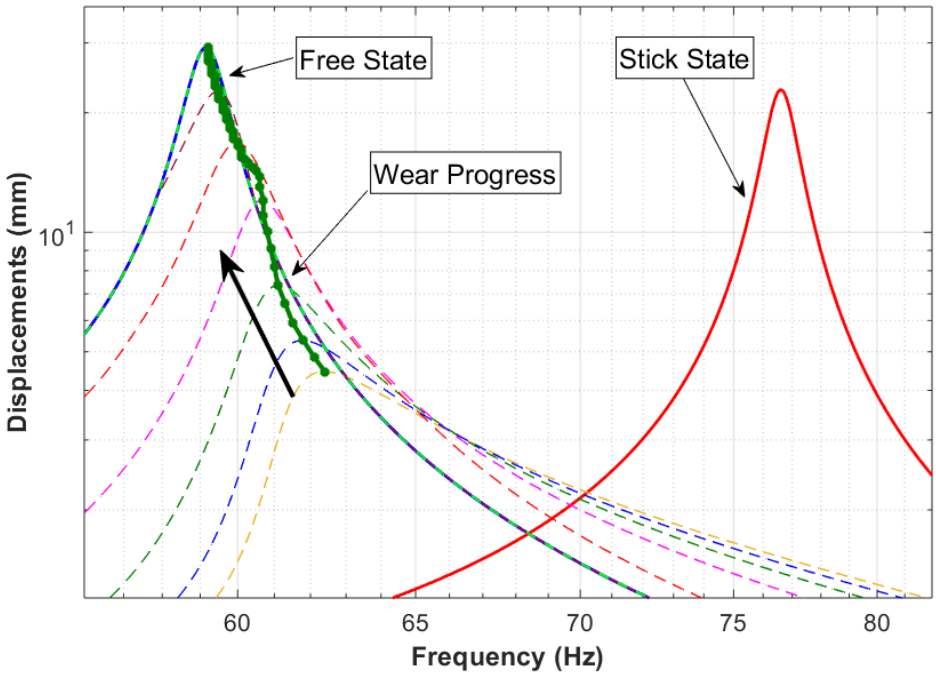

Fig. 4.15 Response graph showing the backbone of the nonlinear response $(EO = 1)$ obtained as wear progresses around first bending mode with free and stick states for reference for $v_{w,max} = 5\%$ of δ_{max}. [Numerical]

Figure 4.16 shows the number of wear cycles Z_W at each wear iteration as wear progresses until the loss of contact. It is important to note that the number of cycles at each wear iteration is changing. It is adapted according to the geometry and loading conditions. It is worthy of mentioning that the shape of the curve shown in this figure is not unique. Rather it depends on the loading conditions and the pressure distribution at the contact as well as on the relative contact kinematics at the excited resonance. Each wear iteration can contain a different number of cycles because depending on the loading conditions and the contact profile, the energy dissipated at each cycle could be very different, hence resulting in a different number of cycles.

It is beneficial to track the maximum response with respect to the cumulative number of cycles as it provides a brief idea of the number of vibration cycles where the amplitude starts to rise considerably. Figure 4.17 shows the maximum response versus the cumulative number of cycles until the full loss of contact. Results show that for higher ratios of $v_{w,max}/\delta_{max}$, the rate of change of the response is underestimated, leading to non-conservative predictions.

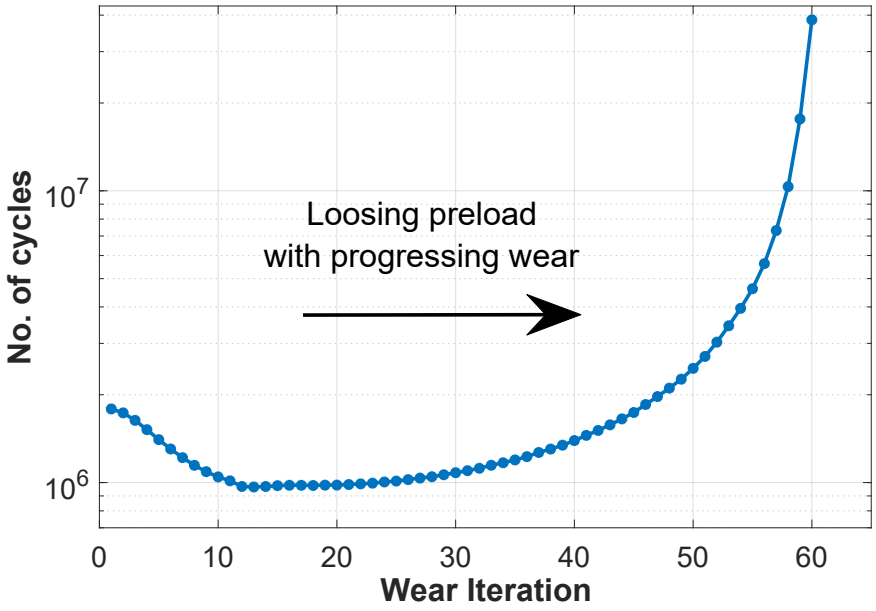

Fig. 4.16 Impact of wear on the number of vibration cycles at each wear iteration until full loss of contact for $v_{w,max} = 5\%$ of δ_{max}. [Note: the number of cycles is adaptive at each wear iteration]. [Numerical]

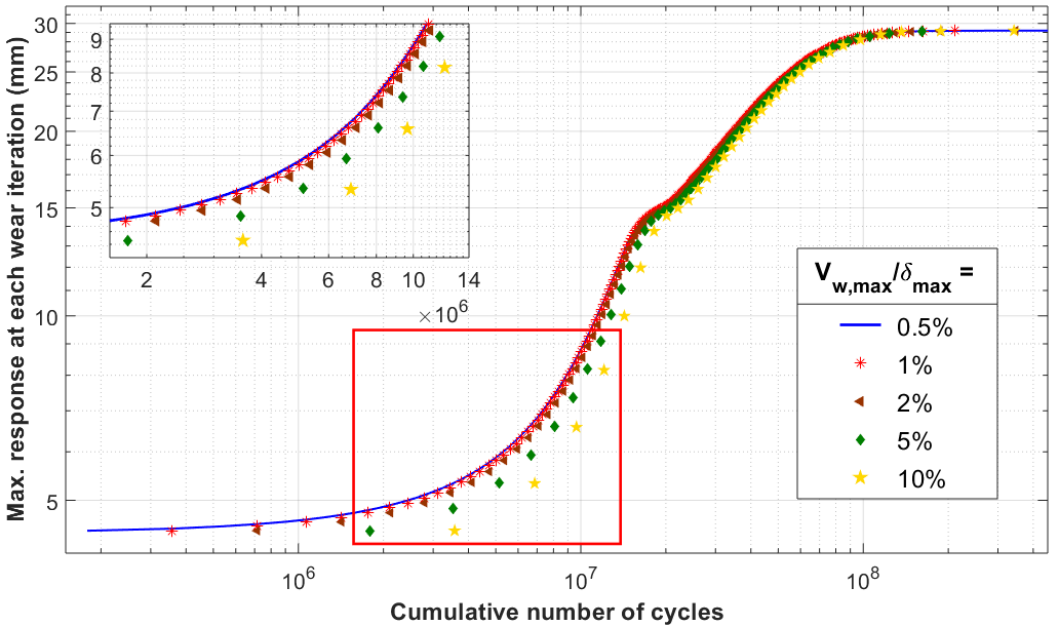

Fig. 4.17 Maximum response at each wear iteration vs the cumulative number of cycles for different values of $v_{w,max}$. [Numerical]

Table 4.4 summarizes the comparison of the effect of the choice of the ratio $v_{w,max}/\delta_{max}$ on the computational time, number of wear iterations necessary for the complete loss of contact, maximum wear depth and the error in the maximum wear depth.

$\frac{v_{w,max}}{\delta_{max}}$	**Computational time**	**Total no. of wear iterations**	**Max. total wear depth (mm)**	**Relative error in wear depth (%)**
0.5 %	5 hr 17 min	596	8.2566	-
1 %	2 hr 38 min	298	8.2572	0.01
2 %	1 hr 19 min	152	8.2916	0.4
5 %	0 hr 35 min	63	8.3808	1.5
10 %	0 hr 17 min	34	8.4697	2.6

Table 4.4 Comparison of the impact of wear analysis with nonlinear dynamic response solver for different values of $v_{w,max}$.

The indicated computational times in Table 4.2 and Table 4.4 are the wall clock time observed when the nonlinear analysis was run on Intel Xeon 4 core processor @ 3.50 GHz and 32 GB RAM stand-alone workstation. A caveat is mandated here for the results presented in both the test cases: the wear results are non-physical as a coarse approach is taken to model fretting wear. Other issues such as tribofilm growth, oxidation making the joint surface harder, grain coarsening and breaking affecting the stiffness of the surface and the simplified wear model itself are some of the aspects to be taken into account. Considering the complexity of dealing with wear and the dynamics and subsequent exponentially increasing computational costs for detailed models, this study is intended as a proof-of-concept and an in-depth analysis for design and convergence may be necessary.

4.4 Summary.

In this chapter, two numerical test cases were investigated, and the forced response dynamics results with the effect of the fretting wear phenomenon were studied. The methodology described in the previous chapter using frequency-domain based coupled HBM solver with wear model was used. For the first test case, a simple cantilever beam with a friction contact patch at the free end was used. The accelerated wear with adaptive wear logic using the wear energy approach was implemented to estimate the effect of wear on the contact, and the forced response dynamics were studied. The intermediate snapshots of the evolution of contact interface, vibration amplitudes and frequency shifts were also studied. The effect of the user-defined parameter to accelerate wear was also presented, and it is effectively making an opposing choice of computational time and accuracy of results. A further sensitivity study and experimental observation are needed for the concrete choice of the parameter. In the second test case, a realistic turbine bladed disk with shroud contacts with cyclic symmetry properties was analyzed. The nonlinear effect arising from the shroud-to-shroud contact coupling and the effective wear due to relative micro-slip and gross-slip at the shrouds was investigated. The evolution of the shroud contact interface and its subsequent effect on forced response dynamics for a particular choice of engine order excitation was presented. These two numerical cases proved as a validation step for the newly developed in-house solver to troubleshoot and enhance the capabilities of the solver. In the next chapter, a novel experimental test rig design will be presented to experimentally study the effect of fretting wear on the forced response of the test rig.

Chapter 5

Novel forced response test rig

5.1 Introduction.

This chapter presents a novel test designed and developed to experimentally study the effect of fretting wear on the long-term forced response of a system. A cantilever beam with a known contact on the free end is used as analogous to a turbine blade with tip shroud contact. A contact loading mechanism is used to load and simulate the changing preload with progressing wear, as seen in blade tips. The first part of the chapter describes the test rig design intent, instrumentation, set-up, calibration, system identification and full-length results of long-term forced response evolution and subsequent contact interface evolution with wear. The results include intermediate wear profiles and dynamic response from frequency sweeps, and evolution of hysteresis loops, energy dissipation, wear volume and contact preload until full loss of contact. The second part of the chapter focuses on the numerical prediction and validation part. It proposes a reformulation of HBM to incorporate the study of the effect of changing static preload and numerical simulation results corresponding to the experimental inputs. Finally, the numerical results are validated against the experimental results. Some of the results are published in [169].

5.2 Novel test rig.

5.2.1 Description of the test rig.

The goal of the new test rig is to experimentally study the effect of fretting wear on the dynamic response of a mechanical system. The system is excited by a harmonic force and undergoes a large number of fretting wear cycles. Table 5.1 shows the adopted criteria and the justification for the design of the test rig.

Criteria	**Justification**
Well-separated resonance peaks in the dominant slip direction.	To isolate and study the effect of wear on the modes of interest.
Permit experimentation for a wide range of contact preload to dynamic excitation ratio.	To study the effect of different contact preload and excitation force independently and the subsequent change in dynamic behaviour.
Replacement of contact specimens.	To allow testing of different contact area, geometry, materials and surface properties with relative ease.
Ability to measure accurate displacement and contact forces close to the contact region.	Measuring closer to the contact region allows capturing the accurate measurement data happening at the contact.
Large enough tangential relative displacement.	To generate high dissipated energy per cycle and simulate severe wear.

Table 5.1 Adopted criteria for the design of the test rig.

This type of response must be exhibited for various normal contact loads so that the changes due to fretting wear are easily detected in the selected range of frequencies. The test article is thought of as analogous to a blade with a tip shroud in a turbine bladed disk, namely a cantilever beam with a friction contact at the free end. The contact is loaded with a known preload given by means of an interference fit, as in the tip shroud. For a full characterization of the contact behaviour, the

measurement system must be capable of measuring the static and dynamic contact forces during operation. The measurement of relative displacement at the contact is also needed to record the slip-stick behaviour and plot hysteresis loops at each fretting cycle. The technical details of the test rig are provided as drawings in Appendix B.

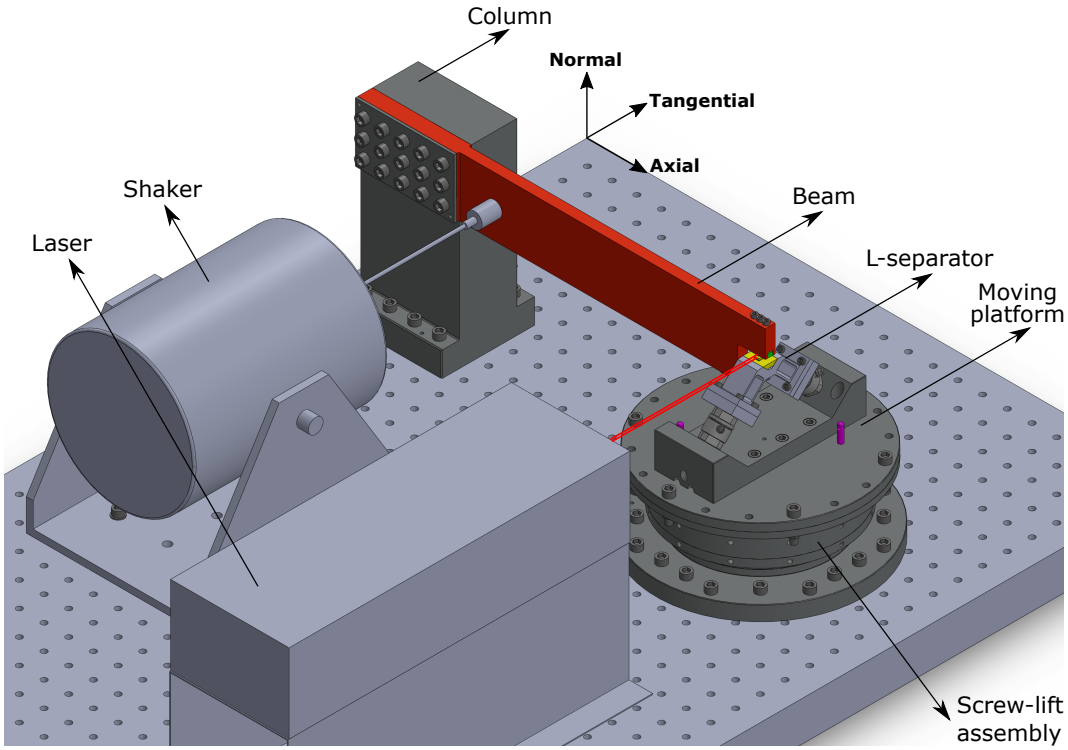

Fig. 5.1 Rendered image of the test rig along with the named reference axes.

The rig is made of two main parts, as shown in Figure 5.1. The first part includes the cantilever beam, connected to a column whose base is fixed to a table. The free length of the beam is 310 mm with a rectangular cross-section of 60 mm x 10 mm, having the first dominant bending mode well separated from other modes. The beam length and cross-section dimensions can be customized in future to simulate different natural frequencies. The column, a bulk component, houses the beam with 15 screw-pair and a cover plate for even tightening and load distribution to enable a rigid connection and avoid unintended flexibility arising at the interface. The column is attached to the table via 8 screws. The actual images of the test rig can be seen in Figure 5.2. The second part includes a contact loading mechanism designed to

load the contact with a certain preload. A detailed explanation of the contact loading mechanism is given in section 5.2.2.

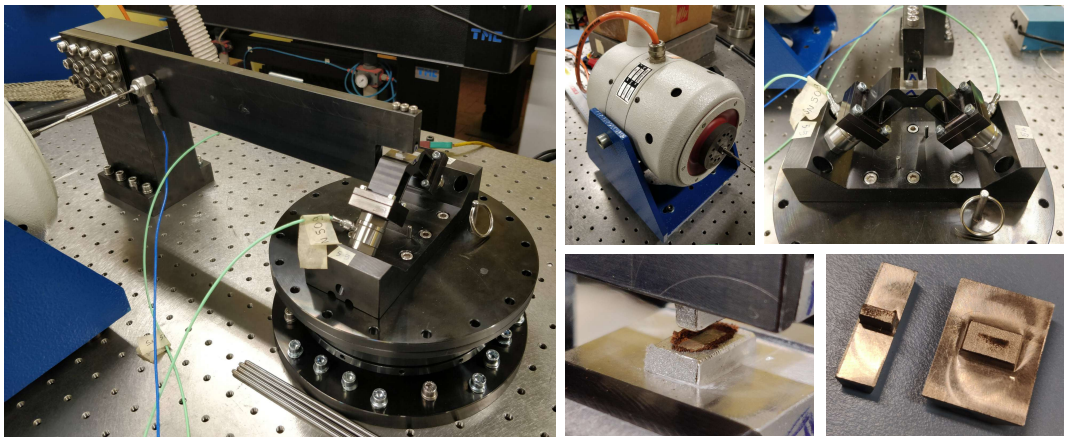

Fig. 5.2 Actual images of the test rig, shaker, L-separator assembly, top and bottom specimens.

The beam has a slot at the free end in which one specimen (the upper specimen) could be mounted via three screws. The other specimen (the lower specimen) is mounted onto the L-separator via three screws. An L-separator, a right-angled component, is mounted on the top of the moving platform with two force transducers mounted at a 45° angle to the normal contact direction. The two force transducers can record the static and dynamic force components throughout the test. Because of its geometry, this device "separates" the contact force into two components along the load cell axis so that the load cell measures the forces without the crosstalk effect. Since this device is made of two limbs at 90 degrees to each other, it makes an "L-shape". Hence the name "L-separator". The design criteria and the functioning of the L-separator are described in detail in [168]. The top specimen has a contact surface of $2mm$ x $5mm$ with a nominal area of $10mm^2$, while the bottom specimen has a larger flat counter surface.

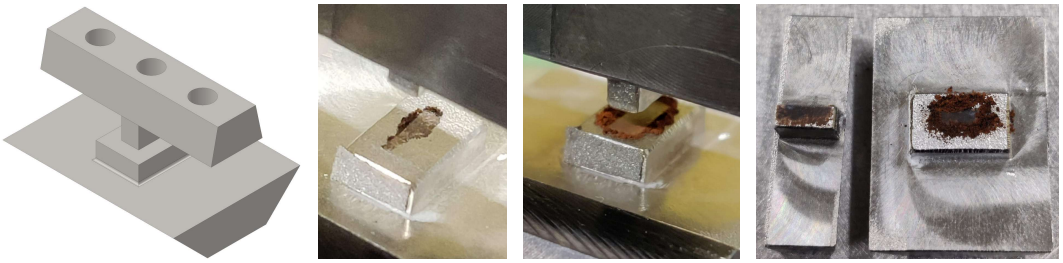

Fig. 5.3 Contact pair, mid-wear and fully worn specimens.

The specimen couple is designed as replaceable parts, which can be customized with known contact geometry and surface properties beforehand. The contact geometry can be modified with different nominal contact area and combinations of flat, cylinder or sphere. Theoretically, the contact area can be modified to as low as $1mm^2$ and up to $25mm^2$. Figure 5.3 shows the rendered and real images of the contact pair with partial and fully worn specimens. The upper and lower specimens are fixed to their respective housing components by inserting into the 'slots' with mating walls and screwed using 3x M3 screws. This way, the specimens are secured well, and any possible uncertainty arising due to the clamping is reduced. Moreover, this clamping system allows assembling the specimen in the same position, at least within the machining tolerances, after disassembling and reassembling the specimen for the surface measurements. Figure 5.4 shows the cross-section of the specimens and their mounting arrangement and a real image of the assembly.

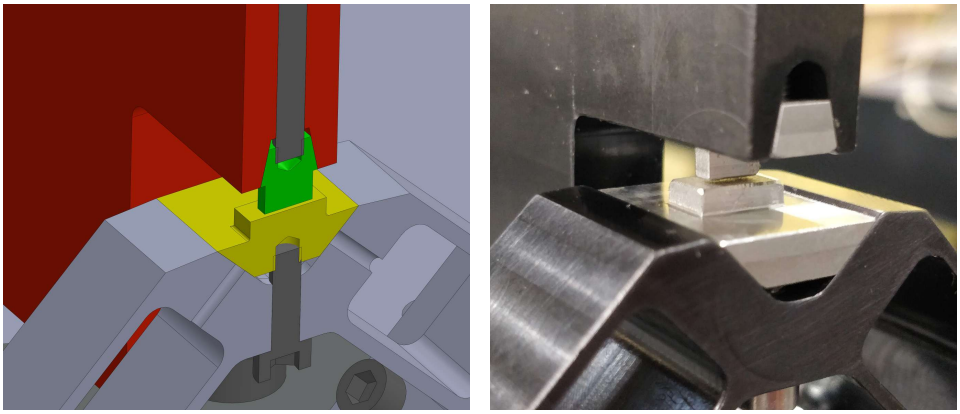

Fig. 5.4 Close-up view and cross-section at the contact (a) rendered image (b) real image.

A split beam laser velocimeter (Polytec OFV-552) in combination with its controller (Polytec OFV-5000) is used to measure the relative velocity between the contact surfaces during the wear test. The displacement is calculated by integrating the velocity signal. The two laser beams are pointed one to the top specimen and the other to the bottom specimen, as close as possible to the contact point. The relative velocity is obtained by taking the difference between the two signals. The time signal is read by the Data Acquisition System (DAQ).

The cantilever beam is excited by an electromagnetic shaker (TIRA-5112 shaker with TIRA BAA-500 controller) close to the fixed support at a low mobility point. This helps to inject the energy into the beam with relatively low amplitudes of the

moving mass of the shaker. The shaker is rated up to 100N. The beam is excited at a fixed frequency for the wear test and a frequency sweep to observe the dynamic response. A load cell (PCB Piezotronics force sensor 208C03) is placed between the beam excitation point and the stinger to measure the applied force.

A uniaxial accelerometer is mounted onto the tip of the beam in the tangential direction to record the acceleration during the frequency sweep to record the response of the system. The whole test rig is mounted on a pneumatic table. The material used for all the components is AISI 304. The test rig is set up at the LAQ AERMEC Lab in Politecnico di Torino. A detailed description and user-manual of the test rig with various electrical connections and software usage is provided in Appendix C for reference.

5.2.2 Contact loading mechanism.

This section provides a detailed description of the contact loading mechanism. The requirements of the loading assembly are to have precise, stable, rigid and separated natural frequencies from that of vibrating beam modes. In this way, the modal participation of the support when the contact is engaged is minimum. One can visualize the effect of wear on the response peaks and frequency shifts, if any. During the design phase, modal analysis has been carried out to study the natural frequencies of the L-separator and the contact loading mechanism so as to not interfere with the interested frequency range. The first modes obtained are over 2000 Hz, and this has been verified using experimental modal analysis and found to be over 1200 Hz, which is well beyond the interested frequency range. Also, to accommodate the changing preload condition with progressing wear, the platform has to be stable and locked at a certain determined height during the test. The principle is based on a standard screw-lift system with a vertical moving platform. The exploded view of the loading assembly is depicted in Figure 5.5.

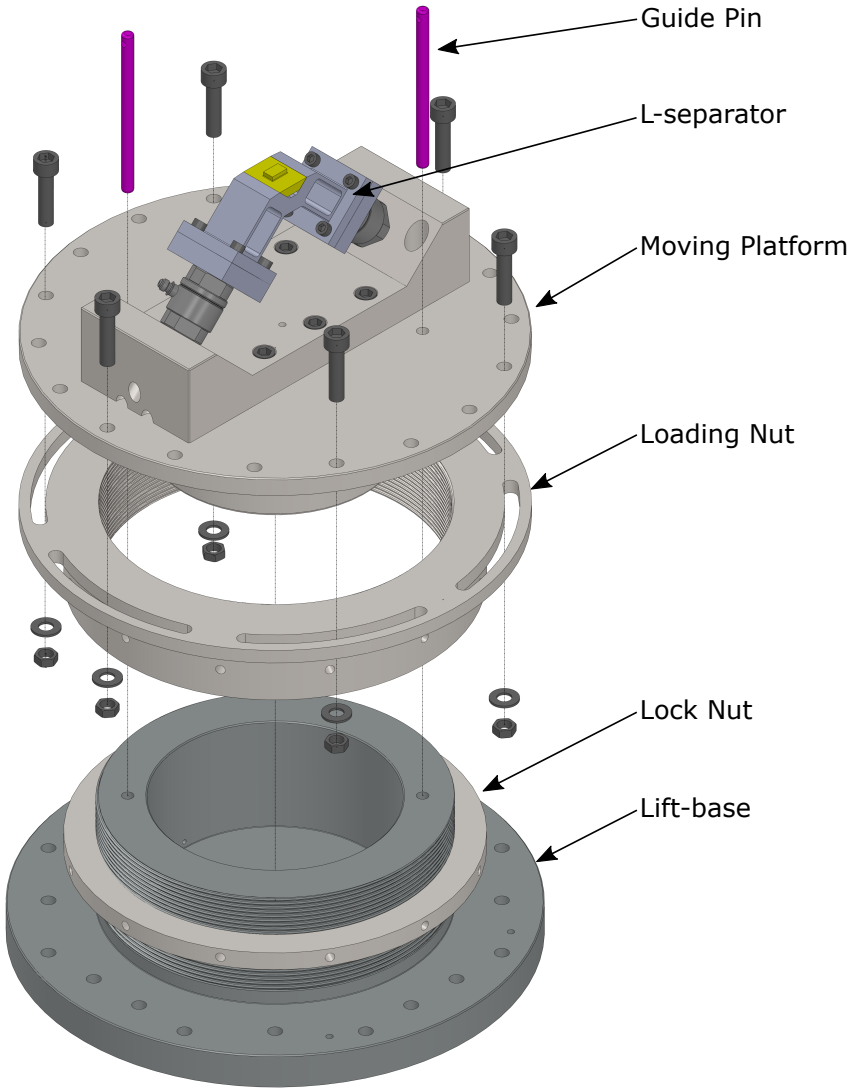

Fig. 5.5 Exploded view of the contact loading system.

The moving platform translates vertically upon the rotation of the loading nut. This motion produces interference fit between the two contact surfaces so that the prescribed static preload is applied. The cross-section of the assembly is shown in Figure 5.6. The figure also shows the forces measured from the two load cells and resolved to obtain the tangential and normal contact forces through the following equations:

$$\begin{aligned} F_t &= F_1 * cos(45^\circ) - F_2 * cos(45^\circ) \\ F_n &= F_1 * cos(45^\circ) + F_2 * cos(45^\circ) \end{aligned} \tag{5.1}$$

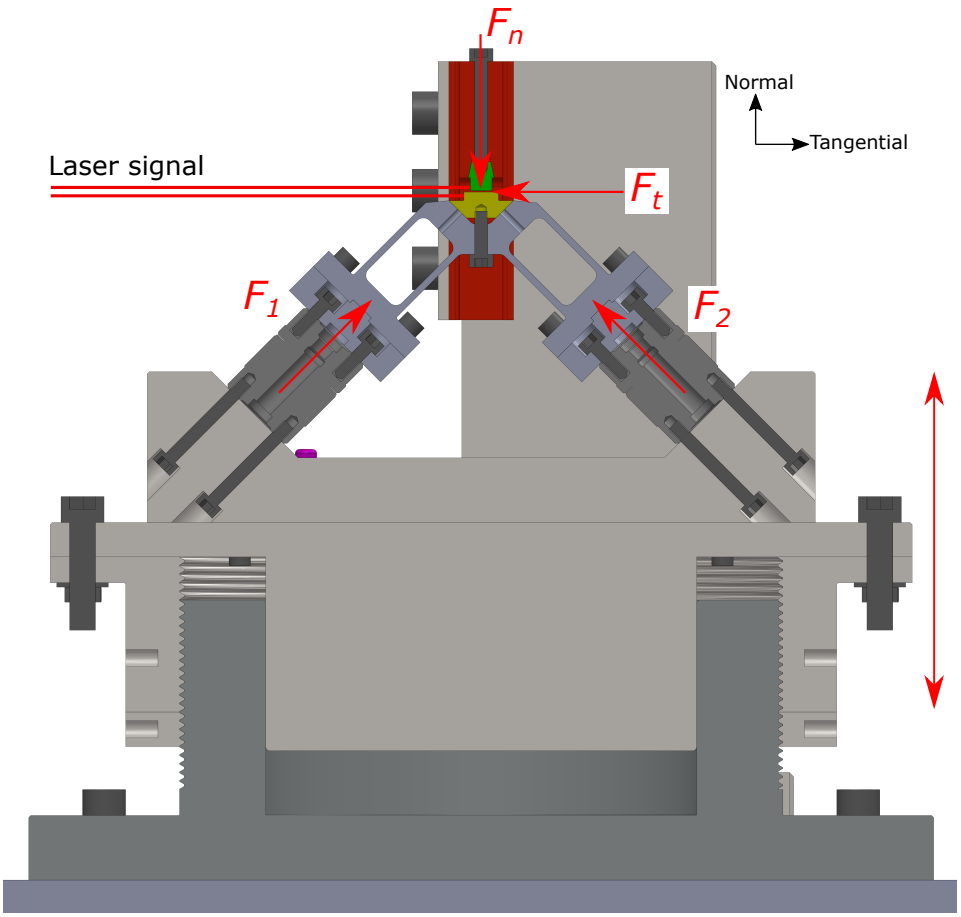

Fig. 5.6 Cross-section of the screw-lift based contact loading mechanism.

The highlight of this arrangement is that there is the possibility of simulating the 'changing preload' with wear. The platform is raised to any desired height and locked at that position. The height of the platform governs the resulting static preload. In this way, the contact between the two elements of the contact pair is engaged and the cantilever beam has a certain deflection. The load cells connected to the L-separator allows measuring the value of static contact preload, when the contact is engaged. As wear occurs and there is loss of material at the contact, the interference between the two bodies in contact reduces as well as the cantilever beam deflection reduces and the normal static preload. This type of changing preload with wear is commonly observed in bladed disks with shroud contacts.

The base has 140mm diameter male screw threads with 40 mm screw length and 2 mm pitch. A loading nut with counter female threads is mounted to the base and also flushes onto the moving platform as shown in Figure 5.6. A lock nut is provided

to ensure the loading nut is secured in place. Two guide pins passing through the moving plate and the base constrain the rotating DOF and maintain the alignment of the platform and contact orientation. Now there is still one DOF left to constrain, i.e. the vertical direction. Six screws with nut and washer connect the moving platform with the loading nut at any given desirable platform height. To achieve this, the loading nut has elongated slots, and the moving plate has 18 through holes. This ensures at any given rotation angle, there are at least six locations where the screws can be used to constraint the moving plate to the loading nut. In this way, all DOFs are constrained.

5.2.3 Instrumentation and data acquisition system.

A 16 channel Siemens SCADAS Mobile data acquisition system is used to acquire the time signals of the shaker stinger-beam force transducer, L-separator left and right force transducers, relative displacement laser, accelerometers, and to control the shaker input signal. The Siemens Simcenter Testlab software modules clubbed to SCADAS Mobile hardware are used to perform the wear tests and also to measure FRFs at defined intervals. Figure 5.7 shows the instrumentation and sensors used by the test rig. The DAQ is connected to the computer, and the time signals are recorded during the wear test and FRFs during the frequency sweep.

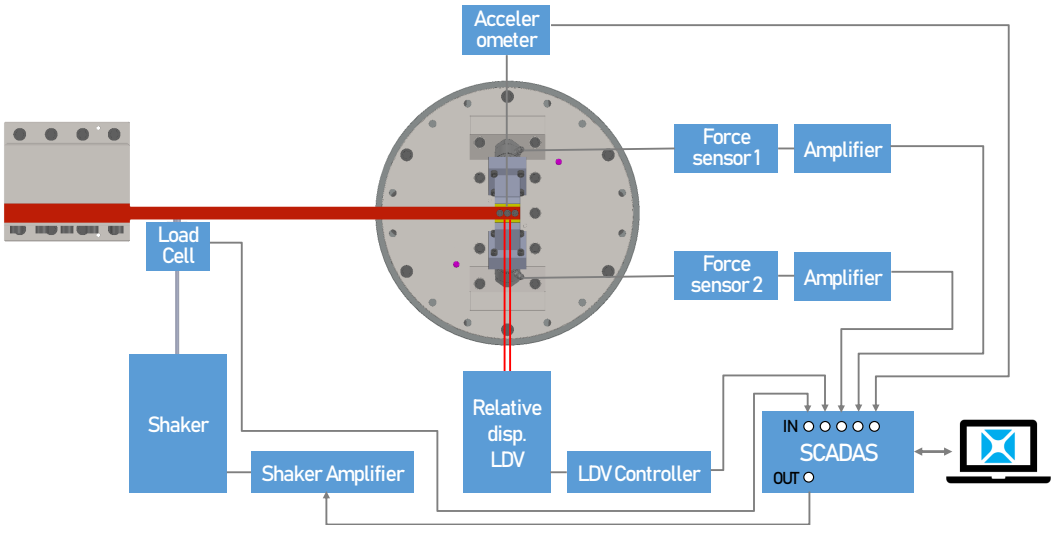

Fig. 5.7 Instrumentation of the test rig.

5.2.4 Test plan.

To study the impact of fretting wear on the dynamics of the beam, one way to achieve is to excite the system is excited at a fixed frequency for a set number of cycles. The choice of the frequency of excitation and excitation force is discussed in the results section. In a typical metal to metal contact with nominal loading conditions subjected to fretting wear, the amount of wear occurred is minuscule in one vibration cycle. However, a few millions of fretting cycles are needed to substantially observe a loss of material at the contact and visualize the effect on the system FRFs. It would also be useful to record surface scans using an optical interferometer at various wear intervals. To avoid uncertainty due to disassembling and assembling the specimens at various intervals for specimen scans during the full-length test, the frequency sweeps has to be performed before the removal and after fixing the specimens at each interval and ensuring the contact is loaded to the same level. To achieve this, the height of the moving platform is closely monitored, and the same height is ensured throughout the test. Hence, a smart test plan is needed to capture surface scans, frequency sweeps and a number of wear cycles at a fixed frequency. Figure 5.8 shows a schematic representation of the test plan to study the effect of wear on the forced response dynamics. The whole test is carried out at room temperature.

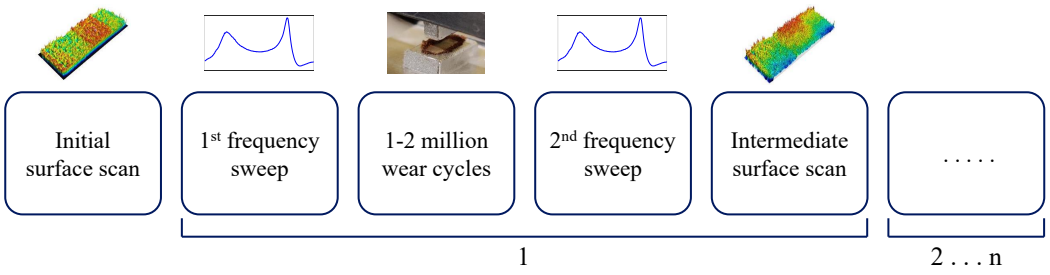

Fig. 5.8 Test plan embedding surface scans, frequency sweeps and wear cycles at a fixed frequency.

The plan for one full range test is devised to be:

- Scan the specimen surfaces of the contact pair using a non-contact 3D optical profilometer.
- Run the frequency sweep with pristine specimen contact pair.

- Run a set number of vibration cycles at a fixed frequency, for example, 0.5 million cycles.
- Run the frequency sweep.
- Remove the specimens and obtain intermediate worn out surface profiles using a profilometer.
- Reassemble the contact pair and repeat the frequency sweeps, fixed frequency wear cycles and surface scans until a desired total number of wear cycles are obtained or full loss of contact.

5.3 Experimental results and discussion.

5.3.1 System identification.

The first step before proceeding with the actual full range test plan is to characterize the test rig and understand its actual dynamic behaviour under open and closed contact conditions by means of experimental modal analysis. The bolted joints and contact interfaces such as the connections between the beam and the column, column and the table, loading mechanism, etc., could differ from the dynamic behaviour as computed by the numerical FE models. The bolted joints are never perfect and can introduce flexibility and damping, undesirable from the numerical analysis point of view. To collect the FRF curves necessary to the experimental modal analysis of a system, two methods were contemplated, namely, roving hammer test and roving accelerometer test. In this case, the roving hammer test was selected as a more suitable option because the accelerometers can be fixed, and numerous hammer impacts could be performed freely and avoid accelerometer mass loading. Hence, a roving hammer test was performed on various locations on the test rig. Figure 5.9 shows the roving hammer impact points setup on the test rig and the three accelerometer locations in the tangential, normal and axial direction from the contact point of view. A total of 107 impact locations were chosen to visualize experimental mode shapes with a fine mesh distribution. Figure 5.10 and Figure 5.11 show a sample mode shape visualization at two different modes to understand the behaviour of the test rig for open and stuck configuration respectively.

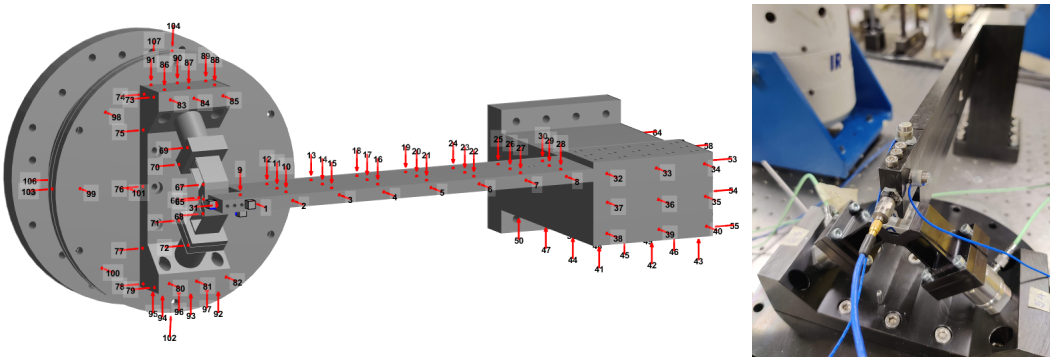

Fig. 5.9 Roving hammer impact locations to characterize the test rig and visualize the experimental mode shapes.

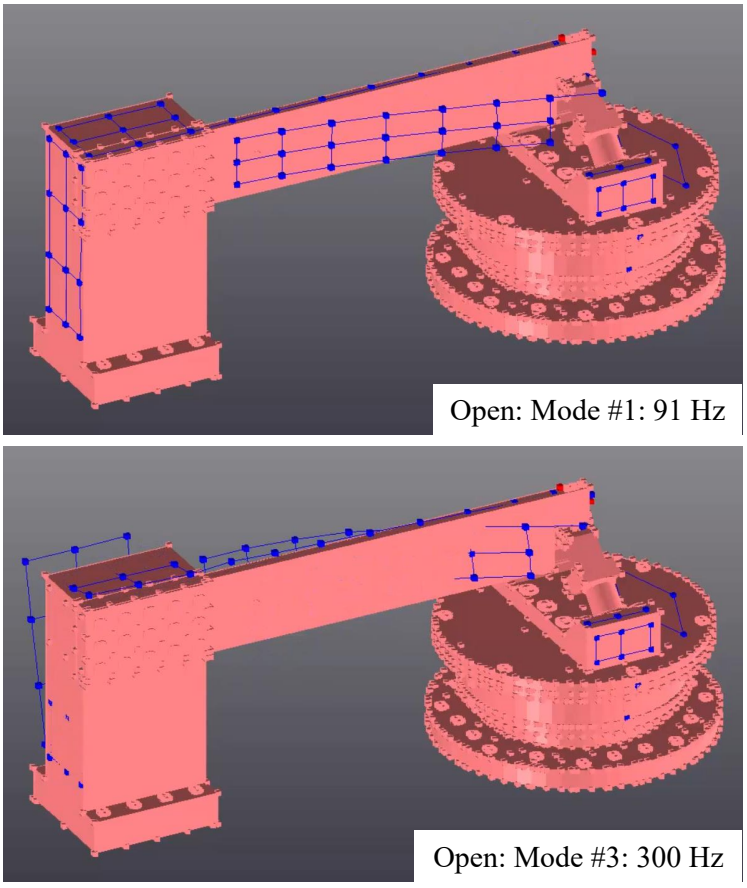

Fig. 5.10 Sample mode shape visualization at two different modes for open configuration.

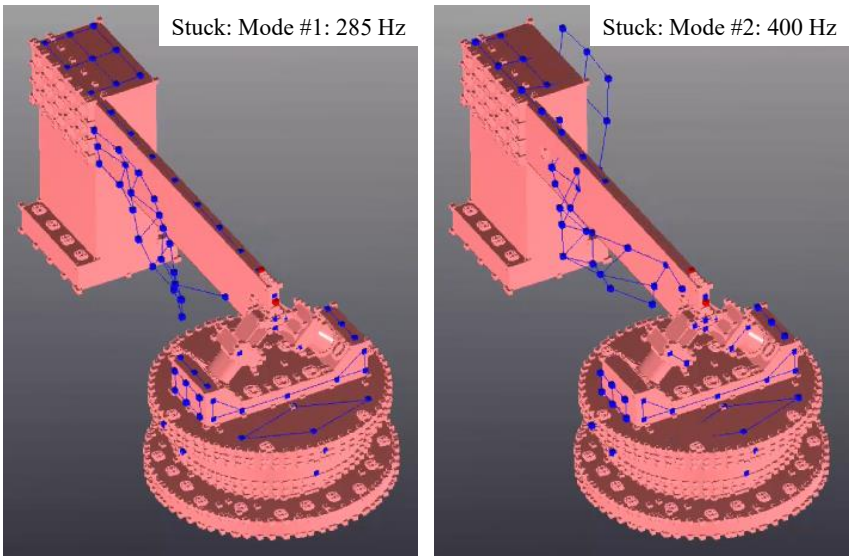

Fig. 5.11 Sample mode shape visualization at two different modes for stuck configuration.

Table 5.2 shows the experimental modal analysis results obtained using the roving hammer test for open and stuck contact. The open case is generated by not engaging the contact and the beam acting as a free cantilever. The stuck case is generated by applying a very high contact preload. For over 150N contact preloads, no relative displacement at the contact was observed by the laser. The dominant displacement direction for the first five modes is shown in the table to understand the behaviour of the test rig. Nevertheless, due to the design of the test rig and the lateral connection of the beam to the column (refer Figure 5.1), in mode shapes dominated by bending in the tangential direction, displacement in normal direction also occurs.

Open contact			Stuck contact		
Mode #	**Natural frequency (Hz)**	**Dominant displacement direction**	**Mode #**	**Natural frequency (Hz)**	**Dominant displacement direction**
1	91	Bending: Tangential	1	285	Bending: Tangential
2	230	Bending: Normal	2	400	Bending: Tangential
3	300	Bending: Tangential	3	868	Twisting
4	575	Bending: Tangential	4	1180	Bending+ Twisting
5	840	Twisting	5	1800	Bending: Complex

Table 5.2 Experimental modal analysis results obtained using roving hammer test for open and stuck contact.

Figure 5.12 shows the dynamic response of the test rig for open and closed contact conditions in the tangential, normal, and axial direction with respect to the contact with shaker excitation. These curves can be used as linear reference open case and stuck case to highlight the nonlinearity due to friction contact and the impact of fretting wear on the evolution of system dynamics.

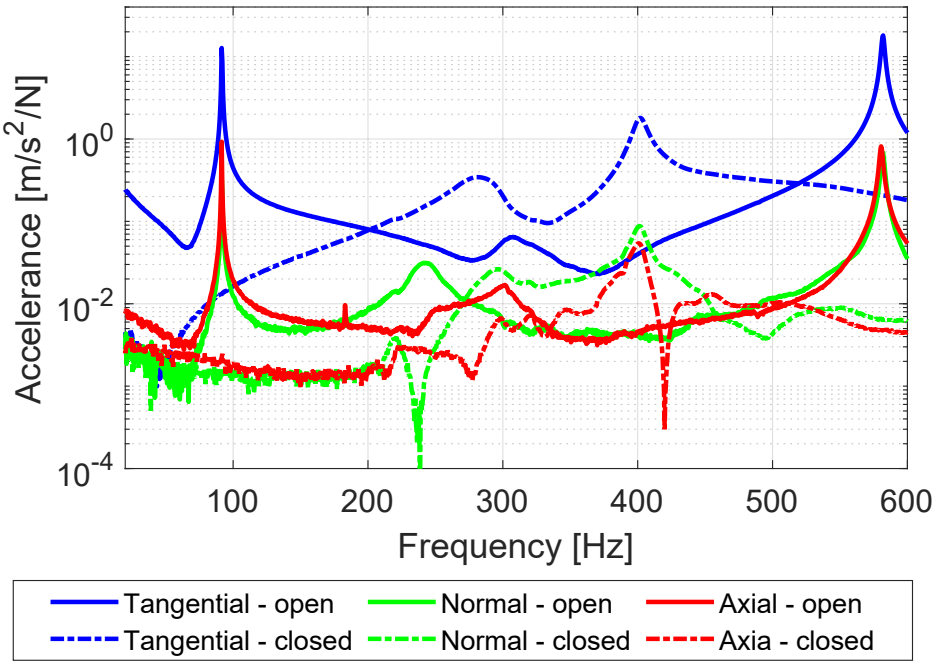

Fig. 5.12 Frequency response function of the test rig with shaker excitation for open and closed contacts. (Tangential, Normal and Axial directions are with respect to the contact). [Experimental]

5.3.2 Effect of excitation amplitude.

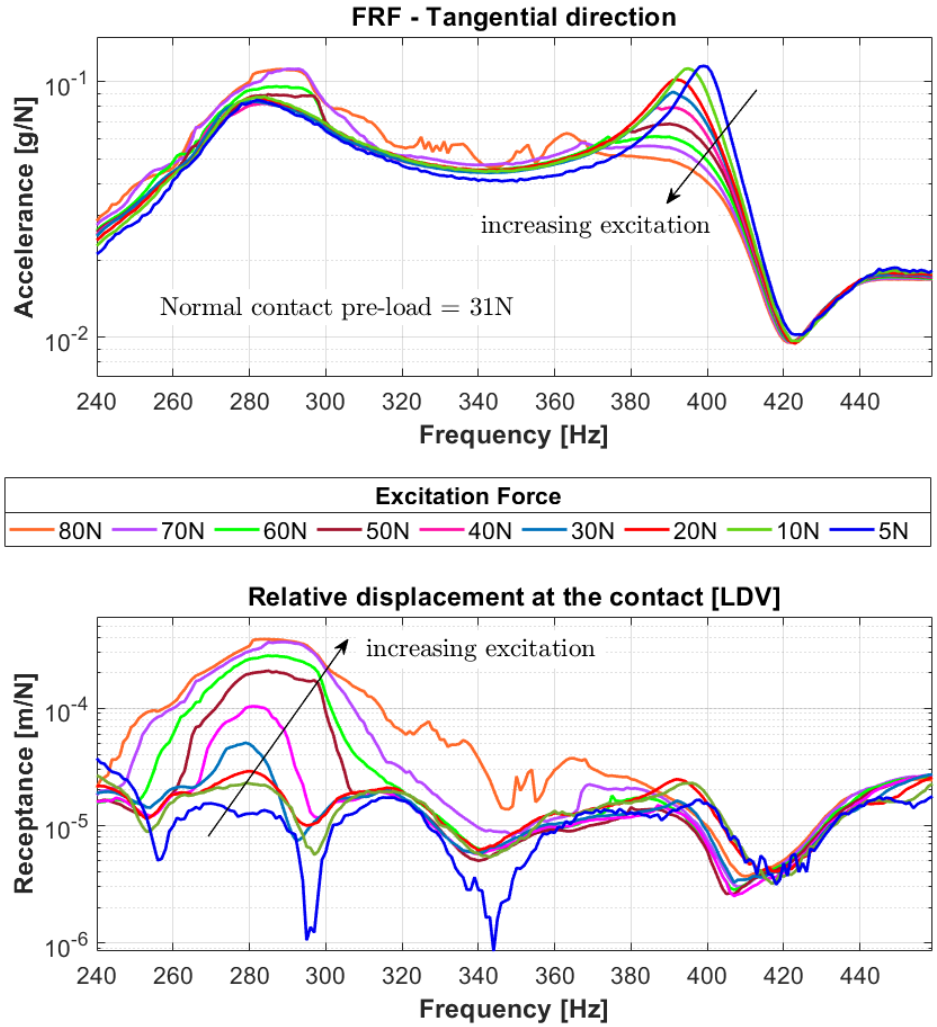

Fig. 5.13 FRF of the test rig for various excitation at a fixed preload as recorded by the accelerometer in tangential direction (top). Corresponding receptance as recorded by the relative displacement laser (bottom). [Experimental]

The resonance peaks of interest are the modes that correspond to the maximum relative displacement in the tangential direction. The frequency range corresponding to these peaks for closed contact is between 240 Hz to 450 Hz. There are two dominant modes to look out for, around 280 Hz and 400 Hz. The upper plot in Figure 5.13 shows the FRFs when the beam is excited using a shaker, and a frequency sweep is run in this frequency range for various excitation forces under a fixed contact preload. The FRFs are recorded using an accelerometer attached in the tangential

direction on the beam close to the contact. Also, the lower plot in Figure 5.13 shows the corresponding receptance as measured by the relative displacement laser close to the contact. The excitation force is varied from 5 N to 80 N in 9 intervals. It is interesting to see the effect of increasing excitation has on the 400 Hz peak. Due to the nonlinearity in the system induced by friction contact, the level of excitation affects the system configuration leading to different operational deflection shapes at different excitation force levels. As a result, the accelerance of the measured DOF becomes force-dependent, as shown in Figure 5.13.

5.3.3 Determination of excitation frequency and excitation force.

So far, the test rig dynamic behaviour under various loading conditions has been experimentally characterized. The next step was to decide the frequency at which the fretting wear to be run for a few millions of cycles to obtain substantial wear up to the potential full loss of contact. From the previous section, it was clear that the contact experiences the maximum relative displacement for the shaker excitation force around 70 N at 280-290 Hz. The energy dissipation is the area under the curve of hysteresis loops, i.e. the product of friction force and the relative tangential displacement. Figure 5.14 shows the hysteresis loops obtained at 290 Hz frequency for various excitation forces. The hysteresis loops acquisition is performed by collecting 60 data points per cycle. It is clear that a large excitation force determined a wider area of the hysteresis cycle, corresponding to a higher value of dissipated energy per cycle. The asymmetry of the hysteresis cycles, clearly visible in Figure 5.14, is due to a variation of normal load during vibration ([69]) possibly due to:

- Asymmetry in the test rig design, already mentioned in Section 5.3.1;
- Non-perfect alignment of the contact surfaces.

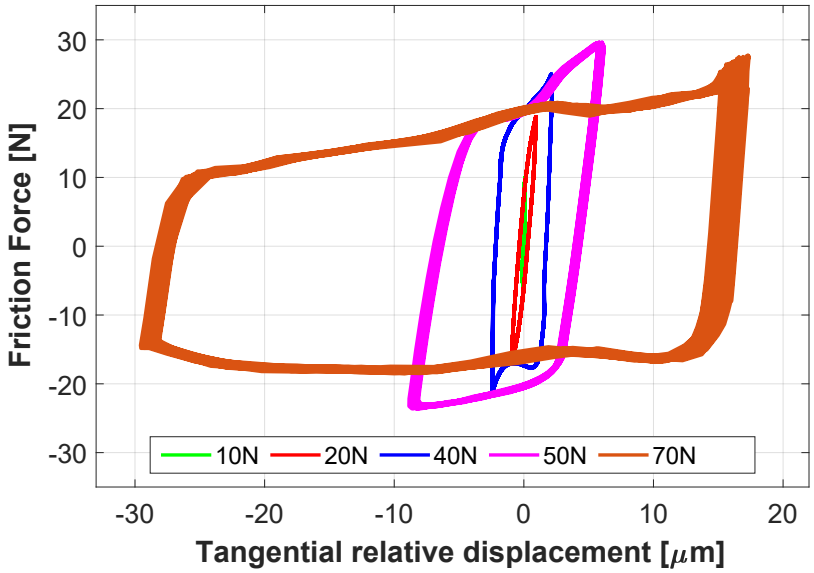

Fig. 5.14 Steady-state hysteresis loops for various excitation at 290Hz frequency. (Each curve plots 100 cycles at each excitation.) [Experimental]

Table 5.3 shows the relationship between the dissipated energy per cycle, the relative displacement and the periodic excitation amplitude. For excitation forces larger than 50 N, the contact experiences stick and full slip behaviour. The transition between stick to slip can also be observed. For excitation forces below 50 N, the contact does not experience full sliding and only stick to a micro-slip regime. The uneven size of the left and right stick regime and the shape of the hysteresis loop can be attributed to the asymmetry of the test rig (beam/column connection) that affects its mode shapes, as shown in Table 5.2. In particular, the mode shape corresponding to the natural frequency of 290 Hz, around which the wear test is performed, shows a dominant tangential displacement of the beam, associated with a non-negligible normal displacement that affects the shape of the hysteresis cycle.

From the above-mentioned results, it was concluded that, for the accelerated wear test, the best option was to excite the test rig at 70-80 N at 290 Hz for the maximum energy dissipation at each cycle amounting to approximately $1400\mu J$ with a relative displacement of $50\mu m$. The energy dissipation and the relative displacement is very sensitive to the magnitude of excitation force in the nonlinear range due to the nonlinearity introduced by the friction contact. Hence, even a small variation in the excitation amplitude could result in large swings in the energy dissipation at each cycle.

Excitation amplitude (N)	**Energy dissipated at each cycle (μJ)**	**Tangential relative displacement (μm)**
10	1.5	0.2
20	20	2
40	150	5
50	450	12
70	1400	50

Table 5.3 Energy dissipated per cycle for various excitation (Normal preload of 31N).

Figure 5.15 shows the normal and tangential contact force at one vibration cycle as recorded by the force transducers (F_1 & F_2). The co-efficient of friction can be computed by drawing an envelope above and below the friction contact force for the $+\mu N$ and $-\mu N$ friction limit. In this way, the coefficient of friction is computed to be approximately 0.9 for the plain AISI 304 metal to metal dry contact as shown in the figure. Figure 5.15 also shows a high-frequency component of the contact forces. A Fourier analysis of the response showed the contribution of the 4th harmonic, whose frequency was very close to one of the higher natural frequencies of the test rig, experimentally identified at around 1160 Hz.

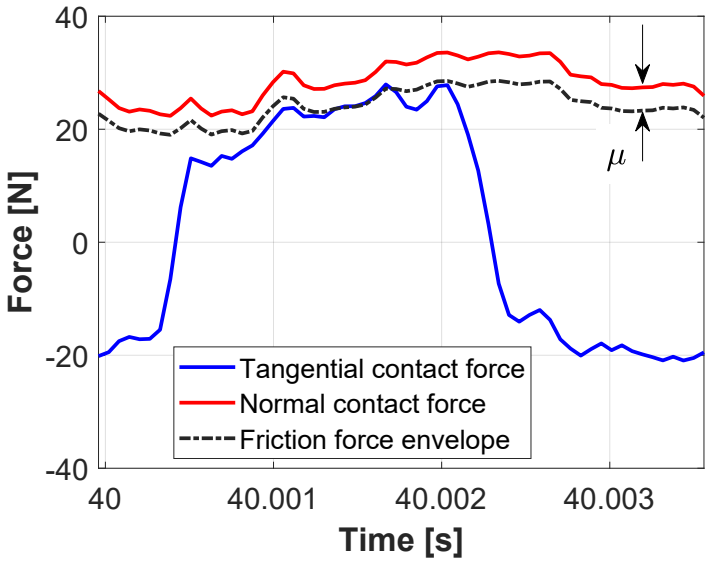

Fig. 5.15 Normal and tangential contact force at one cycle. [Experimental]

5.3.4 Full-range test results.

After the set-up and commissioning of the test rig, the full range test was performed as per the test plan. The test parameters are set to 70 N as excitation force, 31 N contact preload, 290 Hz as excitation frequency for wear test, 240 to 450 Hz frequency range for the frequency sweep. The test was run until the full loss of contact is observed. The full loss of contact occurred for 16 million wear cycles resulting in 8 intervals for the specimen surface scans, and 32 intervals for the intermediate frequency sweeps every 0.5 million cycles to record the effect of wear on the FRFs. The repeatability after disassembly and reassembly procedure of the specimens for surface scans were ensured by performing before and after frequency sweeps, and monitoring and ensuring the moving platform height is precisely the same throughout the test. During the test, the evolution of the following quantities was tracked: contact area, hysteresis loop, contact preload, wear volume, dissipated energy and force response.

5.3.4.1 Contact area evolution.

The surface scans of the upper and lower specimen were obtained using a high-resolution optical 3D surface measurement device. The vertical and lateral resolution achieved during the surface measurements were 2.2 and 0.5 μm respectively. The measured topography was then exported to and analyzed in Digital Surf MountainsMap software. The specimen surfaces were obtained by milling and polishing and resulted in average surface roughness of 1 μm. The specimens were cleaned before the surface scans were obtained. For the worn specimens, the oxide debris was removed, cleaned and then the surface scans were done. For the full test plan, a whole of 8 scans was done at 0 cycles, 0.5 million, 1.5 million, 4 million, 7 million, 10 million, 13 million and 16 million cycles. Figure 5.16 presents the worn surface images of upper and lower specimens at various intervals. The surface is levelled and oriented so that one-on-one visual comparison can be made at the optimal scale. It can be seen through the images that, though the nominal contact area is around 10 mm^2, only a partial initial contact area is established at the beginning of the wear test. This is due to the fact that the cantilever beam deflected by the application of normal load through the loading mechanism makes only an 'edge contact' at the inner edge closest to the column. Also, the ridges at the inner edge of the upper

specimen contribute to the localized edge contact. As the wear progresses, more and more area is engaged and can be seen through the evolution of the surface images. Such localization of the contact area is fully in line with what actually happens in shrouded blades ([170]), where a small portion of the theoretical contact area ends up being actually in contact.

The worn area is representatively similar on the upper and lower specimens. Figure 5.17 shows a better representation of close-up through real images of the upper and lower specimens at different wear intervals. It is calculated that the true area available after machining of the specimens is 7.8 mm^2, though the nominal area mentioned in the design was 10 mm^2. The marginal area is lost at the edges and during the manufacturing process. The figure also highlights the actual perimeter of the worn area for the worn images. The 3D images also show that the specimen surfaces are not completely flat. The upper specimen has two ridges along the longer edges, and these ridges would be the first ones to come in contact and wear out to proceed to establish a larger contact area. The reduction of the ridge is clearly visualized in the intermediate images.

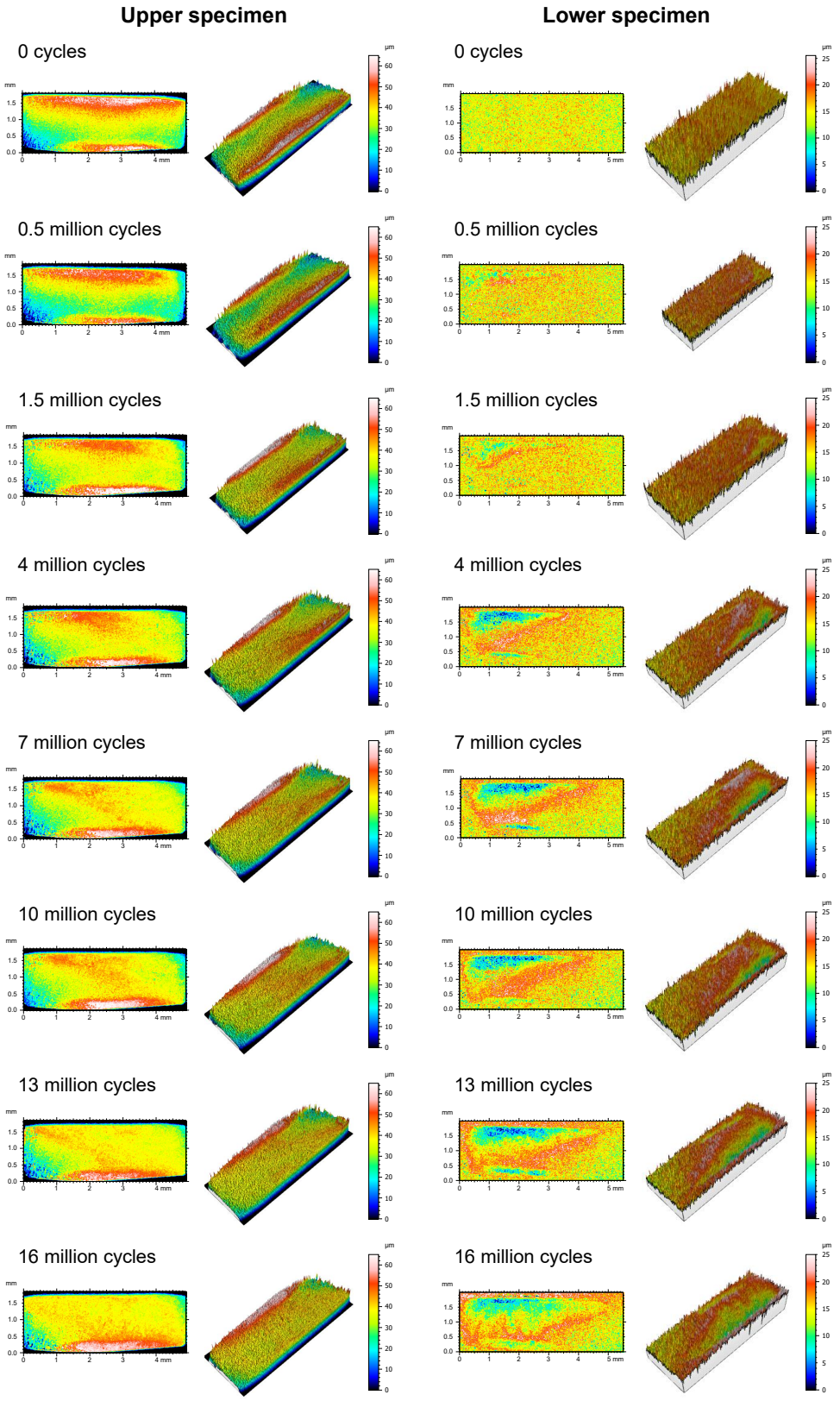

Fig. 5.16 Worn surface images of upper and lower specimens at various wear intervals. [Experimental]

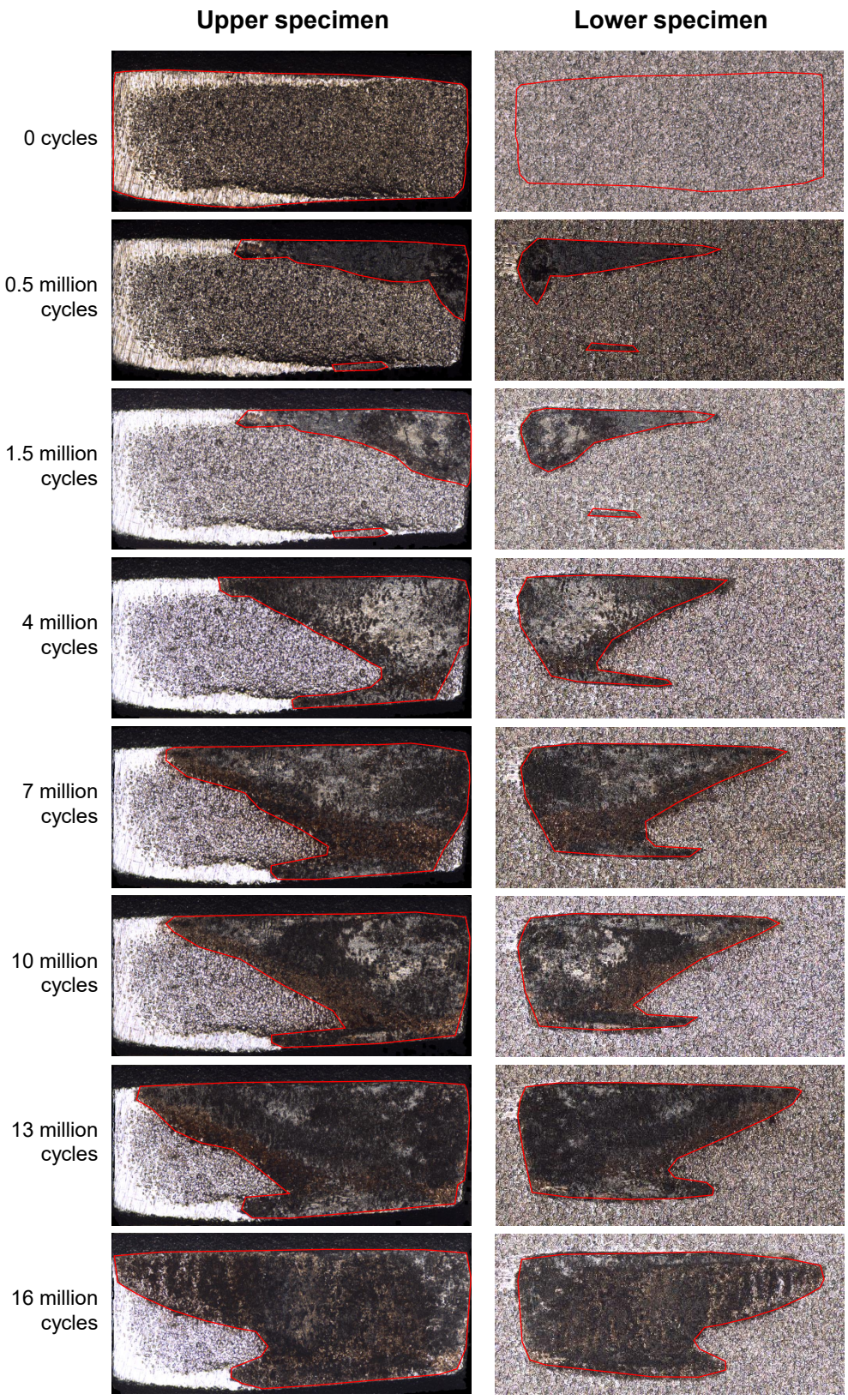

Fig. 5.17 Optical images of the evolution of surface areas of upper and lower specimens. [Experimental]

The worn area profile boundaries from the Figure 5.17 are extracted and plotted over the cumulative energy dissipated to give an idea about the evolution of established contact area in Figure 5.18. Final worn area after 16 million wear cycles and total loss of contact corresponds to only around 80% of nominal area. At the end of the test, though there was a complete loss of contact, we can see that the whole available area is not fully engaged. There are two primary reasons for the same. Firstly, the surface waviness is not even, and the exciting mode shape is not perfectly parallel to the tangential contact plane as discussed before. At 290 Hz, the bending behaviour of the beam is slightly inclined with respect to the nominal contact plane due to the geometry of the test rig and the dynamic behaviour at that mode. The second reason is the beam deflection is dependent on the starting contact preload. Since the starting contact preload is around 31 N, which is quite low, and the magnitude of deflection of the beam is comparable to the surface profile and the ridge height. The contact preload is chosen in such a way as to obtain the maximum energy dissipation to accelerate wear with a relatively low number of cycles. Hence, when the surfaces worn out the ridges, the contact preload was almost zero leading to loss of contact. The worn area profiles stand out because of its asymmetric wear, also attributing to the starting surface profiles and the mode shape of the system at that frequency. In case there was a large contact preload providing large deflection of the beam, though compromising with lower energy dissipation and a larger number of fretting cycles needed, the worn area would be fully established.

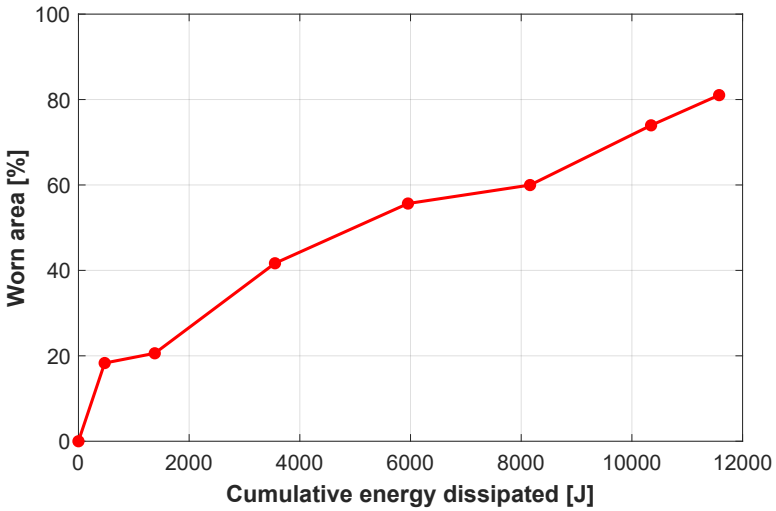

Fig. 5.18 Worn area with respect to the cumulative energy dissipated. [Experimental]

5.3.4.2 Evolution of hysteresis loops and contact preload.

Figure 5.19 shows the evolution of hysteresis loops with the progressing wear up to 16 million cycles. The contact undergoes stick and full slip at each cycle for the given loading conditions. The initial hysteresis loops during the running-in phase are ignored as the interest is in the steady-state behaviour that was achieved in the first few minutes of the test.

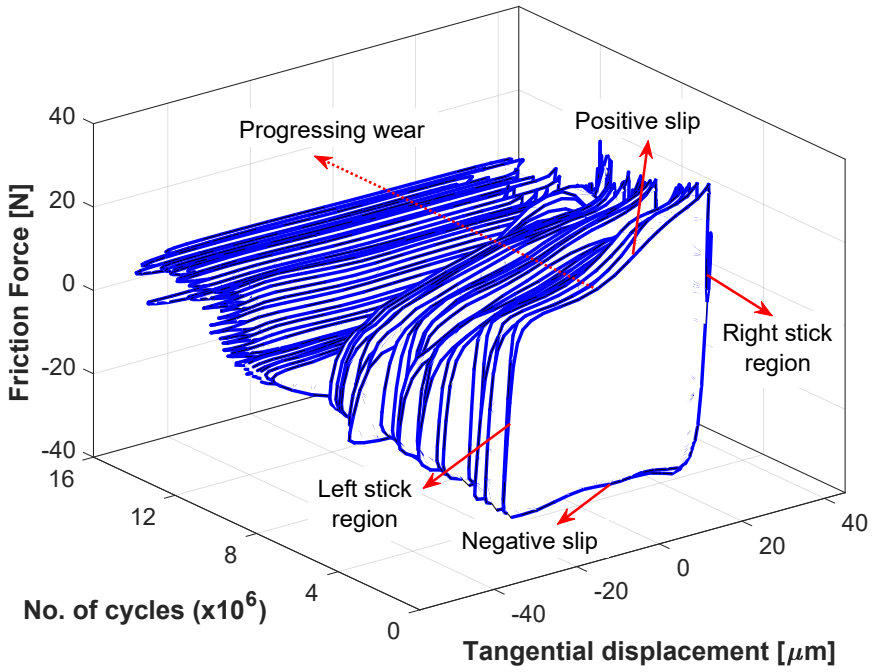

Fig. 5.19 Evolution of hysteresis loops with wear for 16 million cycles. [Experimental]

The plot reveals that, as the wear progresses, the height of the hysteresis loops reduces and the shape changes. The height of the hysteresis loops is governed by the upper $(+\mu N)$ and lower $(-\mu N)$ friction limit.

The friction coefficient is computed during the test, using the normal and tangential contact force time signals, using the procedure described in Section 5.3.3 about the single cycle. As a result, the value of the friction coefficient is obtained to be quite constant at 0.9 throughout the wear test. As a result, the reduction of the height of the hysteresis loops with wear is due to the losing contact preload. The shape of hysteresis loops (Figure 5.19) sticks out, especially in the later stages of wear. Apart from the overall reduced height of the hysteresis loops corresponding to

low contact preloads, the 'left stick region' is also missing with progressing wear, indicating a direct transition from negative slip to positive slip without sticking region. For various reasons, many of the wear tests performed in the literature are under a constant normal load, hence the variation in the height of the hysteresis loops is minimal in the steady-state region. Hence, the huge variation in the evolution of hysteresis loops is not commonly found in the literature for comparison.

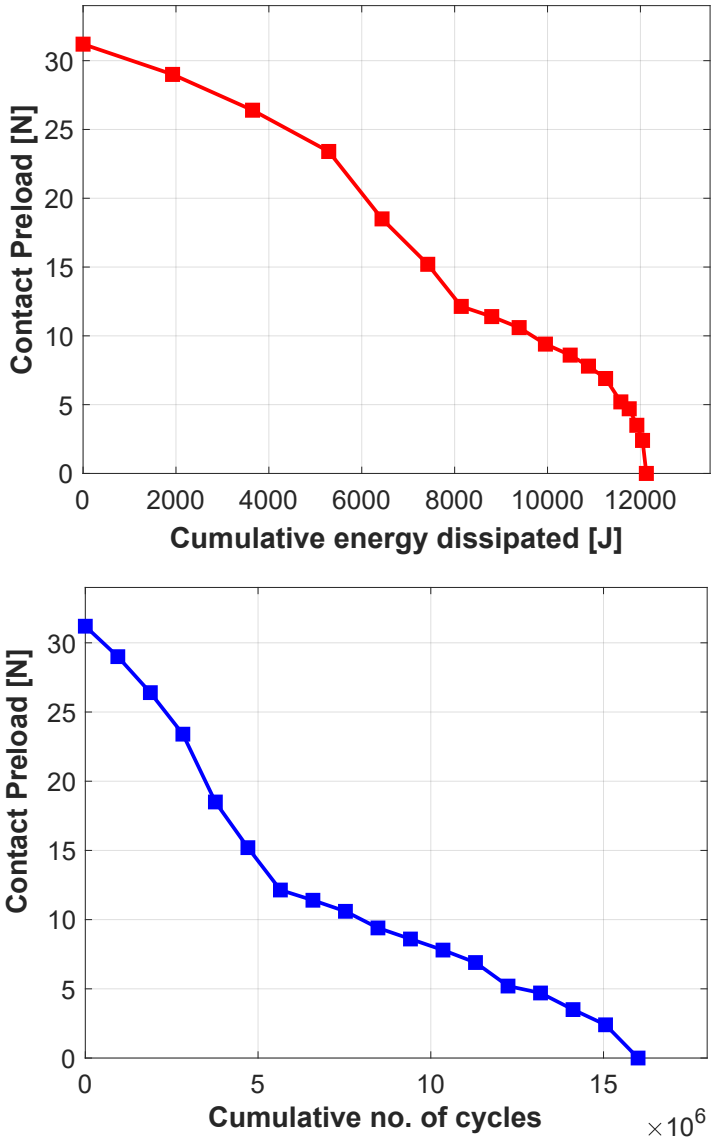

Fig. 5.20 Evolution of contact preload with wear until full loss of contact versus (a) energy dissipated (b) number of cycles. [Experimental]

Figure 5.20 shows the evolution of contact preload with wear. The figure is plotted against the cumulative energy dissipated and also for the cumulative number of cycles. One can see the difference in trend in evolution. The reason being the energy dissipation in each cycle reduces because of the smaller hysteresis loops due to wear with the increasing number of cycles. Ideally, if the hysteresis loops were all the same under constant load, the graphs plotted versus energy dissipated, or the number of cycles would have been the same. Hence, tracking the cumulative energy dissipated is a better choice of a parameter to track the impact of wear. The full range test is performed until the complete loss of contact. For the given specimens and loading conditions, it took roughly 16 million fretting cycles resulting in around 12000 Joules of dissipated energy. The shape of hysteresis loops (Figure 5.19) sticks out especially in the later stages of wear as the contact experiences slip-stick-separation behaviour at very low contact preloads.

The impact of the losing contact preload has a direct impact on the hysteresis loops in terms of dissipated energy in each cycle and the average tangential slip at each cycle. Figure 5.21 shows the evolution of average dissipated energy at each cycle with respect to the cumulative number of cycles. Basically, as the contact preload decreases, the dissipated energy at each cycle decreased due to the reduced height of hysteresis loops and the tangential slip increases due to the reduced normal load.

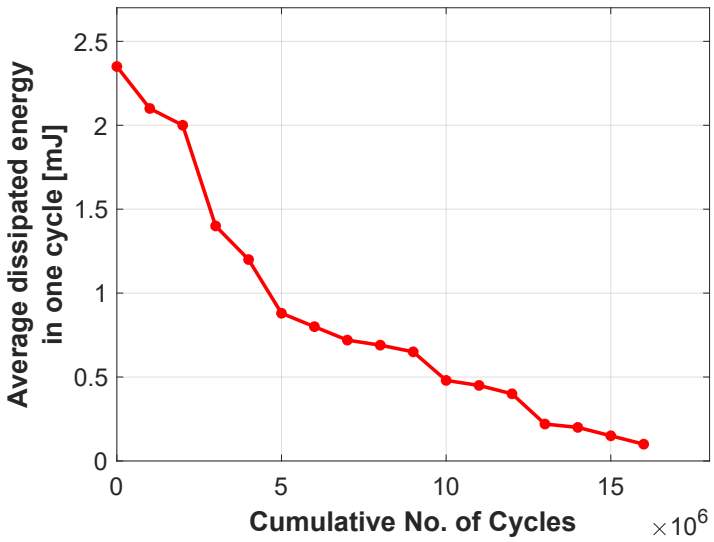

Fig. 5.21 Evolution of average dissipated energy in one cycles versus number of cycles. [Experimental]

5.3.4.3 Wear volume versus dissipated energy.

The wear volumes of the upper and lower specimens are calculated by superimposing the worn surface profile over the unworn surface profile. This method eliminates the computation error introduced due to non-flat initial surface waviness, if any. The procedure is repeated for all wear intervals and for the upper and lower specimens separately. MountainsMap software is used to perform the operations and compute the wear volume. The total wear volume is calculated by summing up the wear volume obtained at the upper and lower specimen. The unevenness of the worn area is due to the initial contact profile and waviness of the surfaces. This poses a certain difficulty in measuring the total wear volume at a low number of cycles. The confidence is greater with larger wear volumes as there is more loss of volume. Figure 5.22 shows the relationship between the total wear volume corresponding to the cumulative energy dissipated during the wear test. A linear relationship can be seen by the plotted data indicating the total wear volume is proportional to the cumulative energy dissipated. A linear regression (dotted blue-line) is performed to obtain an approximate relationship between the total wear volume and cumulative energy dissipated. This is in line with the energy form of the classical Archard wear model in which the product sliding distance times the normal load – that is, the work done on the system – has been substituted by the dissipated energy. The slope of the best fit line represents the wear energy coefficient (α). This is a particularly important parameter for the given material pair as it can be used in numerical prediction software for better wear prediction and the accurate number of wear cycles. Most of the numerical studies in the literature ([171, 149, 147, 152]) studying the effect of fretting wear on the forced response dynamics using the Harmonic Balance Method uses this parameter as an input. The wear energy approach [121, 123] using wear energy coefficient (α) is a convenient method in terms of the accuracy and ease of implementation in large nonlinear dynamic solvers as it is relatively straightforward compared to complex methods such as in ([112, 116–120]) requiring many variables as inputs.

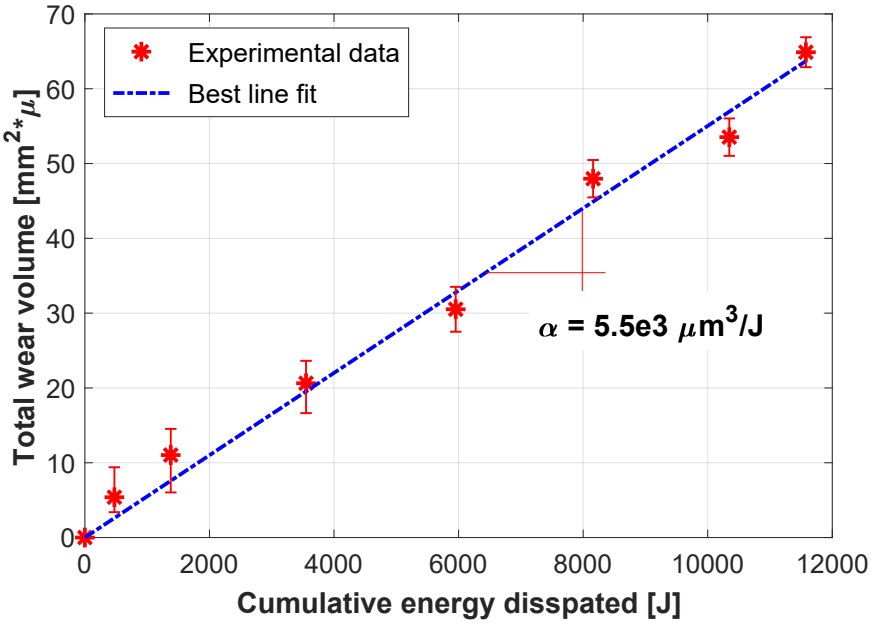

Fig. 5.22 Total wear volume vs. cumulative energy dissipated. [Experimental]

5.3.4.4 Impact of wear on the FRFs.

As the contact loses material due to progressing wear, as seen in the contact evolution images in Figure 5.16 and Figure 5.17, the beam static deflection reduces, while the height of the moving platform is kept fixed throughout the full test. As a result, the static contact preload gets smaller as wear is accumulated. This reduction in static contact preload affects the FRFs of the system, measured at every 0.5 million cycles during the test.

In Figure 5.23, the FRF evolution at different excitation levels are plotted. In each plot, corresponding to a certain excitation level (70N, 50N, 25N and 10N), the FRF curves correspond to different levels of wear accumulated during the test. The nonlinear behaviour of the system is clearly visible in the plots.

At the beginning of the test, the peak around 400 Hz is sharper, being the system closer to the stuck case. As the wear progresses, the FRFs show a softening behaviour of the system, associated with larger relative displacements as the preload is progressively reduced. The increase of relative displacements affects both the stiffness and the damping provided by the contact. Towards the end of the test,

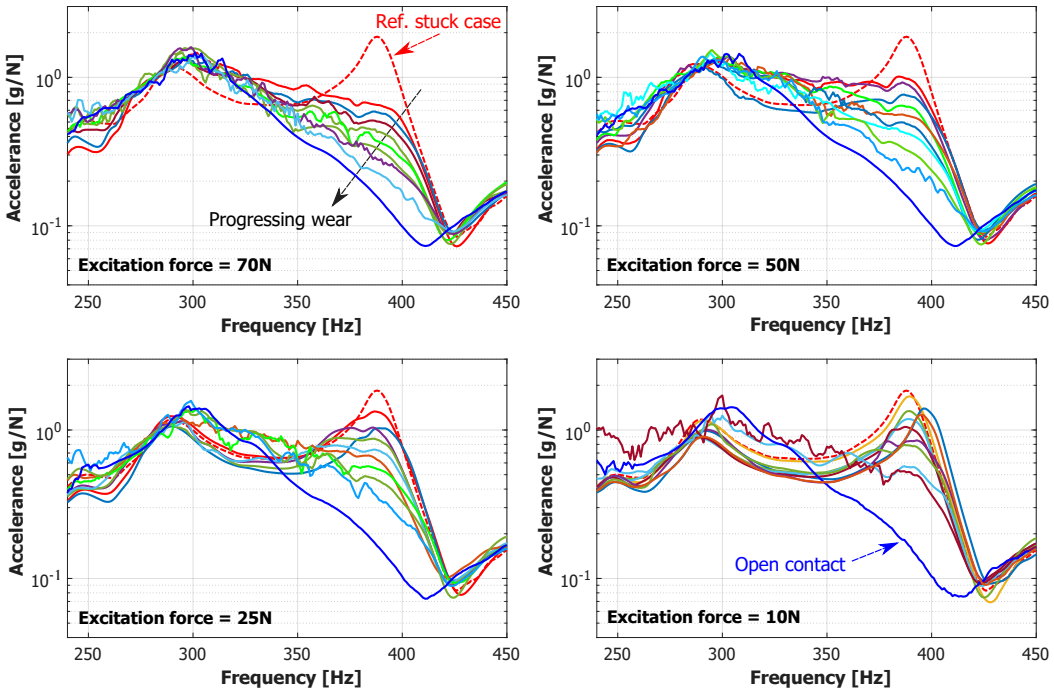

Fig. 5.23 Effect of wear on the FRFs subject to different excitation amplitudes for 16 million wear cycles. [Experimental]

corresponding to a full loss of contact and zero contact preload, the FRF matches the response of the system with open contact. This successfully captures the impact of wear and the evolution of contact surface from the pristine surface and non-zero contact load to worn surfaces with complete separation.

To the authors' knowledge, this is the first study, where: i) a step-by-step experimental analysis of wear evolution and its effect on structural dynamics is performed; ii) the focus is on the effect of wear evolution on the magnitude of contact preload. Such a study was possible due to the purposely designed test rig and to the experimental procedure followed during the tests. Thanks to this approach, the incremental effect of wear on the hysteresis loops, contact surface evolution and system dynamics were tracked until loss of contact.

From the above results, it can be clearly seen that though the amount of wear at the contact is only in the order of a few micrometres, there can be substantial effect in terms of energy dissipation, contact preloads, real contact area engaged, etc. Over a few million cycles, these cumulative effects can be amplified and affect the dynamic response significantly. This strengthens the point that considering

realistic contact interface conditions and their evolution is important in designing high-performance components and predicting the actual lifetime of the components. Robust and efficient nonlinear solvers are needed to predict the effects numerically and conduct parametric studies for optimized turbomachinery components. Taking into account the changes in the contact preload, loss of material, shift in vibration amplitudes and change in the resonance frequencies are crucial in designing the high-performance turbomachinery components for safety and efficiency. Having a robust prediction tool will help for better design for operational performance at the design stage itself and better components in a short turnaround time. The results presented here are the initial set obtained from the test rig, however, a wide range of studies can be performed using this test rig. For example, a parametric study of contact pair material, contact preload, excitation forces, contact geometry, contact area, etc., can be performed and isolated individually to better understand the impact of wear on dynamics in each case. In turn, these experimental results can be used to update the numerical models and iterate to develop a robust prediction tool. This would result in a positive iterative loop strengthening the robustness of the prediction tool.

5.4 Numerical prediction using nonlinear solver.

So far, the full set of experimental results have been presented, and various aspects of the impact of wear on the dynamics and its evolution have been discussed in detail. Now, to complete a full circle and fulfil the main objective of the PhD - numerical prediction, an equivalent FE model of the whole test rig is generated using a 3D CAD model. The idea is to simulate equivalent test conditions and boundary conditions and try to predict the evolution of contact interfaces with fretting wear and the resulting change in the dynamic response of the test rig.

Following the numerical prediction procedure similar to the numerical test cases chapter, to reduce the size of the system for the dynamic analysis, a CB-CMS ROM is obtained. To that end, the upper and lower specimen contact interface nodes have been identified as master nodes along with the static and dynamic excitation nodes and response nodes. The contact interface is discretized by a rectangular mesh with 55 nodes (11 rows and 5 columns). The choice of the discretization is made by keeping in mind the computational effort needed and the number of wear iterations to be run, and also fine enough to capture the contact evolution and coarse enough to perform a nonlinear simulation in a reasonable time. The retained number of nonlinear contact DOFs is one of the major drivers of memory requirements and the computational time needed.

5.4.1 Reformulation of HBM.

Now, there is just one shortfall in the classical coupled HBM for successful application to the current test rig. In the procedure outlined in the methodology chapter, the static and dynamic terms are coupled, where the system of equations is solved for the displacement vector of unknowns. The external forces (static and dynamic) are known beforehand and plugged into the code as input parameters. However, the focus of the test rig is to obtain the evolution of 'changing static preload'. The static force which changes during the wear test cannot be captured as it is an input. This calls for rearranging the vector of unknowns.

In this particular case, the way the contact preload is applied is by rotating the screw-lift contact loading mechanism. The rotation of the loading nut results in translation of the platform containing the lower specimen assembly, hence engaging

the contact and deflecting the beam. The amount of translation of the moving platform governs the level of static preload. Throughout the wear test, the platform height is kept constant. But due to wear causing loss of material at the interface, the beam tries to deflect back to its original position, thereby losing preload. Hence, the HBM has to be reformulated to include the known displacement at the static component of certain DOFs and have the static component of the force of certain DOFs as unknown. This can be achieved by rearranging the vector of unknowns.

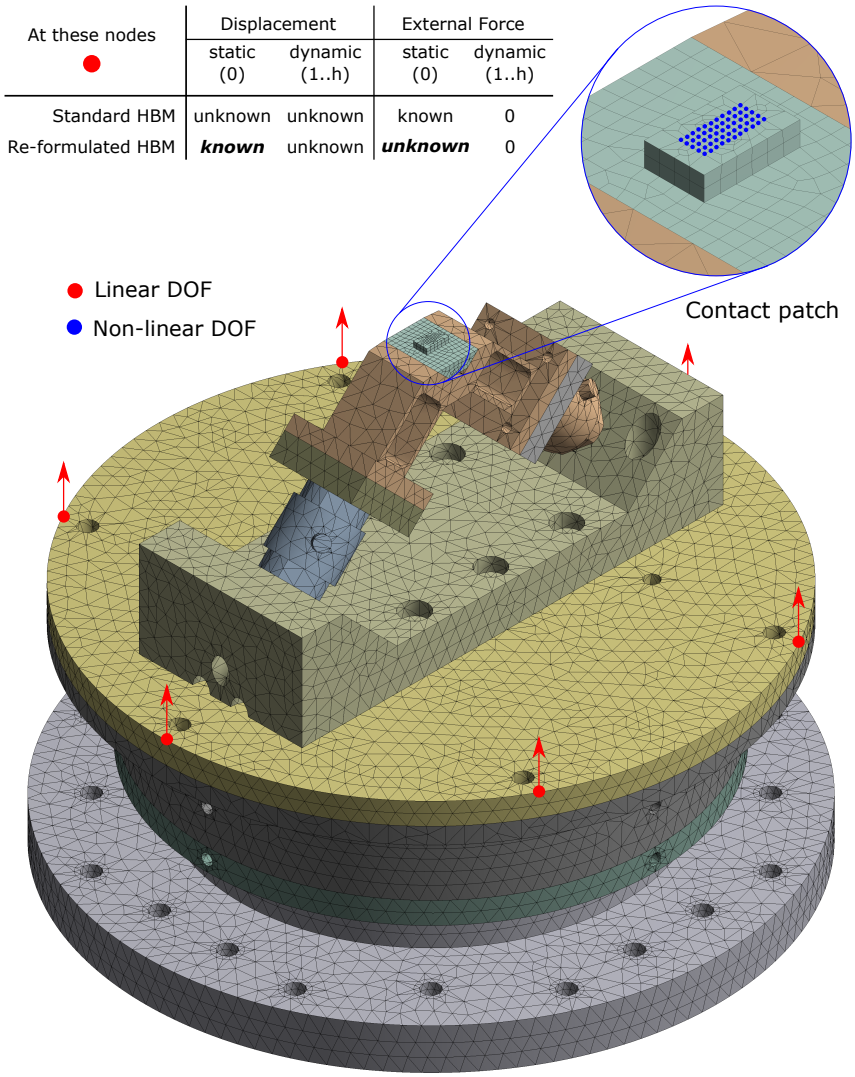

Fig. 5.24 Loading mechanism highlighting the linear DOFs at the moving platform and nonlinear DOFs at the contact patch. (The rest of the test rig which is not shown remains unchanged).

The displacement vector corresponding to the full model is partitioned as follows:

$$X = \begin{bmatrix} {X_k}^T & {X_u}^T \end{bmatrix}^T \tag{5.2}$$

Where the subscript k represents known and u for unknown with respect to the DOFs (marked in red) on the moving platform as referred to in the Figure 5.24. The rest of the master nodes including the upper and lower specimen contact nodes, excitation and accessory nodes fall under subscript u. ($N(X_k) \ll N(X_u)$). For brevity, the figure shows only the contact loading mechanism. The rest of the test rig - column and beam assembly with upper specimen, which is not shown remains unchanged. To note, only the static component (0^{th} harmonic) of the displacement is known as recorded from the height of the platform. The corresponding DOFs static component of the external force is set as unknown. Also, these DOFs correspond only to the linear DOFs of the system, hence the component of nonlinear forces (F_{nl}) is zero.

The original balance equations of the full model for coupled single harmonic with only highlighted partitioned subscripts (known displacement DOFs are marked in red and the corresponding unknown force is marked in blue) are given as:

$$\begin{bmatrix} D^0_{kk} & D^0_{ku} & 0 & 0 \\ D^0_{uk} & D^0_{uu} & 0 & 0 \\ 0 & 0 & D^1_{kk} & D^1_{ku} \\ 0 & 0 & D^1_{uk} & D^1_{uu} \end{bmatrix} \begin{Bmatrix} X^{(0)}_k \\ X^{(0)}_u \\ X^{(1)}_k \\ X^{(1)}_u \end{Bmatrix} = \begin{Bmatrix} F^{(0)}_{e,u} \\ F^{(0)}_{e,k} \\ F^{(1)}_{e,u} \\ F^{(1)}_{e,u} \end{Bmatrix} + \begin{Bmatrix} 0 \\ F^{(0)}_{nl} \\ 0 \\ F^{(1)}_{nl} \end{Bmatrix} \tag{5.3}$$

Only the static part of the system of equations are modified, and the dynamic part of the equations remain the same as in the standard formulation. Re-arranging the equations as below:

$$\begin{aligned} D^0_{kk}X^{(0)}_k + D^0_{ku}X^{(0)}_u &= F^{(0)}_{e,u} && \rightarrow (a) \\ D^0_{uk}X^{(0)}_k + D^0_{uu}X^{(0)}_u &= F^{(0)}_{e,k} + F^{(0)}_{nl} && \rightarrow (b) \\ D^1_{kk}X^{(1)}_k + D^1_{ku}X^{(1)}_u &= F^{(1)}_{e,u} && \rightarrow (c) \\ D^1_{uk}X^{(1)}_k + D^1_{uu}X^{(1)}_u &= F^{(1)}_{e,k} + F^{(1)}_{nl} && \rightarrow (d) \end{aligned} \tag{5.4}$$

Rearrange equation 5.4(a) as:

$$X_k^{(0)} = {D_{kk}^0}^{-1}\left(F_{e,u}^{(0)} - D_{ku}^0 X_u^{(0)}\right) \tag{5.5}$$

Substitute equation 5.5 in equation 5.4(b) and re-write as:

$$D_{uk}^0 {D_{kk}^0}^{-1} F_{e,u}^{(0)} - D_{uk}^0 {D_{kk}^0}^{-1} D_{ku}^0 X_u^{(0)} + D_{uu}^0 X_u^{(0)} = F_{e,k}^{(0)} + F_{nl}^{(0)} \tag{5.6}$$

With the reformulated equations by substituting equation 5.5 and equation 5.6 in 5.3, the updated balance equation with new vector of unknowns to solve are:

$$\begin{bmatrix} I & -D_{ku}^0 & 0 & 0 \\ D_{uk}^0 {D_{kk}^0}^{-1} & (D_{uu}^0 - D_{uk}^0 {D_{kk}^0}^{-1} D_{ku}^0) & 0 & 0 \\ 0 & 0 & D_{kk}^1 & D_{ku}^1 \\ 0 & 0 & D_{uk}^1 & D_{uu}^1 \end{bmatrix} \begin{Bmatrix} F_{e,u}^{(0)} \\ X_u^{(0)} \\ X_k^{(1)} \\ X_u^{(1)} \end{Bmatrix} = \begin{Bmatrix} D_{kk}^0 X_k^{(0)} \\ F_{e,k}^{(0)} \\ F_{e,u}^{(1)} \\ F_{e,u}^{(1)} \end{Bmatrix} + \begin{Bmatrix} 0 \\ F_{nl}^{(0)} \\ 0 \\ F_{nl}^{(1)} \end{Bmatrix} \tag{5.7}$$

Extending the formulation to multi-harmonic up to h number of Harmonics as:

$$\begin{bmatrix} \begin{bmatrix} I & -D_{ku}^0 \\ D_{uk}^0 {D_{kk}^0}^{-1} & (D_{uu}^0 - D_{uk}^0 {D_{kk}^0}^{-1} D_{ku}^0) \end{bmatrix} & 0 \\ 0 & \left[D^{(1..h)}\right] \end{bmatrix} \begin{Bmatrix} \begin{bmatrix} F_{e,u}^{(0)} \\ X_u^{(0)} \end{bmatrix} \\ \left[X^{(1..h)}\right] \end{Bmatrix} = \begin{Bmatrix} \begin{bmatrix} D_{kk}^0 X_k^{(0)} \\ F_{e,k}^{(0)} \end{bmatrix} \\ \left[F_e^{(1..h)}\right] \end{Bmatrix} + \begin{Bmatrix} \begin{bmatrix} 0 \\ F_{nl}^{(0)} \end{bmatrix} \\ \left[F_{nl}^{(1..h)}\right] \end{Bmatrix} \tag{5.8}$$

Splitting the equation 5.8 into its real and imaginary components to solve using MATLAB as:

$$\begin{bmatrix} \Re\begin{bmatrix} I & -D^0_{ku} \\ D^0_{uk}{D^0_{kk}}^{-1} & (D^0_{uu} - D^0_{uk}{D^0_{kk}}^{-1}D^0_{ku}) \end{bmatrix} & 0 & 0 \\ 0 & \Re\left[D^{(1..h)}\right] & -\Im\left[D^{(1..h)}\right] \\ 0 & \Im\left[D^{(1..h)}\right] & \Re\left[D^{(1..h)}\right] \end{bmatrix} \begin{Bmatrix} \Re\begin{bmatrix} F^{(0)}_{e,u} \\ X^{(0)}_u \end{bmatrix} \\ \Im\left[X^{(1..h)}\right] \\ \Re\left[X^{(1..h)}\right] \end{Bmatrix} = \begin{Bmatrix} \Re\begin{bmatrix} D^0_{kk}X^{(0)}_k \\ F^{(0)}_{e,k} \end{bmatrix} \\ \Re\left[F^{(1..h)}_e\right] \\ \Im\left[F^{(1..h)}_e\right] \end{Bmatrix} + \begin{Bmatrix} \Re\begin{bmatrix} 0 \\ F^{(0)}_{nl} \end{bmatrix} \\ \Re\left[F^{(1..h)}_{nl}\right] \\ \Im\left[F^{(1..h)}_{nl}\right] \end{Bmatrix} \tag{5.9}$$

The corresponding changes in the Jacobian matrix arising due to the reformulation has been implemented in the in-house nonlinear solver.

5.4.2 Real surface input.

The contact interfaces in the numerical simulation are usually assumed perfectly flat by default, unless explicitly the real surfaces are given as an input. For accurate simulation of the real-world case and to compare with the experimental results, the initial real surface profiles are needed. Here, the real surface profiles obtained before the start of experiments can be used. The pristine surface data recorded for the upper and lower specimen were cleaned, and then the surface was split into two components - roughness and waviness. Since the contact discretization is only with 55 elements for dynamic analysis, ignoring roughness and considering only waviness data is more than sufficient. The nodal data, which is very fine, is imported into MATLAB and down-sampled by considering elemental area contribution. The data is then distributed and the equivalent coarse grid over the contact area is obtained for both the upper and lower specimen as shown in the Figure 5.25. The counter surfaces are then overlapped and the difference in the waviness is computed. This

data is used in the nonlinear solver and injected into the normal component of the 0^{th} order Fourier coefficient of the contact DOFs.

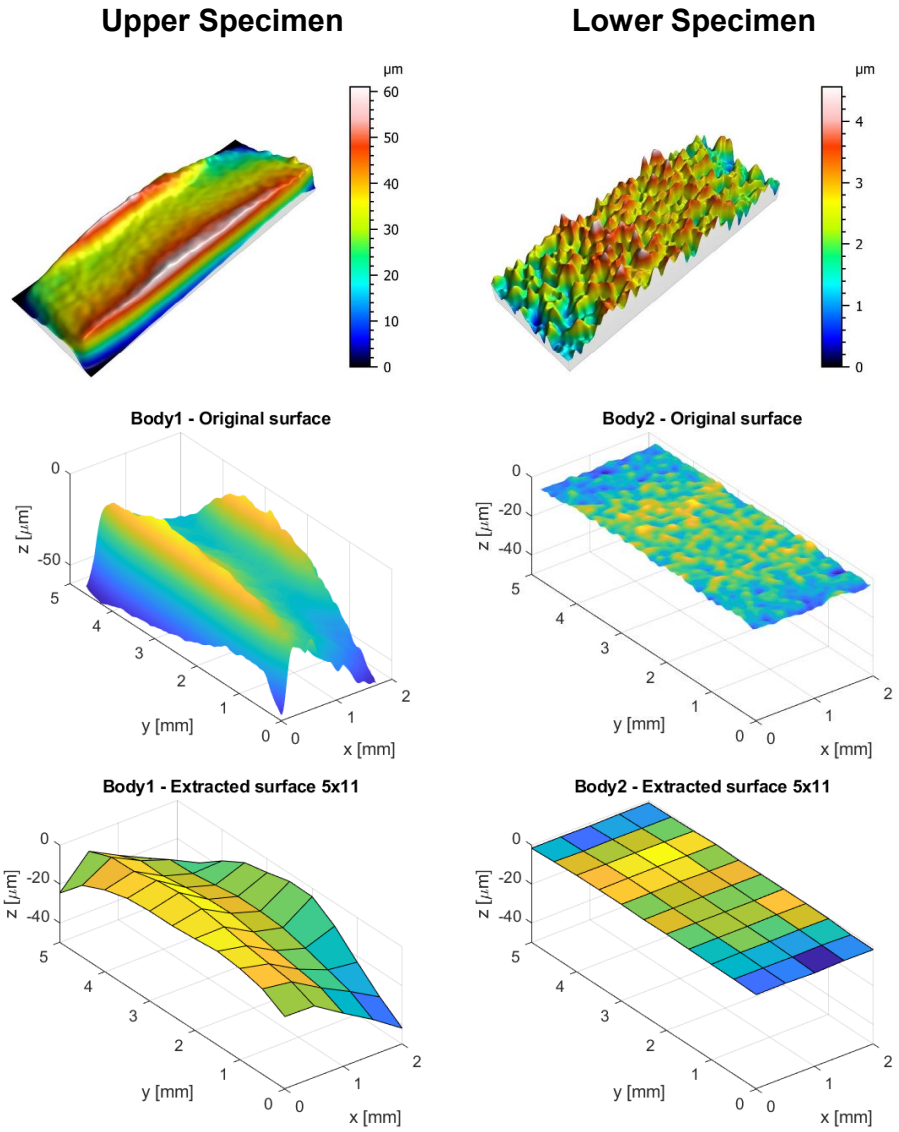

Fig. 5.25 Real surface waviness after discarding roughness and the down-sampled version to match the contact area discretization of upper and lower specimens. [Experimental]

5.5 HBM simulation and comparison with experimental results.

Reformulated HBM with real surface input is used to compute the effect of fretting wear on the dynamics and perform experimental validation. The waviness of the contacting specimen surfaces and the first contact point plays a major role in determining the accurate initial contact preload. The contact preload and the evolution of the test rig dynamics with wear are highly sensitive to the starting profile and initial interference.

The below sources of error through real surface input is possibly introduced and affect the numerical simulation:

- Ignoring the roughness and considering only the waviness of the specimen profiles due to coarse mesh for the dynamics.
- Downsampling error from high-resolution waviness data to a coarse 55 nodal elements data.
- Inherent measurement error of the original specimen surface profiles through the profilometer.

A small variation in the first point of contact of the two mating surfaces, though only a few microns, can greatly affect the corresponding initial static preload, especially for low starting preloads. Hence, to combat the above sources of error, three numerical simulations were performed by varying the initial contact point. These three simulations should help understand the sensitivity of the mating height through resulting hysteresis loops, energy dissipation and the resulting number of cycles for full loss of contact.

The small variation introduced in the simulations is 3 microns apart in the contacting height, the rest else being the same.

- Simulation 1: Actual point of contact of down-sampled specimens surface waviness as obtained through the profilometer data and roughness filter.
- Simulation 2: Simulation 1 + 3 micron (higher interference).
- Simulation 3: Simulation 1 - 3 micron (lower interference).

The final size of the system to perform dynamic analysis after performing CB-CMS and retaining 30 normal modes resulted in 444 DOFs. 70 N excitation force was considered, and the energy dissipation at 290 Hz frequency was chosen for wear computation, similar to the experimental test conditions. The friction coefficient is set to 0.9, which was observed during the experiments. The wear energy coefficient (α) was used as $5.5e3\mu m^3/J$ as obtained from the experiments. The static load was left unknown as briefed before in the reformulation section. The contact preload was obtained by interference fit, considering the starting real surface waviness of the upper and lower specimens. The frequency range was chosen between 240 Hz and 420 Hz as the range of interest. 3 harmonics including the 0^{th} order harmonic was considered for the coupled analysis.

In total, for the full loss of contact, it took 89 wear iterations resulting in roughly around 17 million wear cycles for three simulations. The computational time needed for each simulation was around 15 hours on an Intel Xeon 4 core stand-alone workstation with 32 GB RAM. During the simulation, the variables such as engaged contact area, hysteresis loops (hence, energy dissipation), individual contact status, contact preload and forced dynamic response were saved for post-processing.

5.5.1 Contact area evolution.

Using the real surface waviness data as input in the in-house HBM solver, the nonlinear dynamic simulation with wear was performed. Figure 5.26 shows the evolution of the contact interface obtained from the numerical simulation. The shown contact images correspond to the number of wear cycles from the experimental results. The experimental worn surface images of the upper specimen are shown next to each other for one-on-one comparison. The numerical simulation is a very close match to the experimentally observed ones in terms of the real engaged area and also the position of wear initiation and propagation. This is due to using the real surface topology in the numerical simulations. Thanks to the coupled HBM methodology, which takes care of the static and dynamic part inherently. Throughout the simulation, there is a good correlation between the experiments and numerical results. Only one set of numerical contact area evolution is shown (Simulation 1), as the other two simulations are qualitatively very similar.

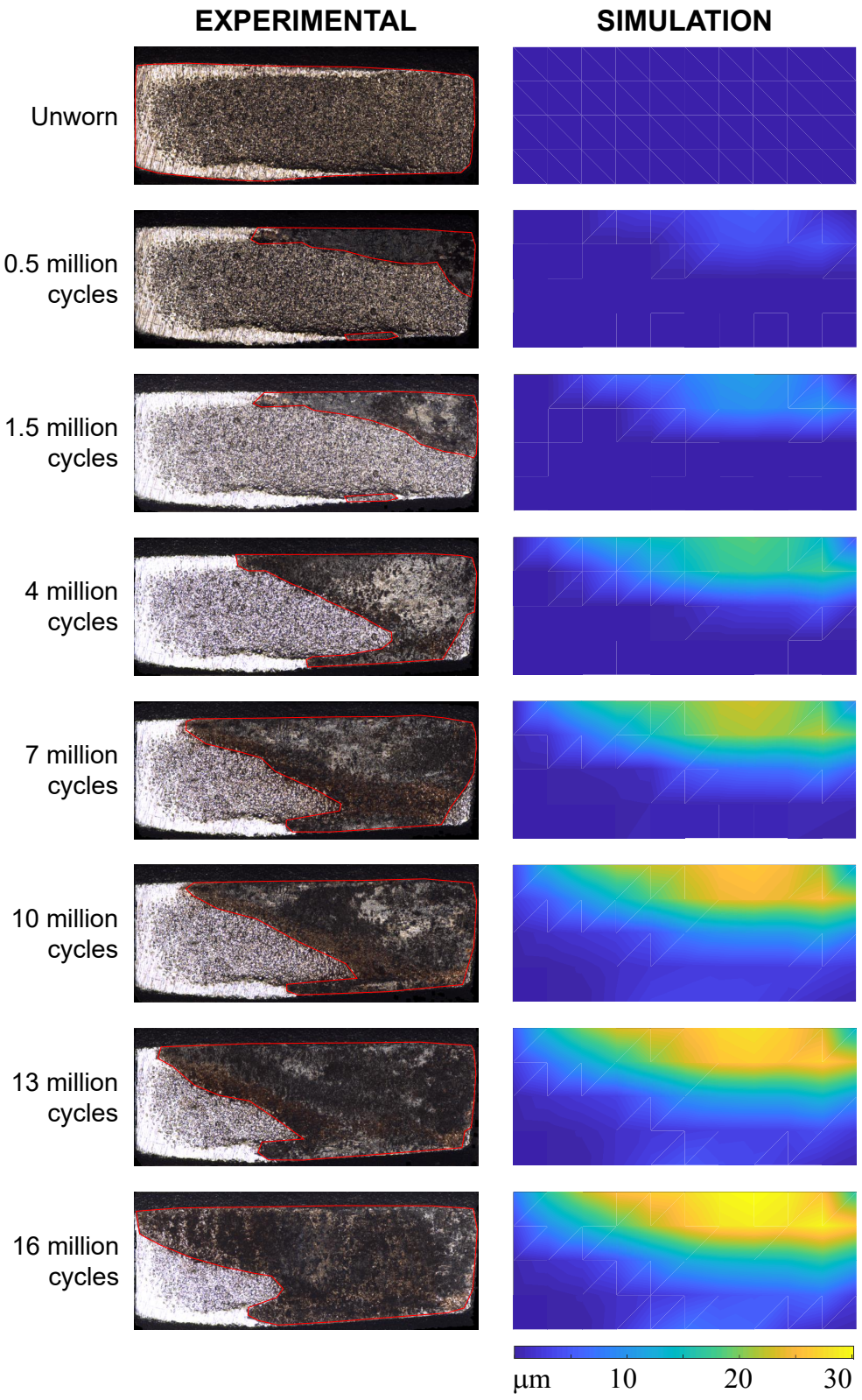

Fig. 5.26 Evolution of contact area on upper specimen with respect to cumulative number of cycles. [Experimental (left), Numerical (right)]

Figure 5.27 shows a 3D profile of total wear obtained through numerical simulation until the full of contact. One can clearly see that the bottom right corner in the figure is untouched, exactly as seen in the final worn experimental wear scan, hence leading to a worn area of around 80%. The cumulative worn profiles are qualitatively similar for all three simulations.

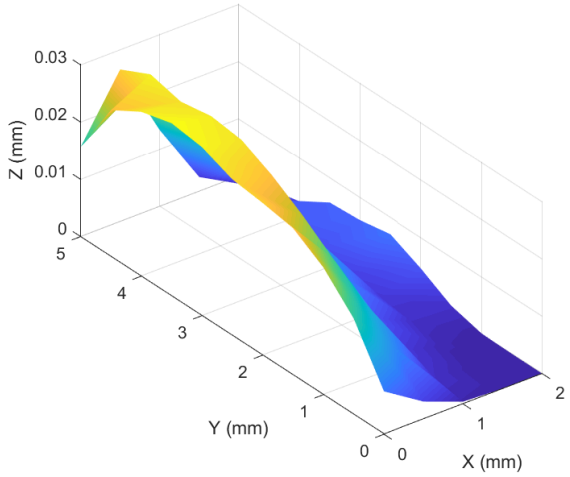

Fig. 5.27 3D profile of total wear obtained through numerical simulation until full of contact. [Numerical]

Figure 5.28 tracks the evolution of worn contact area quantitatively. The results from the three numerical simulations are overlapped against the experimental intermediate surface scans. It can be observed that the three simulations almost overlap each other in the beginning. However, towards the end, the total number of cycles achieved before the full loss of contact in the third simulation is evidently less than the experimentally obtained number of cycles. The second simulation out of the three simulations seems like a very good match to the experiments. As mentioned before, the starting point of contact of two mating surfaces is very crucial and sensitive in terms of the worn area before the full loss of contact. Another observation regarding the deviation between experiments and simulation at the starting number of cycles is because of coarse discretization of the grid in the dynamic analysis. The small variations in waviness cannot be properly captured at tiny ridges smaller than the basic elemental area in the discretization.

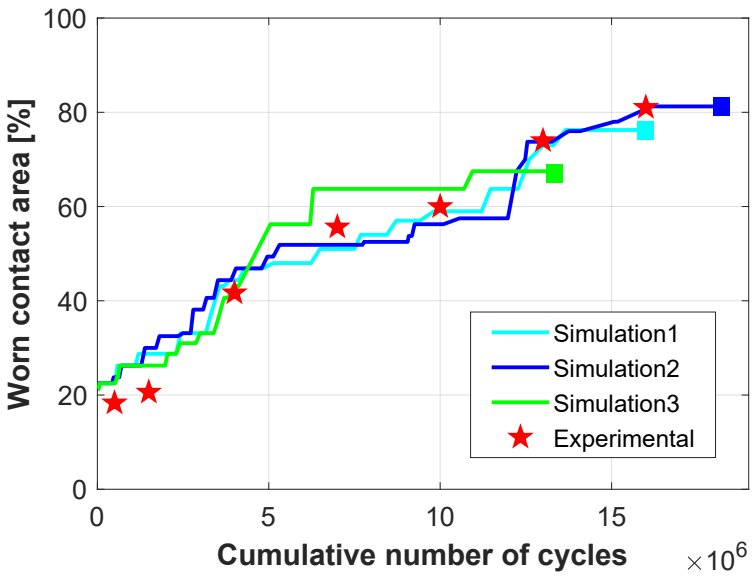

Fig. 5.28 Evolution of worn contact area - comparison of numerical simulations with experimental results.

5.5.2 Evolution of hysteresis loops and contact preload.

Figure 5.28 shows the evolution of hysteresis loops with wear until full loss of contact for both numerical simulation and experimental evolution for comparison. The contact interface undergoes stick and full slip at each vibration cycle for the given loading conditions. The initial hysteresis loops during the starting phase are ignored as the interest is to look at steady-state evolution. The steady-state was achieved in the initial few hundred cycles of the start of the wear test. Refer section 5.3.4.2 for detailed comments on the experimental evolution of hysteresis loops.

As the fretting wear progresses, the contact loses the static preload due to the interfacial loss of material. Here, the third body effect is not considered, and the worn material is assumed to be ejected out of the contact zone, similar to what was observed in the experiments. As evident, the hysteresis loops get smaller in height, corresponding to lower preloads. The height of the hysteresis loops is governed by the friction limit. When the friction coefficient is constant, the only other variable is the normal load. Towards the end of the wear, the contact is fully disengaged, leading to complete loss of contact, making the beam a free-standing cantilever beam. Qualitatively the numerical hysteresis loops can be compared to the experimental

hysteresis loops. The difference in shape is also due to truncated harmonics. In the experiments, it is observed that a 4^{th} harmonic of the excitation frequency is in play. The other reason is the asymmetry in the contact, as seen in the experimental system identification. Fine-tuning the mechanical joints in the numerical case can replicate the similar behaviour, but it is extremely hard to replicate the exact experimental nuances. However, the numerical model is sufficient for an initial comparison and prove the methodology. The three numerical simulations of the evolution of hysteresis loops are visually very similar to the one shown here.

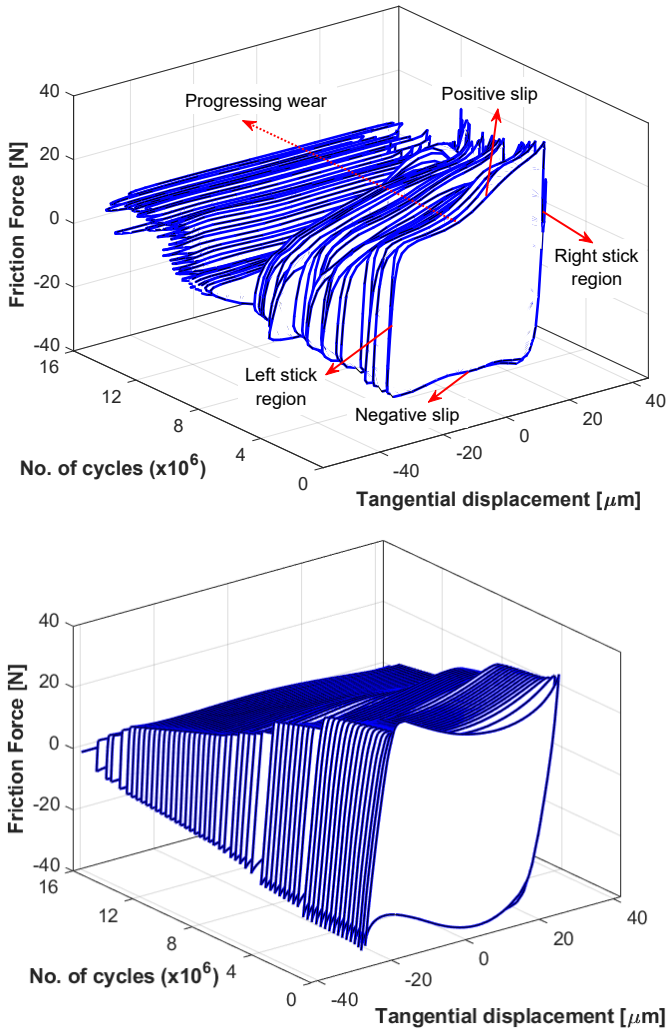

Fig. 5.28 Evolution of hysteresis loops with wear until full loss of contact (a) Experimental (top) (b) Numerical simulation (Simulation 1) (bottom).

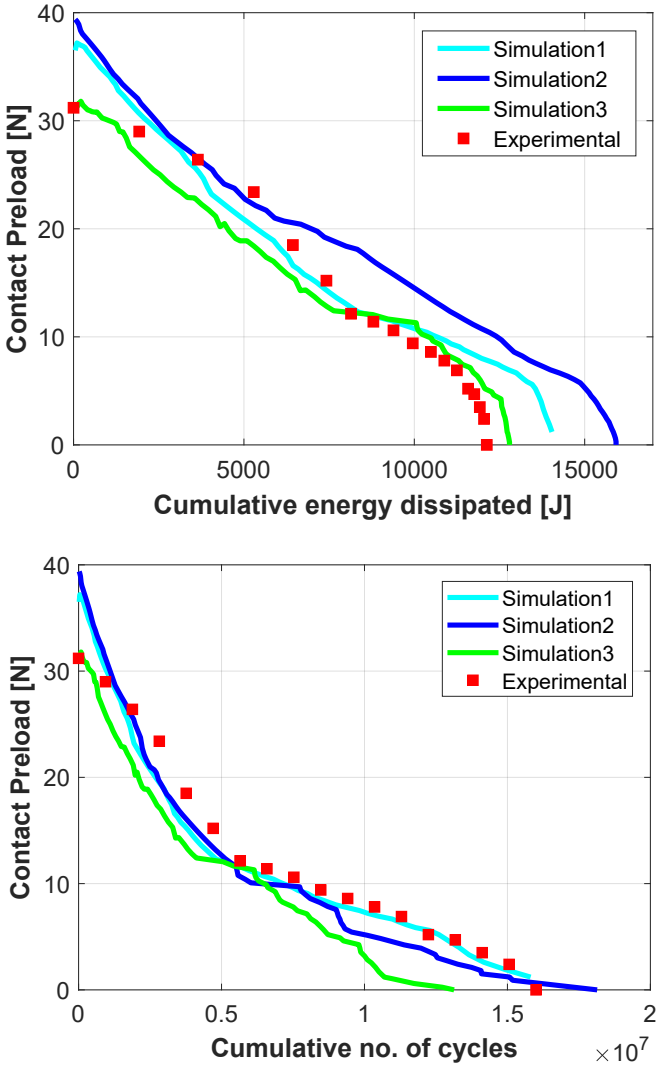

Fig. 5.29 Evolution of contact preload with wear versus (a) cumulative energy dissipated (b) cumulative number of cycles. – experimental and numerical simulation comparison.

Figure 5.29 shows the experimental and numerical simulation comparison of the evolution of contact preload with wear. The figures compare against cumulative energy dissipated and also against the cumulative number of cycles. The contact preload constantly reduced as the wear progressed. The simulations were performed until full loss of contact resulting in zero preload. It is a good idea to compare the preload against the cumulative energy dissipated and the cumulative number of cycles, because, if the height of the hysteresis loops were to remain the same, meaning constant normal load, then both the graphs would have looked identical.

Since the decreasing height of hysteresis loops has an effect on evolution it is necessary to compare with the right parameters. Also, the three simulations provided similar-looking trends, of course, the total energy dissipation and the total number of cycles are quite different. This is possible because, looking closely at the initial contact preload has a greater influence on driving the effect of wear. The accuracy of contact surface waviness is sensitive and here it shows its pronounced effect. Another observation is, by the first 5 million cycles, the contact lost preload at a significant pace and remained quite stable thereon, needing another 10 million cycles to completely lose the contact.

Figure 5.30 shows the tracking of average dissipated energy in each cycle over the cumulative number of cycles. The trend is similar to the contact preload variation figure as the dissipated energy is basically the area under the hysteresis loop. The three numerical simulations also qualitatively follow a similar trend.

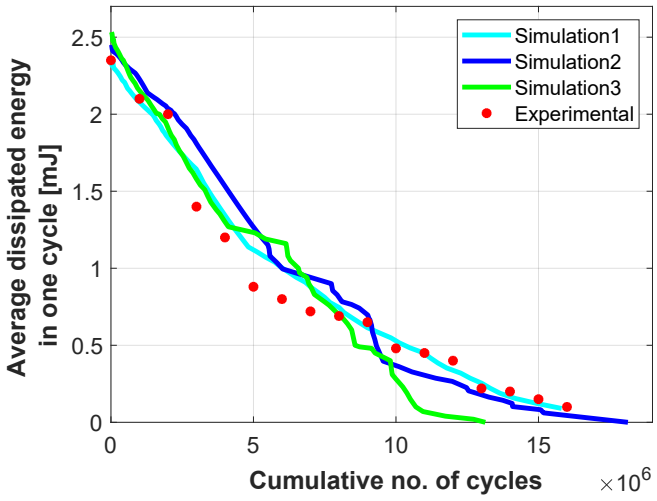

Fig. 5.30 Evolution of average dissipated energy in one cycle versus cumulative number of cycles - experimental and numerical simulation comparison.

These trends uncover many interesting facts on the effect of wear which has not been observed experimentally explicitly so far. This type of experimental evidence is necessary to design better structures with mechanical joints and taking the effect of relative sliding at the joints into consideration. This information also helps one to evaluate and predict the useful life and estimate the remaining life of the components with better confidence. Obtaining this type of data from the robust predictive solvers

can potentially save a lot of costs in terms of maintenance, aid efficient designs and faster design cycles.

5.5.3 Impact of wear on the FRFs.

As wear progresses, the change in contact conditions and losing contact preload must also reflect on the dynamic response of the test rig. Figure 5.31 shows the effect of wear on the forced response dynamics until full loss of contact obtained from numerical prediction and an experimental evolution for comparison. Refer section 5.3.4.4 for the comments on impact of wear on experimental FRFs.

At the beginning of the test, the response is closer to the stuck contact case. As the wear progresses, the contact loosens, and there is more energy dissipation. This leads to lower contact preloads and hence the response slowly moves towards the open contact case. Finally, when the contact is totally lost and the beam behaves as an open case and correspond to the open mode. The numerical prediction is qualitatively similar to the experimental observation. However, there is a small difference in the second resonance frequency of stuck case. This is due to not so accurate model tuning. FE model tuning to match realistic conditions and matching resonance frequencies is very tricky due to various boundary conditions in play. In reality, the mechanical joints introduce flexibility, which is dependent on the external excitation. However, FE modelling assumes a perfect contact. The boundary conditions between the column and the table, beam and the column were relaxed a little to mimic realistic conditions. The open modes and first stuck mode match well with experimental observation. However, the second mode is slightly off in the numerical model. The aim of the current work is to prove the numerical prediction is possible using coupled HBM, and to show that the effect of wear considering friction contact nonlinearity and the nonlinear dynamic response can be successfully computed. This is one of the first studies to study both the experimental evolution of fretting wear on the nonlinear dynamics and then numerically predict the evolution of wear with dynamics and contact interface with changing preload.

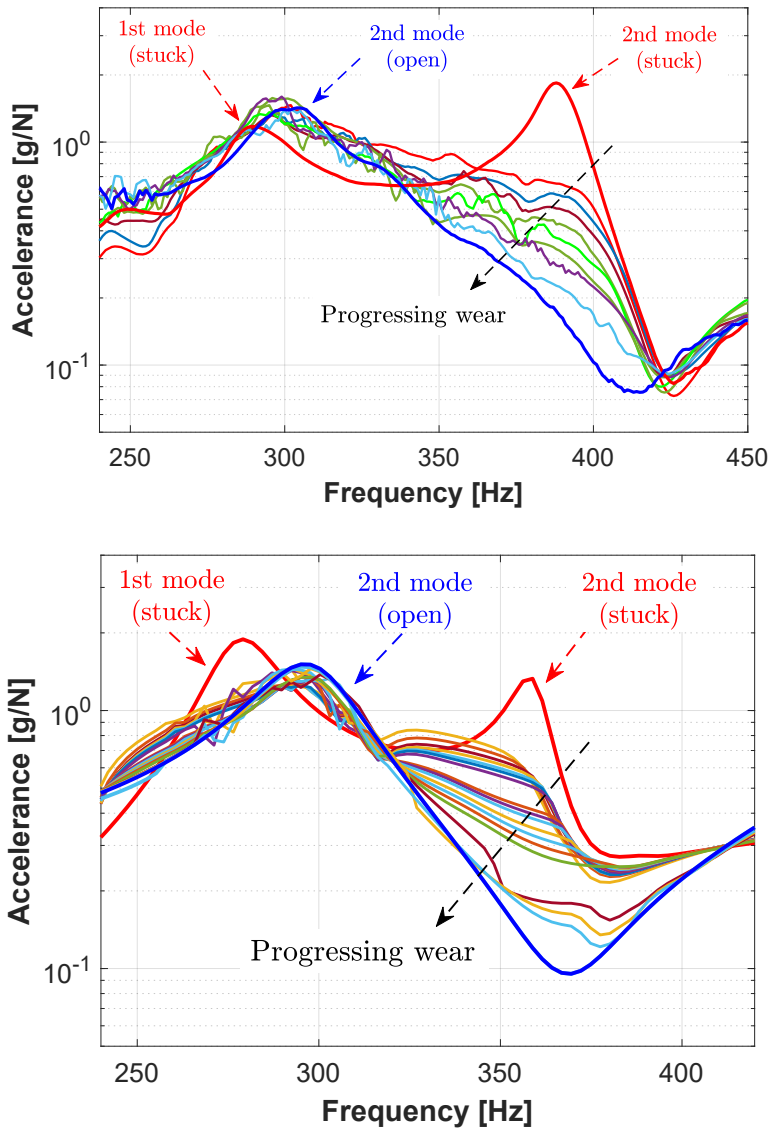

Fig. 5.31 Effect of wear on the forced response dynamics until full of contact (a) Experimental (b) Numerical simulation.

The major outcomes from the study are:

- A first of its kind experimental test rig to study the effect of fretting wear on the dynamic response with changing preload.
- Possibility of experimental investigation for full range test until full loss of contact and recording intermediate surface scans and dynamic response of the test rig.

- The fretting wear affects the dynamic response of the system by changing vibration amplitudes, frequency and damping.
- The wear also affects the contact conditions by changing the effective engaged contact area, contact preload, relative displacement for different forcing conditions.
- A successfully reformulated HBM numerical tool to study the effect of wear on the dynamics with changing preload.
- A successful validation of numerical results with experimental results for wear and dynamics combined.

It is crucial to include the time effects of fretting wear and the contact behaviour in the design of components for dynamic performance and reliability. This research acts as an experimental observation and validation for the numerical prediction tools which are used in the turbomachinery field. This novel test rig is of particular importance to validate the wear on dynamics similar to bladed disk tip shrouds, which experience a changing preload condition. It is quite different from the under-platform dampers, which is studied extensively in the last years. The centrifugal forces help to maintain the contact preload in the under-platform dampers even if wear is observed on the surfaces, which is not the case in the shroud contacts and the contact preload and contact status influence the blade dynamics to a large extent.

5.6 Summary.

This chapter provided a brief description of the novel test rig to experimentally study the effect of fretting wear on the long term forced response dynamics. The first section presented the test rig design, description of the components, instrumentation, calibration, system identification and long-term experimental results. The long-term full range experimental set of results was carried out until full loss of contact. It took roughly 16 million wear cycles to fully separate the contact. The dynamic response sweeps and the specimen surface scans were captured at various intervals throughout the test. The evolution of wear and the system dynamic response was discussed at length.

The second section of the chapter presented a numerical prediction of the equivalent experimental results for validation. A reformulation of the HBM was presented to accommodate the unknown static force DOFs to extract the changing contact preload, which would not be possible in classical HBM. The tool also considered the real surface waviness of the specimens as input to obtain realistic predictions. The numerical results presented include contact surface evolution with wear, hysteresis loops, change in contact preload, the evolution of wear volume and the change in frequency response curves. Later the numerical results were validated with experimental results, and interesting findings and future possibilities were presented.

Chapter 6

Industrial test case: Gas turbine combustor leaf seal

6.1 Introduction.

In this chapter, a gas turbine combustor leaf seal will be used as an industrial test case. Thanks to Expertise project partner organization - Baker Hughes (Nuovo Pignone s.r.l.), Florence, Italy, for providing the test case to study the complex nonlinear dynamic behaviour. The developed methodology with a coupled static/dynamic HBM will be implemented with a modified contact model. Some of the results are published in [172].

The leaf seals are one of the typical sealing systems in gas turbines and jet engines. In Baker Hughes LT family gas turbines, they are used to create sealing between the combustion chamber and the first stage nozzle. Two sets of inner and outer leaf seals provide sealing and prevent the leakage of the combustion mixture from the combustor section to the surroundings. The leaf seals have two curved contact patches, as shown in Figure 6.1 – between the nozzle and leaf seal, and the liner and the leaf seal. Given the location between the end of the combustor section and the high-pressure turbine section, they experience high dynamic forces and acoustic pulsation. These leaf seals work in a high-temperature environment. They are designed to withstand a range of operating and kinematic envelopes and provide the sealing. Due to the curved contact nature, the two contacts on the leaf seal experience partial contact either at the edges or at the centre, given the

positive or negative inclination of the leaf seal and the dynamic behaviour. The leaf seal is mounted to the nozzle via two pins and two spiral springs surrounding the pins to allow sufficient play during the operation. However, the leaf seal may look simplistic in geometry, but its complex dynamic behaviour is primarily governed by the contact conditions and dynamic excitation. From the field tests, it is found the leaf seal experience dominant wear at the contact zones. The wear is caused due to partial intermittent contact at the contact zones. The wear pattern is varied across multiple assemblies, sometimes concentrated at the centre or the edges of the contact patch, meaning the leaf seal experiences different intermittent contact behaviour for different operating conditions. Hence, it is of high importance to investigate the complex nonlinear dynamic behaviour of the leaf seal when subject to various operating and kinematic envelopes, which is almost impossible to capture through commercial solvers.

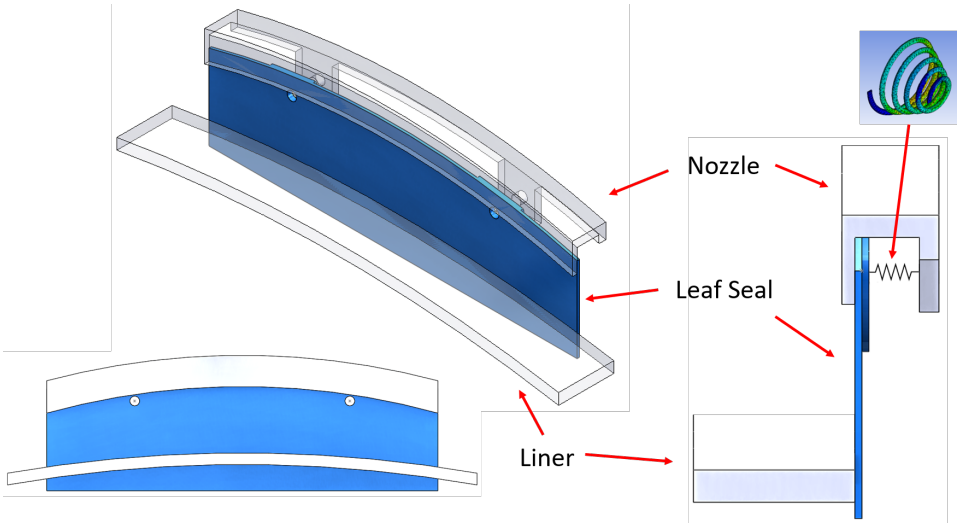

Fig. 6.1 Gas turbine combustor leaf seal.

6.2 Leaf seal description.

Figure 6.2 shows the schematic of the leaf seal system along with the boundary conditions. The leaf is held onto the nozzle via two pins and two encasing spiral springs. The front leg of the nozzle acts as a stopper for the leaf with the compression of the springs and makes contact between the leaf and the nozzle. On the bottom half of the leaf, there is a liner which mates the leaf seal and making it a lower contact

patch. Hence, there are two curved contact patches. The liner can either be stationary or have an independent harmonic displacement. For the dynamic analysis, modelling of the nozzle and the liner can be omitted as they act as a fixed ground at the nozzle and moving ground at the liner contact. The right-side figure shows the simplified schematic with the necessary boundary conditions to model the system for dynamic analysis. As per the field report, no tangential displacement within the leaf seal plane is observed. The wear along the contact patch is likely caused by chattering resulting from the dynamic excitation and complex behaviour of the leaf seal due to wide operating ranges. Hence, the contact is assumed by equivalent springs with normal contact stiffness and ignoring the tangential contact stiffness from the Jenkins element contact model within the in-house solver. Firstly, the complex dynamic response has to be understood before proceeding to the wear analysis and the next step could be to analyse the effect of wear around the pins, which is a cause of concern. The dynamic excitation is applied on one side and static pressure on the other side of the leaf, as shown.

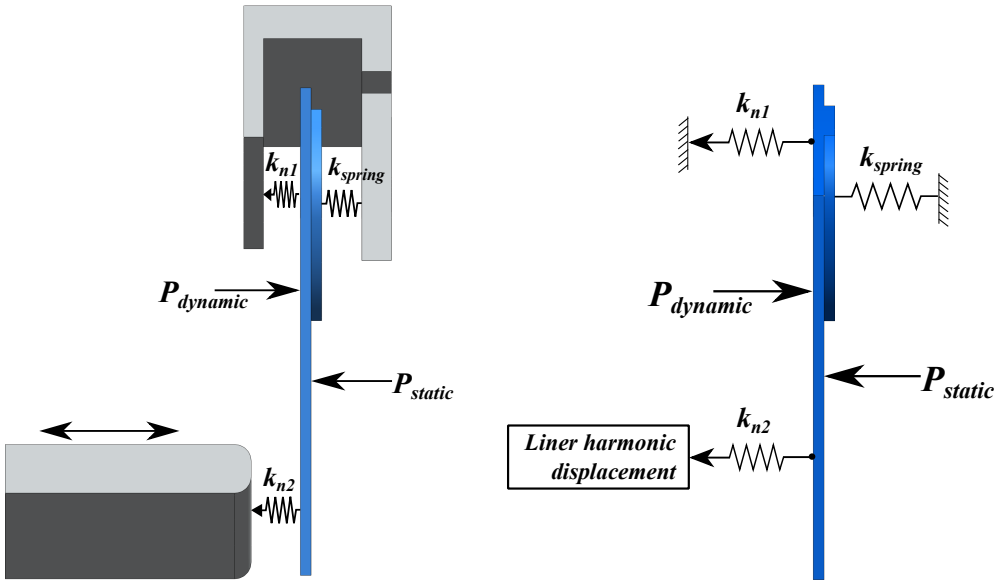

Fig. 6.2 Schematic of the Leaf Seal and the boundary conditions – side view (left), Simplified schematic used for the dynamic analysis (right).

Figure 6.3 shows the 3D FE mesh of the leaf seal. The FE mesh is generated using `ANSYS`. The upper and lower contact patch is highlighted in green colour. Each contact patch is discretized using three rows of 21 node-to-node contact elements as described in the previous section. In total, 126 contact elements for the leaf seal.

This is a sufficient number of contact elements to track the dynamics accurately and to see the change in the contact conditions for various scenarios without being too coarse for improper visualization and too fine for computational burden.

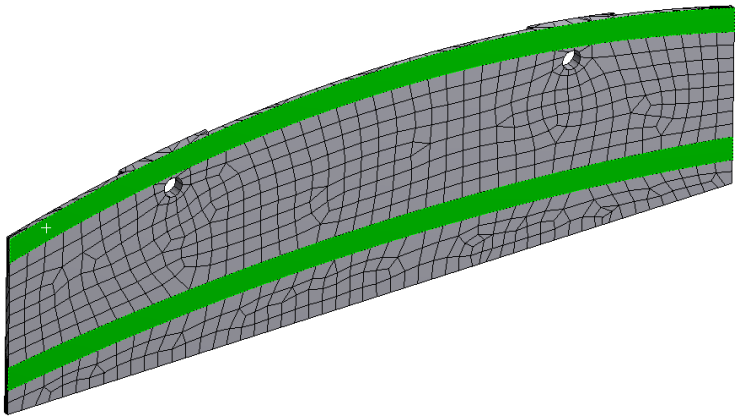

Fig. 6.3 3D FE Mesh of the Leaf Seal with highlighted upper and lower contact patches (in green).

The material properties of standard Steel at room temperature are considered. Though the operating temperature is higher, it is not considered in this study. Also, the dimensions of the leaf seal are academic version. They do not correspond to the actual dimensions out in service in a real GTE. As the intermittent contact is modelled in normal direction alone, any slip in radial direction and friction is omitted. The contact is modelled using a unilateral contact in the normal direction with an assumed normal contact stiffness. As mentioned in the methodology, considering the full size of the leaf seal with all DOFs for dynamic analysis is prohibitively expensive with a computation burden and is unnecessary. Hence, a Craig-Bampton Component Mode Synthesis Reduced Order Modelling (CB-CMS ROM) is performed retaining the contact nodes, excitation and response nodes as master nodes, the rest as slave nodes. With 142 contact nodes resulting in 284 DOFs and 20 retained modes, the size of the dynamic system is 304 DOFs. A coupled approach with 0^{th} and 1^{st} harmonic is considered for the solution procedure.

6.3 Kinematic and operating envelope.

Figure 6.4 shows the range of kinematic envelope the leaf seal experiences in operating conditions. During operation, the leaf can be in any of the conditions -

vertical position or with positive and negative inclination resulting in an outward and inward position. The angled leaf seal creates interesting dynamics because of the curved nature of contacts. The dynamic behaviour of the leaf seal is highly sensitive to the contact conditions. Also, the leaf seal could be excited due to acoustic pulsation, and the dynamic behaviour could change the whole forced response.

A parametrised sensitivity analysis is performed to study the effect of various encompassed operating and kinematic envelope. This would help to study the effect of the individual parameter on the leaf seal dynamics and the contact status conditions. The parameters considered for the analysis are:

1. Effect of Liner displacement (see Table 6.1)
2. Effect of excitation force
3. Effect of liner displacement only – without excitation force
4. Effect of normal contact stiffness (K_n)
5. Effect of pin spring stiffness (K_{spring})

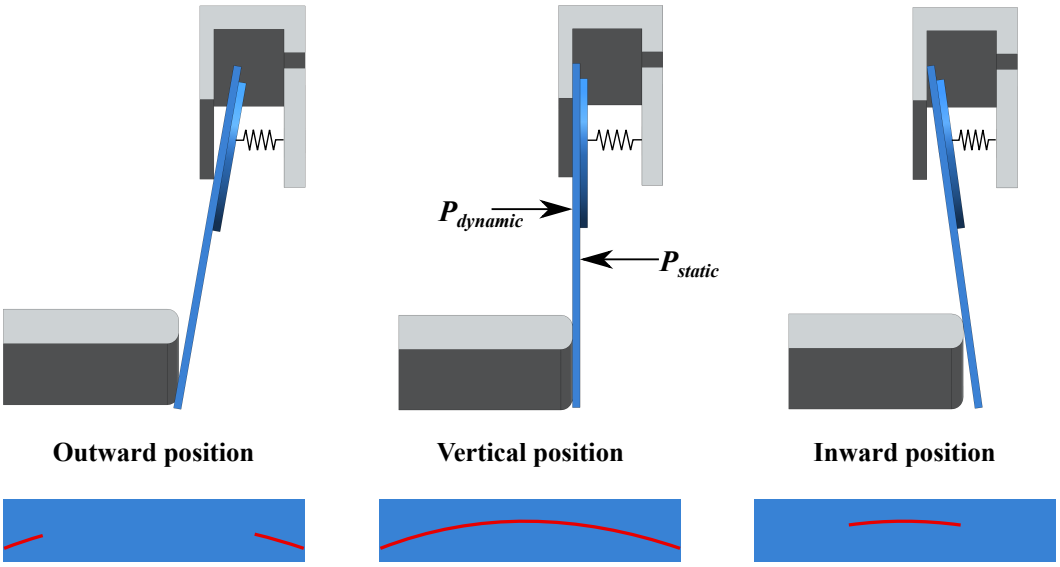

Fig. 6.4 Kinematic envelope showing the inward and outward leaf seal inclination driven by the liner displacement. [Note the partial contact area (edges or centre) when the leaf seal is not in vertical position due to the nature of curved contact].

Condition #	Normalized liner displacement	
	Static (0th harmonic)	Harmonic (1st harmonic)
1	0	0
2	1	0
3	-1	0
4	0	1
5	0	$1i$
6	1	1
7	-1	1

Table 6.1 Tabular representation of various normalized liner displacement conditions.

6.4 Interpretation of the scheme of results presented using sample plots.

Figure 6.5 shows two response curves corresponding to the 'linear free' and 'linear stick' case for the two configurations shown in the boxes, respectively. The nonlinear response is then overlapped on these linear reference curves, which helps to compare the response and to study whether the behaviour is closer to the free or stick case.

Figure 6.6 shows the response plots corresponding to the three nodes of the leaf as highlighted – top figure at the centre node of the upper contact patch, the middle figure at the geometric centre of the leaf seal and the bottom figure corresponding to the bottom corner of the leaf seal. This is hoping to capture most of the dynamics with the help of only these three graphs (as minimum as possible). Ideally, there exists data to plot similar graphs for all the master nodes selected.

The response has two linear free and linear stick cases in blue and green coloured lines, respectively. The red coloured line is the nonlinear dynamic response of the system for a set of boundary conditions.

These response plots show the response amplitude versus frequency for a range of frequencies. However, it does not provide any information on the contact status, contact pressure, etc. Hence, Figure 6.7 provides the complementing information for

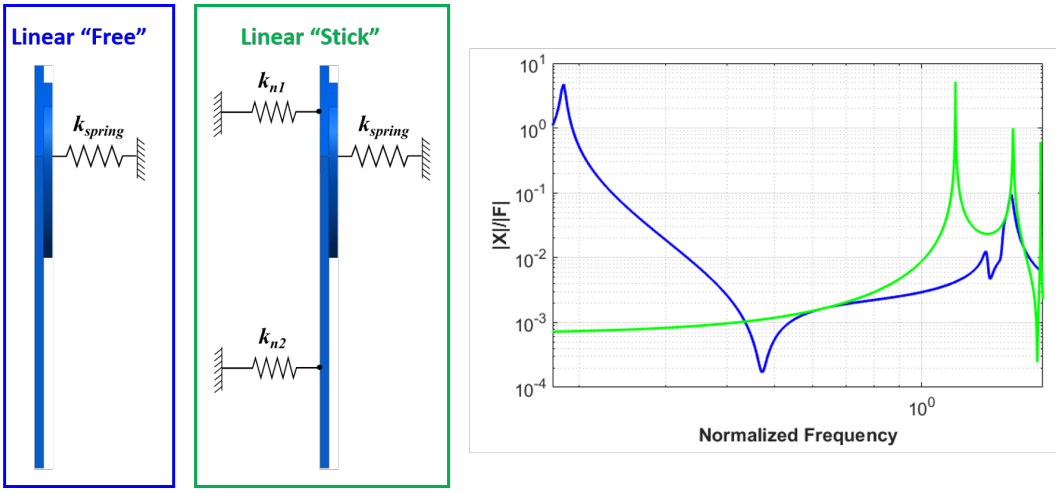

Fig. 6.5 Sample response curve showing "linear free" and "linear stick" cases corresponding to an arbitrary node DOF in order to compare the nonlinear response. [Numerical]

a choice of frequency from the response plots. The two contact pressure plots are shown in this figure corresponding to the upper and lower contact patch. Similarly, the contact status plots for the upper and lower contact patch are shown, indicating whether the contact status at each contact node is in stick, separation-stick or full separation during one vibration cycle at that particular frequency. The contact patch is discretized with three rows of 21 contact elements, which is 63 contact elements for each patch.

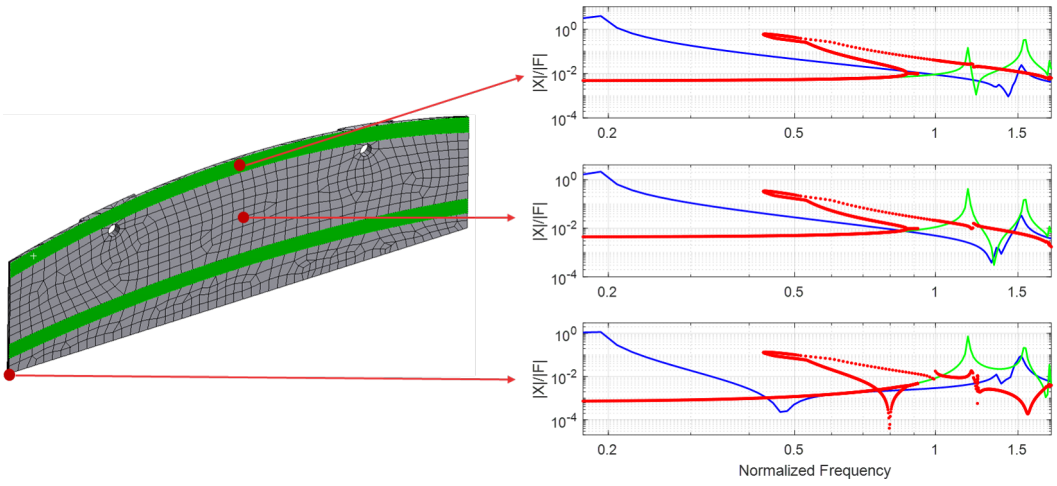

Fig. 6.6 Sample response curves pattern showing the corresponding nodes of the leaf seal to follow the pattern in the results section.

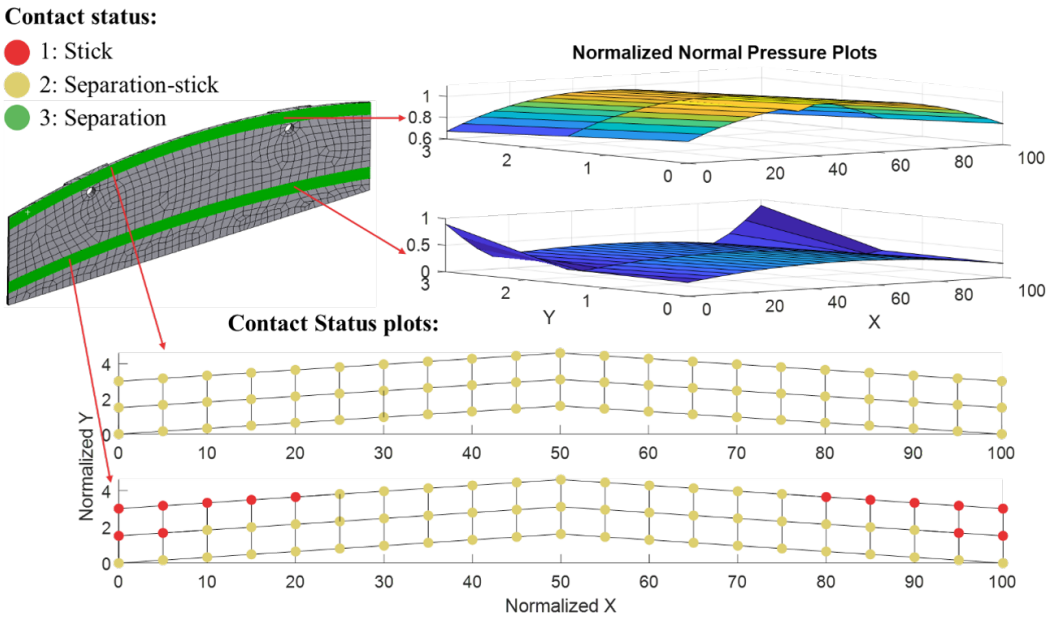

Fig. 6.7 Sample contact pressure plots and contact status plots corresponding to the upper and lower contact patches to follow the pattern in the results section.

6.5 Modal analysis and forced excitation results.

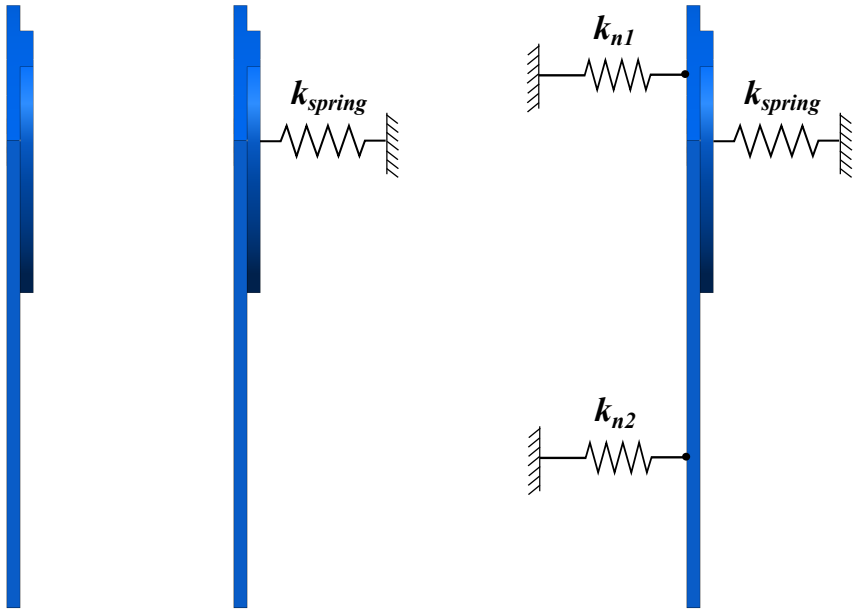

Fig. 6.8 (a) Leaf Seal (free condition), (b) Leaf Seal with springs (free condition), (c) Leaf Seal with springs and grounded contacts (stick condition).

Figure 6.8 shows the different configurations of leaf seal with just the leaf, free, and stick conditions at the contact patches. Table 6.2 lists the natural frequencies of the first 10 modes for the given three conditions. In just the leaf seal configuration, there are two rigid body modes for the given kinematic envelope after imposing the displacement constraints. By imposing the two springs at the pin and spring configuration, the second configuration is obtained. Now the rigid body modes are eliminated, but the natural frequencies are very low because the imposed springs are very soft in nature. In the first two modes, the dynamics are entirely governed by the two springs, and the leaf acts as a rigid body. Of course, in the third configuration, where the contact is fully constrained by the imposed linear springs with normal contact stiffness (K_n), the resonant frequencies are higher as the system is stiffer with fully stuck contacts.

Leaf Seal – Free condition		**Leaf Seal with springs – Free condition**		**Leaf Seal with springs – Fully Stuck condition**	
Mode #	**Normalized Frequency**	**Mode #**	**Normalized Frequency**	**Mode #**	**Normalized Frequency**
1	0.00	1	0.01	1	1.17
2	0.00	2	0.19	2	1.54
3	1.00	3	1.35	3	1.59
4	1.71	4	1.53	4	2.29
5	2.44	5	2.43	5	2.73
6	3.96	6	3.96	6	4.15
7	4.78	7	4.78	7	4.95
8	5.73	8	5.73	8	5.81
9	6.00	9	6.00	9	6.11
10	7.11	10	7.11	10	7.24

Table 6.2 Linear modal analysis of the flat leaf seal with free and fully stuck contact configurations.

6.5.1 Forced response results.

This section presents the complex nonlinear dynamic response plots for a vertical leaf seal with a static liner configuration. Due to space constraints, only one set of results is shown. The normalized stiffness of mounting spring stiffness (K_{spring}) and the normal contact stiffness (K_n) is assumed to be 1 and 25, respectively.

The dynamic response (red line) can be classified into a linear regime and a nonlinear regime. The nonlinear regime corresponds to the frequency range where the 'jump phenomena' ([70, 173]) or the softening behaviour is exhibited and deviates from the linear response. The rest is the linear regime.

Generalizing for various cases performed on the sensitivity study, the leaf seal system exhibits softening behaviour nonlinearity due to intermittent contact behaviour at the two contact patches. This softening behaviour tends to have multiple solutions at a given frequency, as seen in the figure in the nonlinear frequency range. The peak response amplitudes are dominantly higher in the resonance zone and can be destructive if the system continued to operate in this range for a longer period. The partial or full loss of contact on the leaf seal in one vibration period leads to impact behaviour and loss of material, thereby creating wear phenomena. For reference, an experimental investigation of fretting wear behaviour at high temperatures provides insights on the relationship of contact loads and wear properties [98]. The length of the 'softening branch' and peak amplitude for each case is dependent on the static placement and dynamic excitation of the independent liner motion.

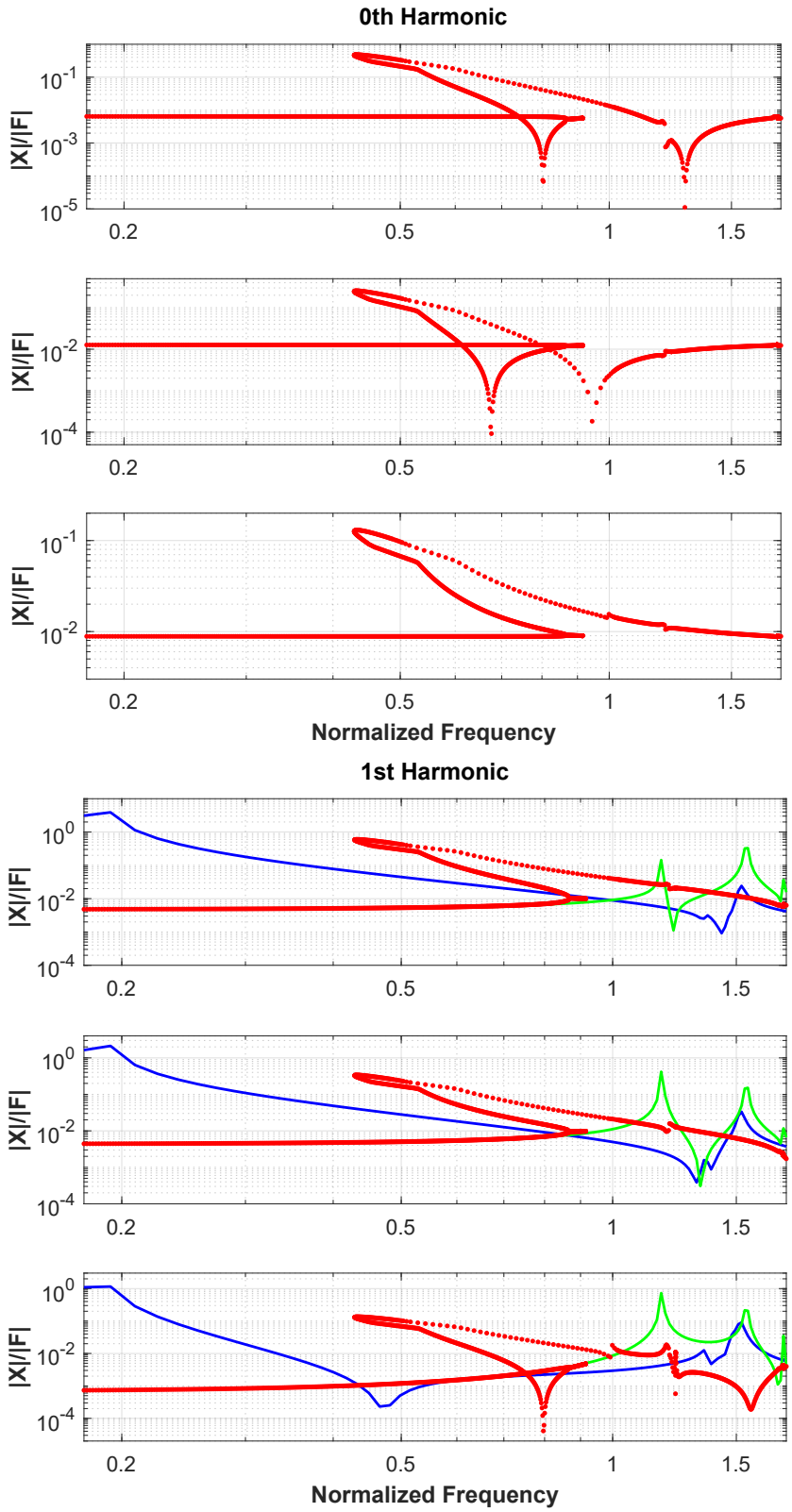

Fig. 6.9 Nonlinear response for the vertical leaf seal with static liner configuration.
Top (0th harmonic); Bottom (1st harmonic)
(blue – linear free state, green – linear stick state, red – nonlinear response). [Numerical]

6.5.2 Contact status insights corresponding to forced response plots.

The contact status and contact pressure plots presented in this section corresponding to the frequencies in response plot Figure 6.9 indicate the general trend of contact behaviour such as fully stuck region, partial separation-stick region and/or full separation region. A few interesting frequency points from the FRFs are picked for further insights and plotted them in the figures through Figure 6.10 to Figure 6.14. In the frequencies corresponding to the linear regime, the contact nodes at the two contact patches are fully stuck (Figure 6.10 and Figure 6.14). In other words, when the leaf seal is subject to operation in these frequencies, the contact between the leaf seal and nozzle, and between liner and leaf seal are fully adherent. So, there is no separation, and likely no wear occurs. However, in the nonlinear regime, where the response exhibits a jump phenomenon through softening behaviour, some of the contact elements exhibit separation behaviour. Subsequently, the vibration amplitudes are also higher. With the partial separation in one vibration cycle, leads to chattering, hence, creating wear. This wear can be amplified with the increase in the number of cycles. Also, the partial separation behaviour could trigger and enhance the complex nonlinear behaviour creating a snowball effect, hence leading to higher vibration amplitudes and branch switching. Especially the frequencies in the strongly nonlinear frequency range (Figure 6.11 to Figure 6.13), where almost all the contact elements experience separation stick behaviour in a given vibration period. This is detrimental to the designed service life and could exceed the permissible vibration amplitudes. Hence it is vital to mitigate and control the high amplitude and jump phenomena behaviour beforehand. However, these results could be seen as qualitative because of simplifications such as assumed normal contact stiffness and only one harmonic considered.

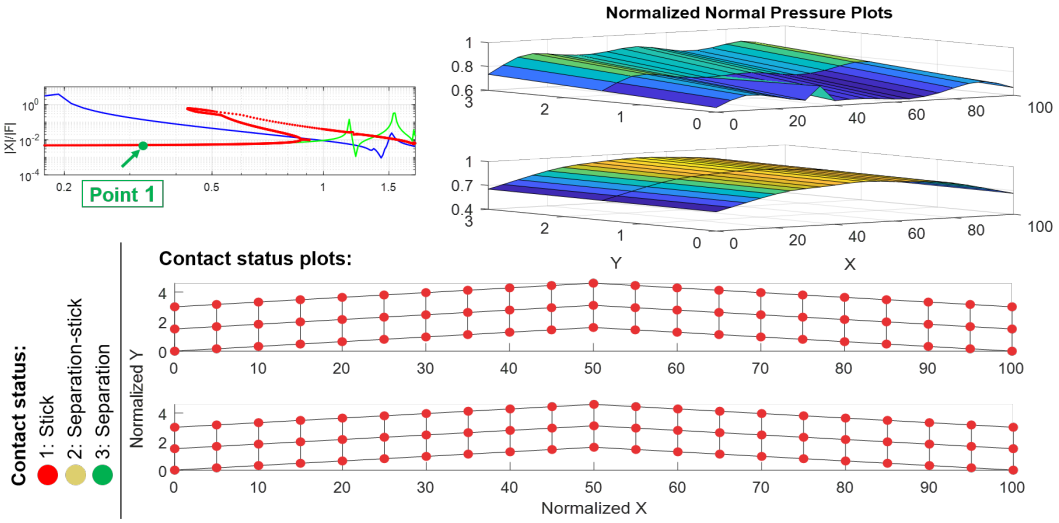

Fig. 6.10 Contact pressure distribution and contact status of the upper and lower contact patch corresponding to the highlighted point 1. [Numerical]

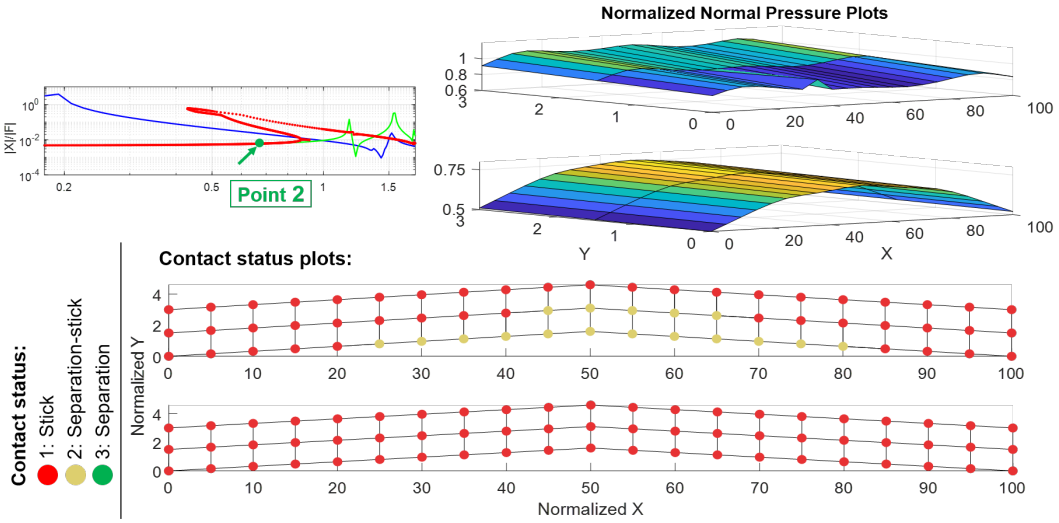

Fig. 6.11 Contact pressure distribution and contact status of the upper and lower contact patch corresponding to the highlighted point 2. [Numerical]

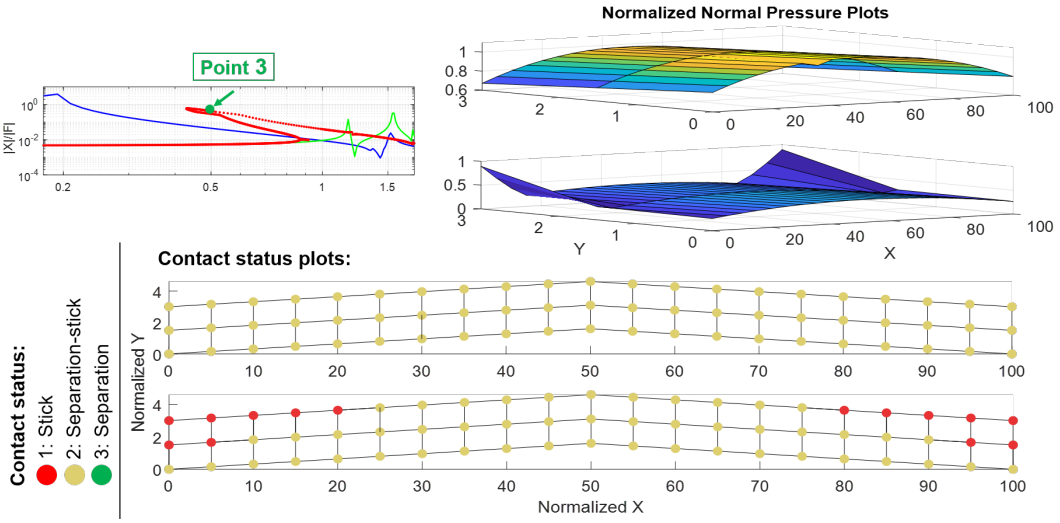

Fig. 6.12 Contact pressure distribution and contact status of the upper and lower contact patch corresponding to the highlighted point 3. [Numerical]

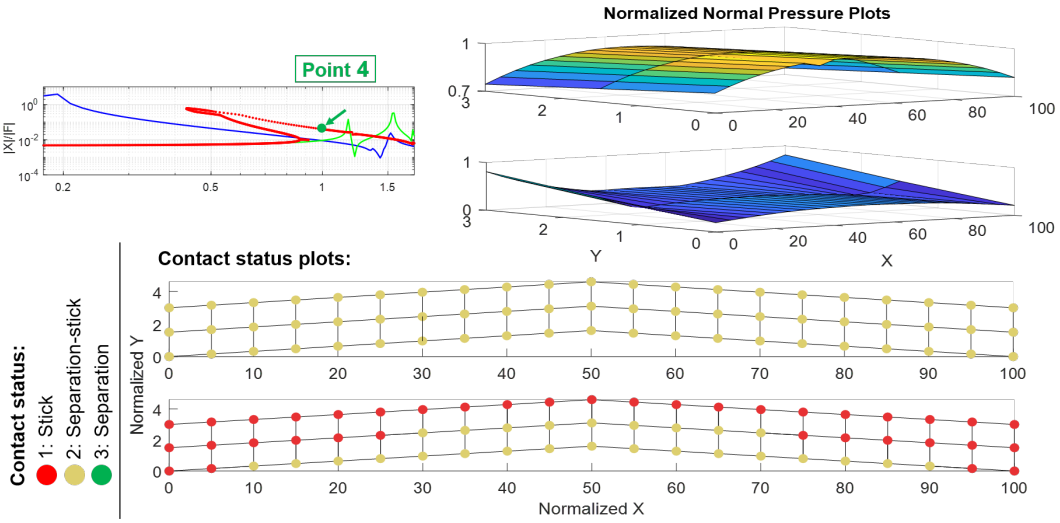

Fig. 6.13 Contact pressure distribution and contact status of the upper and lower contact patch corresponding to the highlighted point 4. [Numerical]

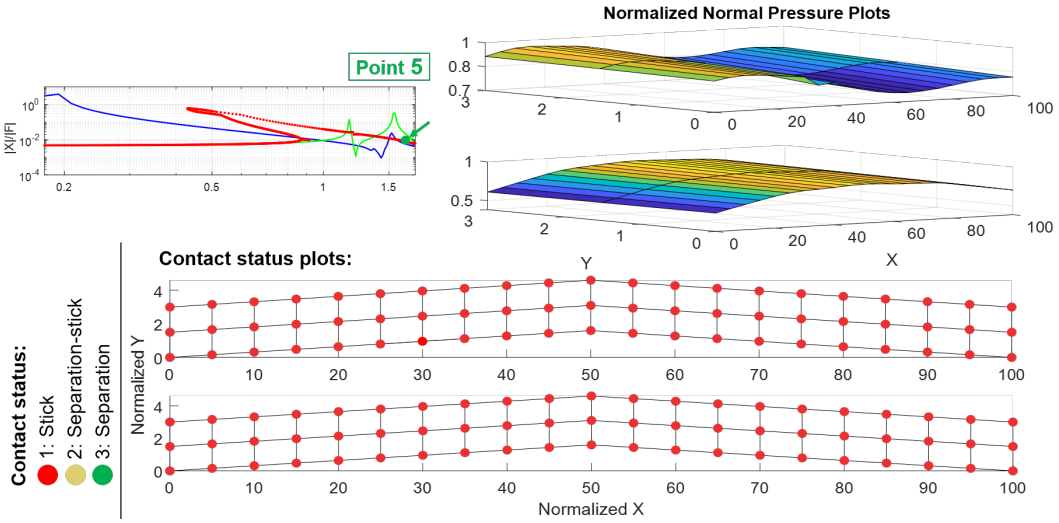

Fig. 6.14 Contact pressure distribution and contact status of the upper and lower contact patch corresponding to the highlighted point 5. [Numerical]

6.6 Discussion.

The nonlinear dynamic analysis is successfully performed on the given combustor leaf seal system using the coupled HBM. Multiple simulations were carried out, subjecting the leaf seal to various operating and kinematic envelopes. A modified 2D Jenkins element with a variable normal load contact model was used by deactivating the tangential part as mentioned before.

Effect of excitation:

It was interesting to see how the leaf seal responds when subjected to different excitation forces. For all the analyses, the normalized static force was fixed at 3, and the dynamic excitation was varied from 0.1, 0.2, 0.5 and 1. The plots are not shown here because they take up a lot of space and add relatively little value because the plots are visually similar. However, the observations are - with low excitation forces, the response tends to follow the linear stick response for the most part with a small softening branch at the resonance like the one shown in the previous section. With increasing excitation force, the peak amplitude and the length of the softening branch increase with increasing the range of nonlinear frequency response giving more chance to have the jump behaviour. Higher excitation forces could cause the

premature failure of the leaf seal because of the larger separation-stick behaviour of contact nodes at the upper and lower contact patches for a wide frequency range.

Effect of normal contact stiffness (K_n):
Similarly, the curiosity of the effect of assumed normal contact stiffness led to span the numerical experiments on the system. When the system is modelled with higher normal contact stiffness, the overall system tends to get stiffer, and the leaf seal dynamic response is very sensitive to the contact stiffness assumption. Because the dynamic behaviour is highly sensitive to the contact conditions such as contact state and contact stiffness. As this is a numerical investigation at this stage, an educated guess of contact stiffness was made from prior experience dealing with other mechanical systems. The more concrete values are usually obtained through the experiments. Also, what was found interesting is for softer normal contact stiffness, the penetration allowed is higher through the contact model and leads to less accurate numerical simulation. Larger normal contact stiffness leads to smaller penetration and thereby minimizing errors.

Effect of pin spring stiffness (K_{spring}):
Similarly, it is found that the dynamics of the leaf seal are extremely sensitive to the pin spring stiffness values (K_{spring}). In the current system, two soft springs with the pins are used to keep the leaf seal in place by resting on the nozzle contact surface in static condition. Hence, the stiffness values of these springs play a major role in governing the dynamics of the leaf. The softer the springs, the dynamic response has high peak amplitudes and longer softening branches. Hence, the choice of spring stiffness is a trade-off between limiting vibration amplitudes or the required sealing capacity by closing the contact to avoid leakage in the operating ranges.

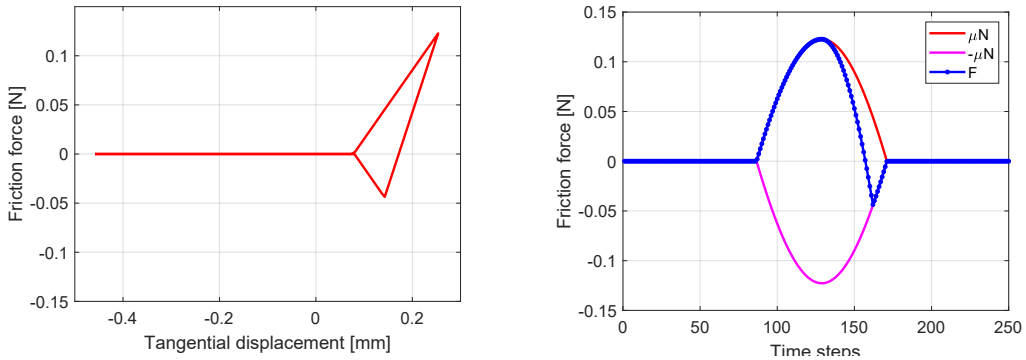

Fig. 6.15 Typical hysteresis loop (a) and nonlinear contact force with friction limit envelope (b) in the nonlinear frequency range. [Numerical]

In the nonlinear range, the contact experiences a combination of stick, slip and lift-off in one vibration cycle leading to intermittent contact and exhibiting softening behaviour. Figure 6.15(a) shows a sample hysteresis loop from one of the contact elements undergoing the said change in contact states in one cycle. Figure 6.15(b) shows a corresponding force limit with the actual force trajectory.

The general observations valid for all configurations presented in the results section is as below:

1. The contact elements experience intermittent contact (chattering) along with the upper and lower contact patch at the resonance region. The resonance region is defined here as the frequencies falling under the length of the branch of the softening curve and separating from the linear regime in the dynamic response plots.

2. The 'jump phenomena' with softening behaviour is prevalent in the resonance region for all the operating and kinematic envelopes. However, the length of the softening branch and peak amplitudes are subject to the underlying configuration.

3. The contact status behaviour and contact pressure plots provide additional information visually, such as the distribution of normal pressure at the contacts and individual contact status at each corresponding frequency on the response plot.

4. The response amplitudes outside the resonance region follow the linear stick solution branches, and there is no contact separation (intermittent contact behaviour - chattering).

5. At the extreme configuration of positive inclination of the leaf seal, the contact occurs only at the edges, thereby leaving the centre elements at the contact patch in full separation during a vibration cycle. Similarly, for the negative inclination of the leaf seal, the contact occurs only at the centre of contact patches leading the edges out of contact during one full vibration period. These extreme behaviours are vital to understand complex behaviour and design the components better.

6. For very low excitation forces, the leaf seal response tends towards the 'stick state' response as the static pressure is larger than excitation pressure caused by acoustic pulsation and tries to keep the leaf seal adhered to the contacts. However, the leaf seal behaves closer to the 'free state' response for very high excitation forces.

7. The length of the softening response branch and maximum vibration amplitude is qualitative as it depends on the number of factors – frequency range discretization, number of harmonics, modelling of the pin, which is omitted here, accurate values of normal contact stiffness and spring stiffness. With higher harmonics, more accurate resonance amplitudes and length of the softening branch can be obtained, at the increased computation cost.

8. Effect of K_{spring} and K_n on the sensitivity of the results are studied briefly. These values greatly affect the dynamic behaviour as the leaf dynamics are highly sensitive and dependent on the contact conditions.

The computation time taken to obtain the solution for one configuration with a given frequency range is only a few minutes with a standard stand-alone PC. Thanks to the in-house forced response solver developed during this doctoral study period. If one had to perform a time-domain analysis to get even the solution at one frequency on the FRF would take hours and sometimes would fail to capture the nonlinear behaviour due to varying contact conditions. The state-of-the-art coupled HBM solver facilitates modelling and visualizing complex dynamic behaviour for highly nonlinear contact problems with the underlying assumption of steady-state condition.

However, the results could be improved by using accurate inputs and modelling fine contact discretization. As a next step, the study can be extended to include fretting wear at the pins due to relative motion and intermittent contact at the two contact patches. Due to time constraints, these additional studies could not be performed. Also, an interesting investigation on the bowed leaf seal was briefly carried out. The bowing, either positive or negative relative to the contacts, can significantly impact on the forced response and contact conditions. Qualitatively, the dynamic behaviour was similar to the flat leaf seal by exhibiting softening behaviour and intermittent contact at the nonlinear frequency range.

6.7 Summary.

This chapter presented a numerical study of an industrial test case - gas turbine combustor leaf seal. A nonlinear dynamic analysis was performed using the in-house coupled HBM solver presented in the previous chapters. The leaf seal undergoes a complex dynamic motion arising due to a large range of kinematic and operating conditions with soft contacts and curved contact nature. The nozzle-leaf seal and liner-leaf seal contacts are modelled as a unilateral contact in the normal direction to the contact surface.

Analyzing the response plots, it is found that the leaf seal experiences intermittent contact behaviour (chattering) around the resonance frequencies and experiences jump phenomena because of exhibited softening behaviour. This causes the leaf seal to wear at the contact regions and lead to high vibrational amplitudes. In almost all kinematic and operating envelopes configurations, the leaf seal was subjected to high amplitudes and intermittent contact. Various time history plots at different interesting frequencies within the operating range were analyzed.

These numerical results can be interpreted as a preliminary qualitative study to give an overall idea of the complex dynamic behaviour and sensitiveness to the boundary conditions and capabilities of the solver. An experimental test bench is necessary to study the dynamics experimentally and perform a refined analysis and validation to validate the numerical results. As a future work recommendation, possible fretting wear at leaf seal-pin can be investigated. The effect of bowed leaf seal on the curved contacts could provide an interesting insight.

Chapter 7

High performance computing

7.1 Introduction.

In the previous chapters, the numerical results of nonlinear dynamic response to generic FE model with numerous DOFs were presented. The nonlinear solution is generally computationally intensive requiring several hours to days to perform one set of full solution to study the dynamics and the effect of wear. These solutions were presented using a standard stand-alone workstation. Naturally, the next step is to look for HPC usage with multi-node capabilities with large processing power and memory.

As part of the current doctoral research defined under the project (MSCA Horizon 2020 - EXPERTISE) with the ultimate objective of the project to virtually perform full-scale simulation of the whole aero-engine, three months were spent at HLRS Supercomputing Center in Stuttgart, Germany at the SPMT (Scalable Programming Models & Tools) team. SPMT team specialize in the field of HPC, catering to a wide variety of scientific applications.

The point of view presented in this chapter is through a lens of novice user with no prior experience in HPC systems and a `MATLAB` user to solve dynamics problems. The researcher codes or development codes are written by individuals or small groups that have pockets of inefficiency during the programming phase of a workable set because of ad-hoc features addition and trying to make the code work. With the help of HPC experts and their vast coding knowledge dealing with such scientific applications, the following goals to achieve were formulated:

1. Improve the efficiency of in-house HBM solver by vectorization and translation to other programming languages (if necessary).
2. Suitability of the code for parallelization and HPC compatibility to run across multiple nodes.
3. Feasibility study for the usage of available open-source third-party libraries.

7.2 Necessity of HPC.

With the increase in computing power, the complexity of problems solved using computational methods are also increasing. Today, there is a possibility to solve dynamical systems with medium complexity using personal desktop computers. Linear solutions are no more valid when designing high-performance components to perform under structural and and operational limits. Hence, more accurate nonlinear solvers are necessary. Regarding solving nonlinear dynamics problems, the development of techniques such as Reduced Order Modelling (ROM), substructuring, usage of frequency-domain based techniques (HBM) for steady-state solutions as opposed to time-domain based methods vastly improve the computational speeds. However, looking at the real-time industry level problem complexity, one soon runs out of the memory and RAM needed to handle such large problems. The next resort after personal workstations is the High Performance Computing (HPC) systems or supercomputers. HPCs are comprised of huge arrays of CPUs and memory storage systems with interconnects between them. They help discretize the large problems into sizable chunks and distribute them to the dedicated number of nodes and cores for an efficient solution.

Leaping from personal computers to HPC comes with additional learning. For example, to establish communication between multiple nodes needs knowledge of inter-node communication protocol and its working. The widely used industry standard is Message Passing Interface (MPI). The MPI is a communication protocol commonly used in HPC which allows two or more computers to share information [174]. Furthermore, there exists a combination of intra-node parallelization known as OpenMP and inter-node parallelization known as MPI. When both the

techniques are implemented simultaneously, it is known as Hybrid programming. Figure 7.1 shows the pictorial representation of MPI vs. OpenMP.

- **OpenMP:** Shared memory parallelization
- **MPI:** Distributed memory parallelization
- MPI & OpenMP implementation is called **Hybrid programming**.

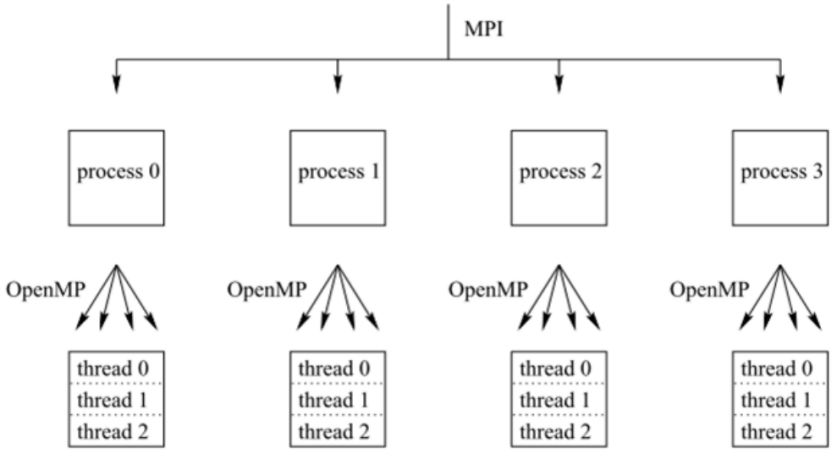

Fig. 7.1 Overview of MPI vs OpenMP [174].

7.3 Challenges of using HPC.

Initially, using HPC might look like a one-step solution for all large problems. It is great to think of all the enormous computing power available in the present day to solve any complex problem at speedy turn-around times. However, the truth is further

Note to `MATLAB` users: `MATLAB` is an auto thread-parallel system. This means if one is using a multi-core CPU, `MATLAB` efficiently parallelizes within the number of threads available in a single CPU. For example, if one is using a 16-core Intel Xeon system, `MATLAB` takes care of the efficient distribution of data needed to compute faster. However, `MATLAB` is not multi-node capable without an additional license package called Distributed Server. This package is unavailable at Politecnico di Torino's HPC systems Hactar, Casper and Legion at the time of this writing and also unavailable at HLRS HPC systems (Hazel Hen). Hence, the study and implementation of the in-house `MATLAB` Forced Response Solver was limited to one node. However, there was a chance to exploit the maximum number of cores available within one node, up to 24 cores in HPC systems. Scalability is another important aspect to be understood for novice HPC users. The Scalability is highly dependent on the type of program and the sequence of code-flow.

from it and comes with its own requirements and challenges. There is an initial learning cost to use HPC. One has to possess basic knowledge of the functioning of HPC and even to be able to submit the job and using a scheduler. If an end-user is using commercial software packages such as `ANSYS`, `ABAQUS`, etc., there is not much to worry. These software mostly handle the distribution and optimization of the number of CPUs and cores internally. However, as in the current case, if one is developing ground-up code in `MATLAB`, there are other set of challenges.

HPC systems do not take a single node program and automatically make it an efficient multi-node program. The user has to meticulously optimize the different sections of the code and write in a HPC compatible language. Most researchers are not expert coders, and especially those who are used to `MATLAB` would face an initial learning curve with HPC systems. HPC domain thrives on the usage of open-source software and codes for many reasons, but `MATLAB` is a proprietary software. So naturally, an user with programming language experience of `C`, `C++` or `FORTRAN` and if the code from the start is already in these languages is at a great advantage. If not, `MATLAB` user needs additional learning which have been discussed in the following sections.

Another good to know point is that the CPUs used in HPC systems are directly comparable to the high-end CPUs used in powerful stand-alone workstations like Intel Xeon. For example, the CPU speeds are similar, hence the number of instructions per second each core can handle. However, the number of cores available in each CPU can differ between 4 to 32 cores per CPU. So initially it could be surprising to see the direct comparison of run-time for a single node `MATLAB` code between the personal workstation and a HPC could be identical.

Chapter 5 of the PhD thesis of Rose [175] beautifully summarized the underlying parallelism in `MATLAB` from an end-user point of view with comments on serial versus parallel code run-times and speed-up improvement with examples. Professor Matloff [176] in his book on parallel programming mentions that the first-time developers of parallel code often find out that the parallel version is slower than the serial version attributing to the lack of at least a high-level understanding of how computer hardware works. It further provides examples of the addition of processors for parallel computing on shared memory systems need not provide linear improvement in speed-up where doubling the number of cores doubles the computational speed.

7.4 Tips for better programming.

The following are some low-hanging tips to implement for better programming and reduce run-time:

- Use vectorized operations where possible as opposed to elemental operations.
- Unroll small iteration for-loops.
- Avoid generic pre-defined functions and write task-specific sub-routines.
- Suppress intermediate outputs such as figures and writing to the command window.
- Use `parfor` loops (parallel for-loops) instead of `for` loops in `MATLAB`.
- Keep track of iteration order in multi-dimensional arrays whether inner-to-outer exection or vice-versa, depending on the choice of programming language.

Code vectorization brings out substantial improvement in run-time reduction because of the usage of array operations instead of an elemental operation, thereby making better use of available computational resources. Gaining efficiency from `parfor` is rather tricky. The reason being when `parfor` is used, `MATLAB` starts a parallel engine within the same node to act virtually as a multi-node system. This creates additional communication overhead, and at times the time spent in these channels are more than the time gained by using a parallel option.

7.5 Code parallelization - identification.

Before proceeding onto the HPC system or thinking about multiple nodes, primarily one has to profile the code at hand for run-time to identify various routines and the time spent on each routine and track the number of calls of those sub-routines. To do this, `MATLAB` has a `Runtime Profiler` option, which tracks various functions of the code and time spent at each line of code and the number of calls made. After identifying the computationally intensive sections, the next step is to check if parts of these can be parallelized. When moving from a single node program to a multi-node,

it is good to keep in mind the communication overhead and node idle times during the serial operation. The overhead time could exceed by a large margin if the work performed is too small in each iteration with a large number of function calls or a large portion of the code is serial. So a few trials and experience play a role to identify whether to make the parallelization decision.

In the literature, there is a handy rule available called Amdahl's law to quantify and make a trade-off comparison between the potential speed-up achieved versus the number of processors [174]. Figure 7.2 shows a comparison between the speed-up gained versus the number of processors with a parallel portion as a variable. The higher the parallel portion the code has, the better speed-up can be achieved in relation to the used computational power. The next thing to keep in mind is the overhead of various parallel portions. So performing initial studies and profiling various sections is of definite help. This figure also shows after a certain number of processors, increasing the number of processors leads to only marginal gain or stagnation, and there is no speed-up possible. This can help to know beforehand the necessary number of processors, and the speed-up gain can be estimated with optimal use of resources.

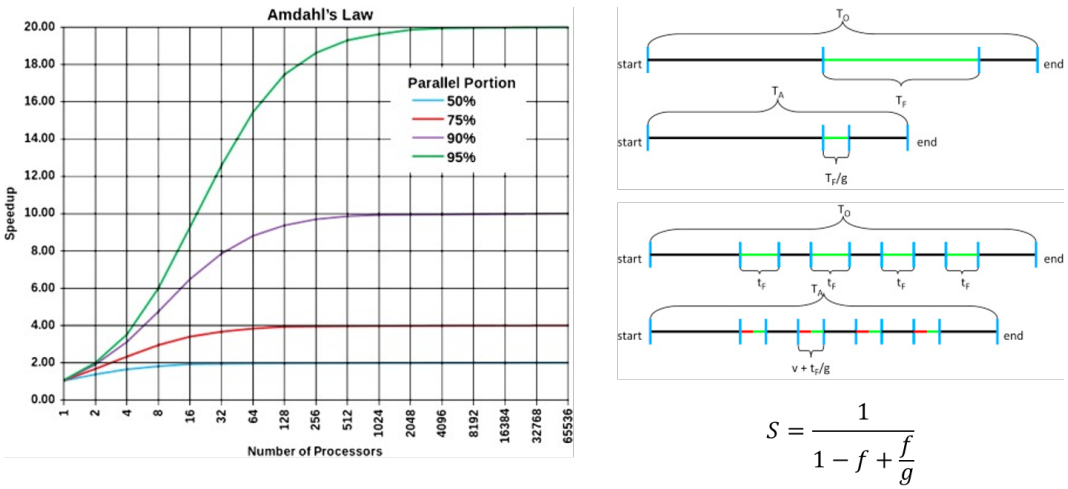

Fig. 7.2 Amdahl's law and parallel portion identification [177, 174].

7.6 HPC test case: Profiling.

With the knowledge equipped the previous sections, now a test case is needed for benchmarking purposes to compare the potential speed-up. The first numerical test

case from Chapter 4 i.e. a cantilever beam with a known friction contact patch is chosen to optimize the code and check the potential gain. The resulting system, after applying boundary conditions and performing CB-CMS ROM has 528 DOFs. For the HBM with the coupled case including static and dynamic components and splitting the complex terms into real and imaginary components results in 528 DOF for 0^{th} harmonic and 528*2 for 1^{st} harmonic, resulting in 1584 equations of unknowns to solve. For subsequent harmonics, 528*2 DOFs add to the unknown equations for each harmonic.

For the following profiler results, the frequency range is divided into 200 steps with natural continuation and 100 time steps for AFT logic. The cantilever beam contact patch is discretized into 169 contact elements with 3 DOFs for each element. The `MATLAB` `fsolve` parallel is set to `false`. The Jacobian is computed and supplied analytically avoiding built-in `MATLAB` Jacobian using finite difference method (FDM). This also results in a multi-fold increase in performance as the analytical Jacobian requires only one pass compared to FDM, requiring passes as many as number of DOFs. The code is set to run for one wear iteration only. The wear iterations cannot really be parallelized because the worn profile from one iteration is needed as an input for the next iteration with an updated contact interface, making the routine sequential with respect to wear iterations.

The code has been vectorized in all the modules and sub-functions by analysing the code line-by-line based on the profiler results. The sub-routines are fully optimized by rewriting parts of code wherever possible instead of using `MATLAB` ready-made functions. The outputs to the command window and plotting figures were turned off. The final resulting performance with 16 cores on a HPC resulted in 100s total run-time. To compare the initial code run on a laptop with two cores without optimization took roughly 600s. Just by carrying out the said changes, the run-time was reduced by 80%. The bigger contributions resulted from suppressing outputs, plotting figures, and vectorization played a key role in performing large iteration `for` loops. `parfor` loops were tried out, especially in the contact model routine to parallelize the contact elements which can run independently. However, it was observed the total run-time doubled compared to simple `for` loops. The reason was bulk of the time was spent in establishing a parallel communication and related overhead. Hence, `parfor` was not really useful for the current problem size and type of problem in hand.

The profiler results presented here are run on the HLRS Hazel Hen HPC system. The results were averaged by conducting atleast three runs. Similar multiple runs were carried out in Politecnico di Torino's HPC Hactar system, and they have resulted in identical run times because of underlying processors with similar specifications.

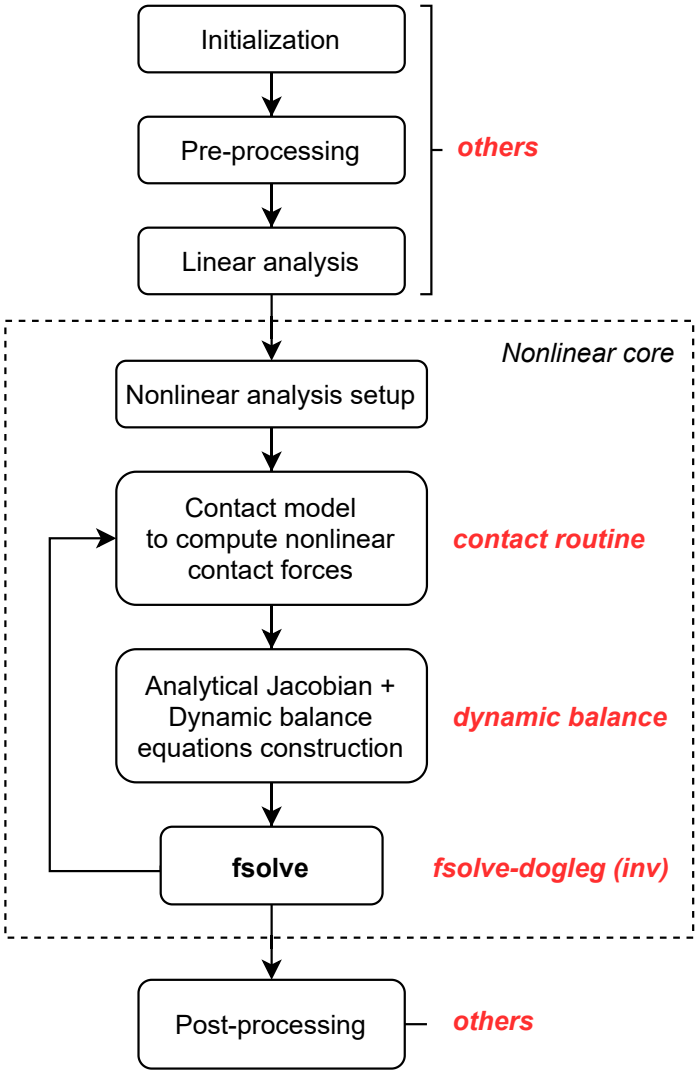

Fig. 7.3 Pseudo code-flow to interpret profiler results.

The number of cores to be utilized effectively can be controlled by defining the parameter `maxNumCompThreads()` in `MATLAB`. Here the idea is to see how inherently thread-parallel effectiveness is the code and how overall time varies depending on the number of cores. The various subheadings of the code are related

to the solution flowchart of performing dynamic analysis of the system. The main routines are listed as contact routine where nonlinear contact forces are computed, dynamic balance where Jacobian is assembled, fsolve-dogleg is the time spent on the inverse operation to solve for the unknowns and other functions including system functions classified as others.

Just changing the number of harmonics in a coupled HBM allows the flexibility of varying the size of the system to be solved. This allows one to study the effect of the number of cores on different problem sizes quite easily. There are many ways a user can code a software to solve the nonlinear dynamic system with friction contact nonlinearity. Presenting detailed profiler results of each line of code is not very useful. Figure 7.3 shows a pseudo code-flow to interpret the profiler results of the current in-house solver. The whole code is grouped under four broad category functions for interpretation, as shown in the profiler results tables.

Table 7.1 shows the profiler results of the code for 0+1 harmonics using a coupled HBM, resulting in 1584 unknown equations. Similarly, Table 7.2 shows the profiler results of the code for 0+3 harmonics resulting in 3696 unknown equations. It is very interesting to see how each sub-routines are affected by the choice of the number of cores. For example, the contact routine and other functions are almost indifferent to the number of cores engaged. This means effectively these routines are running only on one core and the rest being utilized for other functions or are idle. The most significant impact of the number of cores is on the `fsolve-dogleg` inversion process. This line of code performed `MATLAB` specific matrix inversion to solve the vector of unknowns. With an increasing number of cores, the effective time spent comes down significantly. However, there is no linear relationship for the number of cores versus the time reduced. After a certain number of cores, the marginal gain in speed-up is abysmal.

Function	maxNumCompThreads()									
	1		2		4		8		16	
contact routine	42.5s	28%	43s	34.5%	50s	40%	42.5s	42%	44s	44%
dynamic balance	30s	20%	27s	21.5%	30s	24%	26s	26%	26.5s	26.50%
fsolve-dogleg (inv)	68.5s	46%	47s	38%	35s	28%	24s	24%	21s	21%
Others	9s	6%	8s	6%	10s	8%	8.5s	8%	8.5s	8.5%
Total	**150s**	**100%**	**125s**	**100%**	**125s**	**100%**	**101s**	**100%**	**100s**	**100%**
dogleg calls	792		792		792		792		792	
per dogleg inv	189ms		157ms		157ms		127ms		126ms	

Table 7.1 Profiler results: 0+1 harmonics run on 1 HPC node.

Function	maxNumCompThreads()									
	1		2		4		8		16	
contact routine	57s	6%	68s	10%	62s	12%	57s	13.5%	59.5s	16%
dynamic balance	141s	14%	138s	20%	126s	24.5%	123s	29%	117s	31%
fsolve-dogleg (inv)	780s	78%	476s	68%	308s	60%	226s	53%	186s	49%
Others	22s	2%	21s	2%	20s	3.5%	18s	4.5%	16.5s	5%
Total	**16.7m**	**100%**	**11.7m**	**100%**	**8.6m**	**100%**	**7m**	**100%**	**6.3m**	**100%**
dogleg calls	792		792		792		792		792	
per dogleg inv	1.26s		886ms		651ms		530ms		477ms	

Table 7.2 Profiler results: 0+3 harmonics run on 1 HPC node.

Effect of the number of harmonics (nH): To visualize the effect of the number of cores, the test case with 1 harmonic is too small. Hence the number of harmonics is notched up to include up to 5 harmonics, including the zeroth harmonic. Now, the effective size of the system is 5808 unknown equations. In Table 7.3 the effect of the number of harmonics on the total time spent on `fsolve-dogleg` inversion using

16 cores is more evident. Almost 60% of the total time spent is only on one single operation, that is matrix inversion. So the key here is to address this concern to better speed-up the overall computation time needed. From here, one can deduce that the larger the problem size, the large portion of time and resources is spent on just one operation - matrix inversion. Figure 7.4 shows a stacked bar graph representation of the effect of the number of threads on various sub-routines. The matrix inversion could take an even higher portion of total computation times for even larger problem sizes.

Function	**nH**					
	0+1		**0+3**		**0+5**	
contact routine	44s	44%	59.5s	16%	105s	8%
dynamic balance	26.5s	26.5%	117s	31%	402s	30%
fsolve-dogleg (inv)	21s	21%	186s	49%	796s	60%
Others	8.5s	8.5%	16.5s	5%	37s	2%
Total	**100s**	**100%**	**379s**	**100%**	**1340s**	**100%**
Time X-er	1x		3.8x		13.4x	
Jacobi size	1584x1584		3696x3696		5808x5808	
dogleg calls	792		792		792	
per dogleg inv	126ms		477ms		1.69s	

Table 7.3 Effect of number of Harmonics with 16 cores on 1 node.

Figure 7.5 shows the effect of the number of harmonics on the nonlinear frequency response of the test case. One can use this type of comparison to understand how many harmonics are needed to analyse to obtain acceptably accurate results. For example, there is a big difference in FRF curves between 1 and 3 harmonics in the current case, however not much difference between 3 and 5 harmonics. Therefore, one can sufficiently conclude for this test case, including up to 3 harmonics is sufficient. This directly affects the size of the system and the computational time needed for each response curve. In this case, just to include 2 additional harmonics of 3 harmonics for a marginal gain in accuracy, the computational time needed is over 3x. An user can take a call on defining the harmonics going by similar analysis.

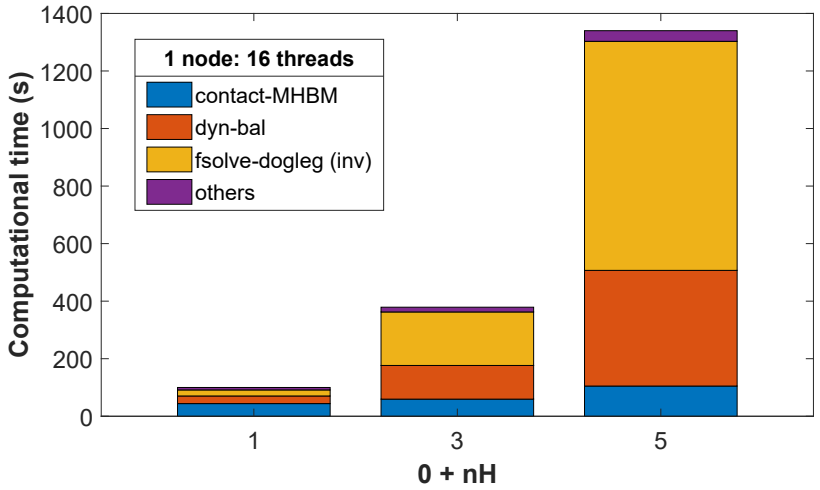

Fig. 7.4 Effect of number of Harmonics on computational speed.

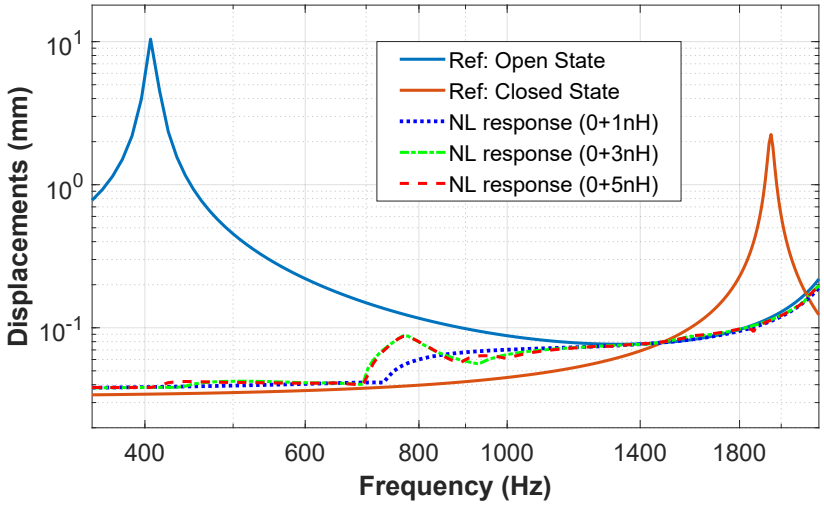

Fig. 7.5 Effect of number of harmonics on FRF. [Numerical]

Now that using the maximum number of cores on a single node has hit an asymptote because of `MATLAB` additional license issue, and plainly increasing cores within a node as not being effective, this naturally leads to the next question. What is to be done to distribute the problem, specifically, the most time-consuming part - the matrix inversion into multiple nodes and reduce the overall computational time? It is time to look at the available external packages and third-party libraries.

7.7 External packages.

Instead of using a bottom-up approach of writing multi-node routines to reinvent the wheel, which takes a lot of time and resources, it is wise to use the already available open-source external third-party libraries/packages which has been developed by various research institutes worldwide. There are two such well-known and proven packages available specifically for scientific applications, namely `PETSc` and `Trilinos`. These two packages offer a wide range of routines based on efficient and highly scalable linear algebra packages (BLAS & LAPACK). At the heart of scientific problems is solving a set of differential equations represented as a set of matrices. These third-party open-source packages come with hundreds of experts contributing thousands of man-hours to develop generic codes for a wide range of scientific problems. One can decide to make use of them and customize them for one's own specific purposes. Of course, they come with their own merits and demerits. These packages are also based on open source programming languages such as `C`, `C++` or `FORTRAN`.

The major hurdle for researchers used to `MATLAB` software is, `MATLAB` is proprietary and licensed software. It is strenuous to interface with open source programming languages such as `C`, `C++` or `FORTRAN`. `MATLAB` offers a very modular and easy to use interface and support, which is helpful to start for researchers with relatively less or no coding experience. It soon turns out to be a bottleneck for highly scalable solution implementation. `MATLAB` is mostly a single node solution, apart from the `Parallel Computing Toolbox (PCT)` which virtually creates a multi-node environment within a single physical node. (However, there is `'MATLAB Parallel Server'` solution for multi-node systems, but it needs an add-on license, and with the current knowledge, it is not readily available at most public research institute supercomputers.) When a researcher tries to look for a multi-node solution for scalability and exploit high-performance computing solutions, one has to move to use these external packages.

7.7.1 `PETSc`.

`PETSc`: https://www.mcs.anl.gov/petsc/index.html

PETSc stands for Portable, Extensible Toolkit for Scientific Computation Toolkit for Advanced Optimization. PETSc is a suite of data structures and routines for the scalable (parallel) solution of scientific applications modelled by differential equations. It supports MPI (multi-node) and GPUs as well as hybrid MPI-GPU parallelism. PETSc also contains the optimization software library.

For the specific case of solving second-order nonlinear ordinary differential equations, PETSc offers an equivalent of MATLAB `fsolve:trust-region` algorithm. PETSc offers Scalable Nonlinear Equation Solvers called SNES. This include line search and trust region based algorithms and many more.

Since PETSc uses C language, there are functions available to communicate between MATLAB and PETSc such as `MATSOLVERMATLAB` and `MATMATSOLVE`. An interested user can start from here and go deeper in implementing the necessary nuances. Interfacing MATLAB with C is not easy and straight-forward. It needs special routines to establish a connection. There are MEX functions available to establish two-way communication between MATLAB and C/C++. Writing MEX functions could be tedious initially.

If one is using Python instead of MATLAB for the base code, PETSc offers interfacing with Python. There is a wrapper called `petsc4py` which can be used to use PETSc in Python environment. Additional information can be found here: https://pypi.org/project/petsc4py/.

7.7.2 Trilinos.

Trilinos: https://www.osti.gov/servlets/purl/1406843

Trilinos is a community of developers and users focused on the collaborative creation of algorithms within an object-oriented software framework for large-scale, complex multi-physics scientific and engineering problems on HPC architectures. Trilinos is organized into product suites and various packages, so that the user can choose on a job-specific basis.

For the current type of problems dealing with nonlinear ordinary differential equations, Trilinos has a combination of packages to offer. `NOX` package for Nonlinear Solver with Globalized Newton's methods and `LOCA` package for parameter continuation and bifurcation tracking. `NOX` also includes MATLAB-`fsolve` equiva-

lent trust-region dogleg and line search methods. Mathematically speaking, similar solutions should be obtained whether using MATLAB-fsolve or Trilinos-NOX package.

Trilinos:NOX & LOCA: https://trilinos.github.io/nox_and_loca.html

Since Trilinos uses C++ programming language, an user can use MEX functions available to establish two-way communication between MATLAB and C++.

Also, Trilinos offers interfacing with Python. There is a wrapper named PyTrilinos to implement Trilinos in Python environment. Additional information can be found here: https://trilinos.github.io/pytrilinos_faq.html. The optional prerequisites for PyTrilinos can be found here: https://trilinos.github.io/pytrilinos_faq.html#what-are-the-optional-prerequisites-for-pytrilinos.

7.7.3 Python.

Python programming language is a versatile programming language and is one of the most widely used across various fields today. Though with some major differences, Python is the closest to the MATLAB working and environment. Python offers NumPy and SciPy fundamental packages for scientific computing. These packages offer a collection of mathematical algorithms and convenience functions performing matrix operations.

scipy.optimize and scipy.optimize.minimize offers MATLAB-fsolve like functions. Trust-region based scipy.minimize(method='dogleg') offers exact version needed to solve the set of nonlinear ordinary differential equations.

Other useful resources on guiding MATLAB to Python interface can be found here:

- https://stackoverflow.com/questions/9845292/a-tool-to-convert-matlab-code-to-python
- https://www.enthought.com/wp-content/uploads/Enthought-MATLAB-to-Python-White-Paper.pdf
- http://mathesaurus.sourceforge.net/matlab-python-xref.pdf

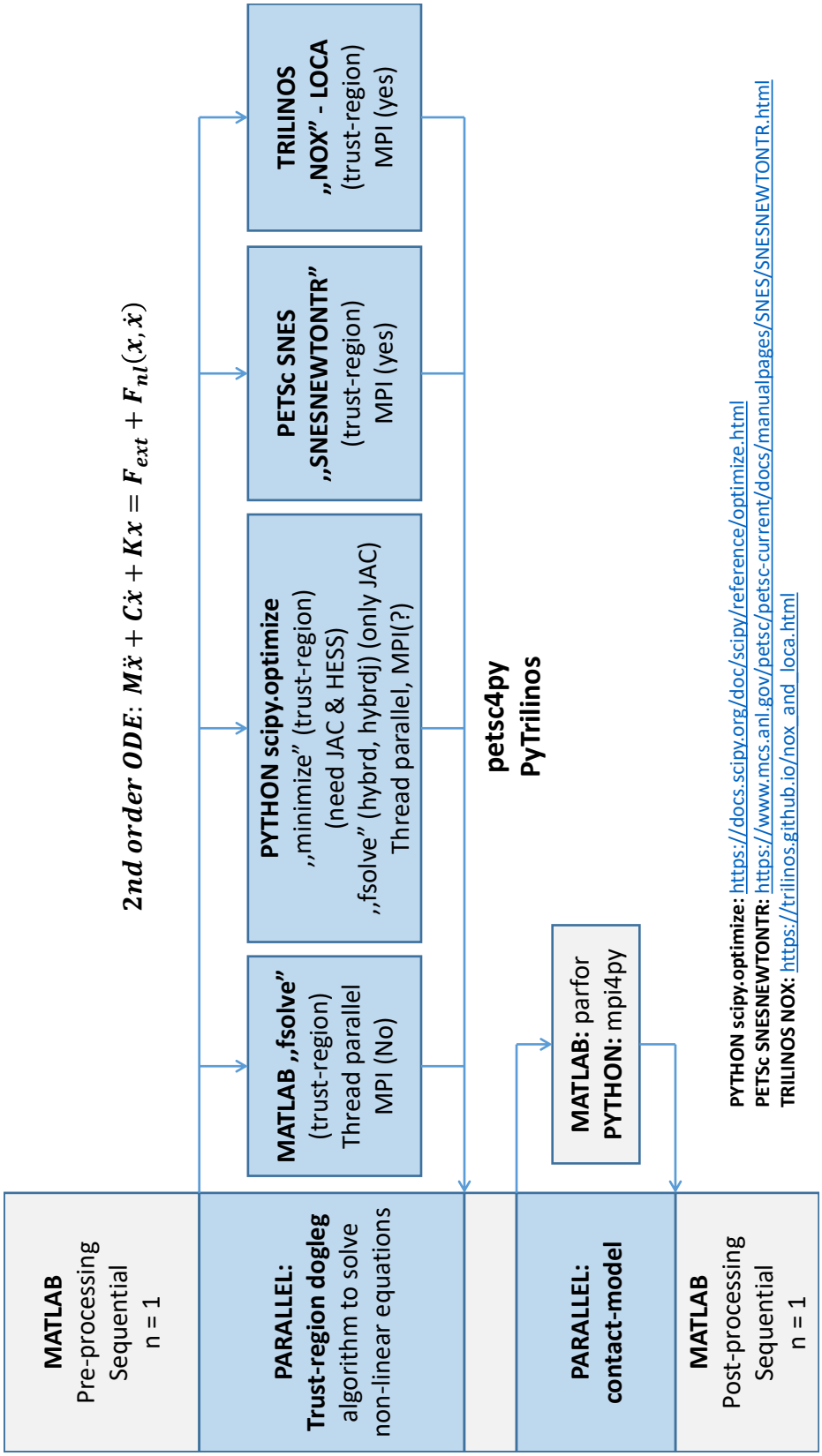

Fig. 7.6 Bird's eye view of various external packages available for parallelization.

Figure 7.6 provides a comprehensive overview to solve the nonlinear dynamic system with friction contact nonlinearity. The figure illustrates the parallelizable sections of the code-flow and various equivalent third-party options available with its features and relating programming languages.

7.8 Comments on programming languages.

- MATLAB: So far, an extensive discussion has been presented in this chapter. MATLAB is a great tool for the initial development of codes, working with features and provides extensive ready-made routines. MATLAB is also thread-parallel and can be used efficiently in a single-node system such as personal workstations. However, MATLAB is a proprietary software. To achieve maximum performance and multi-node capability, one has to use other programming languages. As an alternative to MATLAB, one can explore an equivalent open-source version called GNU-OCTAVE.

- FORTRAN: FORTRAN is one of the first programming languages developed for scientific applications. FORTRAN is still one of the fastest languages. However, writing programs in FORTRAN is not necessarily easy in comparison to MATLAB. When it comes to performance, the more a user works on the code, the faster the computation time is. This is because the user has offloaded the computer's task in giving task-specific instructions. Most of the basic array and matrices core operations used today are written in FORTRAN. So without the user being aware, the underlying core operations use FORTRAN codes routinely.

- C/C++: C/C++ is an open-source high-level programming language generally used to achieve high-performance. C/C++ is compatible with HPC systems. C/C++ needs good programming knowledge and initially takes more time to code compared to MATLAB. However, it pays off in achieving better performance and multi-node capability with minimal necessary code modifications.

- Python: Python is taking the best of both worlds of MATLAB and C/C++. Python is open-source and feels similar to MATLAB with coding and can interface with C/C++ with relative ease. Every merit comes with a trade-off too. Because of interfacing routines to access C/C++ codes, one has to accept a slight communication overhead due to time spent in interfacing,

hence hampering performance. Since Python is open-source, there is a huge repository and community building various routines to enhance performance and ease the developer's job.

To summarize, the user can use MATLAB or Python to start with the software development by playing around, feature addition and debugging for errors. Once the code has reached a stable version, for better performance one has to use C/C++. Spending some time initially in code translation could significantly save a lot of time in performing many simulations and iterations faster. Eventually, a clearly defined goal and expectations will help make better decisions on the choice of programming language and external packages.

7.9 Summary.

In this chapter, an introduction to HPC systems was made with a MATLAB user point of view to perform a numerical dynamic simulation of a generic system. The chapter covered the basics of high-performance computing, example test case, the study of variables affecting HBM simulation, challenges and opportunities. The chapter also briefed over various external packages and the usage of different programming languages. There is a wide scope of incorporating external packages such as PETSc, Trilinos, etc. depending on the suitable programming language. These packages can potentially speed up the simulation and reduce the computational time by many folds using multi-node distributed systems. Also, basic knowledge of HPC systems for a researcher performing numerical simulation in the dynamics field will help tackle computational bottle-necks and design software compatible with HPC systems by needing lesser modifications to the base codes. The takeaway from this chapter is MATLAB is modular and flexible for the development version of codes. However, if one has to achieve multi-node capable software and exploit the maximum performance, the super-user has to move to high-performance languages such as C, C++ or Python to an extent. The choice of the programming language and the external packages is task-specific, and this chapter could serve to make an informed choice. The bird's eye view presented with respect to nonlinear dynamic simulation and the major code-flow can be helpful if one is looking for where to start and what to focus on.

7.10 Further reading resources.

- Message Passing Interface (MPI): https://computing.llnl.gov/tutorials/mpi/
- Vectorization:https://www.mathworks.com/help/matlab/matlab_prog/vectorization.html
- Performance Application Programming Interface (PAPI): http://icl.utk.edu/papi/software/
- `PETSc` tutorial: https://www.mcs.anl.gov/petsc/meetings/2016/slides/tutorial2.pdf
- Using `PETsc` with `MATLAB`: http://web.mit.edu/tao-petsc_v3.7/petsc_manual.pdf
- `MATLAB Parallel Computing`:https://www.mathworks.com/help/parallel-computing/scale-up-parfor-loops-to-cluster-and-cloud.html
- `Python-minimize`: https://docs.scipy.org/doc/scipy/reference/generated/scipy.optimize.minimize.html
- Read MAT file in `C/C++`: https://www.mathworks.com/help/matlab/matlab_external/reading-a-mat-file-in-cc.html
- `MPI` in `Python`: https://www.nesi.org.nz/sites/default/files/mpi-in-python.pdf

Chapter 8

Conclusions

The main goal of the current work was to develop a numerical prediction tool and an experimental test rig to study the effect of fretting wear on the dynamics of structures with friction contacts. The goal with defined objectives with respect to numerical and experimental approach has been fully achieved. The brief overview and main findings of the current research will be summarized here, and future recommendations will be made.

8.1 Brief overview of the current work.

In order to break down the main goal, the focus was first laid on the numerical part - to develop a successful nonlinear solver in `MATLAB`. First, the introduction to linear vibrations was made, and a simple linear dynamic solver was developed. Since the interest is to focus on steady-state results and achieve them right away, a frequency-domain based technique - Harmonic Balance Method (HBM) was implemented. The time domain based solvers first go through the transient phase and then reach steady-state phase. This is a time-consuming path and many commercial packages can do this. The frequency-domain based solution techniques are more research focussed and hence developed in-house. Then, a friction contact nonlinearity was introduced by considering a 2D Jenkins element contact model with AFT logic to compute the nonlinear forces. To speed up even further, the analytical Jacobian formulation was also implemented. This helped to achieve multi-fold speedup, especially evident for large systems. Also, reduced order modelling (ROM) was implemented by retaining

only the necessary information for dynamic analysis by defining DOFs of interest as master nodes and retaining only a few normal modes to significantly reduce the size of the system even further. Also, a more accurate coupled static/dynamic HBM was implemented, given a better match with the accurate results of direct time integration. With this, a numerical prediction tool was born. For bladed disk systems, cyclic symmetry boundary conditions were implemented. Regarding wear modelling, a wear energy approach was chosen for its combination of simplicity and accuracy, and an adaptive wear logic was defined to accelerate wear. Now a prediction tool with coupled forced response dynamics with fretting wear was ready.

The developed prediction tool was used on two numerical test cases. The first test case was a simple cantilever beam with a known friction contact patch on the free end. The beam was excited with an external harmonic force and the contact loaded with a static preload and simulated until full loss of contact. The contact interface evolution results were presented along with the effect on the forced response dynamics. The results also included a user-defined parameter to accelerate wear, and the impact of the choice of parameter on the accuracy of the results and computational time needed was briefed. The second test case chosen was a more realistic turbine bladed disk with a shroud contact. The fretting wear experienced at the shroud contacts was modelled, and the numerical prediction results were presented.

Moving on to the experimental part: simultaneously, a novel experimental test rig was being designed. The goal was to simulate fretting wear over a large number of cycles and record the contact interface evolution and the subsequent effect on the dynamics of the system. Also, a contact loading mechanism was designed to simulate varying preload resulting due to the wear. The test rig was then manufactured, commissioned, instrumented and calibrated. Multiple full-length tests until full loss of contact were carried out. The beam was excited by an electromagnetic shaker, and a preload was applied by a contact loading mechanism. The relative displacement at the contact was recorded by a split-beam laser, and the dynamic behaviour was recorded by an accelerometer. The intermediate surface scans were done by a non-contact profilometer. All of the results were collocated and analyzed to study the evolution of contact interface, hysteresis loops, energy dissipation, variation in static preload, change in dynamic response behaviour, etc. This test rig is the first of its kind to experimentally study the effect of wear on the forced response dynamics with a changing preload. These results aid in making the nonlinear solvers and prediction tools robust by providing experimental evidence and act as a validation step.

The HBM tool was then reformulated to obtain equivalent experiment results for comparison. The real surface inputs and conditions were provided as input to perform numerical simulation using the HBM tool to study the effect of wear on the evolution of nonlinear dynamics. The obtained numerical results were compared against experimental results and validated.

In parallel, an industrial test case was used from an industrial partner. A gas turbine combustor leaf seal was analyzed for complex nonlinear dynamic response arising due to various kinematic and operating envelope and soft contact nature. The in-house HBM tool was used to perform the numerical simulations successfully. The results obtained showed an intermittent contact behaviour with softening behaviour in the nonlinear frequency range on the forced response plots. Looking closely at the individual contact states at the contact patches at the frequencies of interest shows clear stick-separation at each vibration cycle. This leads to chattering behaviour and subsequently cause wear at the contact patches.

As far as the HBM tool was concerned, a three-month secondment was carried out at HLRS Supercomputing center in Stuttgart, Germany. The idea was to improve the efficiency of the solver by optimization and vectorization, and identify the bottlenecks by using the expertise of the HPC users. The code was re-written where necessary and also done a feasibility study of various external packages and comments on the merits of different programming languages. As a long term solution, potentially writing the software in `C/C++` could improve the performance and enable it to run on multi-node capability by using existing third-party packages such as `PETSc`, `Trilinos, etc.` substantially reducing the run-time; however, it comes at the cost of having prerequisite knowledge in these tools.

8.2 Key takeaways.

- The partial or gross slip occurring at the contact interfaces of mechanical joints leads to energy dissipation, hence leading to fretting wear. The energy dissipation over a large number of cycles leads to loss of material and change the contact interface conditions.
- In this study it is shown through long-term experiments and numerical predictions that the wear affects the system dynamic response by altering the

maximum vibration levels, shift in resonant frequencies and change in damping. The wear also affects the contact conditions by changing the effective engaged contact area, contact preload, relative displacement for different forcing conditions.

- This study is intended as a proof-of-concept for methodology to demonstrate that the effect of wear on the forced response dynamics can be studied. An in-depth analysis for design and convergence may be necessary with more refined simulations and broader experimental campaigns.
- The novel test rig is the first of its kind to experimentally study the effect of wear on the forced response dynamics with changing preload caused due to wear.
- The test rig allows the possibility of experimental investigation for full range test until full loss of contact and record intermediate surface scans and the dynamic response.
- A successful demonstration of validation of numerical prediction with equivalent experimental results for wear and dynamics using the in-house HBM solver.
- This study is a full-circle attempt to numerically predict the evolution of contact interface and the dynamics along with the equivalent experimental observation and validation.

8.3 Recommendations and future works.

The current research work has a meaningful contribution to the ongoing research in the field of virtual prediction of steady-state dynamics of structures with friction contact nonlinearity and considering fretting wear. This is done by bringing together the traditionally separate fields of nonlinear vibrations and contact tribology.

Some of the following possible recommendations for further research to better understand include:

1. To focus on accurate FE modelling by tuning the models to correlate to experimental dynamic characteristics by implementing realistic boundary conditions.

2. Speed up HBM solvers to reduce the run-time by implementing numerical techniques such as Finite Element Tearing and Interconnect (FETI), Domain Decomposition Methods (DDM), substructuring, etc. to breakdown the problem into smaller chunks and distribute over multiple computing nodes.

3. Implement computationally efficient, robust solution techniques, numerical stability analysis arising due to strong nonlinear effects in the HBM solver. Especially, the coupled static/dynamic HBM approach faces convergence issues due to non-uniqueness of solution [51, 52].

4. Perform experimental test campaigns to understand the effect of combinations of static preloads and dynamic excitation, contact geometry, contact area, surface roughness, etc., to better understand the effect of wear on the dynamic response.

Lastly, there is a lot of ground to cover to fundamentally understand the nature of friction contacts and interface evolution, as wear is a multi-physics and multi-scale phenomenon. Especially with wear, multiple mechanisms are at play and accounting issues such as growing tribofilm, oxidation making surface harder, grain coarsening dramatically change the stiffness of the interface might be necessary. The intertwining of fretting wear and nonlinear dynamics, and the accuracy of numerical prediction is a function of computational resources and complexity of the models. Fundamentally, friction is still not fully understood even after over three centuries of research. One cannot simply avoid friction because:

"Friction is a necessary evil."

8.4 Dissemination work.

List of journal publications:

1. A. Fantetti, **L.R. Tamatam**, M. Volvert, I. Lawal, L. Liu, L. Salles, M.R. Brake, C.W. Schwingshackl and D. Nowell, "The impact of fretting wear on structural dynamics: Experiment and Simulation," *Tribology International*, vol. 138, pp. 111–124, 2019. URL https://doi.org/10.1016/j.triboint.2019.05.023
2. **L.R. Tamatam**, D. Botto and S. Zucca, "A novel test rig to study the effect of fretting wear on the forced response dynamics with a friction contact," *Nonlinear Dynamics*, vol. 105, pp. 1405–1426, 2021. URL https://doi.org/10.1007/s11071-021-06658-y
3. **L.R. Tamatam**, D. Botto and S. Zucca, "A coupled approach to model the effect of wear on the dynamics of the shrouded bladed disk," *International Journal of Non-Linear Mechanics*, 2020. [under-review]
4. **L.R. Tamatam**, D. Botto and S. Zucca, "Numerical validation of novel test rig results studying the effect of fretting wear on forced response dynamics using Harmonic Balance Method ," 2021. [in-progress]

List of international conference presentations as a presenter:

1. Jan-2019: *IMAC-XXXVII, Orlando, USA*:
   L.R. Tamatam et al. "A Modified Bouc-Wen Model to Identify the Impact of Wear on the Dynamics of Frictional Interfaces with Experimental Validation."
2. Feb-2019: *NODYCON2019, Rome, Italy*:
   L.R. Tamatam et al. "Effect of wear on the dynamics of structures with contact interfaces by a coupled static/dynamic multi-harmonic balance method."
3. Jul-2019: *ICSV-26, Montreal, Canada*:
   L.R. Tamatam et al. "A coupled approach to model the effect of wear on the dynamics of bladed disks."
4. Dec-2019: *IndiaTrib-2019, Bangalore, India*:
   L.R. Tamatam et al. "Modelling the effect of fretting wear on the evolution of contact stiffness: Validation with experimental results."
5. Sep-2020: *ISMA2020, Leuven, Belgium* [online]:
   L.R. Tamatam et al. "Nonlinear dynamic analysis of gas turbine combustor leaf seal."

References

[1] G. E. Aviation. GE9X Commercial Aircraft Engine, 2021. URL https://www.geaviation.com/commercial/engines/ge9x-commercial-aircraft-engine.

[2] K. W. Bushell. Jet and Gas Turbine Engines. In *Encyclopedia of Physical Science and Technology*, pages 127–152. Elsevier, jan 2003. URL https://doi.org/10.1016/b0-12-227410-5/00356-2.

[3] C. L. Proctor. Internal Combustion Engines. In *Encyclopedia of Physical Science and Technology*, pages 33–44. Elsevier, jan 2003. URL https://doi.org/10.1016/B0-12-227410-5/00350-1.

[4] D. Burnes and A. Camou. Impact of fuel composition on gas turbine engine performance. *Journal of Engineering for Gas Turbines and Power*, 141(10), oct 2019. URL https://doi.org/10.1115/1.4044238.

[5] A. V. Srinivasan. Flutter and resonant vibration characteristics of engine blades. *Journal of Engineering for Gas Turbines and Power*, 119(4):742–775, oct 1997. URL https://doi.org/10.1115/1.2817053.

[6] T. Fransson and C. Sieverding. *Aeroelasticity in axial flow turbomachines*. Von Karman Institute for Fluid Dynamics, Rhode St. Gen'ese, Belgium, may 1999. URL https://store.vki.ac.be/aeroelasticity-in-axial-flow-turbomachines.html.

[7] M. Krack, L. Salles, and F. Thouverez. Vibration Prediction of Bladed Disks Coupled by Friction Joints. *Archives of Computational Methods in Engineering*, 24(3):589–636, 2017. URL https://doi.org/10.1007/s11831-016-9183-2.

[8] W. Campbell. The Protection of Steam Turbine Disk Wheels From Axial Vibration. *ASME Transactions*, pages 31–160, 1924.

[9] M. R. Brake. *The Mechanics of Jointed Structures: Recent Research and Open Challenges for Developing Predictive Models for Structural Dynamics*. Springer International Publishing, 2017. ISBN 9783319568188. URL http://link.springer.com/10.1007/978-3-319-56818-8.

[10] C. Siewert, L. Panning, J. Wallaschek, and C. Richter. Multiharmonic forced response analysis of a turbine blading coupled by nonlinear contact forces. *Journal of Engineering for Gas Turbines and Power*, 132(8):082501,

2010. URL http://gasturbinespower.asmedigitalcollection.asme.org/article.aspx?articleid=1475129.

[11] C. Xu, D. Li, M. M. Gola, and C. Gastaldi. A Comparison of Two Microslip Contact Models for Studying the Mechanics of Underplatform Dampers. In *Proceedings of the ASME Turbo Expo*. ASME International, jun 2018. URL https://doi.org/10.1115/gt2018-76007.

[12] D. Li, C. Xu, M. Gola, and D. Botto. Reduced-Order Modeling Friction for Line Contact in a Turbine Blade Damper System. In *Nonlinear Dynamics and Control*, pages 197–205. Springer International Publishing, 2020. URL https://doi.org/10.1007/978-3-030-34747-5_20.

[13] A. I. Vakis, V. A. Yastrebov, J. Scheibert, L. Nicola, D. Dini, C. Minfray, A. Almqvist, M. Paggi, S. Lee, G. Limbert, J. F. Molinari, G. Anciaux, R. Aghababaei, S. Echeverri Restrepo, A. Papangelo, A. Cammarata, P. Nicolini, C. Putignano, G. Carbone, S. Stupkiewicz, J. Lengiewicz, G. Costagliola, F. Bosia, R. Guarino, N. M. Pugno, M. H. Müser, and M. Ciavarella. Modeling and simulation in tribology across scales: An overview. *Tribology International*, 125:169–199, 2018. URL https://doi.org/10.1016/j.triboint.2018.02.005.

[14] O. Vingsbo and S. Söderberg. On fretting maps. *Wear*, 126(2):131–147, sep 1988. URL https://doi.org/10.1016/0043-1648(88)90134-2.

[15] S. R. Pearson and P. H. Shipway. Is the wear coefficient dependent upon slip amplitude in fretting? Vingsbo and Söderberg revisited. *Wear*, 330-331: 93–102, may 2015. URL https://doi.org/10.1016/j.wear.2014.11.005.

[16] P. Arnaud, S. Fouvry, and S. Garcin. A numerical simulation of fretting wear profile taking account of the evolution of third body layer. *Wear*, 376-377: 1475–1488, 2017. URL http://dx.doi.org/10.1016/j.wear.2017.01.063.

[17] A. Dreano, S. Fouvry, and G. Guillonneau. Understanding and formalization of the fretting-wear behavior of a cobalt-based alloy at high temperature. *Wear*, 452-453:203297, jul 2020. URL https://doi.org/10.1016/j.wear.2020.203297.

[18] J. F. Archard. Contact and rubbing of flat surfaces. *Journal of Applied Physics*, 24(8):981–988, 1953. URL https://doi.org/10.1063/1.1721448.

[19] R. B. Waterhouse. Fretting wear. *Wear*, 100(1-3):107–118, 1984. URL https://doi.org/10.1016/0043-1648(84)90008-5.

[20] D. Li, D. Botto, C. Xu, and M. Gola. Fretting wear of bolted joint interfaces. *Wear*, 458-459:203411, oct 2020. URL https://doi.org/10.1016/j.wear.2020.203411.

[21] M. Paggi and D. Hills. *Modeling and Simulation of Tribological Problems in Technology*, volume 593 of *CISM International Centre for Mechanical Sciences*. Springer International Publishing, 2020. ISBN 978-3-030-20376-4. URL http://link.springer.com/10.1007/978-3-030-20377-1.

[22] MSR. Turbines welding - reblading, 2020. URL https://mservicerepairs.eu/turbines-welding-reblading/.

[23] A. Fantetti, L. R. Tamatam, M. Volvert, I. Lawal, L. Liu, L. Salles, M. R. Brake, C. W. Schwingshackl, and D. Nowell. The impact of fretting wear on structural dynamics: Experiment and Simulation. *Tribology International*, 138:111–124, 2019. URL https://doi.org/10.1016/j.triboint.2019.05.023.

[24] R. Lacayo, L. Pesaresi, J. Groß, D. Fochler, J. Armand, L. Salles, C. Schwingshackl, M. Allen, and M. R. Brake. Nonlinear modeling of structures with bolted joints: A comparison of two approaches based on a time-domain and frequency-domain solver. *Mechanical Systems and Signal Processing*, 114: 413–438, 2019. URL https://doi.org/10.1016/j.ymssp.2018.05.033.

[25] N. M. Newmark. A Method of Computation for Structural Dynamics. *Journal of the Engineering Mechanics Division*, 85(3):67–94, jul 1959. URL http://ascelibrary.org/doi/10.1061/JMCEA3.0000098.

[26] M. Krack and J. Gross. *Harmonic Balance for Nonlinear Vibration Problems*. Springer, 2019. ISBN 9783030140229. URL https://link.springer.com/book/10.1007/978-3-030-14023-6.

[27] S. Narayanan and P. Sekar. A frequency domain based numeric-analytical method for non-linear dynamical systems. *Journal of Sound and Vibration*, 211(3):409–424, apr 1998. URL https://doi.org/10.1006/jsvi.1997.1319.

[28] S. Nacivet, C. Pierre, F. Thouverez, and L. Jezequel. A dynamic Lagrangian frequency-time method for the vibration of dry-friction-damped systems. *Journal of Sound and Vibration*, 265(1):201–219, 2003. URL https://doi.org/10.1016/S0022-460X(02)01447-5.

[29] E. P. Petrov and D. J. Ewins. Analytical formulation of friction interface elements for analysis of nonlinear multi-harmonic vibrations of bladed disks. *Journal of Turbomachinery*, 125(2):364–371, 2003. URL http://turbomachinery.asmedigitalcollection.asme.org/article.aspx?articleid=1466592.

[30] C. M. Firrone, S. Zucca, and M. Gola. Effect of static/dynamic coupling on the forced response of turbine bladed disks with underplatform dampers. *Proceedings of the ASME Turbo Expo*, 6(PART A):429–440, 2009. URL https://doi.org/10.1115/GT2009-59905.

[31] C. M. Firrone and S. Zucca. Modelling Friction Contacts in Structural Dynamics and its Application to Turbine Bladed Disks. In P. J. Awrejcewicz, editor, *Numerical Analysis - Theory and Application*, chapter 14, pages 301–334. InTech, 2011. URL http://dx.doi.org/10.5772/intechopen.68547.

[32] S. Zucca, C. M. Firrone, and M. Gola. Modeling underplatform dampers for turbine blades: A refined approach in the frequency domain. *JVC/Journal of*

Vibration and Control, 19(7):1087–1102, 2013. URL https://doi.org/10.1177/1077546312440809.

[33] M. Afzal. *Numerical modelling and analysis of friction contact for turbine blades*. Licentiate thesis, KTH Royal Institute of Technology, Stockholm, 2015. URL http://kth.diva-portal.org/smash/get/diva2:875038/FULLTEXT01.pdf.

[34] C. Gastaldi, A. Fantetti, and T. M. Berruti. Forced response prediction of turbine blades with flexible dampers: The impact of engineering modelling choices. *Applied Sciences (Switzerland)*, 8(1), 2017. URL https://doi.org/10.3390/app8010034.

[35] S. Zucca, C. M. Firrone, and C. Gastaldi. Models and Methods for the Dynamics of Mechanical Components With Contact Interfaces, 2017.

[36] M. Afzal. *On efficient and adaptive modelling of friction damping in bladed disks*. PhD thesis, KTH Royal Institute of Technology, Stockholm, 2017. URL https://www.diva-portal.org/smash/get/diva2:1080367/FULLTEXT01.pdf.

[37] L. Pesaresi, J. Armand, C. W. Schwingshackl, L. Salles, and C. Wong. An advanced underplatform damper modelling approach based on a microslip contact model. *Journal of Sound and Vibration*, 436:327–340, 2018. URL https://doi.org/10.1016/j.jsv.2018.08.014.

[38] M. Krack. Nonlinear modal analysis of nonconservative systems: Extension of the periodic motion concept. *Computers and Structures*, 154:59–71, jul 2015. URL https://doi.org/10.1016/j.compstruc.2015.03.008.

[39] M. Jahn, M. Stender, S. Tatzko, N. Hoffmann, A. Grolet, and J. Wallaschek. The extended periodic motion concept for fast limit cycle detection of self-excited systems. *Computers and Structures*, 227:106139, jan 2020. URL https://doi.org/10.1016/j.compstruc.2019.106139.

[40] R. J. Kuether and M. S. Allen. Computing nonlinear normal modes using numerical continuation and force appropriation. In *Proceedings of the ASME Design Engineering Technical Conference*, volume 1, pages 329–340. American Society of Mechanical Engineers Digital Collection, sep 2012. URL https://doi.org/10.1115/DETC2012-71257.

[41] H. Festjens, G. Chevallier, and J. L. Dion. A numerical tool for the design of assembled structures under dynamic loads. *International Journal of Mechanical Sciences*, 75:170–177, oct 2013. URL https://doi.org/10.1016/j.ijmecsci.2013.06.013.

[42] N. N. Balaji and M. R. Brake. A quasi-static non-linear modal analysis procedure extending Rayleigh quotient stationarity for non-conservative dynamical systems. *Computers and Structures*, 230:106184, apr 2020. URL https://doi.org/10.1016/j.compstruc.2019.106184.

[43] M. Umer and D. Botto. Measurement of contact parameters on under-platform dampers coupled with blade dynamics. *International Journal of Mechanical Sciences*, 159:450–458, aug 2019. URL https://doi.org/10.1016/j.ijmecsci.2019.06.010.

[44] M. Umer, C. Gastaldi, and D. Botto. Friction damping and forced-response of vibrating structures: An insight into model validation. *International Journal of Solids and Structures*, 202:521–531, oct 2020. URL https://doi.org/10.1016/j.ijsolstr.2020.07.002.

[45] A. Fantetti and C. Schwingshackl. Effect of friction on the structural dynamics of built-up structures: An experimental study. In *Proceedings of the ASME Turbo Expo*, volume 11. ASME International, sep 2020. URL https://doi.org/10.1115/GT2020-14945.

[46] D. Li, D. Botto, C. Xu, T. Liu, and M. Gola. A micro-slip friction modeling approach and its application in underplatform damper kinematics. *International Journal of Mechanical Sciences*, 161-162:105029, oct 2019. URL https://doi.org/10.1016/j.ijmecsci.2019.105029.

[47] D. Li, C. Xu, D. Botto, Z. Zhang, and M. Gola. A fretting test apparatus for measuring friction hysteresis of bolted joints. *Tribology International*, 151, nov 2020. URL https://doi.org/10.1016/j.triboint.2020.106431.

[48] L. Pesaresi, A. Fantetti, F. Cegla, L. Salles, and C. W. Schwingshackl. On the Use of Ultrasound Waves to Monitor the Local Dynamics of Friction Joints. *Experimental Mechanics*, 60(1):129–141, jan 2020. URL https://doi.org/10.1007/s11340-019-00550-y.

[49] C. M. Firrone, S. Zucca, and M. M. Gola. The effect of underplatform dampers on the forced response of bladed disks by a coupled static/dynamic harmonic balance method. *International Journal of Non-Linear Mechanics*, 46(2):363–375, 2011. URL http://dx.doi.org/10.1016/j.ijnonlinmec.2010.10.001.

[50] S. Zucca and C. M. Firrone. Nonlinear dynamics of mechanical systems with friction contacts: Coupled static and dynamic Multi-Harmonic Balance Method and multiple solutions. *Journal of Sound and Vibration*, 333(3):916–926, 2014. URL https://doi.org/10.1016/j.jsv.2013.09.032.

[51] E. Ferhatoglu and S. Zucca. Determination of periodic response limits among multiple solutions for mechanical systems with wedge dampers. *Journal of Sound and Vibration*, 494:115900, mar 2021. URL https://doi.org/10.1016/j.jsv.2020.115900.

[52] E. Ferhatoglu and S. Zucca. On the non-uniqueness of friction forces and the systematic computation of dynamic response boundaries for turbine bladed disks with contacts. *Mechanical Systems and Signal Processing*, 160:107917, nov 2021. URL https://linkinghub.elsevier.com/retrieve/pii/S0888327021003125.

[53] P. J. Gray and C. T. McCarthy. A global bolted joint model for finite element analysis of load distributions in multi-bolt composite joints. *Composites Part B: Engineering*, 41(4):317–325, jun 2010. URL https://doi.org/10.1016/j.compositesb.2010.03.001.

[54] J. Kim, J. C. Yoon, and B. S. Kang. Finite element analysis and modeling of structure with bolted joints. *Applied Mathematical Modelling*, 31(5):895–911, may 2007. URL https://doi.org/10.1016/j.apm.2006.03.020.

[55] D. Li, D. Botto, C. Xu, and M. Gola. A new approach for the determination of the Iwan density function in modeling friction contact. *International Journal of Mechanical Sciences*, 180:105671, aug 2020. URL https://doi.org/10.1016/j.ijmecsci.2020.105671.

[56] D. Li, C. Xu, T. Liu, M. M. Gola, and L. Wen. A modified IWAN model for micro-slip in the context of dampers for turbine blade dynamics. *Mechanical Systems and Signal Processing*, 121:14–30, apr 2019. URL https://doi.org/10.1016/j.ymssp.2018.11.002.

[57] V. N. Kaliakin and J. Li. Insight into deficiencies associated with commonly used zero-thickness interface elements. *Computers and Geotechnics*, 17(2):225–252, jan 1995. URL https://doi.org/10.1016/0266-352X(95)93870-O.

[58] J. H. Griffin. Friction damping of resonant stresses in gas turbine engine airfoils. *Journal of Engineering for Gas Turbines and Power*, 102(2):329–333, 1980. URL http://dx.doi.org/10.1115/1.3230256.

[59] K. Y. Sanliturk and D. J. Ewins. Modelling two-dimensional friction contact and its application using Harmonic balance method. *Journal of Sound and Vibration*, 193(2):511–523, 1996. URL http://www.sciencedirect.com/science/article/pii/S0022460X96902990.

[60] W. D. Iwan. A distributed-element model for hysteresis and its steady-state dynamic response. *Journal of Applied Mechanics, Transactions ASME*, 33(4):893–900, 1964. URL http://appliedmechanics.asmedigitalcollection.asme.org/article.aspx?articleid=1397974.

[61] D. J. Segalman. A four-parameter Iwan model for lap-type joints. *Journal of Applied Mechanics, Transactions ASME*, 72(5):752–760, 2005. URL https://doi.org/10.1115/1.1989354.

[62] D. J. Segalman. Modelling joint friction in structural dynamics. *Structural Control and Health Monitoring*, 13(1):430–453, jan 2006. URL http://doi.wiley.com/10.1002/stc.119.

[63] M. Ismail, F. Ikhouane, and J. Rodellar. The hysteresis Bouc-Wen model, a survey. *Archives of Computational Methods in Engineering*, 16(2):161–188, 2009. URL https://doi.org/10.1007/s11831-009-9031-8.

[64] E. P. Petrov and D. J. Ewins. State-of-the-art dynamic analysis for non-linear gas turbine structures. *Proceedings of the Institution of Mechanical Engineers, Part G: Journal of Aerospace Engineering*, 218(3):199–211, mar 2004. URL https://doi.org/10.1243/0954410041872906.

[65] A. Rizvi, C. W. Smith, R. Rajasekaran, and K. E. Evans. Dynamics of dry friction damping in gas turbines: Literature survey. *JVC/Journal of Vibration and Control*, 22(1):296–305, jan 2016. URL http://journals.sagepub.com/doi/10.1177/1077546313513051.

[66] G. M. Jenkins. Analysis of the stress-strain relationships in reactor grade graphite. *British Journal of Applied Physics*, 13(1):30–32, 1962. URL https://doi.org/10.1088/0508-3443/13/1/307.

[67] E. Cigeroglu, W. Lu, and C. H. Menq. One-dimensional dynamic microslip friction model. *Journal of Sound and Vibration*, 292(3-5):881–898, may 2006. URL https://doi.org/10.1016/j.jsv.2005.09.019.

[68] W. Sextro, K. Popp, and I. Wolter. Improved reliability of bladed disks due to friction dampers. In *Proceedings of the ASME Turbo Expo*, volume 4. American Society of Mechanical Engineers (ASME), dec 1997. URL https://doi.org/10.1115/97-GT-189.

[69] B. D. Yang, M. L. Chu, and C. H. Menq. Stick-slip-separation analysis and non-linear stiffness and damping characterization of friction contacts having variable normal load. *Journal of Sound and Vibration*, 210(4):461–481, mar 1998. URL https://doi.org/10.1006/jsvi.1997.1305.

[70] B. D. Yang and C. H. Menq. Characterization of 3D Contact Kinematics and Prediction of Resonant Response of Structures Having 3D Frictional Constraint. *Journal of Sound and Vibration*, 217(5):909–925, 1998. URL https://doi.org/10.1006/jsvi.1998.1802.

[71] J. J. Chen, B. D. Yang, and C. H. Menq. Periodic forced response of structures having three-dimensional frictional constraints. *Journal of Sound and Vibration*, 229(4):775–792, jan 2000. URL https://doi.org/10.1006/jsvi.1999.2397.

[72] K. Popp, L. Panning, and W. Sextro. Vibration damping by friction forces: Theory and applications. *JVC/Journal of Vibration and Control*, 9(3-4):419–448, mar 2003. URL http://journals.sagepub.com/doi/10.1177/107754603030780.

[73] M. Afzal, I. Lopez Arteaga, and L. Kari. An analytical calculation of the Jacobian matrix for 3D friction contact model applied to turbine blade shroud contact. *Computers and Structures*, 177:204–217, 2016. URL https://doi.org/10.1016/10.1016/j.compstruc.2016.08.014.

[74] M. Afzal, I. Lopez Arteaga, and L. Kari. Numerical analysis of multiple friction contacts in bladed disks. *International Journal of Mechanical Sciences*, 137:224–237, 2018. URL https://doi.org/10.1016/j.ijmecsci.2018.01.016.

[75] M. R. Brake. A reduced Iwan model that includes pinning for bolted joint mechanics. *Nonlinear Dynamics*, 87(2):1335–1349, 2017. URL https://doi.org/10.1007/s11071-016-3117-2.

[76] R. Bouc. A Mathematical Model for Hysteresis. *Acustica*, 24(1):16–25, 1971.

[77] Y.-K. Wen. Method for Random Vibration of Vibrating System. *Nanotechnology*, 8287:142–145, 1976. URL https://doi.org/10.1002/mop.

[78] K. Valanis. Fundamental consequences of a new intrinsic time measure. Plasticity as a limit of the endochronic theory. *Archives of Mechanics*, 32: 1–68, apr 1978. URL https://apps.dtic.mil/sti/citations/ADA302661.

[79] C. C. de Wit, P. Lischinsky, K. J. Åström, and H. Olsson. A New Model for Control of Systems with Friction. *IEEE Transactions on Automatic Control*, 40(3):419–425, 1995. URL http://doi.org/10.1109/9.376053.

[80] P. R. Dahl. Solid friction damping of mechanical vibrations. *AIAA Journal*, 14(12):1675–1682, may 1976. URL https://arc.aiaa.org/doi/abs/10.2514/3.61511.

[81] B. D. Yang and C. H. Menq. Characterization of contact kinematics and application to the design of wedge dampers in turbomachinery blading: Part 1-stick-slip contact kinematics. *Journal of Engineering for Gas Turbines and Power*, 120(2):410–417, apr 1998. URL http://doi.org/10.1115/1.2818138.

[82] B. D. Yang and C. H. Menq. Characterization of contact kinematics and application to the design of wedge dampers in turbomachinery blading: Part 2-Prediction of forced response and experimental verification. *Journal of Engineering for Gas Turbines and Power*, 120(2):418–423, apr 1998. URL http://doi.org/10.1115/1.2818139.

[83] M. H. Jareland and G. Csaba. Friction damper mistuning of a bladed disk and optimization with respect to wear. In *Proceedings of the ASME Turbo Expo*, volume 4. American Society of Mechanical Engineers (ASME), aug 2000. URL https://doi.org/10.1115/2000-GT-0363.

[84] C. H. Menq, J. Bielak, and J. H. Griffin. The influence of microslip on vibratory response, part I: A new microslip model. *Journal of Sound and Vibration*, 107(2):279–293, jun 1986. URL https://www.sciencedirect.com/science/article/pii/0022460X86902385.

[85] D. Li and C. Xu. Modelling of Mechanical Systems With Friction Interfaces Considering Variable Normal Contact Load and Tangential Micro/Macro Slip. In *Proceedings of the ASME International Mechanical Engineering Congress and Exposition*. ASME International, nov 2016. URL https://doi.org/10.1115/IMECE2016-65995.

[86] D. Wang, C. Xu, X. Fan, and Q. Wan. Reduced-order modeling approach for frictional stick-slip behaviors of joint interface. *Mechanical Systems and Signal Processing*, 103:131–138, mar 2018. URL https://doi.org/10.1016/j.ymssp.2017.10.001.

[87] D. Li, C. Xu, J. Kang, and Z. Zhang. Modeling tangential friction based on contact pressure distribution for predicting dynamic responses of bolted joint structures. *Nonlinear Dynamics*, 101(1):255–269, jul 2020. URL https://doi.org/10.1007/s11071-020-05765-6.

[88] S. Catalfamo, S. A. Smith, F. Morlock, M. R. Brake, P. Reuß, C. W. Schwingshackl, and W. D. Zhu. Effects of experimental methods on the measurements of a nonlinear structure. In *Conference Proceedings of the Society for Experimental Mechanics Series*, volume 4, pages 491–500. Springer New York LLC, 2016. URL https://link.springer.com/chapter/10.1007/978-3-319-29763-7_48.

[89] T. Dossogne, T. W. Jerome, D. P. Lancereau, S. A. Smith, M. R. Brake, B. R. Pacini, P. Reuß, and C. W. Schwingshackl. Experimental assessment of the influence of interface geometries on structural dynamic response. In *Conference Proceedings of the Society for Experimental Mechanics Series*, pages 255–261. Springer New York LLC, 2017. URL https://link.springer.com/chapter/10.1007/978-3-319-54930-9_22.

[90] M. R. Brake, C. W. Schwingshackl, and P. Reuß. Observations of variability and repeatability in jointed structures. *Mechanical Systems and Signal Processing*, 129:282–307, aug 2019. URL https://doi.org/10.1016/j.ymssp.2019.04.020.

[91] A. T. Mathis, N. N. Balaji, R. J. Kuether, A. R. Brink, M. R. Brake, and D. D. Quinn. A Review of Damping Models for Structures with Mechanical Joints. *Applied Mechanics Reviews*, 72(4), jul 2020. URL https://doi.org/10.1115/1.4047707.

[92] M. R. Brake, J. G. Stark, S. A. Smith, D. P. Lancereau, T. W. Jerome, and T. Dossogne. In situ measurements of contact pressure for jointed interfaces during dynamic loading experiments. In *Conference Proceedings of the Society for Experimental Mechanics Series*, pages 133–141. Springer New York LLC, 2017. URL https://link.springer.com/chapter/10.1007/978-3-319-54930-9_13.

[93] M. Brøns, T. A. Kasper, G. Chauda, S. W. Klaassen, C. W. Schwingshackl, and M. R. Brake. Experimental investigation of local dynamics in a bolted lap joint using digital image correlation. *Journal of Vibration and Acoustics, Transactions of the ASME*, 142(5), oct 2020. URL https://doi.org/10.1115/1.4047699.

[94] J. H. Porter, C. R. Little, N. N. Balaji, and M. R. Brake. An assessment of the applicability and epistemic uncertainties inherent to different classes of friction

models for modeling bolted interfaces. In *Conference Proceedings of the Society for Experimental Mechanics Series*, pages 291–294. Springer, 2021. URL https://link.springer.com/chapter/10.1007/978-3-030-47626-7_42.

[95] N. N. Balaji and M. R. Brake. The surrogate system hypothesis for joint mechanics. *Mechanical Systems and Signal Processing*, 126:42–64, jul 2019. URL https://doi.org/10.1016/j.ymssp.2019.02.013.

[96] N. N. Balaji, T. Dreher, M. Krack, and M. R. Brake. Hyper-reduction approaches for contact modeling with small tangential displacements: Applications for a bolted joint. In *Conference Proceedings of the Society for Experimental Mechanics Series*, pages 295–299. Springer, 2021. URL https://link.springer.com/chapter/10.1007/978-3-030-47626-7_43.

[97] N. N. Balaji, T. Dreher, M. Krack, and M. R. Brake. Reduced order modeling for the dynamics of jointed structures through hyper-reduced interface representation. *Mechanical Systems and Signal Processing*, 149:107249, feb 2021. URL https://doi.org/10.1016/j.ymssp.2020.107249.

[98] D. Botto and M. Lavella. High temperature tribological study of cobalt-based coatings reinforced with different percentages of alumina. *Wear*, 318(1-2): 89–97, 2014. URL http://dx.doi.org/10.1016/j.wear.2014.06.024.

[99] K. L. Johnson. *Contact Mechanics*. Cambridge University Press, Cambridge, 1989. ISBN 0521347963. URL http://ebooks.cambridge.org/ref/id/CBO9781139171731.

[100] J. Jäger. A New Principle in Contact Mechanics. *Journal of Tribology*, 120 (4):677–684, 1998. URL http://doi.org/10.1115/1.2833765.

[101] M. Ciavarella, D. A. Hills, and G. Monno. The influence of rounded edges on indentation by a flat punch. *Proceedings of the Institution of Mechanical Engineers, Part C: Journal of Mechanical Engineering Science*, 212(4):319–327, 1998. URL http://doi.org/10.1243/0954406981521259.

[102] M. Allara. *Experimental and numerical investigation of friction damping in blade root joints of bladed disks*. PhD thesis, Politecnico di Torino, Italy, 2007.

[103] M. Allara. A model for the characterization of friction contacts in turbine blades. *Journal of Sound and Vibration*, 320(3):527–544, 2009. URL http://doi.org/10.1016/j.jsv.2008.08.016.

[104] H. Andresen, D. A. Hills, and J. Vázquez. Closed-form solutions for tilted three-part piecewise-quadratic half-plane contacts. *International Journal of Mechanical Sciences*, 150:127–134, jan 2019. URL http://doi.org/10.1016/j.ijmecsci.2018.09.024.

[105] H. Andresen, D. A. Hills, J. R. Barber, and J. Vázquez. Frictional half-plane contact problems subject to alternating normal and shear loads and tension in the steady state. *International Journal of Solids and Structures*, 168:166–171, aug 2019. URL https://www.sciencedirect.com/science/article/abs/pii/S0020768319301490.

[106] H. Andresen, D. A. Hills, J. R. Barber, and J. Vázquez. Steady state cyclic behaviour of a half-plane contact in partial slip subject to varying normal load, moment, shear load, and moderate differential bulk tension. *International Journal of Solids and Structures*, 182-183:156–161, jan 2020. URL https://www.sciencedirect.com/science/article/abs/pii/S0020768319303476.

[107] G. Chauda and D. J. Segalman. Two-dimensional contact analysis using trigonometric polynomials: Some early verification problems. In *Proceedings of the ASME Design Engineering Technical Conference*, volume 8. American Society of Mechanical Engineers (ASME), nov 2018. URL http://doi.org/10.1115/DETC2018-86099.

[108] G. Chauda and D. J. Segalman. A First Violation Contact Algorithm that Correctly Captures History Dependence. *International Journal of Mechanical Sciences*, 198:106375, may 2021. URL http://doi.org/10.1016/j.ijmecsci.2021.106375.

[109] D. Botto and M. Lavella. A numerical method to solve the normal and tangential contact problem of elastic bodies. *Wear*, 330-331:629–635, may 2015. URL http://dx.doi.org/10.1016/j.wear.2015.02.046.

[110] L. Ciuffreda. Dynamics simulations of fretting wear for aero-engine applications. Master's thesis, Politecnico di Torino, Torino, Apr 2020. URL https://webthesis.biblio.polito.it/14294/.

[111] J. Armand, L. Salles, and C. W. Schwingshackl. Numerical simulation of partial slip contact using a semi-Analytical method. *Proceedings of the ASME Design Engineering Technical Conference*, 8:1–8, 2015. URL http://doi.org/10.1115/DETC201546464.

[112] H. C. Meng and K. C. Ludema. Wear models and predictive equations: their form and content. *Wear*, 181-183(PART 2):443–457, 1995. URL https://doi.org/10.1016/0043-1648(95)90158-2.

[113] J. Archard and W. Hirst. The wear of metals under unlubricated conditions. *Proceedings of the Royal Society of London. Series A. Mathematical and Physical Sciences*, 236(1206):397–410, aug 1956. URL https://doi.org/10.1098/rspa.1956.0144.

[114] E. Rabinowicz. *Friction and Wear of Materials*. Wiley, 2nd edition edition, 1965. URL https://www.wiley.com/en-us/Friction+and+Wear+of+Materials%2C+2nd+Edition-p-9780471830849.

[115] B. E. Klamecki. Wear - an entropy production model. *Wear*, 58(2):325–330, feb 1980. URL https://doi.org/10.1016/0043-1648(80)90161-1.

[116] K. L. Doelling, F. F. Ling, M. D. Bryant, and B. P. Heilman. An experimental study of the correlation between wear and entropy flow in machinery components. *Journal of Applied Physics*, 88(5):2999–3003, sep 2000. URL http://aip.scitation.org/doi/10.1063/1.1287778.

[117] F. F. Ling, M. D. Bryant, and K. L. Doelling. On irreversible thermodynamics for wear prediction. *Wear*, 253(11-12):1165–1172, dec 2002. URL https://doi.org/10.1016/S0043-1648(02)00241-7.

[118] A. Zmitrowicz. A thermodynamical model of contact, friction and wear: I governing equations. *Wear*, 114(2):135–168, feb 1987. URL https://doi.org/10.1016/0043-1648(87)90086-X.

[119] M. D. Bryant, M. M. Khonsari, and F. F. Ling. On the thermodynamics of degradation. In *Proceedings of the Royal Society A: Mathematical, Physical and Engineering Sciences*, volume 464, pages 2001–2014. Royal Society, aug 2008. URL https://royalsocietypublishing.org/doi/abs/10.1098/rspa.2007.0371.

[120] M. Dragon-Louiset. On a predictive macroscopic contact-sliding wear model based on micromechanical considerations. *International Journal of Solids and Structures*, 38(9):1625–1639, feb 2001. URL https://doi.org/10.1016/S0020-7683(00)00065-2.

[121] M. Z. Huq and J. P. Celis. Expressing wear rate in sliding contacts based on dissipated energy. *Wear*, 252(5-6):375–383, 2002. URL https://doi.org/10.1016/S0043-1648(01)00867-5.

[122] S. Fouvry, T. Liskiewicz, P. Kapsa, S. Hannel, and E. Sauger. An energy description of wear mechanisms and its applications to oscillating sliding contacts. *Wear*, 255(1-6):287–298, 2003. URL https://doi.org/10.1016/S0043-1648(03)00117-0.

[123] S. Fouvry, P. Duó, and P. Perruchaut. A quantitative approach of Ti-6Al-4V fretting damage: Friction, wear and crack nucleation. *Wear*, 257(9-10):916–929, 2004. URL https://doi.org/10.1016/j.wear.2004.05.011.

[124] S. Toumi, S. Fouvry, and M. Salvia. Prediction of sliding speed and normal force effects on friction and wear rate evolution in a dry oscillating-fretting PTFE/Ti-6Al-4V contact. *Wear*, 376-377:1365–1378, 2017. URL http://dx.doi.org/10.1016/j.wear.2017.02.021.

[125] G. K. Sfantos and M. H. Aliabadi. Wear simulation using an incremental sliding Boundary Element Method. *Wear*, 260(9-10):1119–1128, 2006. URL https://doi.org/10.1016/j.wear.2005.07.020.

[126] G. K. Sfantos and M. H. Aliabadi. Application of BEM and optimization technique to wear problems. *International Journal of Solids and Structures*, 43 (11-12):3626–3642, 2006. URL https://doi.org/10.1016/j.ijsolstr.2005.09.004.

[127] J. J. O'Connor and K. L. Johnson. The role of surface asperities in transmitting tangential forces between metals. *Wear*, 6(2):118–139, 1963. URL https://doi.org/10.1016/0043-1648(63)90125-X.

[128] L. Gallego, D. Nélias, and C. Jacq. A comprehensive method to predict wear and to define the optimum geometry of fretting surfaces. *Journal of Tribology*, 128(3):476–485, 2006. URL https://doi.org/10.1115/1.2194917.

[129] M. Lavella and D. Botto. Fretting wear characterization by point contact of nickel superalloy interfaces. *Wear*, 271(9-10):1543–1551, 2011. URL http://dx.doi.org/10.1016/j.wear.2011.01.064.

[130] D. Botto, M. Lavella, and M. M. Gola. Test rig for extraction of the contact parameters for plane on plane contact. *Proceedings of the ASME Design Engineering Technical Conference*, 1(PARTS A AND B):417–422, 2012. URL https://doi.org/10.1115/DETC2012-70950.

[131] S. Medina, D. Nowell, and D. Dini. Analytical and numerical models for tangential stiffness of rough elastic contacts. *Tribology Letters*, 49(1):103–115, 2013. URL https://doi.org/10.1007/s11249-012-0049-y.

[132] B. D. Leonard. *An experimental and numerical investigation of the effect of coatings and the third body on fretting wear*. PhD thesis, Purdue University, jan 2012. URL https://docs.lib.purdue.edu/dissertations/AAI3544276.

[133] A. E. H. Love. IX. The stress produced in a semi-infinite solid by pressure on part of the boundary. *Philosophical Transactions of the Royal Society of London. Series A, Containing Papers of a Mathematical or Physical Character*, 228(659-669):377–420, jan 1929. URL https://doi.org/10.1098/rsta.1929.0009.

[134] J. Armand. *Nonlinear dynamics of jointed structures: a multiscale approach to predict fretting wear and its effects on the dynamic response*. PhD thesis, Imperial College London, UK, 2018. URL https://spiral.imperial.ac.uk/handle/10044/1/59072.

[135] Y. Abdelaziz and A. Hamouine. A survey of the extended finite element. *Computers and Structures*, 86(11-12):1141–1151, jun 2008. URL https://doi.org/10.1016/j.compstruc.2007.11.001.

[136] M. Calamaz, J. Limido, M. Nouari, C. Espinosa, D. Coupard, M. Salaün, F. Girot, and R. Chieragatti. Toward a better understanding of tool wear effect through a comparison between experiments and SPH numerical modelling of machining hard materials. *International Journal of Refractory Metals and Hard Materials*, 27(3):595–604, may 2009. URL https://doi.org/10.1016/j.ijrmhm.2008.09.005.

[137] F. Spreng, P. Eberhard, and F. Fleissner. An approach for the coupled simulation of machining processes using multibody system and smoothed particle hydrodynamics algorithms. *Theoretical and Applied Mechanics Letters*, 3(1): 013005, jan 2013. URL https://doi.org/10.1063/2.1301305.

[138] N. Stenberg, A. Delić, and T. Björk. Using the SPH Method to Easier Predict Wear in Machining. In *Procedia CIRP*, volume 58, pages 317–322. Elsevier B.V., jan 2017. URL https://doi.org/10.1016/j.procir.2017.03.234.

[139] V. L. Popov, S. G. Psakhie, A. Gervé, B. Kehrwald, E. V. Shilko, and A. I. Dmitriev. Wear in combustion engines: experiment and simulation on the base of movable cellular automata method. *Physical Mesomechanics*, 4(4):71–80, 2001. URL mechanik.tu-berlin.de/popov/software/mca/PhysMesomWear_new.pdf.

[140] V. L. Popov and S. G. Psakhie. Numerical simulation methods in tribology. *Tribology International*, 40(6):916–923, jun 2007. URL https://doi.org/10.1016/j.triboint.2006.02.020.

[141] S. Goel, X. Luo, and R. L. Reuben. Molecular dynamics simulation model for the quantitative assessment of tool wear during single point diamond turning of cubic silicon carbide. *Computational Materials Science*, 51(1):402–408, jan 2012. URL https://doi.org/10.1016/j.commatsci.2011.07.052.

[142] J. Knudsen. *Vibro-lmpact Dynamics of Fretting Wear*. PhD thesis, Lulea University of Technology, Lulea, 2001. URL https://www.diva-portal.org/smash/get/diva2:991601/FULLTEXT01.pdf.

[143] J. Knudsen. *Some Aspects of Wear and Structural Dynamics*. PhD thesis, Lund Institute of Technology, Lund, 2005. URL https://lup.lub.lu.se/search/publication/6854f7ef-86ad-4f73-b213-e6fa76b50711.

[144] E. P. Petrov. Analysis of nonlinear vibrations upon wear-induced loss of friction dampers in tuned and mistuned bladed discs. In *Proceedings of the ASME Turbo Expo*, volume 7 A. American Society of Mechanical Engineers Digital Collection, nov 2013. URL https://doi.org/10.1115/GT2013-95566.

[145] L. Salles, L. Blanc, F. Thouverez, A. M. Gouskov, and P. Jean. Dynamic analysis of a bladed disk with friction and fretting-wear in blade attachments. *Proceedings of the ASME Turbo Expo*, 6(PART A):465–476, 2009. URL http://proceedings.asmedigitalcollection.asme.org/proceeding.aspx?articleid=1647364.

[146] L. Salles, A. M. Gouskov, L. Blanc, F. Thouverez, and P. Jean. Dynamic analysis of fretting-wear in joint interface by a multiscale harmonic balance method coupled with explicit or implicit integration schemes. *Proceedings of the ASME Turbo Expo*, 6(PARTS A AND B):1003–1013, 2010. URL https://doi.org/10.1115/GT2010-23264.

[147] L. Salles, L. Blanc, F. Thouverez, and A. M. Gouskov. Dynamic analysis of fretting-wear in friction contact interfaces. *International Journal of Solids and Structures*, 48(10):1513–1524, 2011. URL http://dx.doi.org/10.1016/j.ijsolstr.2011.01.035.

[148] L. Salles, L. Blanc, F. Thouverez, A. M. Gouskov, and P. Jean. Dual time stepping algorithms with the high order harmonic balance method for contact interfaces with fretting-wear. *Journal of Engineering for Gas Turbines and Power*, 134(3):032503–1–7, 2012. URL http://arxiv.org/abs/1405.3615%0Ahttp://dx.doi.org/10.1115/1.4004236.

[149] J. Armand, L. Pesaresi, L. Salles, and C. W. Schwingshackl. A Multiscale Approach for Nonlinear Dynamic Response Predictions with Fretting Wear. *Journal of Engineering for Gas Turbines and Power*, 139(2):1–7, 2017. URL https://doi.org/10.1115/1.4034344.

[150] J. Armand, L. Salles, C. W. Schwingshackl, D. Süß, and K. Willner. On the effects of roughness on the nonlinear dynamics of a bolted joint: A multiscale analysis. *European Journal of Mechanics, A/Solids*, 70(February):44–57, 2018. URL https://doi.org/10.1016/j.euromechsol.2018.01.005.

[151] L. R. Tamatam, D. Botto, and S. Zucca. Effect of wear on the dynamics of structures with contact interfaces by a coupled static/dynamic multi-harmonic balance method. In *First International Nonlinear Dynamics Conference. Book of abstracts*, pages 129–130, 2019.

[152] L. R. Tamatam, D. Botto, and S. Zucca. A coupled approach to model the effect of wear on the dynamics of bladed disks. In *Proceedings of the 26th International Congress on Sound and Vibration, ICSV 2019*, pages 1–8, Montreal, Canada, 2019.

[153] G. Levy. Modelling of Coulomb damping and wear of vibrating systems. *Wear*, 64(1):57–82, oct 1980. URL https://doi.org/10.1016/0043-1648(80)90094-0.

[154] M. J. Pettigrew and C. E. Taylor. Vibration analysis of shell-and-tube heat exchangers: An overview - Part 2: Vibration response, fretting-wear, guidelines. *Journal of Fluids and Structures*, 18(5):485–500, nov 2003. URL https://doi.org/10.1016/j.jfluidstructs.2003.08.008.

[155] W. Sextro. *Dynamical contact problems with friction: Models, methods, experiments and applications*. Springer Berlin Heidelberg, 2007. ISBN 3540695354. URL https://doi.org/10.1007/978-3-540-45317-8.

[156] M. Lavella, D. Botto, and M. M. Gola. Design of a high-precision, flat-on-flat fretting test apparatus with high temperature capability. *Wear*, 302(1-2):1073–1081, 2013. URL http://dx.doi.org/10.1016/j.wear.2013.01.066.

[157] C. W. Schwingshackl. Measurement of friction contact parameters for nonlinear dynamic analysis. *Conference Proceedings of the Society for Experimental Mechanics Series*, 5:167–177, 2012. URL https://doi.org/10.1007/978-1-4614-2425-3_16.

[158] R. R. Craig and M. C. Bampton. Coupling of substructures for dynamic analyses. *AIAA Journal*, 6(7):1313–1319, 1968. URL https://doi.org/10.2514/3.4741.

[159] R. H. MacNeal. A hybrid method of component mode synthesis. *Computers and Structures*, 1(4):581–601, dec 1971. URL https://doi.org/10.1016/0045-7949(71)90031-9.

[160] S. Rubin. Improved component-mode representation for structural dynamic analysis. *AIAA Journal*, 13(8):995–1006, may 1975. URL https://arc.aiaa.org/doi/abs/10.2514/3.60497.

[161] E. P. Petrov. A method for use of cyclic symmetry properties in analysis of nonlinear multiharmonic vibrations of bladed disks. *Journal of Turbomachinery*, 126(1):175–183, 2004. URL http://turbomachinery.asmedigitalcollection.asme.org/article.aspx?articleid=1466726.

[162] S. M. Pourkiaee and S. Zucca. A Reduced Order Model for Nonlinear Dynamics of Mistuned Bladed Disks with Shroud Friction Contacts. *Journal of Engineering for Gas Turbines and Power*, 141(1):011031, jan 2019. URL http://asmedigitalcollection.asme.org/gasturbinespower/article-pdf/141/1/011031/6372032/gtp_141_01_011031.pdf.

[163] T. M. Cameron and J. H. Griffin. An alternating frequency/time domain method for calculating the steady-state response of nonlinear dynamic systems. *Journal of Applied Mechanics, Transactions ASME*, 56(1):149–154, 1989. URL http://doi.org/10.1115/1.3176036.

[164] O. Poudou and C. Pierre. Hybrid frequency-time domain methods for the analysis of complex structural systems with dry friction damping. *Collection of Technical Papers - AIAA/ASME/ASCE/AHS/ASC Structures, Structural Dynamics and Materials Conference*, 1(April):111–124, 2003. URL http://arc.aiaa.org/doi/10.2514/6.2003-1411.

[165] D. Süß and K. Willner. Investigation of a jointed friction oscillator using the Multiharmonic Balance Method. *Mechanical Systems and Signal Processing*, 52-53(1):73–87, feb 2015. URL https://doi.org/10.1016/j.ymssp.2014.08.003.

[166] A. Cardona, A. Lerusse, and M. Géradin. Fast Fourier nonlinear vibration analysis. *Computational Mechanics*, 22(2):128–142, 1998. URL http://doi.org/10.1007/s004660050347.

[167] T. F. C. Chan and H. B. Keller. Arc-Length Continuation and Multigrid Techniques for Nonlinear Elliptic Eigenvalue Problems. *SIAM Journal on Scientific and Statistical Computing*, 3(2):173–194, jun 1982. URL https://doi.org/10.1137/0903012.

[168] D. Botto and M. Umer. A novel test rig to investigate under-platform damper dynamics. *Mechanical Systems and Signal Processing*, 100:344–359, 2018. URL http://dx.doi.org/10.1016/j.ymssp.2017.07.046.

[169] L. R. Tamatam, D. Botto, and S. Zucca. A novel test rig to study the effect of fretting wear on the forced response dynamics with a friction contact. *Nonlinear Dynamics*, 105(2):1405–1426, 2021. URL https://doi.org/10.1007/s11071-021-06658-y.

[170] S. Zucca, M. M. Gola, and F. Piraccini. Non-linear dynamics of steam turbine blades with shroud: Numerical analysis and experiments. In *Proceedings of the ASME Turbo Expo*, volume 6, pages 665–674. American Society of Mechanical Engineers Digital Collection, jul 2012. URL http://asmedigitalcollection.asme.org/GT/proceedings-pdf/GT2012/44724/665/2418136/665_1.pdf.

[171] J. Armand, L. Pesaresi, L. Salles, C. Wong, and C. W. Schwingshackl. A modelling approach for the nonlinear dynamics of assembled structures undergoing fretting wear. *Proceedings of the Royal Society A: Mathematical, Physical and Engineering Sciences*, 475(2223):1–20, 2019. URL https://doi.org/10.1098/rspa.2018.0731.

[172] L. R. Tamatam, D. Botto, S. Zucca, and F. Funghi. Nonlinear dynamic analysis of gas turbine combustor leaf seal. In *Proceedings of ISMA 2020 - International Conference on Noise and Vibration Engineering and USD 2020 - International Conference on Uncertainty in Structural Dynamics*, pages 2187–2202, 2020.

[173] E. Cigeroglu, N. A. C. H. An, and C. H. Menq. Forced response prediction of constrained and unconstrained structures coupled through frictional contacts. *Journal of Engineering for Gas Turbines and Power*, 131(2), 2009. URL https://doi.org/10.1115/1.2940356.

[174] W. Cunningham. An introduction to parallel programming: Openmp, sse/avx, and mpi, 2016. URL http://perimeterinstitute.ca/personal/wcunningham/parallel.pdf.

[175] G. K. Rose. *Computational Methods for Nonlinear Systems Analysis With Applications in Mathematics and Engineering*. PhD thesis, Old Dominion University, 2017. URL https://digitalcommons.odu.edu/cgi/viewcontent.cgi?article=1031&context=mae_etds.

[176] N. Matloff. *Programming on Parallel Machines: GPU, Multicore, Clusters and More*. University of California, Davis, 2012. URL http://heather.cs.ucdavis.edu/$\sim$matloff/158/PLN/ParProcBook.pdf.

[177] T. Sterling, M. Anderson, and M. Brodowicz. Chapter 6 - symmetric multiprocessor architecture. In *High Performance Computing*, pages 191–224. Morgan Kaufmann, Boston, 2018. URL https://www.sciencedirect.com/science/article/pii/B978012420158300006X.

[178] M. P. Castanier, Y. C. Tan, and C. Pierre. Characteristic constraint modes for component mode synthesis. *AIAA Journal*, 39(6):1182–1187, may 2001. URL https://arc.aiaa.org/doi/abs/10.2514/2.1433.

[179] R. J. Kuether, P. B. Coffin, and A. R. Brink. On Hurty/Craig-Bampton substructuring with interface reduction on contacting surfaces. In *Proceedings of the ASME Design Engineering Technical Conference*, volume 8. American Society of Mechanical Engineers (ASME), nov 2017. URL https://doi.org/10.1115/DETC2017-67553.

[180] D. Krattiger, L. Wu, M. Zacharczuk, M. Buck, R. J. Kuether, M. S. Allen, P. Tiso, and M. R. Brake. Interface reduction for Hurty/Craig-Bampton substructured models: Review and improvements. *Mechanical Systems and Signal Processing*, 114:579–603, jan 2019. URL https://doi.org/10.1016/j.ymssp.2018.05.031.

Appendix A

Craig-Bampton Component Mode Synthesis

This appendix briefs the methodology to perform a Craig-Bampton Component Mode Synthesis (CB-CMS) reduced order modelling technique for a generic system with a friction contact. When the finite element models are prohibitively large to perform dynamic analysis, an efficient ROM can be performed to condense the system to a small set of DOFs and retain the dynamic properties of the structure. The resulting small system can then be efficiently handled to compute the nonlinear dynamic response of the system.

An equation of motion of a structure with friction contact interfaces is written as:

$$\mathbf{M}\,\ddot{X} + \mathbf{C}\,\dot{X} + \mathbf{K}\,X = F_E + F_{NL} \tag{A.1}$$

where $\mathbf{M}, \mathbf{C}, \mathbf{K}$ are the mass, damping and stiffness matrices of the system respectively. F_E is the external force vector and F_{NL} is the nonlinear contact force vector. X represents the displacement vector.

Now, the homogeneous undamped linear system is represented as:

$$\mathbf{M}\,\ddot{X} + \mathbf{K}\,X = 0 \tag{A.2}$$

The DOFs of the system is partitioned into master DOFs (X_M) and slave DOFs (X_S). Master DOFs mostly consist of contact interface DOFs, excitation and preload

application DOFs and some accessory DOFs to record the responses. The rest are considered under slave DOFs. Usually, $N(X_M) \ll N(X_S)$.

$$X = \begin{bmatrix} X_M{}^T & X_S{}^T \end{bmatrix}^T \tag{A.3}$$

The partitioned mass and stiffness matrix into master and slave DOFs components is rewritten as:

$$\mathbf{M} = \begin{bmatrix} \mathbf{M}_{MM} & \mathbf{M}_{MS} \\ \mathbf{M}_{SM} & \mathbf{M}_{SS} \end{bmatrix}; \ \mathbf{K} = \begin{bmatrix} \mathbf{K}_{MM} & \mathbf{K}_{MS} \\ \mathbf{K}_{SM} & \mathbf{K}_{SS} \end{bmatrix} \tag{A.4}$$

In CB technique, only master DOFs are included in the reduced model as physical DOFs. The slave DOFs are replaced by a series of modal DOFs η. The displacement vector is expressed in terms of hybrid physical and modal DOFs as:

$$\begin{Bmatrix} X_M \\ X_S \end{Bmatrix} = \begin{bmatrix} \mathbf{I} & 0 \\ \Psi_C & \Phi_f \end{bmatrix} \begin{Bmatrix} X_M \\ \eta \end{Bmatrix} = \mathbf{R}_{CB} \begin{Bmatrix} X_M \\ \eta \end{Bmatrix} \tag{A.5}$$

where $\mathbf{I}$ is the identity matrix, Φ_f is the fixed interface normal mode shapes constrained at the master DOFs. $\Psi_C = -\mathbf{K}_{SS}^{-1}\mathbf{K}_{SM}$ are the static constraint modes. The static deflection shapes are computed by imposing a unit displacement at each master DOF while other master DOFs are fixed. This is repeated for each master DOF.

Using the reduction matrix $\mathbf{R}_{CB}$, the reduced mass and stiffness matrices can be obtained as:

$$\begin{aligned} \mathbf{M}_{CB} &= \mathbf{R}_{CB}{}^T \cdot \mathbf{M} \cdot \mathbf{R}_{CB} = \begin{bmatrix} \mathbf{M}_{CC} & \mathbf{M}_{Cf} \\ \mathbf{M}_{fC} & \mathbf{I} \end{bmatrix} \\ \mathbf{K}_{CB} &= \mathbf{R}_{CB}{}^T \cdot \mathbf{K} \cdot \mathbf{R}_{CB} = \begin{bmatrix} \mathbf{K}_{CC} & 0 \\ 0 & \Lambda \end{bmatrix} \end{aligned} \tag{A.6}$$

The individual partitions of $\mathbf{M}_{CB}$ and $\mathbf{K}_{CB}$ are given by:

$$\begin{aligned}
\mathbf{M}_{CC} &= \mathbf{M}_{MM} + \Psi_C^T \mathbf{M}_{SS} \Psi_C + \mathbf{M}_{MS} \Psi_C + \Psi_C^T \mathbf{M}_{SM} \\
\mathbf{M}_{Cf} &= \Phi_f^T \mathbf{M}_{SS} \Psi_C + \Phi_f^T \mathbf{M}_{SM} = \mathbf{M}_{fC}^T \\
\mathbf{K}_{CC} &= \mathbf{K}_{MM} - \mathbf{K}_{MS} \mathbf{K}_{SS}^{-1} \mathbf{K}_{SM} \\
\Lambda &= \Phi_f^T \mathbf{K}_{SS} \Phi_f
\end{aligned} \tag{A.7}$$

Similarly, the reduced external force and nonlinear contact force vectors are obtained using $\mathbf{R}_{CB}$ as:

$$\begin{aligned}
F_{E,CB} &= {\mathbf{R}_{CB}}^T \cdot F_E \\
F_{NL,CB} &= {\mathbf{R}_{CB}}^T \cdot F_{NL}
\end{aligned} \tag{A.8}$$

This set of reduced matrices corresponding to the reduced model can be used to perform the subsequent nonlinear analysis. The reduced system provides accurate results when enough normal modes are retained.

Here, only the reduction of the system corresponding to linear DOFs is presented. Sometimes, the number of interface DOFs could be so large that performing only linear DOF reduction might be insufficient. A further reduction on nonlinear DOFs can be performed to reduce the size of the system even further, for example, using the System Characteristic Constraint modes (SCC) technique. However, this method converts all remaining physical DOFs to modal DOFs, but retaining some physical DOFs are useful to apply preloads and record responses. To cater to this, there exists an expansion to SCC theory called System Level Constraint Modes Expansion (SCCe), where the system is augmented with constraint modes similar to CB method and some physical DOFs are retained. An interested reader can refer to the refs [178–180].

Appendix B

Novel forced response test rig drawings

This appendix includes 2D drawings of assembly level and component level technical drawings with various cross-sections relating to the novel forced response test rig described in Chapter 5. SolidWorks CAD software was used for 3D solid modelling and drafting.

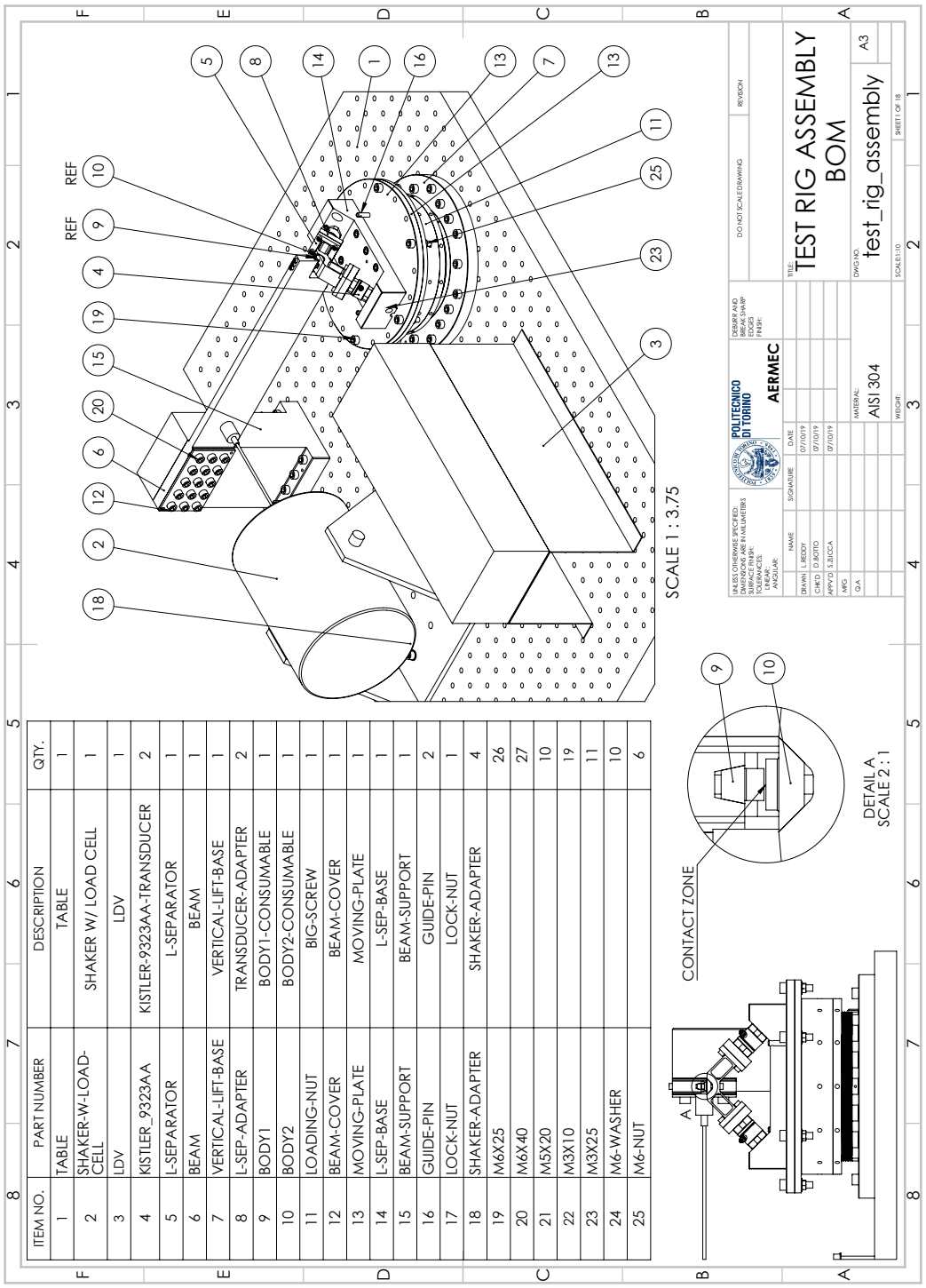

ITEM NO.	PART NUMBER	DESCRIPTION	QTY.
1	TABLE	TABLE	1
2	SHAKER-W-LOAD-CELL	SHAKER W/ LOAD CELL	1
3	LDV	LDV	1
4	KISTLER_9323AA	KISTLER-9323AA-TRANSDUCER	2
5	L-SEPARATOR	L-SEPARATOR	1
6	BEAM	BEAM	1
7	VERTICAL-LIFT-BASE	VERTICAL-LIFT-BASE	1
8	L-SEP-ADAPTER	TRANSDUCER-ADAPTER	2
9	BODY1	BODY1-CONSUMABLE	1
10	BODY2	BODY2-CONSUMABLE	1
11	LOADING-NUT	BIG-SCREW	1
12	BEAM-COVER	BEAM-COVER	1
13	MOVING-PLATE	MOVING-PLATE	1
14	L-SEP-BASE	L-SEP-BASE	1
15	BEAM-SUPPORT	BEAM-SUPPORT	1
16	GUIDE-PIN	GUIDE-PIN	2
17	LOCK-NUT	LOCK-NUT	1
18	SHAKER-ADAPTER	SHAKER-ADAPTER	4
19	M6X25		26
20	M6X40		27
21	M5X20		10
22	M3X10		19
23	M3X25		11
24	M6-WASHER		10
25	M6-NUT		6

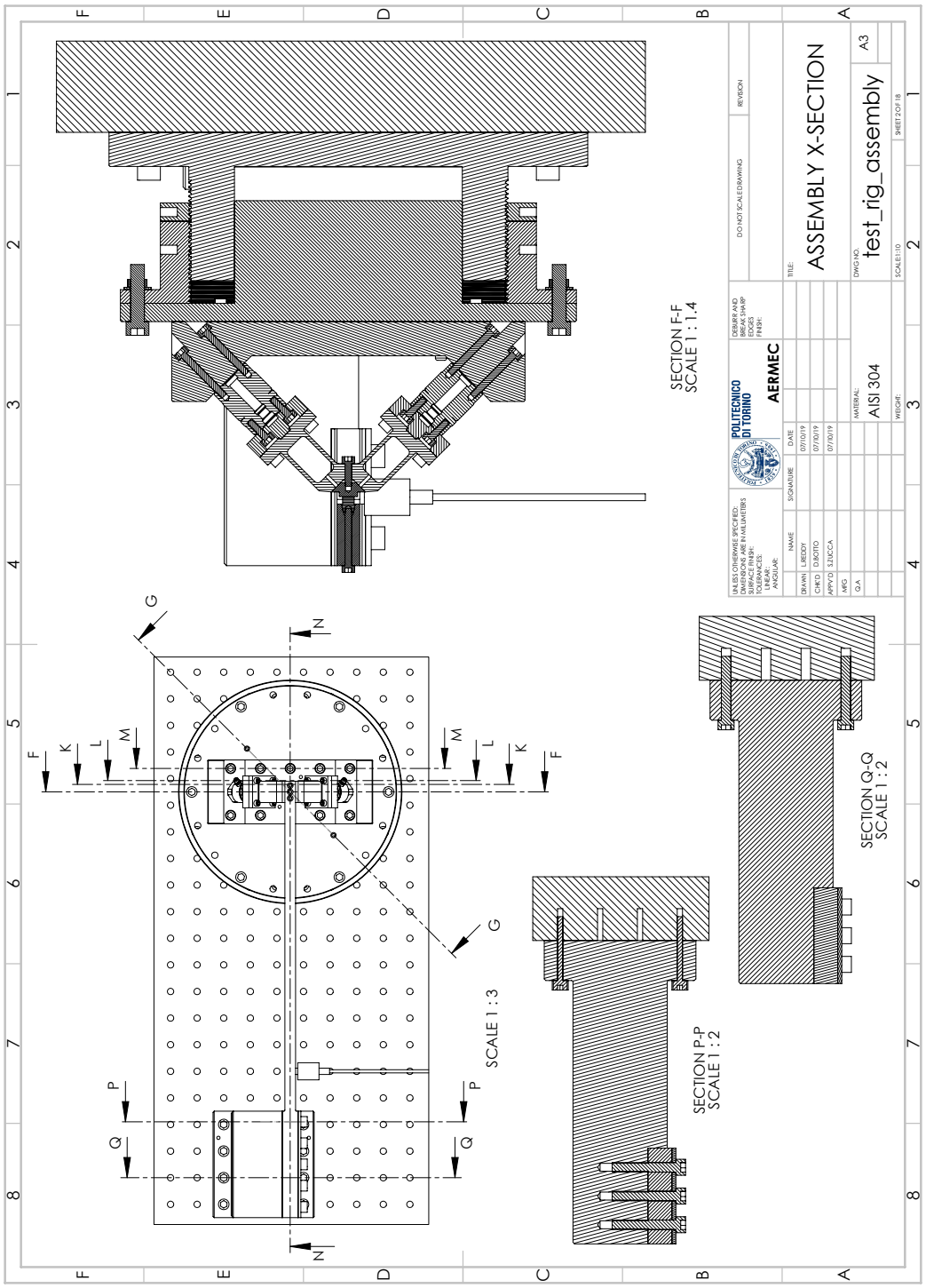
SECTION F-F
SCALE 1 : 1.4
SCALE 1 : 3
SECTION P-P
SCALE 1 : 2
SECTION Q-Q
SCALE 1 : 2
POLITECNICO DI TORINO
AERMEC
ASSEMBLY X-SECTION
test_rig_assembly
AISI 304
A3

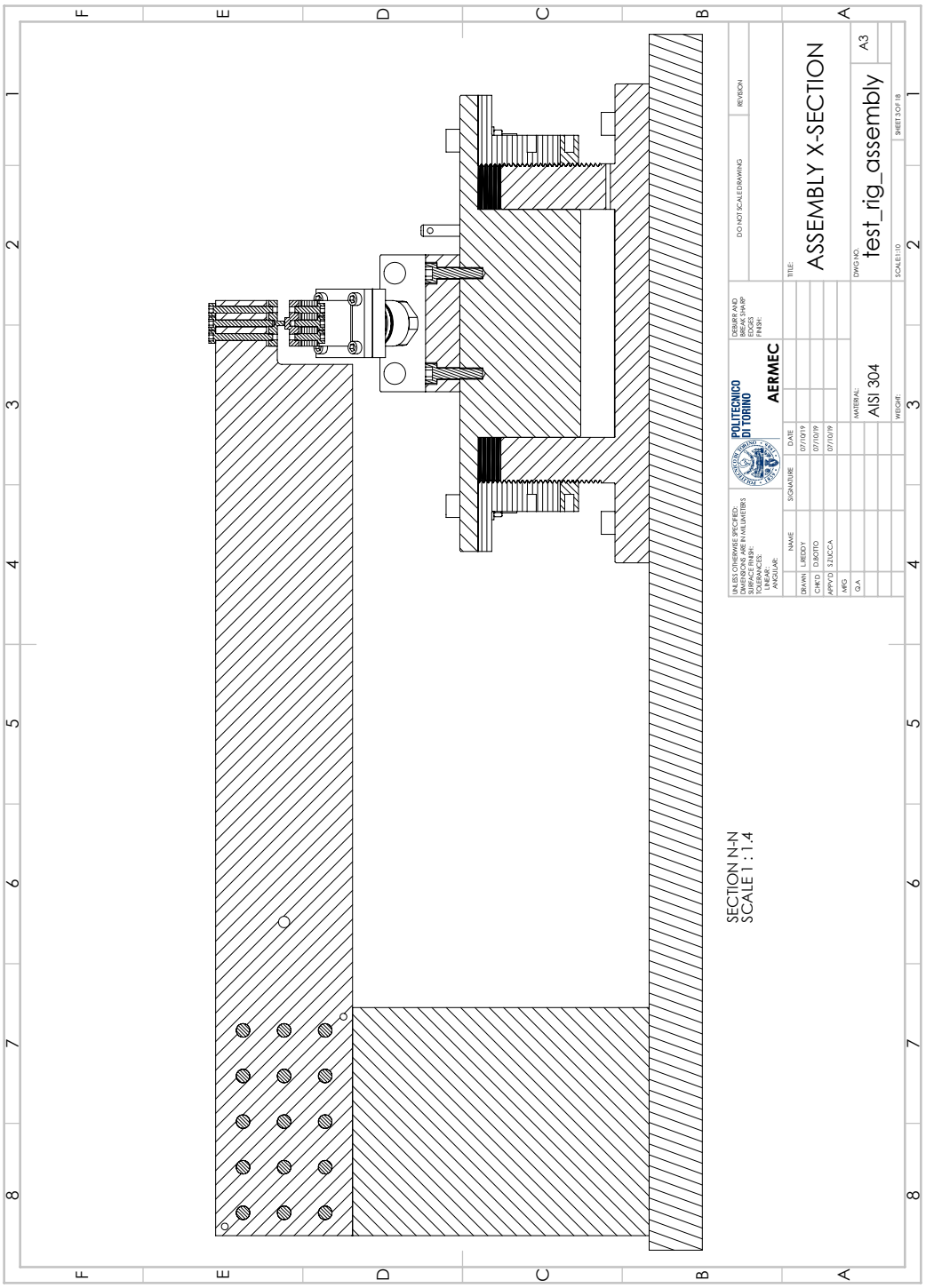
SECTION N-N
SCALE 1 : 1.4
ASSEMBLY X-SECTION
test_rig_assembly
AISI 304
A3
POLITECNICO DI TORINO
AERMEC
DO NOT SCALE DRAWING
REVISION
DEBURR AND BREAK SHARP EDGES
UNLESS OTHERWISE SPECIFIED:
DIMENSIONS ARE IN MILLIMETERS
SURFACE FINISH:
TOLERANCES:
LINEAR:
ANGULAR:
NAME
SIGNATURE
DATE
DRAWN
LIBEDDY
07/10/19
CHK'D
DIBOTTO
07/10/19
APP'D
SZUCCA
07/10/19
MFG
Q.A
MATERIAL:
WEIGHT:
TITLE:
DWG NO.
SCALE:1:10
SHEET 3 OF 18

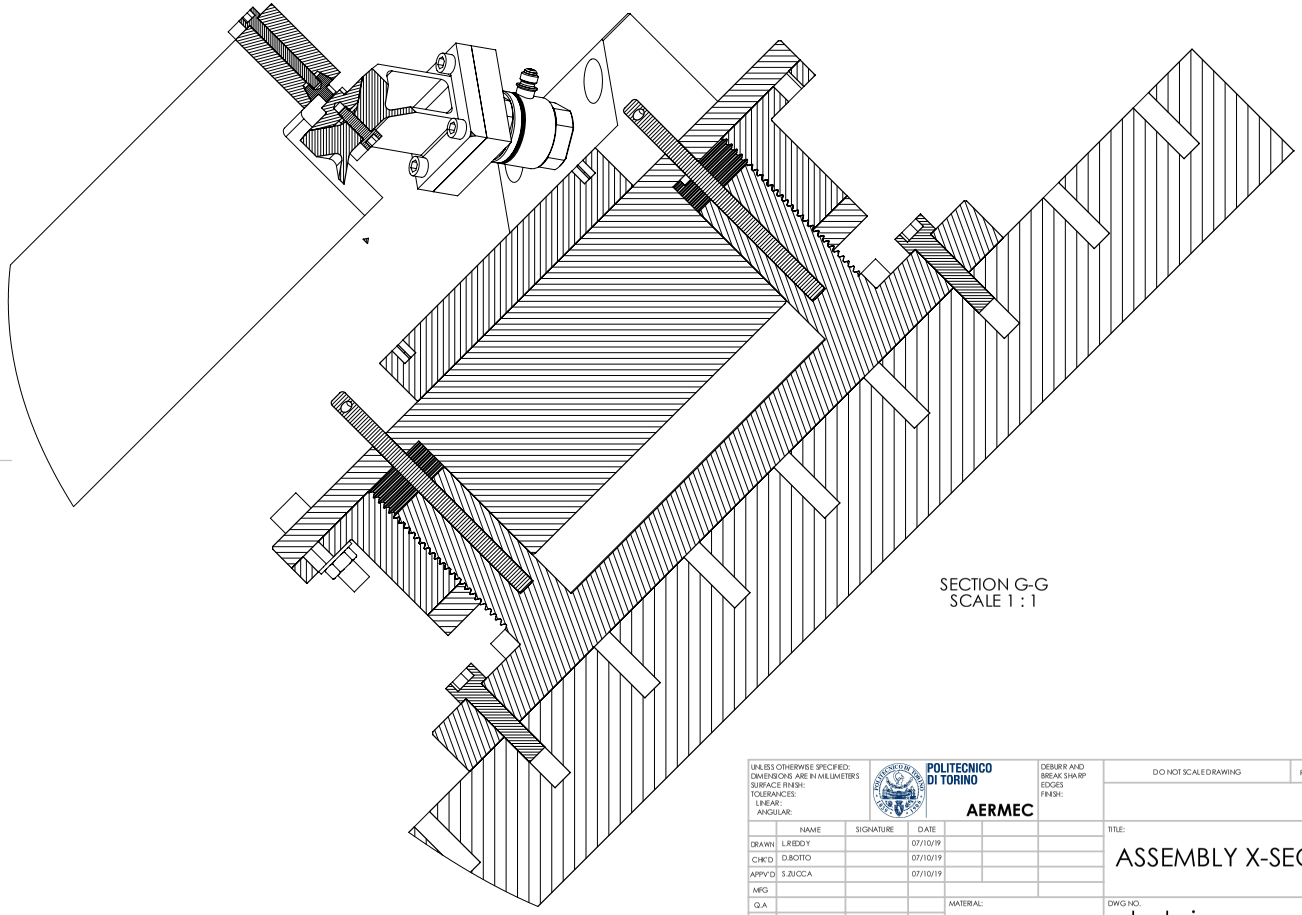

SECTION G-G
SCALE 1 : 1

UNLESS OTHERWISE SPECIFIED: DIMENSIONS ARE IN MILLIMETERS SURFACE FINISH: TOLERANCES: LINEAR: ANGULAR:	POLITECNICO DI TORINO AERMEC			DEBURR AND BREAK SHARP EDGES FINISH:	DO NOT SCALE DRAWING	REVISION
	NAME	SIGNATURE	DATE		TITLE: ASSEMBLY X-SECTION	
DRAWN	L.REDDY		07/10/19			
CHK'D	D.BOTTO		07/10/19			
APPV'D	S.ZUCCA		07/10/19			
MFG						
Q.A				MATERIAL: AISI 304	DWG NO. test_rig_assembly	A3
				WEIGHT:	SCALE:1:10	SHEET 4 OF 18

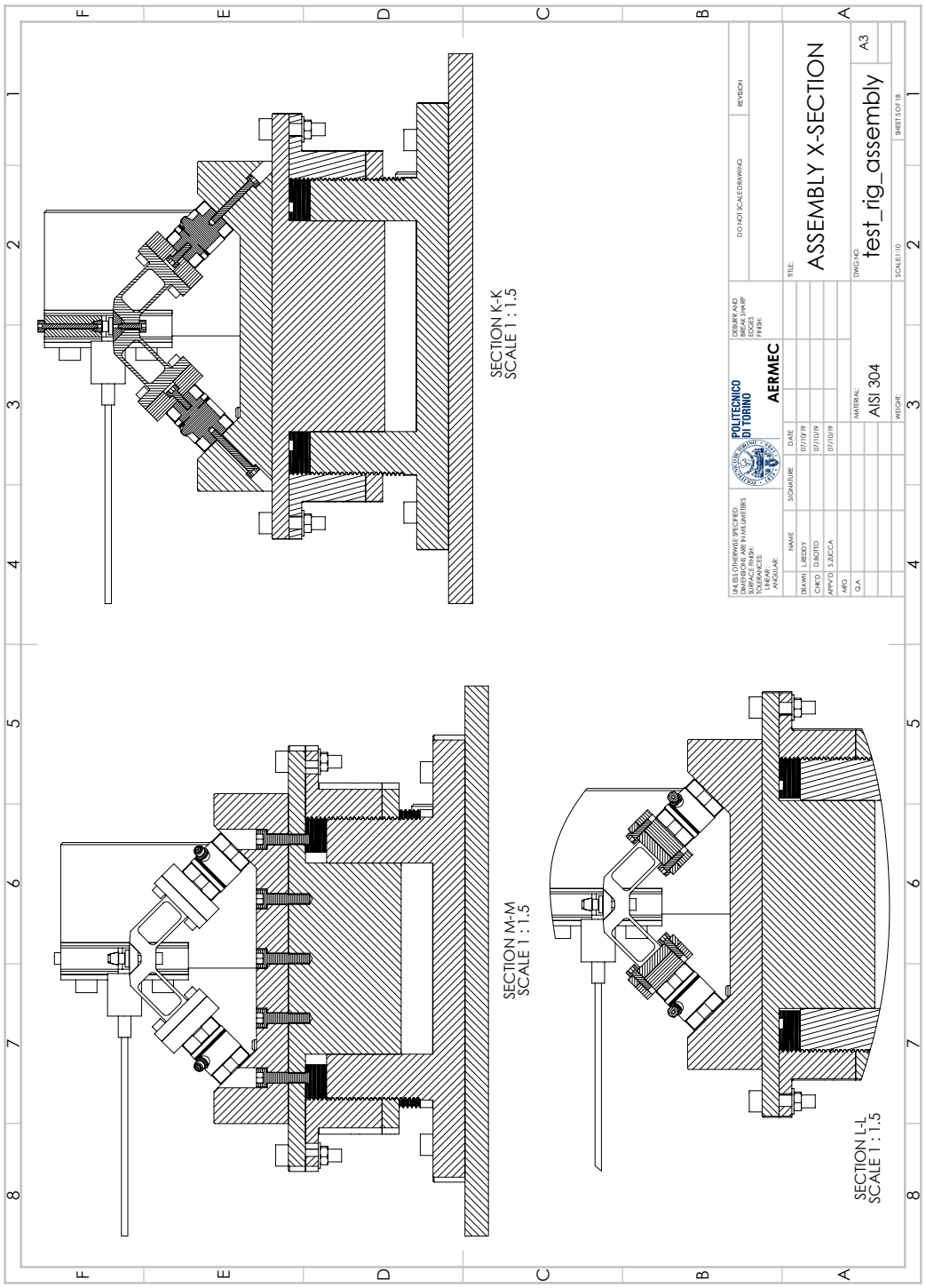
SECTION K-K
SCALE 1 : 1.5
SECTION M-M
SCALE 1 : 1.5
SECTION L-L
SCALE 1 : 1.5
POLITECNICO DI TORINO
AERMEC
ASSEMBLY X-SECTION
test_rig_assembly
AISI 304
A3

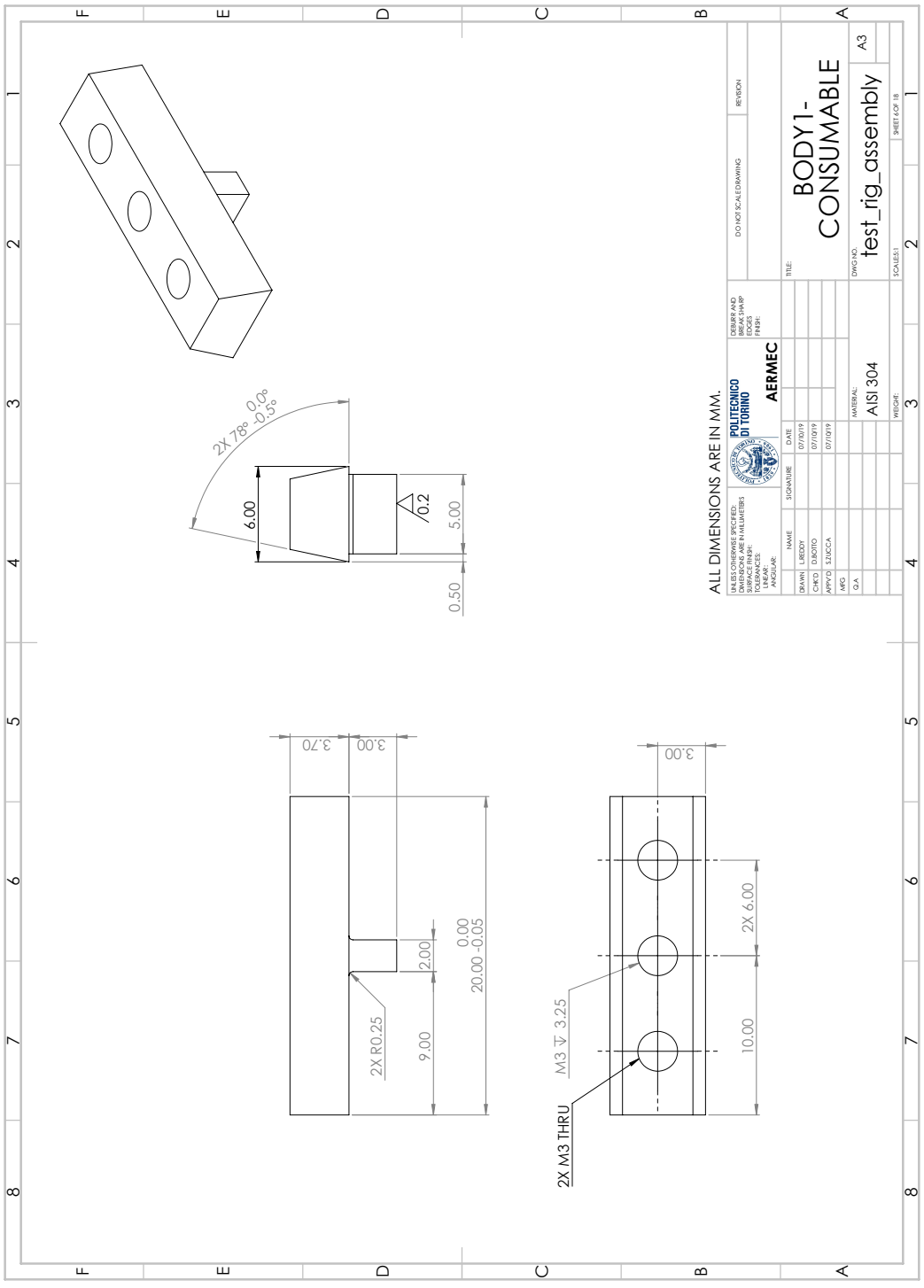
ALL DIMENSIONS ARE IN MM.
UNLESS OTHERWISE SPECIFIED:
DIMENSIONS ARE IN MILLIMETERS
SURFACE FINISH:
TOLERANCES:
LINEAR:
ANGULAR:
DEBURR AND BREAK SHARP EDGES
FINISH:
DO NOT SCALE DRAWING
REVISION
POLITECNICO DI TORINO
AERMEC
NAME
SIGNATURE
DATE
DRAWN
LIBEDDY
07/10/19
CHK'D
DIBOTTO
07/10/19
APPV'D
SZUCCA
07/10/19
MFG
Q.A
MATERIAL:
AISI 304
WEIGHT:
TITLE:
BODY1-CONSUMABLE
DWG NO.
test_rig_assembly
A3
SCALE:1:1
SHEET 1 OF 1
2X 78° 0.0° -0.5°
6.00
0.2
5.00
0.50
3.70
3.00
2.00
9.00
2X R0.25
20.00 0.00 -0.05
M3 ↧ 3.25
2X M3 THRU
3.00
2X 6.00
10.00

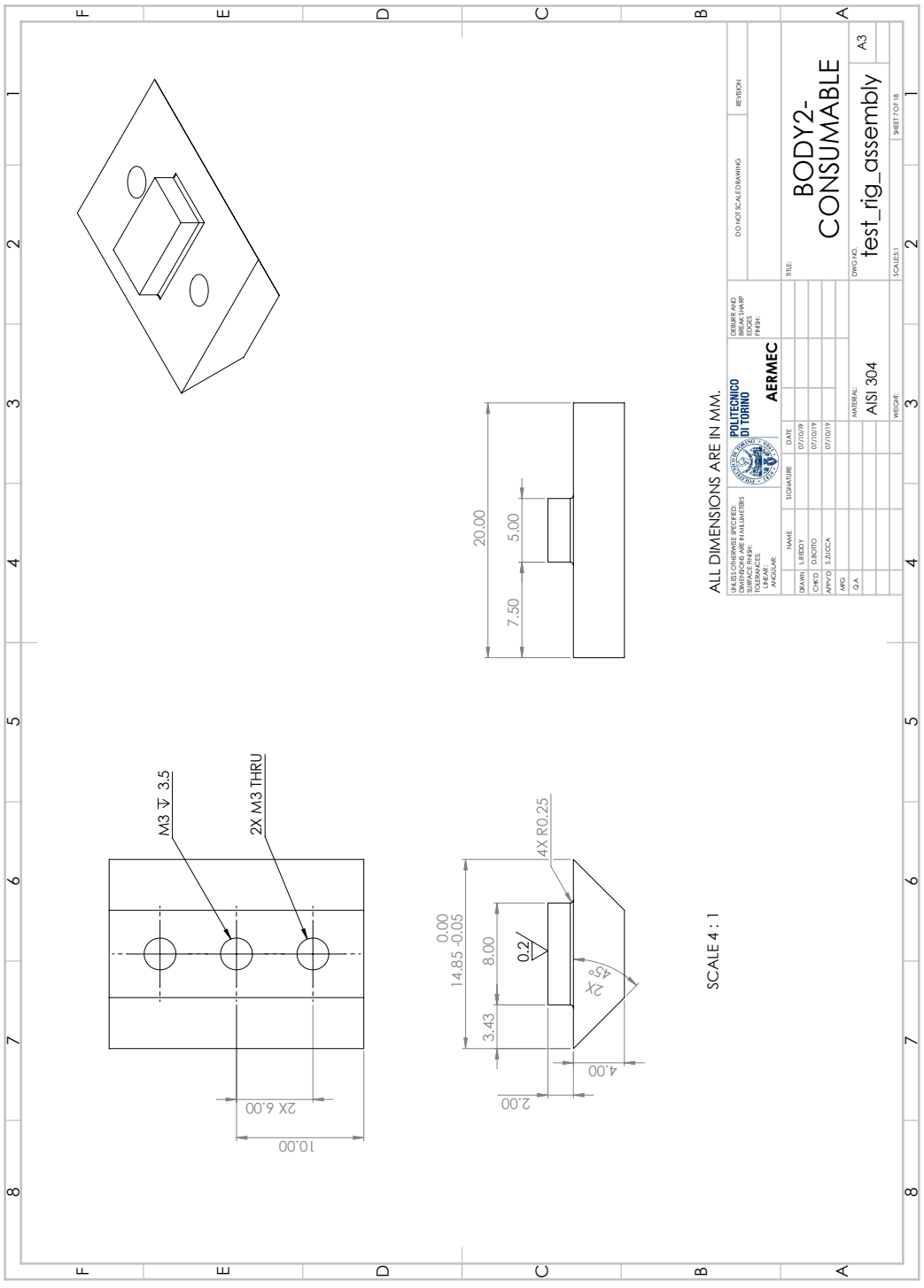
ALL DIMENSIONS ARE IN MM.
SCALE 4 : 1
M3 ↧ 3.5
2X M3 THRU
2X 6.00
10.00
20.00
5.00
7.50
4X R0.25
0.00
14.85 -0.05
8.00
3.43
0.2
45°
2X
4.00
2.00
BODY2-CONSUMABLE
test_rig_assembly
AISI 304
A3
POLITECNICO DI TORINO
AERMEC

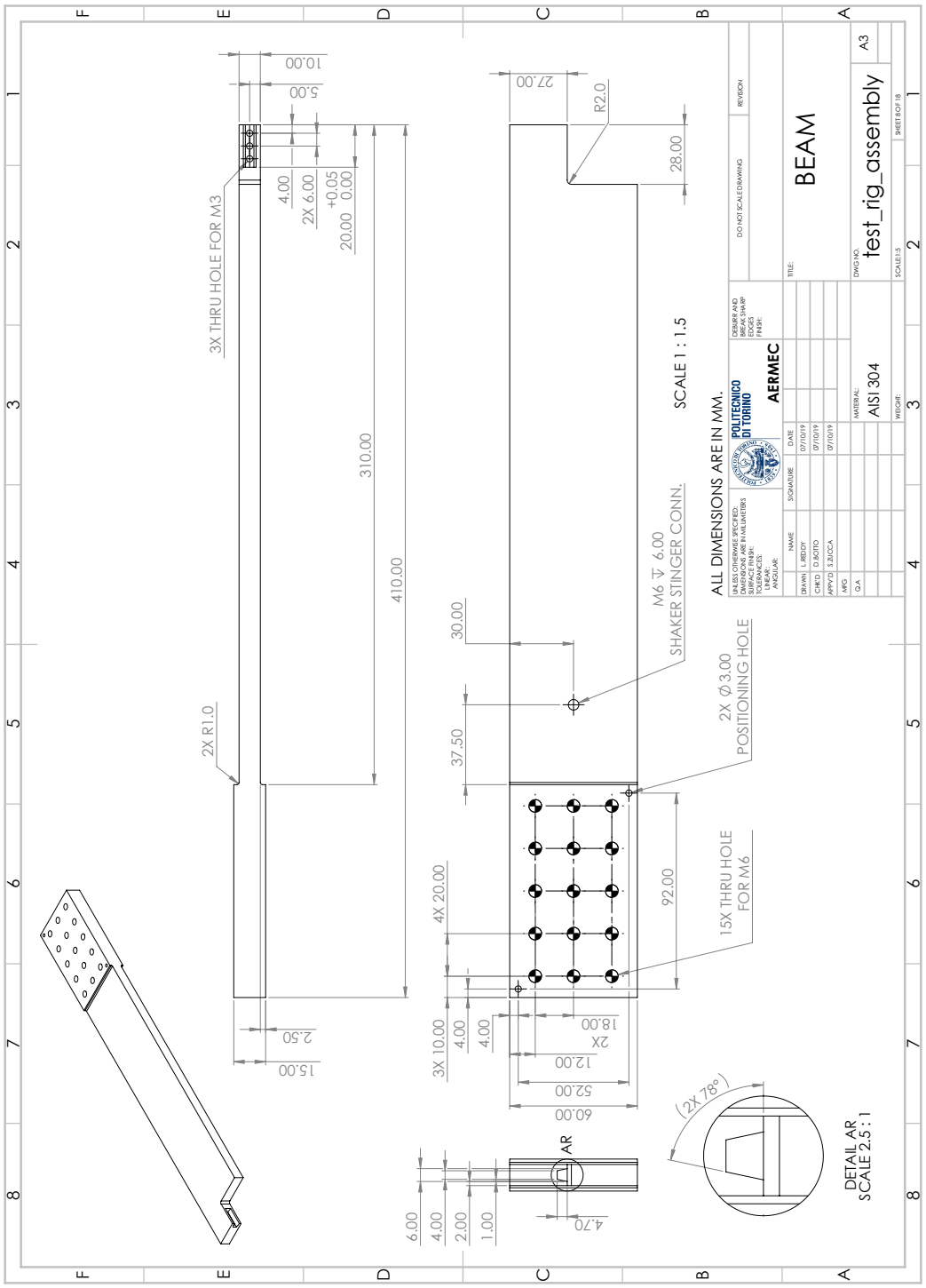
ALL DIMENSIONS ARE IN MM.
SCALE 1 : 1.5
DETAIL AR
SCALE 2.5 : 1
BEAM
test_rig_assembly
AISI 304
A3
POLITECNICO DI TORINO
AERMEC
DO NOT SCALE DRAWING
3X THRU HOLE FOR M3
2X R1.0
M6 ⊽ 6.00
SHAKER STINGER CONN.
2X ⌀ 3.00
POSITIONING HOLE
15X THRU HOLE
FOR M6
(2X 78°)
AR

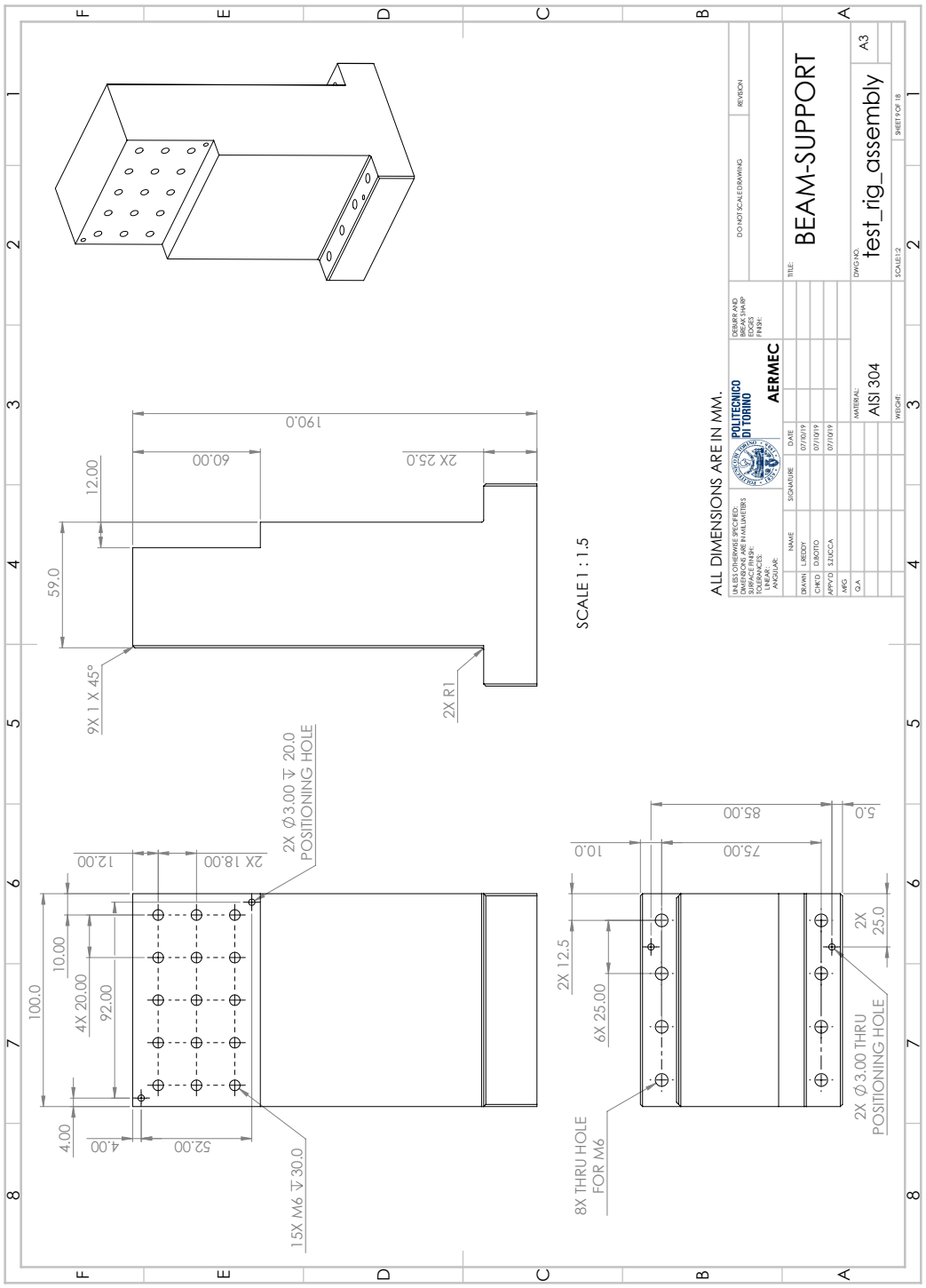
ALL DIMENSIONS ARE IN MM.
UNLESS OTHERWISE SPECIFIED:
DIMENSIONS ARE IN MILLIMETERS
SURFACE FINISH:
TOLERANCES:
LINEAR:
ANGULAR:
DEBURR AND BREAK SHARP EDGES
FINISH:
DO NOT SCALE DRAWING
REVISION
NAME
SIGNATURE
DATE
DRAWN
L.REDDY
07/10/19
CHK'D
D.BOTTO
07/10/19
APPV'D
S.LUCCA
07/10/19
MFG
Q.A
POLITECNICO DI TORINO
AERMEC
TITLE:
BEAM-SUPPORT
MATERIAL:
AISI 304
DWG NO.
test_rig_assembly
A3
WEIGHT:
SCALE: 1:2
SHEET 1 OF 1
SCALE 1 : 1.5
190.0
60.00
2X 25.0
12.00
59.0
9X 1 X 45°
2X R1
2X Ø3.00 ↧ 20.0
POSITIONING HOLE
2X 18.00
12.00
10.00
4X 20.00
92.00
100.0
4.00
4.00
52.00
1.5X M6 ↧ 30.0
85.00
5.0
75.00
10.0
2X 12.5
6X 25.00
2X
25.0
8X THRU HOLE
FOR M6
2X Ø3.00 THRU
POSITIONING HOLE

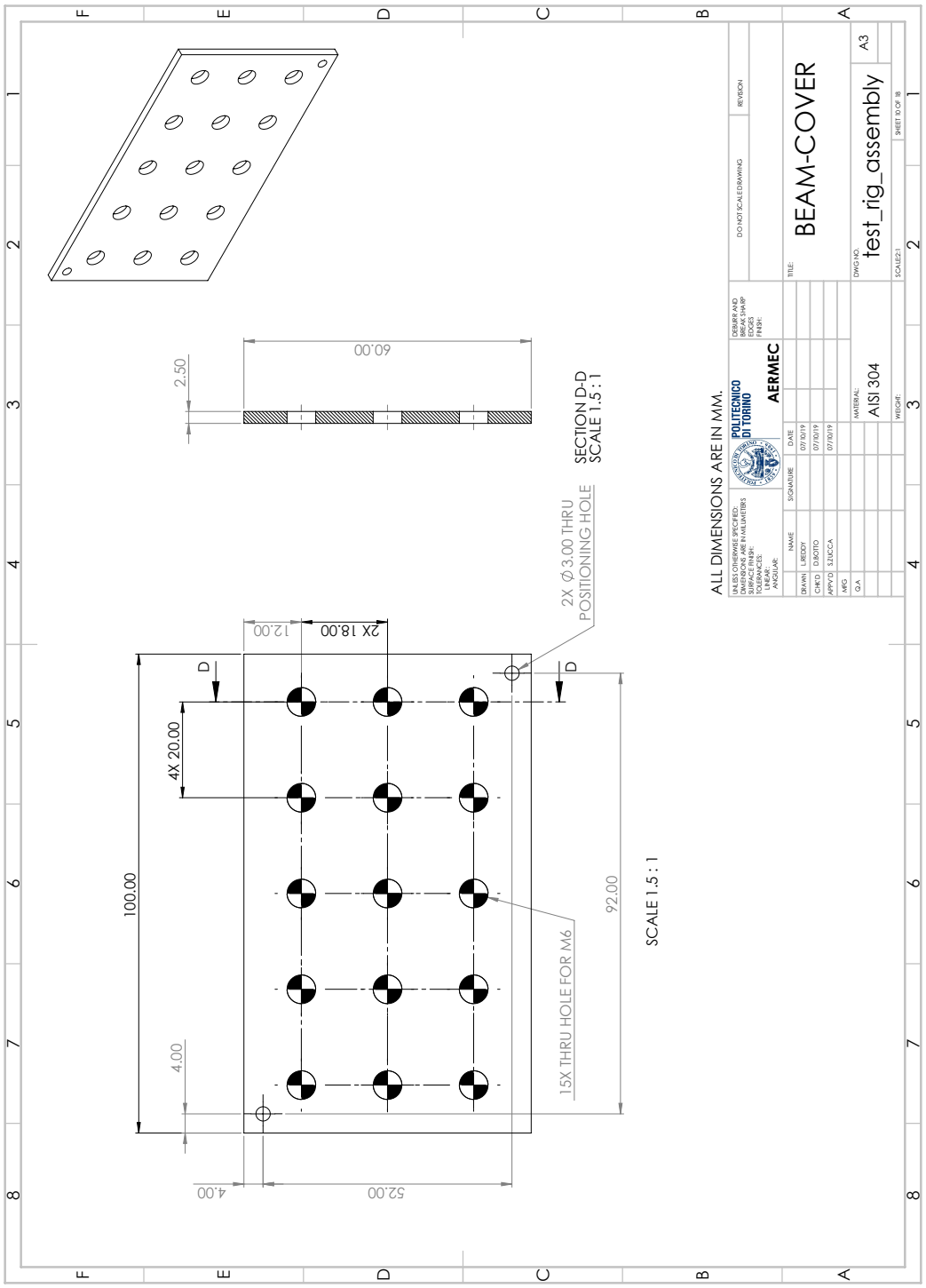
ALL DIMENSIONS ARE IN MM.
POLITECNICO DI TORINO
AERMEC
BEAM-COVER
test_rig_assembly
AISI 304
A3
SECTION D-D
SCALE 1.5 : 1
2X Ø 3.00 THRU
POSITIONING HOLE
SCALE 1.5 : 1
15X THRU HOLE FOR M6
4X 20.00
2X 18.00
100.00
92.00
52.00
60.00
2.50
12.00
4.00

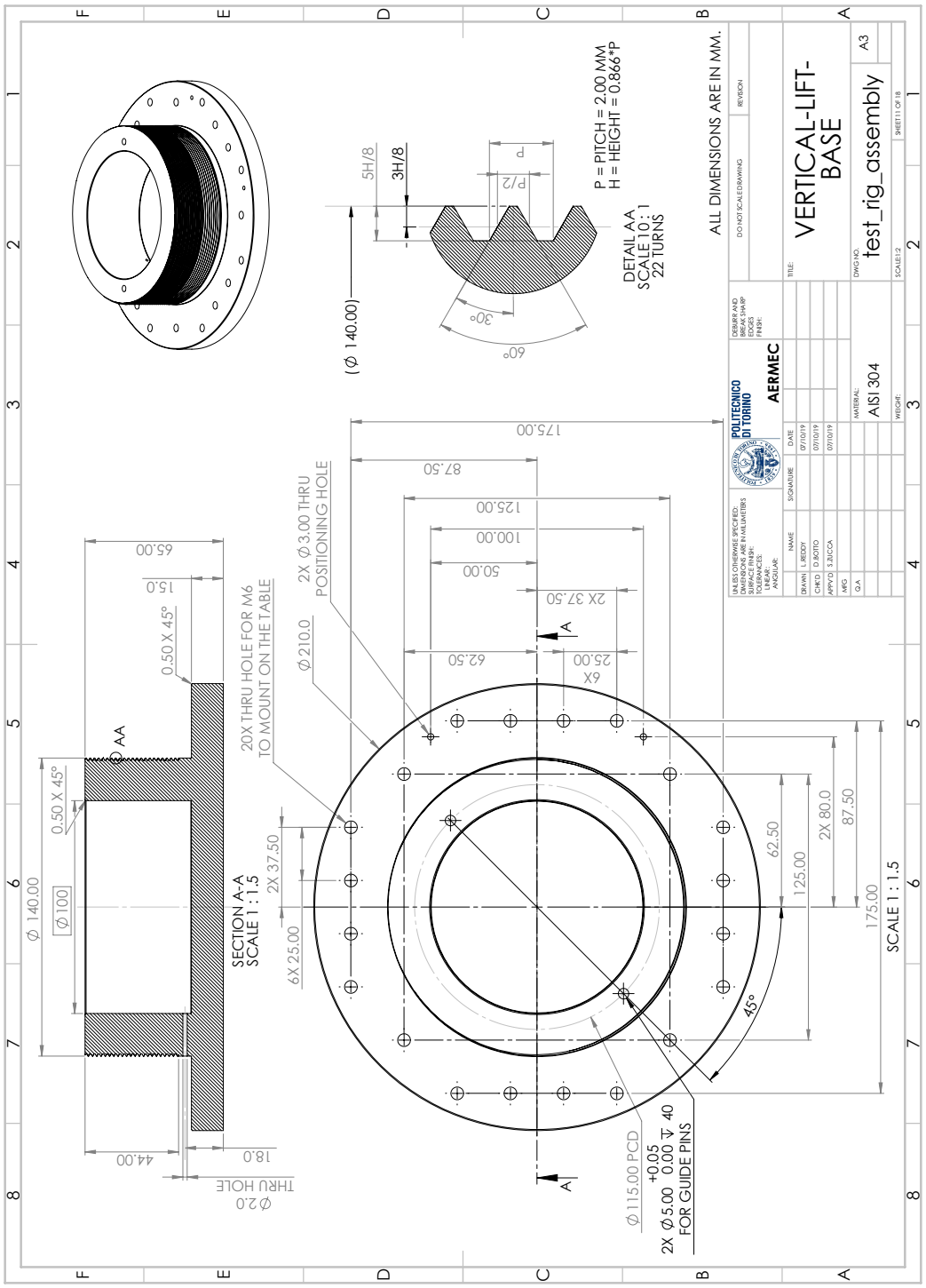
ALL DIMENSIONS ARE IN MM.
DO NOT SCALE DRAWING
REVISION
VERTICAL-LIFT-BASE
A3
test_rig_assembly
AISI 304
SCALE 1 : 1.5
SECTION A-A
SCALE 1 : 1.5
DETAIL AA
SCALE 10 : 1
22 TURNS
P = PITCH = 2.00 MM
H = HEIGHT = 0.866*P
5H/8
3H/8
30°
60°
20X THRU HOLE FOR M6
TO MOUNT ON THE TABLE
2X Ø3.00 THRU
POSITIONING HOLE
Ø210.0
Ø115.00 PCD
2X Ø5.00 +0.05 0.00 ▽ 40
FOR GUIDE PINS
6X 25.00
2X 37.50
2X 80.0
87.50
125.00
175.00
62.50
45°
Ø 140.00
Ø100
0.50 X 45°
65.00
15.0
44.00
18.0
THRU HOLE
Ø2.0
POLITECNICO DI TORINO
AERMEC

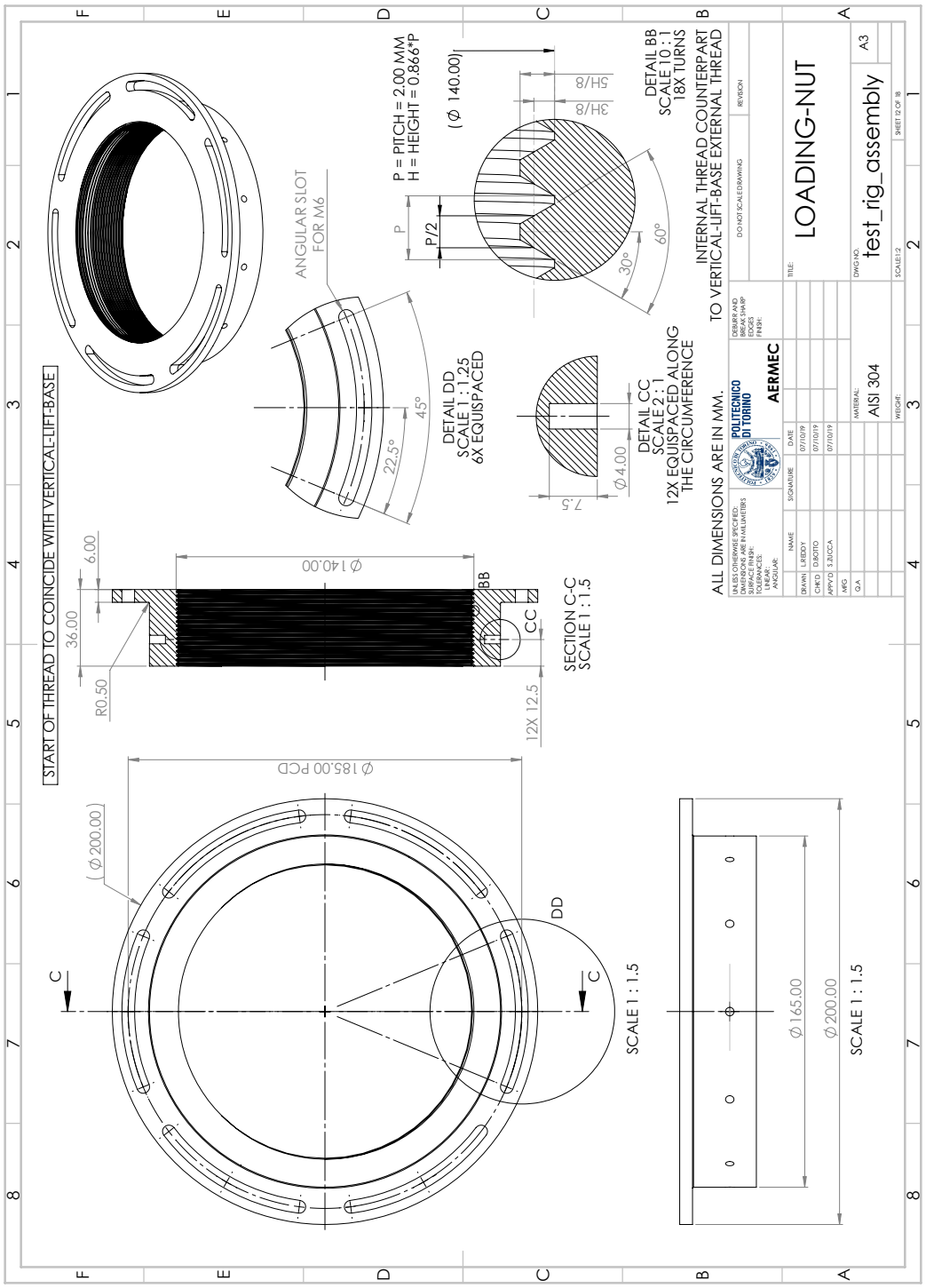
START OF THREAD TO COINCIDE WITH VERTICAL-LIFT-BASE
ANGULAR SLOT FOR M6
P = PITCH = 2.00 MM
H = HEIGHT = 0.866*P
DETAIL DD SCALE 1 : 1.25 6X EQUISPACED
DETAIL BB SCALE 10 : 1 18X TURNS
DETAIL CC SCALE 2 : 1 12X EQUISPACED ALONG THE CIRCUMFERENCE
INTERNAL THREAD COUNTERPART TO VERTICAL-LIFT-BASE EXTERNAL THREAD
SECTION C-C SCALE 1 : 1.5
SCALE 1 : 1.5
SCALE 1 : 1.5
ALL DIMENSIONS ARE IN MM.
LOADING-NUT
test_rig_assembly
AISI 304
A3
POLITECNICO DI TORINO
AERMEC

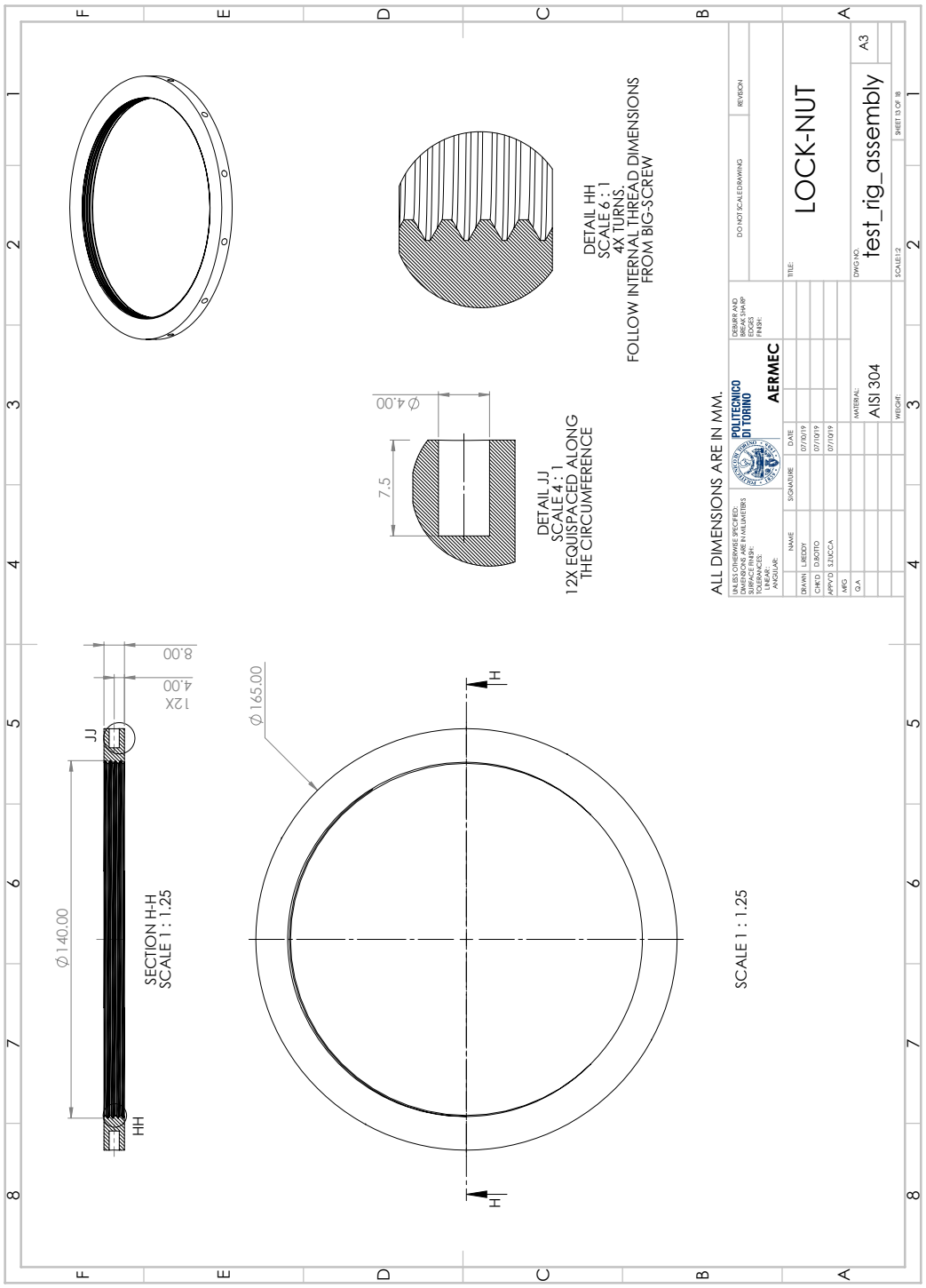
LOCK-NUT
test_rig_assembly
AISI 304
A3
AERMEC
POLITECNICO DI TORINO
ALL DIMENSIONS ARE IN MM.
DO NOT SCALE DRAWING
DEBUR AND BREAK SHARP EDGES FINISH:
UNLESS OTHERWISE SPECIFIED: DIMENSIONS ARE IN MILLIMETERS SURFACE FINISH: TOLERANCES: LINEAR: ANGULAR:
NAME SIGNATURE DATE
DRAWN L.REDDY 07/10/19
CHK'D D.ROTTO 07/10/19
APP'D S.LUCCA 07/10/19
MFG
Q.A
MATERIAL:
DWG NO.
WEIGHT:
SCALE:1:2
SHEET 13 OF 18
DETAIL HH
SCALE 6 : 1
4X TURNS.
FOLLOW INTERNAL THREAD DIMENSIONS FROM BIG-SCREW
DETAIL JJ
SCALE 4 : 1
12X EQUISPACED ALONG THE CIRCUMFERENCE
Ø4.00
7.5
SECTION H-H
SCALE 1 : 1.25
Ø140.00
12X
4.00
8.00
JJ
HH
Ø165.00
H
SCALE 1 : 1.25

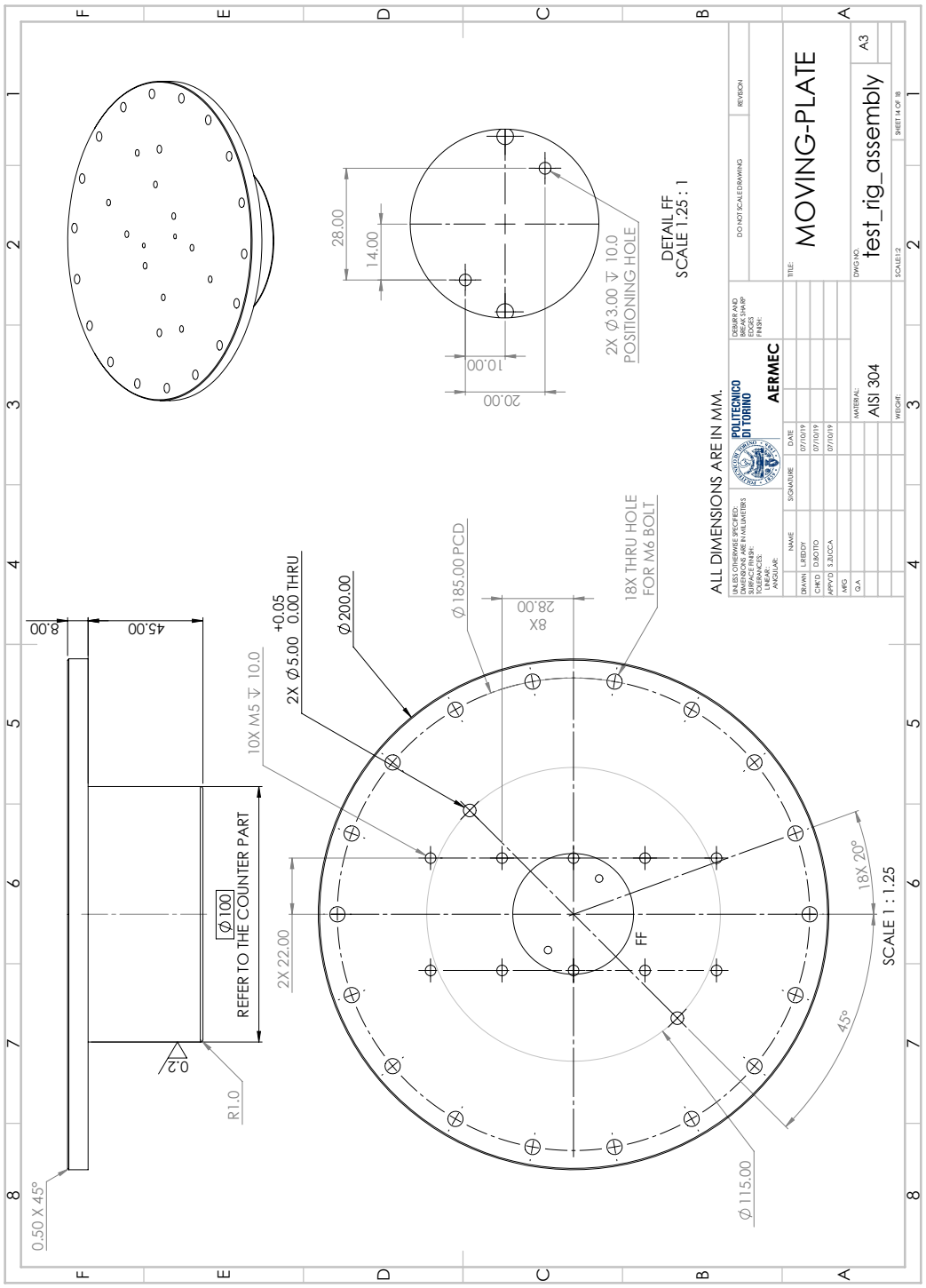
MOVING-PLATE
test_rig_assembly
AISI 304
A3
SCALE 1 : 1.25
ALL DIMENSIONS ARE IN MM.
POLITECNICO DI TORINO
AERMEC
DETAIL FF
SCALE 1.25 : 1
FF
Ø 200.00
Ø 185.00 PCD
Ø 115.00
18X THRU HOLE FOR M6 BOLT
10X M5 ↧ 10.0
2X Ø 5.00 +0.05 0.00 THRU
2X Ø3.00 ↧ 10.0 POSITIONING HOLE
REFER TO THE COUNTER PART
Ø 100
0.50 X 45°
R1.0
18X 20°
45°
2X 22.00
8X 28.00
28.00
14.00
10.00
20.00
45.00
8.00

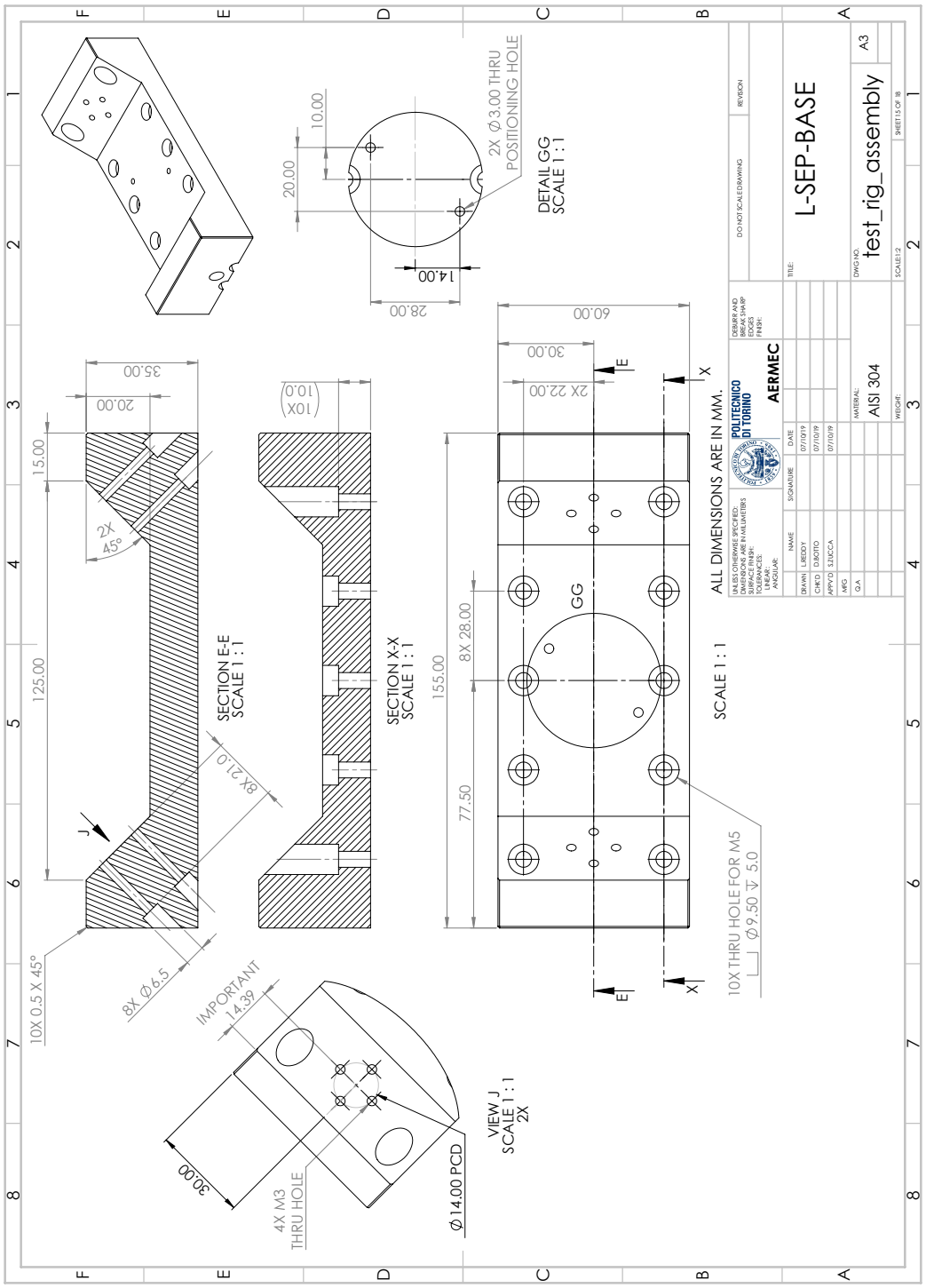
L-SEP-BASE
test_rig_assembly
AISI 304
A3
AERMEC
POLITECNICO DI TORINO
ALL DIMENSIONS ARE IN MM.
SCALE 1 : 1
DO NOT SCALE DRAWING
DEBURR AND BREAK SHARP EDGES
FINISH:
TITLE:
DWG NO.
MATERIAL:
SCALE:1:2
WEIGHT:
SHEET 1 OF 1
SECTION E-E
SCALE 1 : 1
SECTION X-X
SCALE 1 : 1
DETAIL GG
SCALE 1 : 1
VIEW J
SCALE 1 : 1
2X
2X Ø3.00 THRU
POSITIONING HOLE
10X THRU HOLE FOR M5
Ø9.50 ↧ 5.0
10X 0.5 X 45°
8X Ø6.5
4X M3
THRU HOLE
Ø14.00 PCD
IMPORTANT
14.39
30.00
35.00
20.00
15.00
125.00
155.00
77.50
8X 28.00
60.00
30.00
2X 22.00
10.00
20.00
14.00
28.00
10X
10.0
8X 2.0
2X
45°

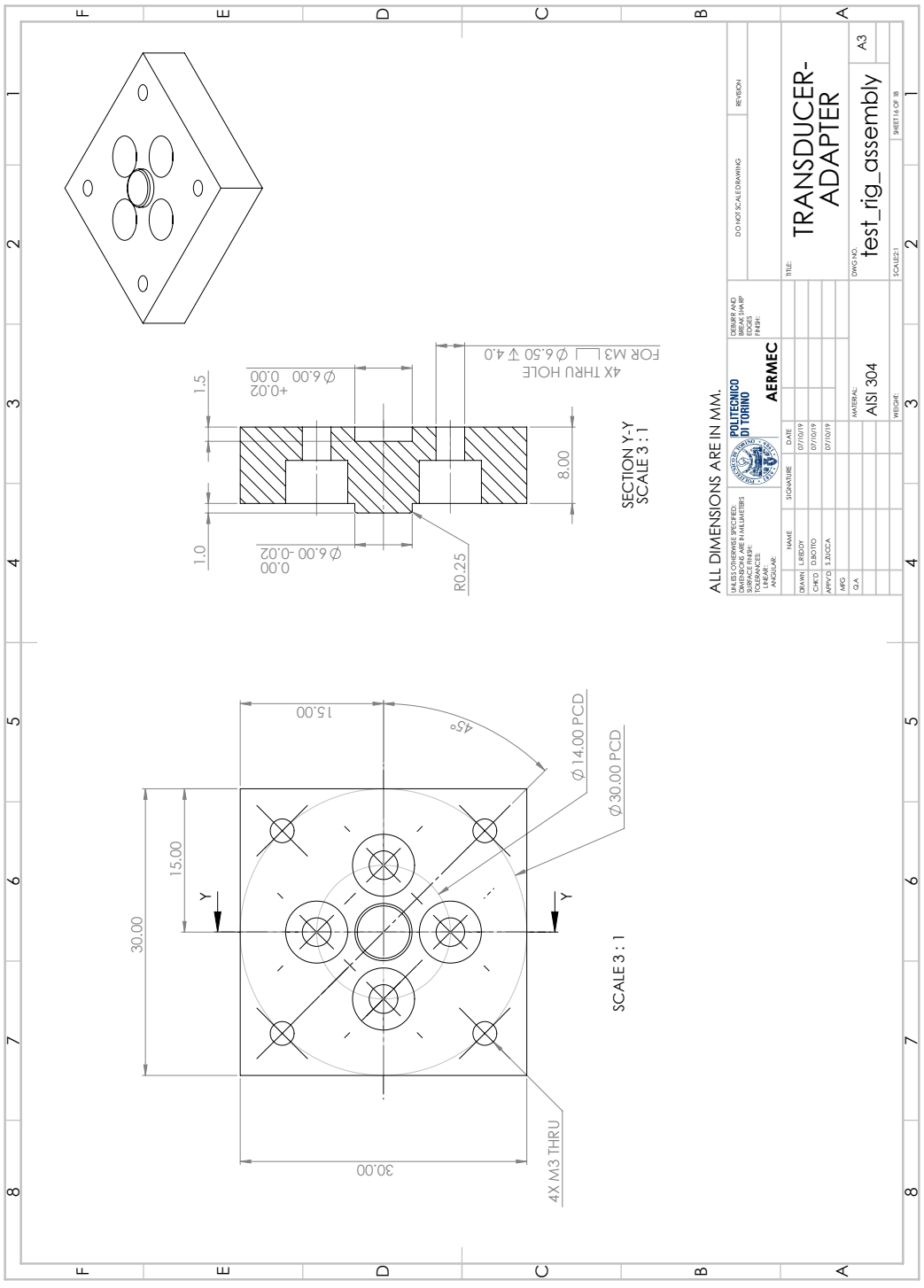
ALL DIMENSIONS ARE IN MM.
UNLESS OTHERWISE SPECIFIED:
DIMENSIONS ARE IN MILLIMETERS
SURFACE FINISH:
TOLERANCES:
LINEAR:
ANGULAR:
POLITECNICO DI TORINO
AERMEC
DEBURR AND BREAK SHARP EDGES
FINISH:
DO NOT SCALE DRAWING
REVISION
NAME
SIGNATURE
DATE
DRAWN L.REDDY 07/10/19
CHK'D D.BOTTO 07/10/19
APP'V'D S.ZUCCA 07/10/19
MFG
Q.A
MATERIAL:
AISI 304
TITLE:
TRANSDUCER-ADAPTER
DWG NO.
test_rig_assembly
A3
WEIGHT:
SCALE:1
SHEET 16 OF 18
4X THRU HOLE
FOR M3 ⌴ Ø6.50 ↧ 4.0
Ø6.00 +0.02 0.00
Ø6.00 0.00 -0.02
1.5
1.0
8.00
R0.25
SECTION Y-Y
SCALE 3 : 1
15.00
45°
Ø 14.00 PCD
Ø 30.00 PCD
30.00
15.00
Y
Y
30.00
4X M3 THRU
SCALE 3 : 1

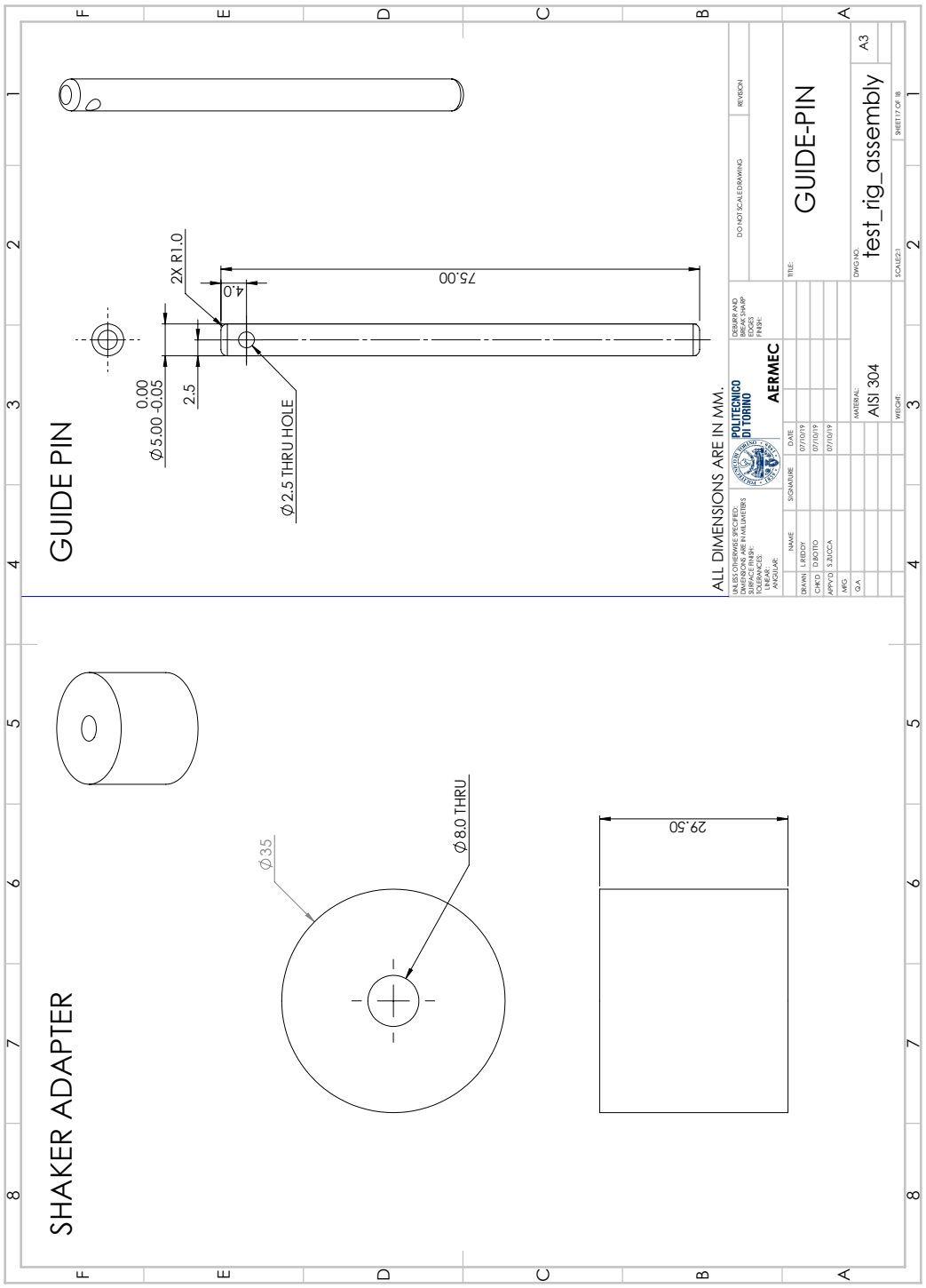
GUIDE PIN
2X R1.0
4.0
75.00
0.00
Ø5.00 -0.05
2.5
Ø2.5 THRU HOLE
SHAKER ADAPTER
Ø35
Ø8.0 THRU
29.50
ALL DIMENSIONS ARE IN MM.
UNLESS OTHERWISE SPECIFIED:
DIMENSIONS ARE IN MILLIMETERS
SURFACE FINISH:
TOLERANCES:
LINEAR:
ANGULAR:
DEBURR AND BREAK SHARP EDGES
FINISH:
DO NOT SCALE DRAWING
REVISION
NAME
SIGNATURE
DATE
DRAWN L.REDDY 07/10/19
CHK'D D.BOTTO 07/10/19
APP'D S.ZUCCA 07/10/19
MFG
Q.A
MATERIAL:
AISI 304
WEIGHT:
TITLE:
GUIDE-PIN
DWG NO.
test_rig_assembly
A3
SCALE:1:1
SHEET 17 OF 18
POLITECNICO DI TORINO
AERMEC

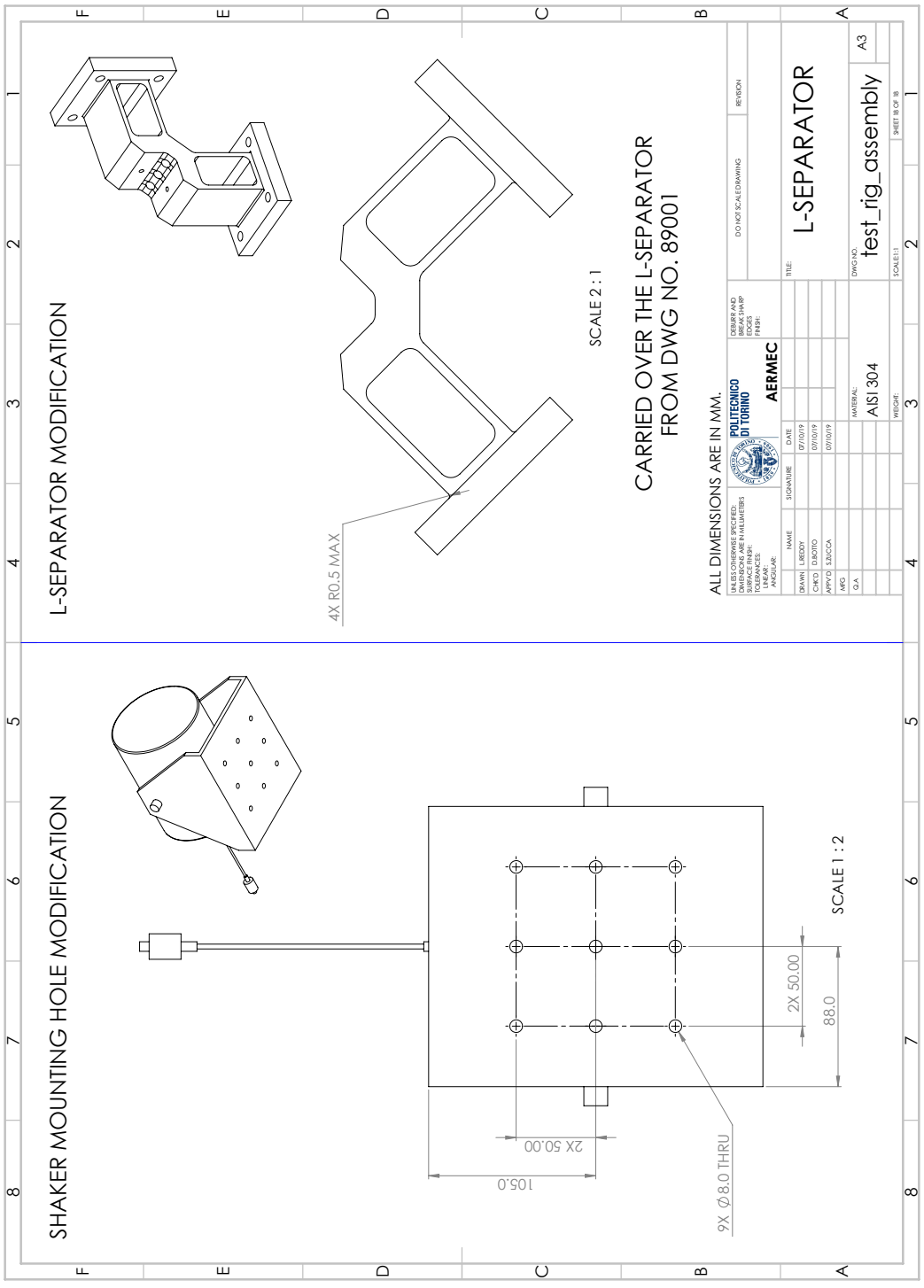
L-SEPARATOR MODIFICATION
4X R0.5 MAX
SCALE 2 : 1
CARRIED OVER THE L-SEPARATOR
FROM DWG NO. 89001
ALL DIMENSIONS ARE IN MM.
UNLESS OTHERWISE SPECIFIED:
DIMENSIONS ARE IN MILLIMETERS
SURFACE FINISH:
TOLERANCES:
LINEAR:
ANGULAR:
POLITECNICO DI TORINO
AERMEC
DEBUR AND BREAK SHARP EDGES
FINISH:
DO NOT SCALE DRAWING
REVISION
NAME
SIGNATURE
DATE
DRAWN LIBEDDY 07/10/19
CHK'D D.BOTTO 07/10/19
APP'D S.BUCCA 07/10/19
MFG
Q.A
MATERIAL:
AISI 304
WEIGHT:
TITLE:
L-SEPARATOR
DWG NO.
test_rig_assembly
A3
SCALE:1:1
SHEET 18 OF 18
SHAKER MOUNTING HOLE MODIFICATION
9X Ø8.0 THRU
105.0
2X 50.00
2X 50.00
88.0
SCALE 1 : 2

Appendix C

User manual for the novel forced response test rig

This appendix acts as a stand-alone user manual for the novel forced response test rig to set-up different components of the test rig, electrical connections and instructions to perform wear test and FRF sweeps using Siemens Testlab software. The individual test rig components are assembled as shown through various cross-sections in the assembly level drawings in Appendix B.

C.1 Test rig components.

The main components of the test rig and necessary instruments to enable measurement and record the responses are listed below:

- Test rig core assembly
  - Cantilever beam with column support and the upper specimen.
  - Contact loading mechanism with L-separator assembly and the lower specimen.
  - Two force transducers (Kistler Type 9323AA).
  - Two charge amplifiers (Kistler Type 5015A).

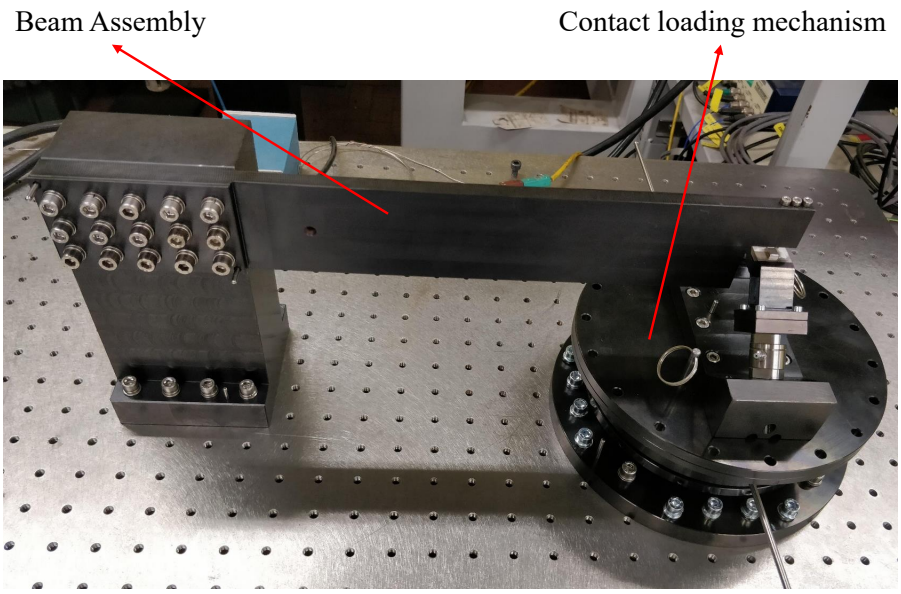

Fig. C.1 Core components of the test rig.

- Shaker system
  - Shaker (TIRA S514).
  - Shaker power amplifier (TIRA BAA-500).
  - Suitable shaker stinger.
  - Load cell between the beam and the stinger (PCB 208C3).
- Laser system
  - Relative displacement split beam laser (LDV - Polytec OFV-552).
  - Vibrometer controller (OFV-5000).
- Data Acquisition system
  - Siemens SCADAS Mobile with vibration control power buffer and emergency stop box.
- Uniaxial or multiaxial accelerometer(s) (PCB 352B10).

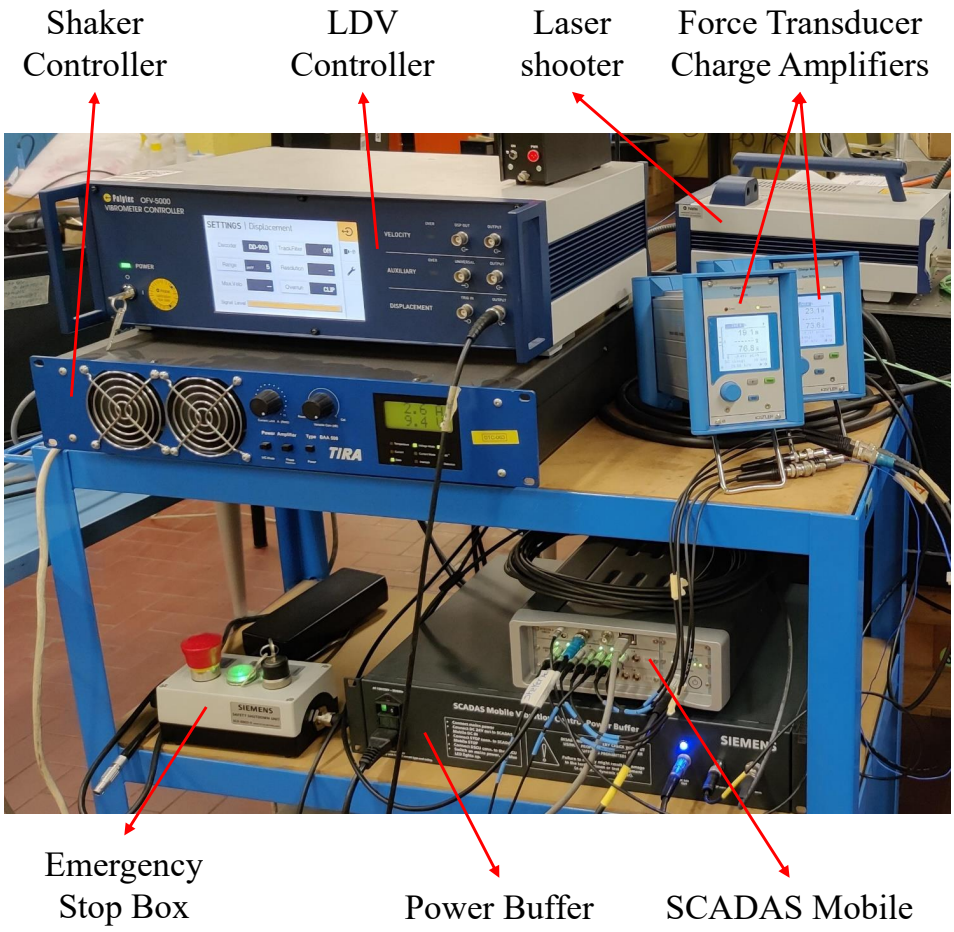

Fig. C.2 Associated electrical and electronic instruments of the test rig.

C.2 Instrumentation and connections.

Refer to figure 5.7, which shows a schematic representation of various electronic instruments and its connections. The list below expands on the exact connections to be made necessary to power the test rig.

- Connect SCADAS Power Buffer `STOP conn.` to SCADAS Mobile `STOP`.
- Connect SCADAS Power Buffer `DC 24V OUT` to SCADAS Mobile `DC IN`.
- Connect SCADAS Power Buffer `DSCU conn.` to Emergency Stop `IN`.
- Connect shaker-beam load cell output to SCADAS Mobile `Input 1`.

- Connect a BNC cable between laser controller `Displacement Output` to SCADAS Mobile `Input 2`.
- Connect 2x output of L-separator Kistler force transducers to the respective Kistler charge amplifiers. Press `Measure` when ready to start the experiment.
- Connect 2x BNC cables betwee Kistler charge amplifier `Output` to SCADAS Mobile `Input 3 & 4`.
- Mount accelerometer(s) on the test rig as necessary and connect them to SCADAS Mobile `Input 5+`.
- Connect a BNC cable between shaker amplifier `Input - AC` and SCADAS Mobile `Out1` for closed-loop control of shaker force.
- Connect Ethernet cable between SCADAS Mobile and the computer using Testlab software.
- Turn the "key" to indicate green light on the emergency stop box.

Tip: Before launching Testlab software, connect the ethernet cable to the computer and turn on SCADAS system.

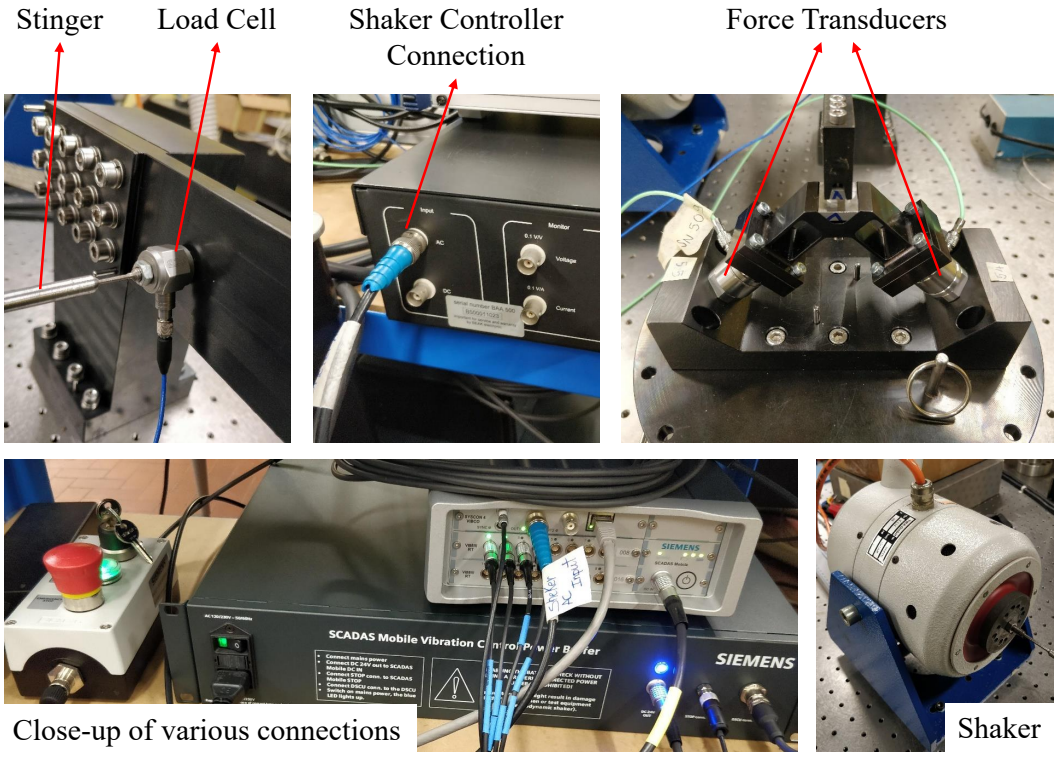

Fig. C.3 Close-up images of various connections for clarity.

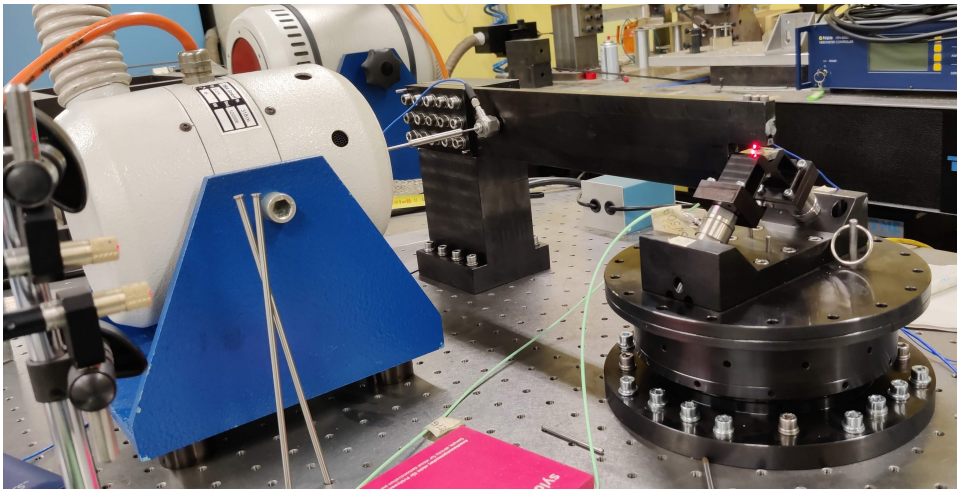

Fig. C.4 Final view of the test rig.

C.3 Specimen preparation.

The pristine surfaces of upper and lower specimens are first scanned using `Alicona` optical profilometer to save the unworn profile and later to compare the worn surfaces with the pristine surface. For the intermediate surface scans, the specimens are unmounted from the test rig and cleaned for debris and then the surface scans are captured.

The saved profile data can then be exported to the software `Digital Surf MountainsMap` to do further analysis, such as data clean up, levelling, extract surface properties, visualization, split the surface to roughness and waviness components and wear volume loss computation.

Later, the pristine surface data of the upper and lower specimen (waviness) can be exported to `MATLAB`, where the surfaces can be downsampled to match the contact interface mesh grid and obtain localized nodal data. This nodal information can be used in the HBM solver as a starting real surface input to study the evolution of wear and the subsequent dynamic response.

C.4 Setting up Testlab software for conducting experiments.

Siemens Simcenter SCADAS Mobile DAQ is used for data acquisition. Since this is a general-purpose system, there are various modules available, which are intended to a perform different type of tests for different applications.

In the current case, a full-length test is divided into two parts as per the test plan devised in section 5.2.4 - fretting wear for a preset number of cycles at a constant frequency and fixed excitation, and intermediate FRF sweeps for a given frequency range with controlled shaker excitation force. To achieve this, two different Simcenter modules should be used.

For the FRF sweeps, `"MIMO Sine Sweep and Stepped Sine Testing"` module can be used. The channel setup is appropriately defined with the right input mode, coupling and sensitivity values for the components used. The shaker channel is set to `control`, and the other active channels are set to `measure`. The actual sensitivities

of the laser range, force transducers force range and accelerometer sensitivity are defined in the channel setup. The frequency range, sweep direction and input force with amplitude control are defined by the user, and three averages of FRF sweeps are taken for better accuracy of the results. Also, sweeps can be performed in both forward and backward directions to see if the system behaves differently due to nonlinearities.

For the wear test, `"MIMO FRF Testing"` module can be used. However, there exists no module in Testlab to excite the system at a fixed frequency with a particular excitation force for a large number of cycles. Hence, this module is tweaked by using options for the current purpose and with the help of Siemens expert executive. To achieve the objective, sine testing can be activated and by enabling the option `"Enable Throughput"`. This option records the time signals and saves them for the user. The number of wear cycles can be defined by seconds. For example, running at 100 Hz for 10000 seconds produces 1 million cycles. The drawback of this method is only raw signals in real-time can be seen. The important graph - hysteresis loops can be obtained only after post-processing the results. Since the full-length test is split into many pieces, the user can post-process piece-by-piece data to visualize the evolution and analyze the data in the meantime. Also, the enable throughput option saves the full-time signals. Especially, this requires a lot of memory to store the whole raw signal for 10-20 million cycles, and post-processing the signals and data in `MATLAB` also demands powerful computers. The other solution is to custom make the software using `LabView` and NI data card, which has not been done in the current research.

C.5 Additional notes.

- Use reflective tape on the upper and lower specimen where the laser beams are pointed to, to increase reflectivity and signal quality.
- Turn on all the electronics - laser with the beam on, force transducers with charge amplifiers and wait for at least 30 minutes before the start of the actual test to allow to heat up the components and stabilize for stable measurements.
- Ensure the LDV "range" is set according to the magnitude of relative displacement, and the equivalent sensitivity is entered in the channel setup of Testlab

software. When the LDV is turned off and back on, the displacement range could reset to the default value, and the Testlab channel setup might not reflect matching sensitivity value, and one could read the incorrect measurement.

- During intermediate surface scans for wear test, the contact loading mechanism moving platform has to be released to disassemble the specimens. One tip to ensure the same platform height every time, the loading nut and locknut position can be marked using tape. So that, even with eventual wear and loss of contact preload, the contact is engaged at the same height every time.

- Force transducer drift: The piezoelectric force transducers experience static drift over time. This causes an issue in getting an accurate measurement, especially the static component of the signal. Because of losing contact preload, measuring the static component of the transducer signal is crucial. One way to overcome the drift is to meticulously note down the display readings before and after the wear interval test and then post-process the signal data to correct the mean obtained from the initial and final static reading. Also, the contact loading platform is physically maintained at the same height for a given loading throughout the wear test by using tape markers. So, in a way, this eliminates incorrect preload setting. Alternatively, the right way to measure the accurate static force is using a strain gauge type transducer. The piezoelectric type transducer is very accurate for dynamic measurements, and only for a short duration static measurements.

Appendix D

How to run a MATLAB program in a HPC

This appendix briefly shows how to run a MATLAB program in a HPC with a sample script to run the job for Windows and Linux operating system. The example uses `SBATCH` scheduler similar to the one at Politecnico di Torino high performance computing systems.

****

How to run your MATLAB program in the HPC PoliTo

Created by Reddy on 02-06-2020

For AERMEC | DIMEAS, POLITO

****

Contents

1. Using Windows 1

2. Using Linux 3

3. Running the job 5

Read the Gentlemen's Agreement before using HPC ☺

There are 3 HPC systems available to us:
- CASPER
- HACTAR [my preference as the fastest execution for our type of programs]
- LEGION

1. Using Windows

Pre-requisites:
- Granted access from HPC PoliTo hpc.dauin@polito.it
- Install PuTTY https://www.putty.org/
- Install FileZilla https://filezilla-project.org/
- Basic Linux commands:
  - ➔ ls (list the files)
  - ➔ cd (change directory)
  - ➔ pwd (print path of the working directory)
  - ➔ mkdir (make directory)
  - ➔ rmdir (remove directory)
  - ➔ cp (copy)
  - ➔ scp (secure copy)
- In your MATLAB program, remove any figure plot commands and suppress write to Command Window

****

Install PuTTY software on Windows and use **'hactarlogin.polito.it'** as Host Name.

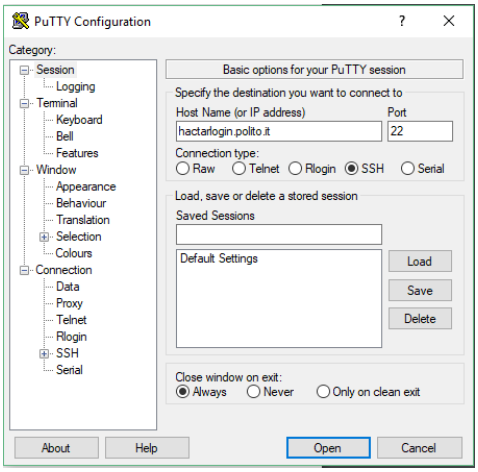

Login using your 'username' and 'password'.
You should be able to see something like this.

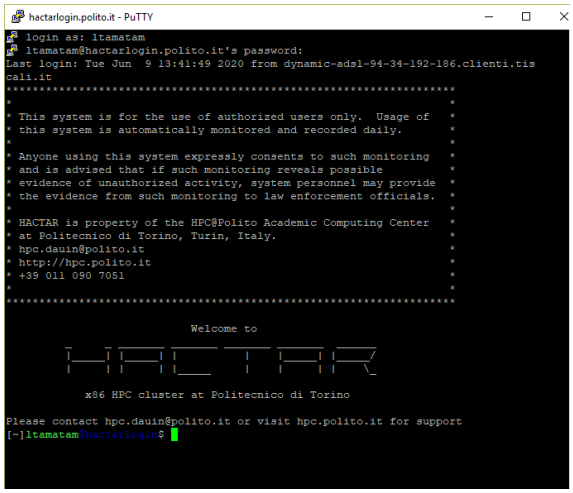

Now you are logged into the supercomputer!

To transfer your program and functions from your local computer to the cluster: Install **FileZilla**. This enables you to use GUI instead of command line.

In FileZilla, use **hactarlogin.polito.it** as Host and your username and password. Port **22**.

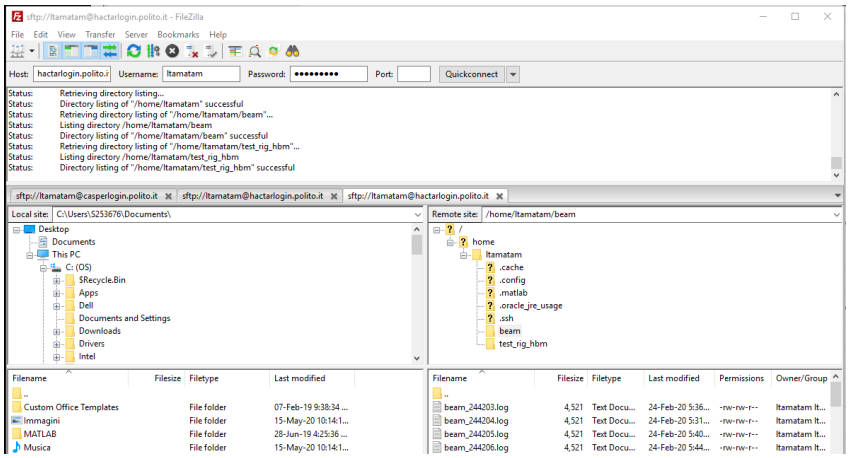

Copy the files and folders using drag and drop.

Jump to section ‘Running the job’ for next steps.

2. Using Linux

Pre-requisites:

- Granted access from HPC PoliTo hpc.dauin@polito.it
- Linux on your local system (if not see next section)
- Basic Linux commands:
  - ➔ ls (list the files)
  - ➔ cd (change directory)
  - ➔ pwd (print path of the working directory)
  - ➔ mkdir (make directory)
  - ➔ rmdir (remove directory)
  - ➔ cp (copy)
  - ➔ scp (secure copy)
- In your MATLAB program, remove any figure plot commands and suppress write to Command Window

****

Installing Linux (Ubuntu distribution) on your Windows based computer using Oracle VM Virtualbox:

Follow the steps: https://www.virtualbox.org/wiki/Linux_Downloads
If stuck, there are a lot of Youtube videos showing how to proceed.

****

Once Linux is installed, login to your system:

- Launch Terminal Window (Alt+T):
  - ➔ sudo apt-get install vim

Copy your MATLAB scripts to a folder into your Linux system (use Google Drive / email / other cloud storage).

Test if your access to the HPC supercomputer works:
Open Terminal Window:

- ➔ ssh {username}@hactarlogin.polito.it
- ➔ {password}
- ➔ something like below must appear

- ➔ pwd (copy the output path: this is path_of_hpc)

How to copy the MATLAB scripts from your local Linux system to the HPC Cluster:
In the Terminal Window, go to the folder of interest using ‘cd’ command

- ➔ cd {path of interest}
- ➔ scp -r * {username}@hactarlogin.polito.it:{path of hpc}
- ➔ {password}

****

3. Running the job

Now create a batch file to submit your job to the computer:

- ➔ touch {job_name}.sbatch
- ➔ vim {job_name}.sbatch (this opens the editor)
  - If vim is not available, use the command: sudo apt-get install vim
- ➔ i (insert mode)
- ➔ Paste the following:

```
#!/bin/bash
#SBATCH --job-name={your_job_name}
#SBATCH --mail-type=NONE
#SBATCH --mail-user={your_email}@polito.it
#SBATCH --partition=global
#SBATCH --time=00:30:00 {hh:mm:ss}
#SBATCH --nodes=1
#SBATCH --ntasks-per-node=32
#SBATCH --output={job_name}_%j.log
#SBATCH --mem-per-cpu=1024M
module load matlab/2019a
matlab -nodisplay -nosplash < main.m
```

- ➔ ‘esc key’ :wq (to exit)

To submit and run the job in the terminal window:

- ➔ sbatch {job_name}.sbatch

To Check the status of the job:

- ➔ squeue -u {username} (ex.: ltamatam)

To cancel the job:

- ➔ scancel ...

****

REMEMBER: The cluster processes are ‘batch processes’. Which means it is not interactive and have to wait until the job is done.

Once the program is successfully run, to post-process the data, copy the results to your local system [Linux / Windows] using command line or GUI.

Copy the results and other files from HACTAR Cluster to your local system:

In the Terminal Window type:

- ➔ scp -r {username}@hactarlogin.polito.it:/home/{username}/* {path to local folder in your Linux system}

OR use FileZilla using GUI.

How to obtain local path folder:
Go to the directory to your local folder using ‘cd’ command. Then type:

- ➔ pwd (print working directory).

****

If stuck/any questions, contact me at lakshminarayana.tamatam@polito.it

Official HPC PoliTo guide: https://hpc.polito.it/docs/guide-slurm-en.pdf